University of Alberta

Development of the Multi-Axis Biomechanical Testing Apparatus to Experimentally Measure In-Vitro Stresses on Knee Cortex under Gait Level Loads

by

Jena Lee Dressler   ©

A thesis submitted to the Faculty of Graduate Studies and Research in partial fulfillment of the requirement for the degree of *Master of Science.*

Department of Mechanical Engineering

Edmonton, Alberta
Fall 2008

Canada

Abstract

The multi-axis biomechanical testing apparatus (MABTA) is a six-degree of freedom quasi-static loading frame designed and developed to conduct *in vitro* experiments on cadaveric human, animal and composite specimens. MABTA features three manually adjustable rotational axes: flexion-extension, varus-valgus and internal-external plus three translational load applications: proximal-distal, medial-lateral and anterior-posterior.

MABTA can provide acceptable strain results and good repeatability between tests when testing with a third generation composite tibia and femur. A patient-specific finite element (FE) model of a composite tibia and femur was experimentally verified using MABTA. The FE von Mises (VM) strains satisfactorily predicted the experimental strain results for the composite tibia; however, the FE VM strain results cannot predict the experimental strain results as well for the femur. Further development and comparison with a FE bovine model is needed before concluding that MABTA produces reasonable and accurate experimental results with biological specimens; preliminary conclusions are encouraging.

Acknowledgements

I would like to extend my greatest thanks to my advisors Jason Carey and Alidad Amirfazli for allowing me the opportunity to work in this field. The knowledge, motivation, inspiration and constant support they have provided me has helped me to succeed in the completion of this thesis.

I would like to extend my love to my husband, family and friends for their constant support, understanding and knowledge throughout the completion of my studies.

I would like to extend my gratitude to Dr. Adrian Liggins and Mr. James Raso for supplying me with valuable knowledge in the area of biomechanics, to Richard Ng for designing MABTA, and to Anthony Au for all the information he has provided.

Finally, a special thanks to the technicians at the Mechanical Engineering Shop for offering their invaluable knowledge on design, software control and experimental work.

Table of Contents

List of Tables

List of Figures

Nomenclature

A: Cross sectional area

E: Modulus of elasticity also referred to as Young's modulus

$Flat$: Force applied to the lateral condyle when using custom-made loading jig

$Fmed$: Force applied to the medial condyle when using custom-made loading jig

$Ftot$: Total force applied to tibial and femoral condyles when using custom-made loading jig

Fx: Force applied in the x-direction, measured by the six degree of freedom load cell

Fy: Force applied in the y-direction, measured by the six degree of freedom load cell

Fz: Force applied in the z-direction, measured by the six-degree of freedom load cell

G: Shear modulus

Ix: Moment of inertia about the x-axis of a specimen

Ixy: Product of inertia

Iy: Moment of inertia about the y-axis of a specimen

Mx: Moment in the x-axis acting about the centre of gravity

Mx_{CG}: Moment acting at the centre of gravity of a particular cross section

Mx_E: Moment acting at the centre of the bone pot

Mx_{LC}: Moment acting at the centre of the six-degree of freedom load cell

My: Moment in the y-axis acting about the centre of gravity

My_{CG}: Moment acting at the centre of gravity of a particular cross section

My_E: Moment acting at the centre of the bone pot

My_{LC}: Moment acting at the centre of the six-degree of freedom load cell

Mz_E: Moment acting at the centre of the bone pot

Mz_{CG}: Moment acting at the centre of gravity of a particular cross section

Mz_{LC}: Moment acting at the centre of the six-degree of freedom load cell

x: Distance from centre of gravity of a particular cross section to an area of interest

y: Distance from centre of gravity of a particular cross section to an area of interest

ε': von Mises strain

ε_1: First principal strain

ε_2: Second principal strain

ε_3: Third principal strain

ε_D: Strain acting into the depth of the specimen

ε_L: Longitudinal strain acting along the cortex of composite and bovine bone

ε_T: Transverse strain

γ_{xy}: Shear strain

σ': von Mises stress

σ_1: First principal stress

σ_2: Second principal stress

σ_3: Third principal stress

σ_D: Stress acting into the depth of the specimen

σ_L: Longitudinal stress acting along the cortex of composite and bovine bone

σ_T: Transverse stress

τ_{xy}: Shear stress

v: Poisson's ratio

dA: Associated error of the cross sectional area

dE: Error in the modulus of elasticity value

dFlat: Relative error in the force applied to the lateral condyle when using custom-made loading jig

dFmed: Relative error in the force applied to the medial condyle when using custom-made loading jig

dFtot: Error in the total force applied to tibial and femoral condyles when using custom-made loading jig

dFx: Error in the force applied in the x-direction, measured by the six degree of freedom load cell

dFy: Error in the force applied in the y-direction, measured by the six degree of freedom load cell

dFz: Error in the force applied in the z-direction, measured by the six-degree of freedom load cell

dG: Error in shear modulus

dIx: Error in the moment of inertia about the x-axis of a specimen

dIxy: Error in the product of inertia

dIy: Error in the moment of inertia about the y-axis of a specimen

dMx: Error in the moment about the x-axis

dMx$_{CG}$: Error in the moment acting at the centre of gravity of a particular cross section

dMx$_E$: Error in the moment acting at the centre of the bone pot

dMx$_{LC}$: Error in the moment acting at the centre of the six-degree of freedom load cell

dMy: Error in the moment about the y-axis

dMy$_{CG}$: Error in the moment acting at the centre of gravity of a particular cross section

dMy$_E$: Error in the moment acting at the centre of the bone pot

dMy_{LC}: Error in the moment acting at the centre of the six-degree of freedom load cell

dMz_{CG}: Error in the moment acting at the centre of gravity of a particular cross section

dMz_E: Error in the moment acting at the centre of the bone pot

dMz_{LC}: Error in the moment acting at the centre of the six-degree of freedom load cell

dx: Surface reconstruction error

dy: Surface reconstruction error

$d\varepsilon'$: Error in von Mises strain

$d\varepsilon_1$: Error in first principal strain

$d\varepsilon_2$: Error in second principal strain

$d\varepsilon_3$: Error in third principal strain

$d\varepsilon_D$: Associated error of the strain acting into the depth of the specimen

$d\varepsilon_L$: Error associated with the longitudinal strain

$d\varepsilon_T$: Transverse strain associated error

$d\gamma_{xy}$: Shear strain associated error

$d\sigma'$: Error in von Mises stress

$d\sigma_1$: Error in first principal stress

$d\sigma_2$: Error in second principal stress

$d\sigma_D$: Associated error of the stress acting into the depth of the specimen

$d\sigma_L$: Associated error of the longitudinal stress

$d\sigma_T$: Transverse stress associated error

$d\tau_{xy}$: Error in the shear stress

dv: Relative error in Poisson's ratio

Glossary

1. Anatomical terminology:

Readers may refer to Figure 1.1: Anatomical Planes for practical illustrations.

- Anterior: The front surface of the body[2]

- Abduction: Moving a limb away from the median plane in the frontal plane[1]

- Adduction: Moving a limb towards the median plane in the frontal plane[1]

- Distal: Attachment farther away from the centre of the body (i.e. the femoral condyles of the knee are at the distal end of the femur); antonym: proximal

- Extension: Straightening or increasing the angle between parts of the body with a common joint[2]

- Flexion: Bending or decreasing the angle between parts of the body with common joints[2]

- Frontal plane: Vertical planes passing through the body orthogonal to the median plane; also known as coronal[4]

- Inferior: Refers to a structure situated nearer the lower section of the body[2] (i.e. the tibial condyles are inferior to the femoral condyles); antonym: superior

- Lateral: Further from the median plane of the body[2]

- Longitudinal: lengthwise or parallel to the long axis of the body[3]

---

[1]Moore, K.L., Dalley, A.F., 2006. Clinically Oriented Anatomy. 5th ed. Baltimore, MD: Lippincott Williams and Wilkins, pg 11.

[2] Moore, K.L., Dalley, A.F., 2006. Clinically Oriented Anatomy. 5th ed. Baltimore, MD: Lippincott Williams and Wilkins, pg 7.

[3] Moore, K.L., Dalley, A.F., 2006. Clinically Oriented Anatomy. 5th ed. Baltimore, MD: Lippincott Williams and Wilkins, pg 6.

- Median plane: The vertical plane passing longitudinally through the body, dividing the body into left and right halves[4]

- Medial: Nearer to the median plane of the body[2]

- Posterior: The back surface of the body or nearer to the back[2]

- Proximal: Attachment nearest to the centre of the body (i.e. the tibial condyles of the knee are at the proximal end of the tibia); antonym: distal

- Sagittal plane: Vertical planes passing through body parallel to median plane[4]

- Superior: Refers to a structure situated towards the upper section of the body[2] (i.e. the femoral neck is superior to the femoral condyles); antonym: inferior

- Transverse planes: Pass through body at right angle to the frontal and median planes

- Valgus: Outward bending of the knee joint

- Varus: Inward bending of the knee joint

2. Acronyms:

- 3D: three dimensional

- ACL: Anterior cruciate ligament

- A-P: Anterior-posterior

- BW: Body weight

- CMM: Coordinate measuring machine, MicroVal, Brown and Sharpe, (North Kensington, RI)

- DIC: Digital image correlation

- DOF: Degree of freedom

---

[4] Moore, K.L., Dalley, A.F., 2006. Clinically Oriented Anatomy. 5th ed. Baltimore, MD: Lippincott Williams and Wilkins, pg 5.

- F-E: Flexion-extension

- I-E: Internal-external

- MABTA: Multi-axis biomechanical testing apparatus

- M-L: Medial-lateral

- PVC: polyvinyl chloride

- P-D: Proximal-Distal

- TKA: Total knee arthroplasty

- TKR: Total knee replacement

- VM: von Mises

- V-V: Varus-valgus

Chapter 1: Introduction

The number of knee injuries and knee realignments is continuously rising and is no longer being performed only on the elderly but on the general public who have an increased desire to remain active and engage in sports activities. The two most studied and frequent knee surgeries are anterior cruciate ligament (ACL) reconstruction and total knee replacement (TKR). This thesis is focused on the development of an apparatus that will allow the testing of (1) ACL fixation device performance, (2) model studies including TKR components and (3) long bones in the lower limb for general stress/strain analysis. This chapter provides the necessary background information needed to fully understand the content presented in this thesis. The motivation, objective and scope are defined, followed by a detailed description of the knee anatomy.

1.1 Motivation

TKR is a procedure to treat severe arthritis and other knee degenerative diseases. In 2000, TKR was the most frequent arthritis-related procedure in Canada (Health Canada, 2003) with 23,130 people having knee replacements (Canadian Institute for Health Information, 2004). This number has continuously increased and by 2005-2006 there were 33,590 Canadians with TKRs, a rise of 125% since 1994-1995 and 12.5% from the previous year (Canadian Institute for Health Information, 2006). In 2004-2005, 94% of all TKRs were primary TKR with the remaining 6% being revision surgeries (Canadian Institute for Health Information, 2006). Aseptic loosening of the tibial prosthesis component accounted for 35% of all revision surgeries followed by poly wear,

1

osteolysis and instability at 30%, 18% and 13%, respectively (Canadian Institute for Health Information, 2006).

Aseptic loosening is a major concern. It is caused from the redistribution of applied loads on the implant, thus effectively shielding (i.e. stress shielding) the bone from loading, leading to bone resorption and weakening (Huiskies, 1998). Researchers believe that to decrease the number of revision knee surgeries, an effective understanding of stress shielding can be obtained through a finite element (FE) model of knee arthroplasty. Our research group at the Department of Mechanical Engineering, University of Alberta, as well as others, has been working on the development of such a FE model. Experimental equipment is needed to verify the results of this model. Also, such equipment can be useful for studying the development of various TKR systems, from an experimental perspective.

Ligaments are an essential component of the knee and act as joint stabilizers (Boskey and Posner, 1984). The anterior cruciate ligament (ACL) is one of the most commonly injured ligaments of the knee and occurs most frequently from sports injuries (Daniel et al., 1994). The various ACL fixation devices developed need to be examined and therefore equipment is needed to investigate the strengths and weaknesses of each design.

Lastly, the designed equipment can be used for the stress/strain analysis of lower limb long bones. The equipment can conduct *in vitro* experiments on a composite, animal or human bone or joint in various physiological loading conditions. The equipment will be useful for all three points discussed but this thesis will specifically present the equipment development in the context of TKR and bone modelling.

2

1.2 Thesis Objectives

This thesis describes the development, instrumentation, and calibration of a multi-axis biomechanical testing apparatus (MABTA). This includes further refinement of a previously designed and partly manufactured apparatus, the establishment of a robust data acquisition system (DAQ) to control, monitor and record output values throughout experimentation, the development of an experimental protocol that includes specimen preparation, loading requirements, health and safety considerations and the verification of MABTA's measured results.

A primary objective of this project is to develop MABTA into an apparatus with a high standard for experimenting with composite and biological tissues. In order to accomplish this objective, MABTA must provide accurate and repeatable results, be versatile to accommodate complete or partial human, bovine or composite specimens, be able to investigate the specimens under a variety of physiological loading conditions and through protocols and mechanical components be able to provide precise alignment of the specimens.

The developed MABTA was used to conduct *in vitro* experiments; first with specimens of known geometries and material property (i.e. polyvinyl chloride (PVC) simple cylinder), second with composite bones (third generation composite bones from Pacific Research Laboratories, Inc. Vashon, WA), and finally bovine specimens. Additionally *in vitro* experiments on composite bones were used to validate a patient-specific FE model for knee arthroplasty by measuring the strain distribution along the cortex of composite bones. In all experiments strain values were recorded using strain gauges.

3

It should be acknowledged that Richard Ng, a NSERC summer student and Dean's Research Award student from the Department of Mechanical Engineering, University of Alberta, completed the initial design of MABTA from May 2005 to April 2006.

1.3 Scope of Thesis

To achieve the objectives of this thesis the experimentation was restricted to a known geometry PVC pipe, third generation composite bone models (Pacific Research Laboratories, Inc. Vashon, WA) and bovine tibia and femur specimens. All loading was considered static and all analysis occurred at the macroscopic level. Soft tissue was removed from bovine specimens as the focus is on MABTA, and not necessarily biological investigations.

This work does not specifically focus on the validation of any model, but is focused on developing and validating experimental equipment and protocol for use in current and future studies related to the knee.

1.4 Background

To put the development of MABTA into context, the background information necessary to gain an understanding of the basic biomechanical definitions, the anatomy of the knee, how the different structures of the knee relate to its proper function, the mechanics associated with the knee and how the mechanics change based on surgical techniques is discussed in this section.

1.4.1 Anatomical Planes

Anatomical planes, described in many reference texts such as (Moore and Dalley, 2006, pg 5-6) and illustrated in Figure 1.1, are used to provide consistent descriptions of various anatomical positions. There are four anatomical planes, namely, the median, sagittal, coronal, and transverse planes. The median plane is the longitudinal plane that passes through the body dividing it into left and right halves. Sagittal planes pass through the body parallel to the median plane. Coronal or frontal planes are vertical planes that pass through the body at right angles to the median planes dividing the body into anterior and posterior sections. Transverse planes pass through the body at right angles to the median and frontal planes dividing the body into superior and inferior sections.
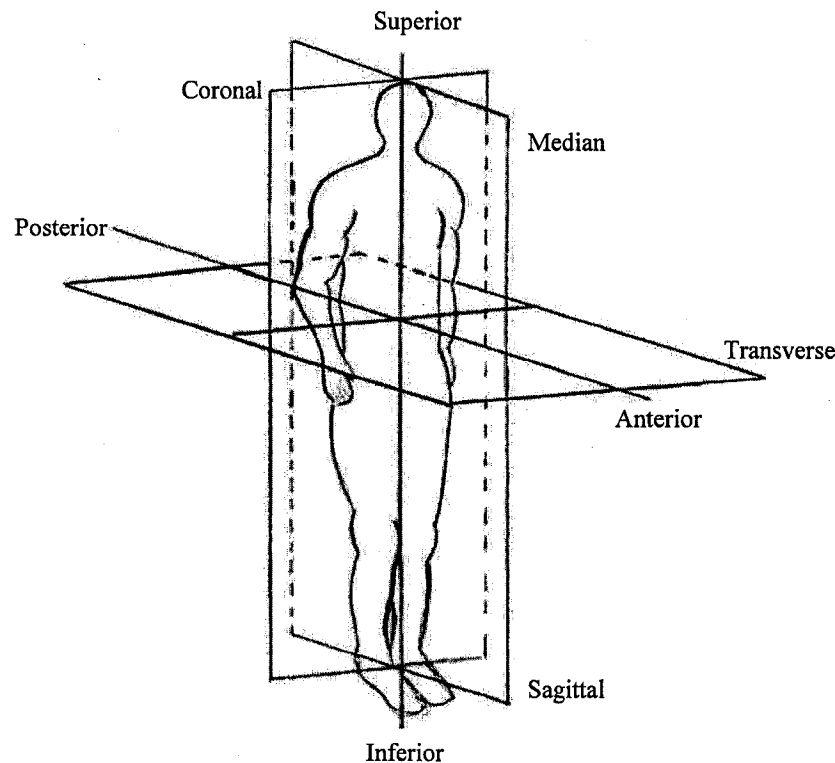
Figure 1.1: Anatomical Planes[5]

---

[5] Adapted from Wright and Radin, 1993, pg 41

1.4.2 The Knee Joint

Motion between segments occurs through a joint or articulation, defined as a junction between two or more bones (Salter, 1993). Joints have three functions: provide segmentation of the skeleton, permit varying amounts of skeletal growth and permit varying degrees of motion between segments (Salter, 1993).

The knee joint is classified as a synovial joint and is "one in which the opposing surfaces are covered by hyaline articular cartilage and are held together, or joined peripherally by ligaments and a fibrous capsule enclosing a joint cavity that contains synovial fluid" (Salter, 1993, pg 1). A typical human knee joint (Figure 1.2) consists of various structures such as articular cartilage, synovial membrane, ligaments, menisci, a fibrous membrane, a fat pad and in the case of the knee, the patella (Salter, 1993).

Muscle

Patella

Meniscus

Femur

Tibia

Fibrous Capsule

Synovial Membrane

Fat Pad

Articular Cartilage
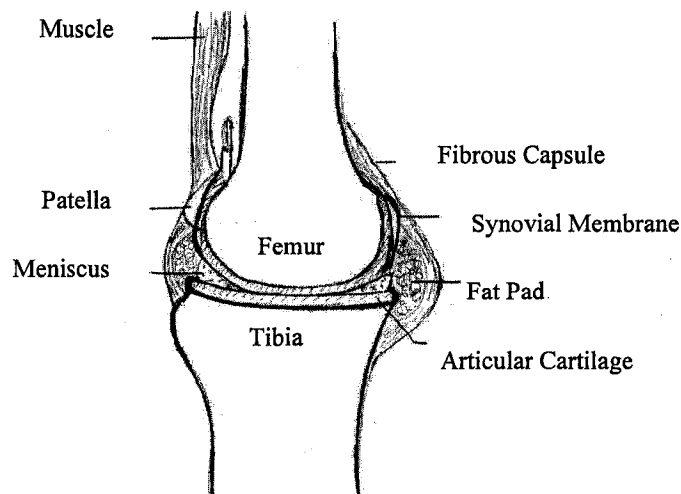
Figure 1.2: Sagittal section of the knee showing a typical human synovial joint[6]

The knee (Figure 1.3), associated with lower body motion, is one of the largest and most complex joints. It has both static and dynamic functions (Levangie and Norkin, 2001, pg 327). The knee joint works along with the hip and ankle joint to support the

---

[6] Adapted from Salter, 1993 pg 2

weight of the body while in a static upright position. It is also responsible for the transfer of weight during locomotion and supporting the body in many daily activities such as walking, squatting and sitting (Levangie and Norkin, 2001, pg 327). The knee joint is often classified as an idealized hinge type of synovial joint, which allows flexion and extension. These hinge movements are also combined with gliding, rolling and a rotation about a vertical axis (Moore and Dalley, 2006, pg 684).
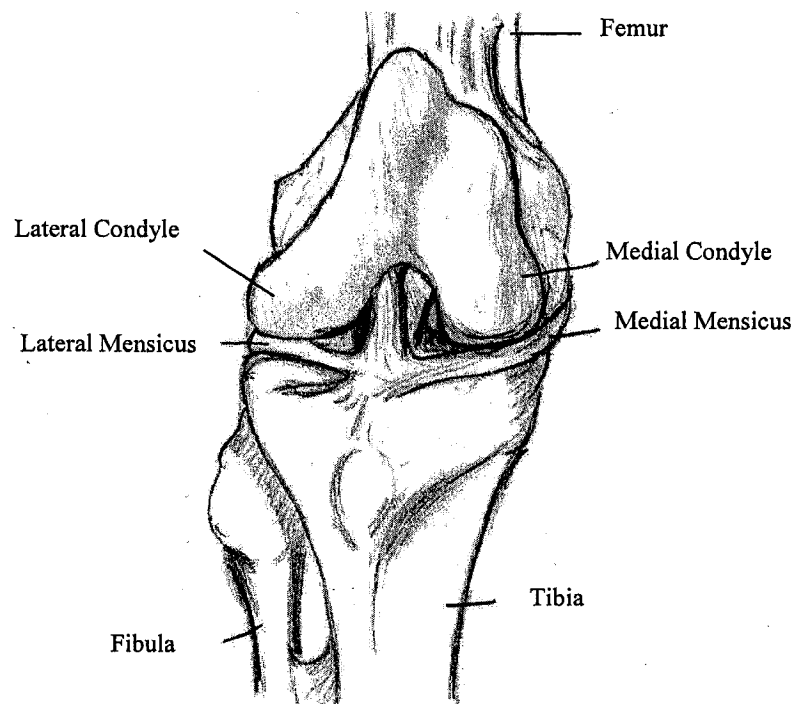
Figure 1.3: Anterior view of right knee joint[7]

The knee joint, composed of the distal femur, proximal tibia, patella and collateral ligaments (Hawk, 1993), consists of two articulating joints: the tibio-femoral joint, articulation between the proximal tibia and the distal femur, and the patella-femoral joint, articulation between the patella and the femur (Levangie and Norkin, 2001, pg 327). The femur (Figure 1.4) is the strongest and longest bone in the body while the tibia (Figure

[7] Adapted from http://www.bartleby.com/107/93.html. Accessed March 2007.

7

1.5) is known as the weight bearing bone of the lower limb (Wasielewski, 2003, pg 56).

The fibula, which lies parallel and lateral to the tibia, does not participate in weight

bearing but provides muscle and tendon attachment, while completing the ankle joint

(Wasielewski, 2003, pg 57).
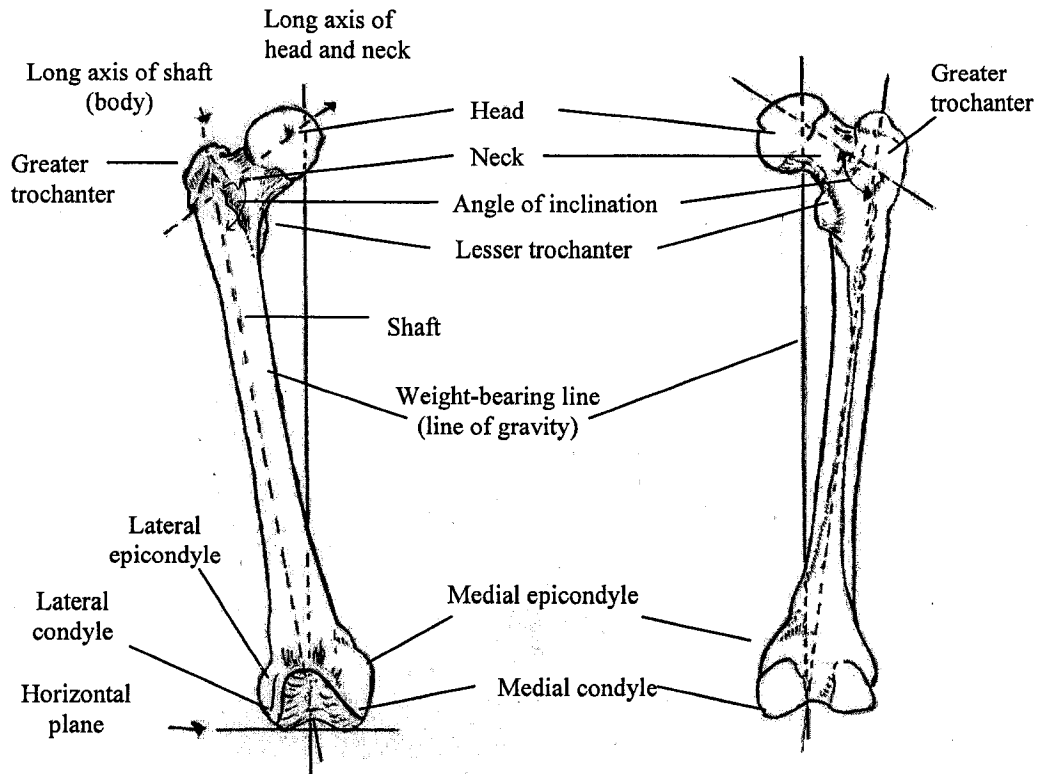
Figure 1.4: Bony features of adult right femur[8]

---

[8] Adapted from Moore and Dalley, 2006, pg 564

8
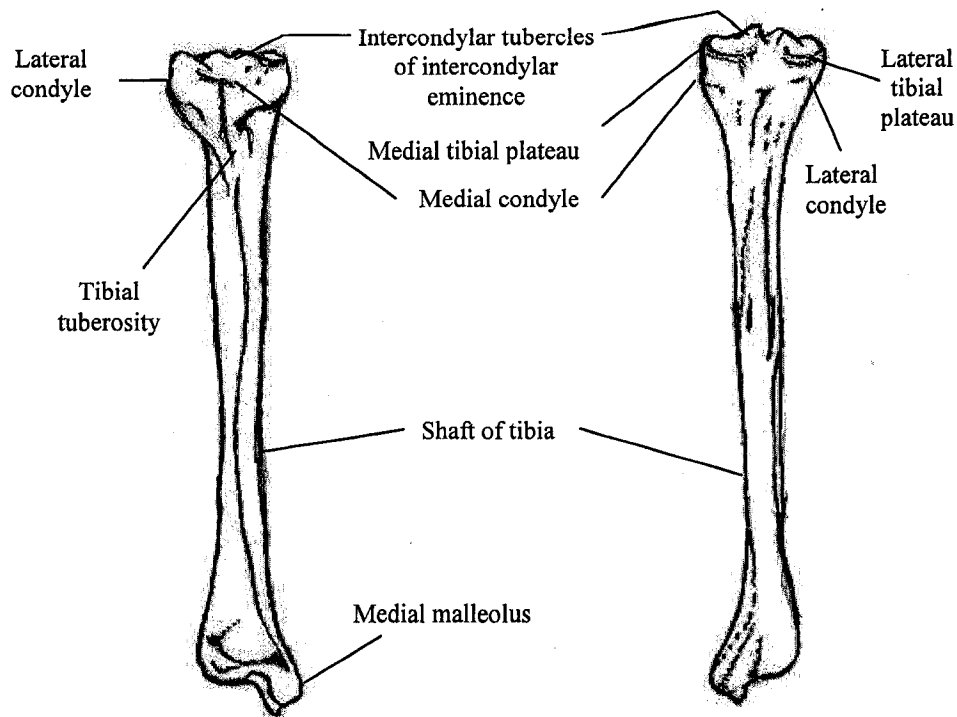
Figure 1.5: Bony landmarks of adult right tibia[9]

The knee joint is a complex six-degrees of freedom (DOF) joint: flexion-extension (F-E), varus-valgus (V-V) and internal-external (I-E) rotations plus anterior-posterior (A-P), medial-lateral (M-L) and proximal-distal (P-D) translations. Given the complexity and the 6 DOF of the knee joint, the specifications required for MABTA were unique in that the system was required to allow tri-axial load application at relatively small loads while allowing the specimen to be oriented in all three axes of rotation

The knee joint is relatively weak mechanically as it relies on the strength and behaviour of the surrounding muscles and their tendons, and the ligaments that connect the femur and tibia. The proper function of the knee joint not only depends on individual components but also on the collective structure of all components working as a single

---

[9] Adapted from Moore and Dalley, 2006, pg 567

9

unit. The structure and function of long bones (tibia, femur), tendons, ligaments, articular

cartilage, synovial joint/fluid and menisci are described below.

1.4.2.1 Long Bones
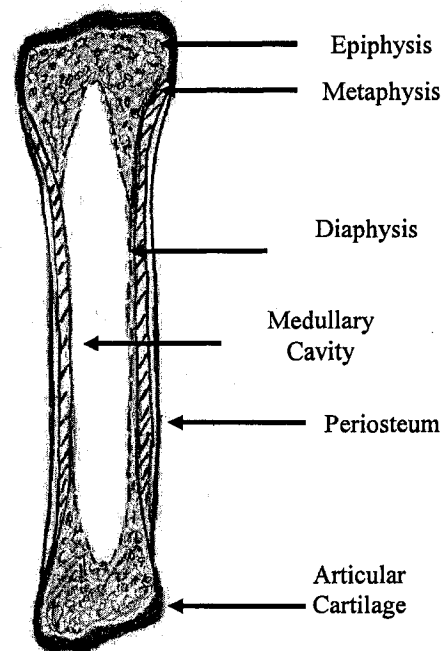
Figure 1.6: Structure of the long bone[10]

A typical mature long bone (i.e. tibia or femur), Figure 1.6, consists of a diaphysis

(shaft), with an expansion at each end called the metaphysis. At the end of the metaphysis

are the epiphyses (Fung, 1981). Articular cartilage, which forms the gliding surface of the

joint, covers the ends of the epiphyses (Fung, 1981).

The diaphysis is a hollow tube with the walls consisting of dense cortex or

compactum. The central space within the diaphysis, which contains bone marrow, is

called the medulla or medullary cavity. (Fung, 1981)

---

[10] Adapted from Fung, 1981, pg 386

10

The periosteum, which has two layers, covers most of the external surface of a mature long bone except for the area of articulation, is very thin and loosely attached. Ligaments are attached to the expanded ends of the long bones and heavy fascial septa are attached to the ridges along the diaphyses (Fung, 1981).

There are two types of bone: cortical and cancellous bone. Both of these types of bone are different in microstructure, which in turn will influence their structural properties and their function. Cortical bone is mostly found in the shafts of long bones (Boskey and Posner, 1984) and is made up of densely packed collagen fibrils that form the outer layer wall of all bones (Jee, 2001). Approximately 80% of the skeletal mass consists of cortical bone and is responsible for the supportive and protective function of the skeleton (Jee, 2001). The remaining 20% of the skeletal mass is formed from cancellous bone (Jee, 2001). It is mostly found in the epiphyseal and metaphyseal region of long bones and within the cortical confinements of flat and short bones (Boskey and Posner, 1984).

Cortical bone provides most of the loading support (Askew and Lewis, 1981); as such strain gauges will be placed on the cortex of the composite and bovine bones. This will allow the stress/strain distribution on the surface of composite and bovine bones to be measured and analysed and thus the third objective can be achieved.

1.4.2.2 Ligaments

Ligaments are soft-tissue connections between bones, which allow movement at the joint but provide physical restraints to an unwanted range of motion (Hartright et al., 2006). They act as stabilizers both inside and about the joint from the proximal end of the bone to the distal end of the joint (Boskey and Posner, 1984). The main function of

11

ligaments is to "guide joint movements, to maintain joint congruency, and to act as a positional bend or strain sensor for the joint" (Ambrosio et al., 2002, pg 357). In a general sense, the main mechanical function of ligaments is to transmit loads between the skeletal elements that they connect (Ambrosio et al., 2002).
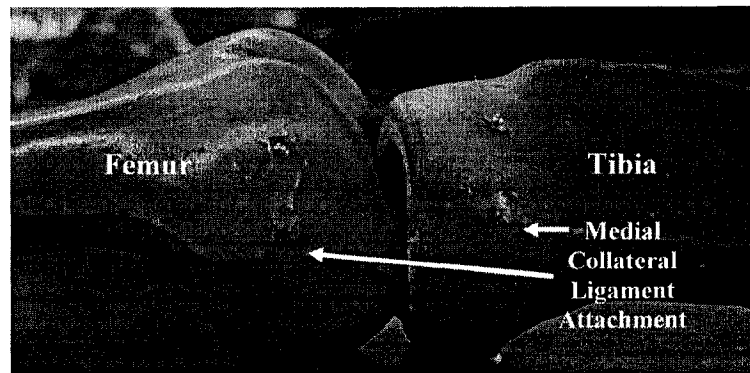
Figure 1.7: Ligament attachments on the medial side of left composite knee joint
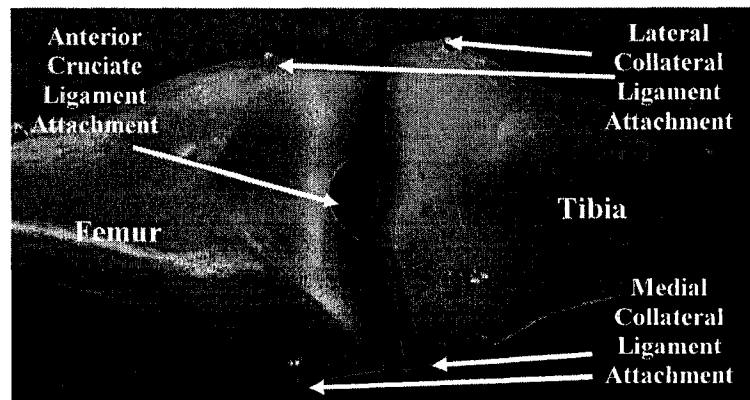
Figure 1.8: Ligament attachments from the anterior side of left composite knee joint
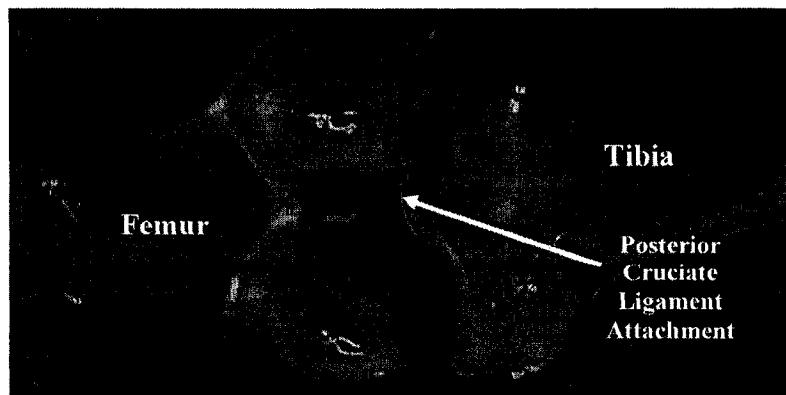
Figure 1.9: Ligament attachments on the posterior side of left composite knee joint

12

Figure 1.7 through Figure 1.9 indicates the different ligament attachments of the knee. Ligaments consist of water (60-80% wet weight), elastin, glycolipids, proteoglycans, fibroblasts, and collagens (Hartright et al., 2006). Since collagen is one of the strongest fibrous proteins and given its parallel longitudinal arrangement, the anterior cruciate ligament can have tensile strengths and stiffness in the range of 1725 ± 269 N and 182 ± 33 N/mm (Seedhom, 1993, pg 170; Noyes and Grood, 1976), respectively.

As listed above, ligaments provide extensive advantages to the knee joint. ACL reconstructive surgery is another topic where much research is continually completed to determine the best ACL fixation device. The robust functional capability of MABTA, the height adjustability to include many types of specimens and the capacity to place the knee joint under various physiological loading conditions, enables MABTA to examine the design and functionality of various ACL fixation devices.

1.4.2.3 Synovial Joints/Fluid

The synovial membrane, which has the ability to secrete and absorbs fluid, covers the entire surface of the joint cavity except the surfaces of the articular cartilage and menisci (Salter, 1993). Synovial fluid is a clear or slightly yellow viscous fluid contained in the joint cavities, tendon sheaths and bursae mucosae (Barnett et al., 1961). Synovial fluid provides the articular cartilage with nourishment and lubrication to the joint surfaces (Salter, 1993).

13

1.4.2.4 Articular Cartilage

Articular cartilage, or hyaline cartilage, can be found on the articular surface of bones. The purpose of articular cartilage is to act as a shock absorber for impact loads, provide lubrication for joint surfaces, and serve as a load bearing surface in normal function (Fung, 1981). It is a resilient material that exhibits viscoelastic behaviour, which makes it the ideal material in synovial joints as it can withstand the shear and compression forces of normal joint function (Salter, 1993).

Additionally articular cartilage has unique and extraordinary lubricating properties. It has a coefficient of friction (Table 1.1) many times less than the best artificial material (Fung, 1981) and possesses a coefficient of friction 1/5 of that between two pieces of ice (Salter, 1993).

Table 1.1: Coefficients of friction values for articular cartilage in various synovial joints[11]

Researcher	Coefficient of Friction	Studied Joint
Charnley, 1960	0.005-0.02	Human Ankle
McCutchen, 1962	0.02-0.35	Porcine Shoulder
Linn, 1968	0.005-0.01	Canine Ankle
Unsworth et al., 1975	0.01-0.04	Human Hip
Malcom, 1976	0.002-0.03	Bovine Shoulder

One of the most significant weaknesses of cartilage is its lack of ability to heal or regenerate (Salter, 1993). Once articular cartilage has extensively deteriorated and is no longer acting as a shock absorber for impact loads, TKR is suggested. This then relates back to the objectives of this thesis: develop a machine that can investigate the design of TKR devices designed for a specific patient.

---

[11] adapted from Mow and Ateshian, 1997, pg 287

14

1.4.2.5 Menisci

Menisci are fibrocartilagenous tissues located on the perimeter of the tibial condyles (Ahmed and Burke, 1983; Levangie and Norkin, 2001, pg 328) with a concave femoral surface and a flat tibial surface (Aagaard and Verdonk, 1999). The shape of the menisci, Figure 1.10, varies depending on the location: the medial meniscus is almost a semicircle while the lateral meniscus is approximately four-fifths of a ring (Bannister et al., 1995 pg 703-704).
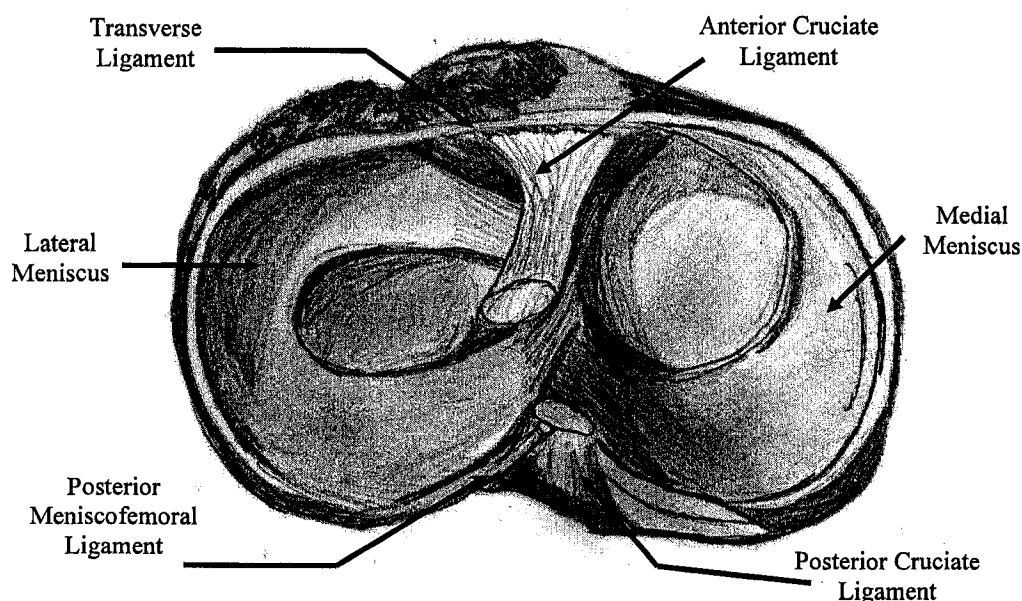
Figure 1.10: Superior aspect of the left tibia, indicating the menisci and the tibial attachments of the cruciate ligaments[12]

The menisci are known as accessory joint structures that assist in the balance between mobility and stability and improve the congruity needed by the joint (Levangie and Norkin, 2001, pg 328) by partially filling the dead spaces between the tibial and femoral articulating surfaces (Ahmed and Burke, 1983; Steindler, 1995, pg 340) and increasing the radius of curvature of the tibial condyles (Levangie and Norkin, 2001, pg

---

[12] adapted from Bannister et al., 1995, pg 702

15

329). By increasing this articular contact, the menisci are able to distribute the weight-bearing forces throughout the knee, reduce the friction between the joint segments and serve as shock absorbers (Aagaard and Verdonk, 1999). Additionally the menisci protect the capsular wall from being damaged between the tibia and femur and expand the shallow tibial sockets (Steindler, 1995, pg 340).

It has been found that the menisci transmit at least 50% of the compressive load across the knee joint in full extension (Ahmed and Burke, 1983, Abbot et al., 2003, pg 94). This load distribution remains relatively constant through flexion up to 60° but increases to approximately 85% at 90° flexion (Abbot et al., 2003 pg 94).

1.4.3 Knee Mechanics

Together, topics such as the motion and range of motion of the knee, gait, loading and contact area all describe the mechanics of the knee. These topics provide essential but brief details needed to understand the knee joint.

The knee joint is associated with two motions: flexion-extension rotation and medial-lateral translation. The knee uses a combination of rolling and gliding of the femur on the tibia to allow for flexion-extension motion (Tencer, 2003 pg 125). Due to the knee's complexity, neither rolling nor gliding motion can occur independently, both must be done conjointly otherwise full extension of the knee is not accomplished. With rolling motion alone, maximum flexion could not be achieved as the femoral condyle would roll off of the tibial plateau and similarly, with gliding alone the femoral shaft would impose on the tibia (Tencer, 2003, pg 126). The anterior cruciate ligament (ACL) and posterior cruciate ligament (PCL) guide the motion of the knee. These cruciate ligaments are arranged in a cross configuration (Figure 1.11) with attachments to the tibia

16

and femur perfectly located as to guide the femur as it travels on the tibia (Tencer, 2003, pg 126).
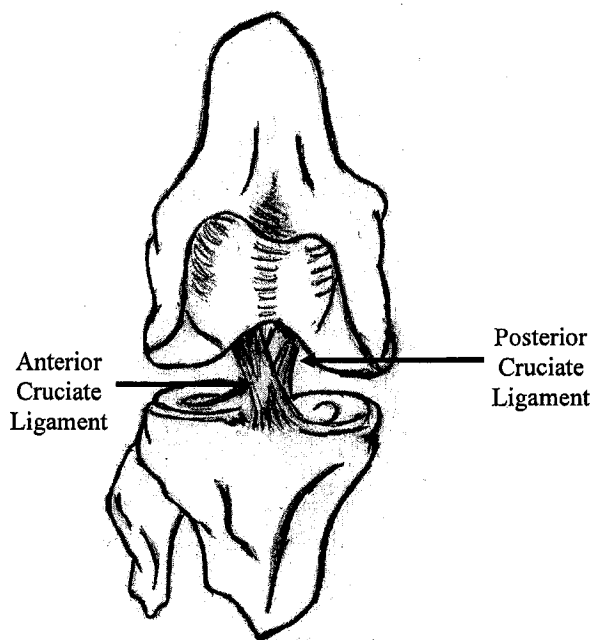
Figure 1.11: Sketch illustrating the cross configuration of the cruciate ligaments[13]

According to Hawk (Hawk, 1993), a person normally obtains between 120° and 140° flexion from a fully straight position (0°), a medial rotation of 30° to 40° and lateral rotation of 60°. There is approximately 6° valgus between the normal anatomical axis of the femur and the axis of the tibia and a 2° or 3° valgus between the tibia axis and the vertical axis of the body measured from the feet (Hawk, 1993). MABTA was designed to achieve 100° flexion and 50° hyperextension, ± 20° V-V rotation and 30° I-E rotation to increase the robustness and ability to apply all the different types of loading.

To fully comprehend the mechanics of the knee, an understanding of the different phases of knee motion and the required angles of flexion during gait is invaluable. Gait can be described in four phases: heel-strike, stance, toe-off and swing, with the stance and

---

[13] Adapted from Kapandji, 1987, pg 127

17

swing phase corresponding to 60% and 40% of the total gait cycle, respectively (Ramsey et al., 2001). All of these phases require a different range of flexion. Several studies found that maximum flexion occurs during the swing phase (Kettelkamp et al, 1970; Freeman and Pinskerova, 2005; Morrison, 1970) with a required flexion angle of approximately 67° (Kettelkamp et al, 1970). Studies done by both Freeman and Pinskerova (Freeman and Pinskerova, 2005) and Kettelkamp (Kettelkamp et al, 1970) found that a flexion angle of approximately 20° is needed for the stance phase (Freeman and Pinskerova, 2005; Morrison, 1970; Kettelkamp et al, 1970) and increases between 40° (Freeman and Pinskerova, 2005) to 55° (Morrison, 1970) at toe off.

The knee is subjected to a range of joint forces depending on the gait phase; highest loads occur at heal strike and toe-off and the lightest loads occur during the swing phase (Mow and Ateshian, 1997; Abbot et al., 2003 pg.93). The joints of the lower limb are most frequently subjected to a variety of loads depending on the activity; level surface walking and stance are the two most common daily activities (Paul, 1976).

During level walking, a force along the tibia axis may reach more than twice body weight (BW) following heel strike due to the knee's absorption of the impact between foot and ground. This increases to four times BW near toe-off when the leg's extensor muscle contracts to propel the body forward (Tencer, 2003 pg 125). Mow and Ateshian (Mow and Ateshian, 1997) found that the average load at the joint is approximately three times BW and occurs for 60% of the walking cycle (Abbot et al., 2003 pg.93). To attempt to achieve these physiological loading conditions, MABTA can apply a P-D load of 4448 N (1000 lb) and a M-L and A-P load of 2224 N (500 lb).

18

From Morrison's study (Morrison, 1968) of the force actions on the human knee joint, it was found that a maximum joint force of 4.0 times BW and a mean maximum value of 3.03 times BW were required for normal level walking. Morrison (Morrison, 1969) later found that the average maximum forces required for ascending and descending stairs and ramps were 12% to 25% higher than the average maximum forces calculated in the joint during level walking.

Studies have been done to determine the contact area and load distribution between the lateral and medial condyles in the knee joint (Kettelkamp and Jacobs, 1972; Thambyah et al., 2005; Brown and Shaw, 1984; Harrington, 1983; Werner et. al, 2005). The medial contact area is approximately 1.6 times larger than the lateral contact area (Kettelkamp and Jacobs, 1972). Similarly, Morrison (Morrison, 1969) found that during the stance phase, the medial condyles transmitted the greater part of the joint force. Andriacchi and Hurwitz (Andriacchi and Hurwitz, 1997) also saw this fact in a study on gait biomechanics and TKA where the medial condyle of the knee sustained approximately 70% of the load. Harrington (Harrington, 1983) concluded that the majority of the total joint load was located in the medial condyle during static and dynamic testing with the lateral compartment carrying absolutely no force during static testing.

1.4.4 Knee Surgical Procedures

Once the knee joint is no longer performing its primary functions, knee surgery may be necessary. Meniscectomy and TKR are two surgical procedures used to remedy joint pain and improve functionality of the knee joint but can also cause issues of their own.

19

1.4.4.1 Meniscectomy

The menisci are an important addition to the knee joint and if removed would be detrimental to the proper function of the joint. The menisci contact area varies with load and ranges from 72% of the total tibial area on the medial side at 200 N to 64% at 1000 N and on the lateral side, from 95% to 80% (Tencer, 2003, pg 130; Fukubayshi and Kurosawa, 1980). The removal of the menisci decreases the contact area of the knee joint more than half its original size (Fukubayshi and Kurosawa, 1980; Tencer, 2003, pg 130), therefore, it can be concluded that the menisci are essential for widening the tibiofemoral contact area (Fukubayshi and Kurosawa, 1980). In the study completed by Fukubayshi and Kurosawa (Fukubayshi and Kurosawa, 1980) it was found that the medial meniscus had a contact area 25% greater than that of the lateral meniscus at a load of 1000 N; this difference increased to 30% after the removal of the menisci. Fukubayshi and Kurosawa (Fukubayshi and Kurosawa, 1980) recommended that partial meniscectomy should be chosen over total meniscectomy.

Ahmed and Burke (Ahmed and Burke, 1983) performed an extensive study of the effects of partial and total meniscectomy. It was found that in total meniscectomy 50%-70% of the tibiofemoral contact area was lost and consequently caused an increase in peak pressure, high pressure area and the pressure gradient at the edges of the contact area. Furthermore the average contact stress was considerably higher and increased more rapidly with increasing compressive load and had a much higher peak value than that found in an intact joint (Abbot et al., 2003 pg 94).

Fairbank (Fairbank, 1948) suggested that after meniscectomy the knee joint undergoes various degenerative changes such as ridge formation, flattening of the

20

femoral condyle and narrowing of the joint space. It was suggested that these degenerative changes could be caused from the loss of the weight-bearing function of the menisci.

Future TKR designs can be examined in MABTA so that the above observations are avoided and to ensure that the best design is implemented for each patient.

1.4.4.2 Total Knee Replacement

TKR, also known as total knee arthroplasty (TKA) is the final treatment for knee arthritis. Arthroplasty can be defined as the "the plastic surgery of a joint or joints, or the formation of movable joints" (Brugioni and Falkel, 2004, pg 24). In TKA surgery, as described in "Total Knee Replacement and Rehabilitation (Brugioni and Falkel, 2004), the femoral condyles, tibial plateau and patella are resurfaced, replacing the cartilage surfaces with metal and plastic components. The femoral condyles and tibial plateau are surgically removed with the femoral condyles being replaced by a cobalt-chromium alloy and the tibial plateau being replaced by a metal tray and plastic insert. The resurfaced femoral condyles slide along the high-density, high-molecular weight polyethylene insert, relying on the mechanics of the preserved tendons, ligaments and muscles for proper alignment of the joint surfaces. The ability to test TKR implants is one criterion for the development of MABTA.

1.4.5 Knee Bone Mechanical Properties

Reilly and Burstein (Reilly and Burstein, 1975) found the elastic properties of human and bovine compact bone. These properties are summarized in Table 1.2 where E and v are the respective elastic modulus and Poisson's ratio for transverse or radial

21

specimens, E' and v' are the respective elastic modulus and Poisson's ratio for longitudinal specimens and G' is the shear modulus.

Table 1.2: Mechanical properties of human and bovine femoral compact bone

Bone	Human Femoral Compact Bone	Bovine Haversian Femoral Compact Bone
E	11.5×10^9 N/m^2	10.2×10^9 N/m^2
E'	17.0×10^9 N/m^2	22.6×10^9 N/m^2
G'	3.28×10^9 N/m^2	3.6×10^9 N/m^2
v	0.58	0.51
v'	0.46	0.36

Mature cortical bone is composed of approximately 20% water (Carter and Spengler, 1978) therefore the mechanical properties of bone listed in Table 1.2 are affected by the condition and preparation of the specimen. This includes the level of moisture, preservation and temperature.

A study done by Adharapurapu et al. found that dry bone has a higher strength and lower strain to failure than wet bone (Adharapurapu et al., 2006). Evans and Lebow (Evans and Lebow, 1951) studied the effect of drying on cortical bone on 242 specimens from 12 femurs. Results from this study show that air-drying increased the average ultimate tensile strength by 31.3%, the modulus of elasticity by 17.6% and the hardness by 54.3%. The shearing strength and tensile strain were reduced by 18.3% and 45%, respectively. Also it was found that drying reduces the energy-absorbing capacity of bone (Evans and Lebow, 1951).

Another factor that could change the mechanical properties of bone is the preservation or storage method used between collecting and testing of the specimen. The main concerns with preservation are to prevent the specimen from drying and degrading. The degradation of mechanical properties begins immediately after the life to death

22

transition and leads to changes in the bone mineral properties therefore changing the mechanical properties of the tissue. Immediate preservation after removal from the body can minimize this problem. Different methods of preservation include storing the specimen in water, physiological saline solution, embalming fluid, alcohol or freezing it (Langton and Njeh, 2004). The mechanical properties of biological specimens seemed to be unaffected by the freezing and thawing of the specimen to body temperature as long as the tissue is adequately hydrated (Langton and Njeh, 2004). Freeze-drying has been shown to produce a significant decrease in the ultimate strength and modulus of elasticity (Cornu et al., 2005) and embalmed material provides different values of strength and elasticity when compared with fresh tissue (Langton and Njeh, 2004).

Temperature is another factor that will affect the modulus of elasticity of biological materials but was shown to be reversible (Smith and Walmsley, 1959).

In this chapter, the issues relevant to the thesis at hand were discussed. The design, development and verification of the multi-axis biomechanical testing apparatus are presented in the next chapter.

References

Aagaard, H., Verdonk, R., 1999. Function of the normal meniscus and consequences of meniscal resection. Scandinavian Journal of Medicine and Science in Sports 9, 134-140.

Abbot, A.E., Levine, W.N., Mow, V.C. Biomechanics of the Articular Cartilage and Menisci of the Adult Knee. In: Callaghan, John. C, et al. eds. *The Adult Knee*. Vol. 1. Philadelphia, PA: Lippincott Williams and Wilkins, 2003.

Adharapurapu, R.R., Jiang, F., Vecchio K.S., 2006. Dynamic fracture of bovine bone. Materials Science and Engineering C (26), 1325 – 1332.

Ahmed, A.M., Burke, D.L., 1983. In-vitro measurement of static pressure distribution in synovial joints – Part I: Tibial surface of the knee. Journal of Biomechanical Engineering 105, 216-225.

Ambrosio, L., Netti, P.A., Nicolais, L., 2002. Soft Tissue. In: Barbucci, R. ed. *Integrated Biomaterials Science*. New York: Kluwer Academic / Plenum Publishers, 347-365.

Andriacchi, T.P., Hurwitz, D.E., 1997. Gait Biomechanics and Total Knee Arthroplasty. The American Journal of Knee Surgery 10(4), 255-260.

Askew, M.J, Lewis, J.L., 1981. Analysis of model variables and fixation post length effects on stresses around a prosthesis in the proximal tibia. Transactions of ASME, Journal of Biomechanical Engineering 103, 239-245.

Bannister, L.H., Berry, M.M. Collins, P., Dyson, M., Dussek, J.E., Ferguson, M.W.J. Gray's Anatomy: the anatomical basis of medicine and surgery. 38th Ed. New York: Churchill Livingstone, 1995.

Barnett, C.H., Davies, D.V., MacConaill, M.A.. Synovial Joints: Their Structure and Mechanics. London: Longmans, Green and Co Ltd., 1961.

Boskey, A.L., Posner, A.S., 1984. Structure and Formation of Bone Mineral. In: Hastings, G.W., Ducheyne, P. eds. Natural and Living Biomaterials. Florida: CRC Press, 27-41.

Brown, T.D., Shaw, D.T., 1984. In vitro contact stress distribution on the femoral condyles. Journal of Orthopaedic Research 2, 190-199.

Brugioni, D.J., Falkel J. Total Knee Replacement and Rehabilitation: The Knee Owner's Manual. Alemeda, CA: Hunter's House Inc, 2004.

Canadian Institute for Health Information (2004). *Canadian Joint Replacement Registry. 2004 Report: Total hip and total knee replacements in Canada.* Ottawa: Health Canada.

Canadian Institute for Health Information (2006). *Canadian Joint Replacement Registry (CJRR) 2006 Report: Hip and total knee replacements in Canada.* Ottawa: Health Canada.

Carter, D.R., Spengler, D.M., 1978. Mechanical Properties and Composition of Cortical Bone. Clinical Orthopaedics and Related Research 135, 192-217.

Charnley, J., 1960. The lubrication of animal joints in relation to surgical reconstruction by arthroplasty. Annals of Rheumatic Diseases 19, 10-19.

Cornu, O. et al., 2000. Effect of Freeze-Drying and Gamma Irradiation on the Mechanical Properties of Human Cancellous Bone. Journal of Bone and Joint Surgery 18, 426-431.

Daniel, D.M., Stone, M.L., Dobson, B.E., Fithian, D.C., Rossman, D.J., Kaufman, K.R., 1994. Fate of the ACL-injured patient. A prospective outcome study. American Journal of Sports Medicine 22 (5), 632-644.

Evans, F.G., Lebow M., 1951. Regional Differences in Some Physical Properties of the Human Femur. Journal or Applied Physiology 3(9), 563-572.

Fairbank, T. J., 1948. Knee joint changes after meniscectomy. Journal of Bone and Joint Surgery 30 B (4), 664-670.

Freeman, M.A.R., Pinskerova, V., 2005. The movement of the normal tibio-femoral joint. Journal of Biomechanics 38, 197-208.

Fukubayshi, T., Kurosawa H., 1980. The contact area and pressure distribution pattern of the knee: A study of normal and osteoarthrotic knee joints. Acta Orthopaedica Scandinavica 51, 871-879.

Fung, Y.C., 1981. Bone and Cartilage. In: *Biomechanics: Mechanical Properties of Living Tissues*. New York: Springer-Verlag New York Inc., 383-415.

Harrington, I.J., 1983. Static and dynamic loading patterns in knee joints with deformities. The Journal of Bone and Joint Surgery 65-A(2), 247-259.

Hartright, D., Butler, A.M., Gillies, R.M., Bruce, W.J., Walsh, W.R., 2006. Biomechanical and Clinical Evaluation of Tendons and Ligaments. In: Walsh, W.R. ed. Repair and Regeneration of Ligaments, Tendons, and Joint Capsule. Totowa, New Jersey: Humana Press, 185-199.

Hawk, A., 1993. Recreating the Knee: The History of Knee Arthroplasty. Caduceus 9 (3), 175-194.

Health Canada (2003). *Arthritis in Canada. An ongoing challenge.* Ottawa: Health Canada (Cat. #H39-4/14-2003E).

Huiskes R., 1998. The causes of failure for hip and knee arthroplasties. Ned Tijdschr Geneeskd 142, 2035–2040 (English translation of abstract).

Jee, W.S.S., 2001. Integrated Bone Tissue Physiology: Anatomy and Physiology. In Cowin, S.C. ed. *Bone Mechanics Handbook*. New York: CRC Press LLC, 1-68.

Kapandji, I. A., 1987. The Physiology of the Joints: Volume Two Lower Limb. New York, USA: Churchill Livingstone.

Kettelkamp, D.B., Jacobs, A.W., 1972. Tibiofemoral contact area – determination and implications. Journal of Bone and Joint Surgery 54-A(2), 349-356.

Kettelkamp, D.B., Johnson, R.J., Smidt, G.L., Chao, E.Y.S., Walker, M., 1970. An electrogoniometric study of knee motion in normal gait. Journal of Bone and Joint Surgery 52-A(4), 775-790.

Langton, C.M., Njeh, C.F., 2004. The Physical Measurement of Bone. Bristol: Institute of Physics Publishing. Ebrary. University of Alberta Library, Edmonton. 23 Nov. 2006. <http://www.physicsnetbase.com/books/3026/IP736_Ch05.pdf>.

Levangie, P.K., Norkin C. C., 2001. The Knee Complex. In: Levangie, P.K., Norkin C. C. Joint Structure and Function: A Comprehensive Analysis. 3rd edition. Philadelphia, PA, USA: F. A. Davis Company, 326-366.

Linn, F. C., 1968. Lubrication of animal joints: I. The arthrotrip-someter. J. Bone and Joint Surgery 49A, 1079-1098.

Linn, F.C., 1968. Lubrication of animal joints: II. The mechanism. J. Biomechanics 1, 193-205.

Malcom, L. L., 1976. An experimental investigation of the frictional and deformational responses of articular cartilage interfaces to static and dynamic loading. Ph.D. Thesis, University of California, San Diego.

McCutchen, C.W., 1962. The frictional properties of animal joints. Wear 5, 1-17.

Moore, K.L., Dalley, A.F., 2006. Clinically Oriented Anatomy. 5th ed. Baltimore, MD, USA: Lippincott Williams and Wilkins.

Morrison, J.B., 1968. Bioengineering analysis of force actions transmitted by the knee joint. Biomedical Engineering 3(4), 164-170.

Morrison, J.B., 1969. Function of the knee joint in various activities. Biomedical Engineering 4(12), 573-580.

Morrison, J.B., 1970. The mechanics of the knee joint in relation to normal walking. Journal of Biomechanics 3, 51-61.

Mow, V.C., Ateshian, G.A., 1997. Lubrication and Wear of Diarthrodial Joints. In: Mow VC, Hayes WC, eds. Basic Orthopaedic Biomechanics. 2nd ed. Philadelphia, PA: Lippincott - Raven Publishers, 275-315.

Noyes, F.R., Grood, E.S., 1976. The strength of the anterior cruciate ligament in humans and Rhesus monkeys: Age-related and species-related changes. Journal of Bone and Joint Surgery [Am] 58, 1074-1082.

Paul, J.P., 1976. Approaches to design. Force actions transmitted by joints in the human body. Proceedings of the Royal Society of London – Biological Sciences 192 (1107), 163-172.

Ramsey, V., Horvat, M., Croce, R., 2001. Gait characteristics before and after knee replacement surgery: a case study. Clinical Kinesiology 55(3), 59-64.

Reilly, D.T., Burstein, A.H., 1975. The elastic and ultimate properties of compact bone tissue. Journal of Biomechanics 7, 393-405.

Salter, R.B. Normal Structure and Function of Joint Tissues, 1993. In: Salter, R.B. Continuous Passive Motion (CPM): A Biological Concept for the Healing and Regeneration of Articular Cartilage, Ligaments, and Tendons. Baltimore, Maryland, USA: Williams & Wilkins, 1-8.

Seedhom, B.B. Ligament Reconstruction with Reference to the Anterior Cruciate Ligament of the Knee. Mechanics of Human Joints. Wright ed. 1993 Marcel Dekker, Inc. New York, NY, USA, 163-201.

Smith, J.W., Walmsley, R., 1959. Factors Affecting the Elasticity of Bone. Journal of Anatomy 93(4), 503-523.

Steindler, A, 1995. Mechanics of the Knee Joint. In: Steindler, A. Kinesiology of the Human Body under Normal and Pathological Conditions. Springfield, Illinois, USA: Charles C. Thomas Publisher, 326-349.

Tencer, A.F., 2003. Biomechanics of the Knee. In: Callaghan, John. C, et al. eds. The Adult Knee. Vol. 1. Philadelphia, PA, USA: Lippincott Williams and Wilkins, 2003.

Thambyah, A., Goh, J.C.H., Das De, S., 2005. Contact stresses in the knee joint in deep flexion. Medical Engineering and Physics 27, 329-335.

Unsworth, A., Dowson, D., Wright, V., 1975. Some new evidence on human joint lubrication. Annals of Rheumatic Diseases 34, 277-285.

Wasielewski, R.C., 2003. Surgical Anatomy of the Knee. In: Callaghan, John. C, et al. eds. The Adult Knee. Vol.1 Philadelphia, PA, USA: Lippincott Williams and Wilkins, 55-79.

Werner, F.W., Ayers, D.C., Maletsky, L.P., Rullkoetter, P.J., 2005. The effect of valgus/varus malalignment on load distribution in total knee replacements, Journal of Biomechanics 38, 349-355.

Wright, Verna and Eric L. Radin. Mechanics of Human Joints: Physiology, Pathophysiology, and Treatment. New York, USA: Marcel Dekker, Inc., 1993.

Chapter 2: Development, Validation and Testing of the Multi-Axis Biomechanical Testing Apparatus

2.1 Introduction

In-vitro testing of the knee joint is a much-explored topic. Typical applications are testing ligament fixations, evaluating wear of knee prostheses, investigating the dynamic loads and range of motion of the knee in various daily activities and validating finite element models of the knee joint.

Numerous *in-vitro* studies have been completed on the knee using different types of apparatii for testing knee tissue, some for ligaments (Bach and Hull, 1994; Whiteside et al., 1987; Li et al. 1999b; Hashemi et al., 2007; Biden and O'Connor, 1990) and several for complete knees. Of the full or complete knee apparatii a few are robotic simulators (Fujie et al., 2004; Kiguchi et al., 1999; Li et al., 1999b; Li et al., 1999a), others are dynamic knee apparatii and have been developed to test the wear of knee prostheses (Currier et al., 1998; Bosma et al., 1979; Walker et al., 1997; Shaw and Murray, 1973; DesJardins et al., 2000; Burgess et al., 1997; Chao et al., 1994; Maletsky and Hillberry, 2005, Zachman et al, 1978; Wilson et al., 1996; Pavlovic et al., 1994; Dowson et al., 1977; DiAngelo and Harrington, 1992; Maletsky and Hillberry, 1999), while others reproduce the loading of various activities on the knee (Guess and Maletsky, 2005; Walker et al., 1997; Maletsky and Hillberry, 2000; Maletsky and Hillberry; 2005, Sheshadri et al., 1997; Wilson et al., 1996; Paul et al., 1977; Szklar and Ahmed, 1987; DiAngelo and Harrington, 1992; Maletsky and Hillberry, 1999).

Other apparatii are quasi-static devices and have a similar overall design in which the knee can be placed and loaded in a desired flexion-extension position either through bone or muscle (Maletsky and Hillberry, 2005) type activation, but usually have distinctive features between each design. Maletsky and Hillberry (Maletsky and Hillberry, 2005) discussed two advantages of quasi-static devices: first the loading of the apparatus is quite robust, depending on the design, the loading can simulate various muscles across the joint; and second, depending on the exact function of the apparatus, certain degrees of freedom can be controlled. Several quasi-static devices have been developed and are discussed below.

Bach and Hull (Bach and Hull, 1994) designed a six-degree of freedom (DOF) apparatus to study the mechanics of knee ligamentous injuries over a full range of flexion angles. The knee is inserted into the apparatus horizontally and at full extension. Rotations, external forces and simulated muscle forces (quadriceps, hamstrings, and gastrocnemius) are subsequently applied to the specimen via rotary and linear pneumatic actuators.

Whiteside et al. (Whiteside et al., 1987) designed an apparatus to investigate the stability of the knee at various degrees of flexion when subjected to constant body weight and loading of the quadriceps. In this particular apparatus, flexion and extension angles were adjusted through the shortening and lengthening of the quadriceps muscle and the tibia was free to move around the femur.

Another quasi-static apparatus was designed by van Kampen (van Kampen and Huiskes, 1990) to measure the three-dimensional tracking pattern of the patella. The

apparatus allowed tibiofemoral flexion-extension and prescribed tibial rotation. The quadriceps muscles were loaded using a system of weights and pulleys.

To measure pressure distribution on the retropatellar surfaces, Ahmed and Burke (Ahmed and Burke, 1983) developed a machine to replicate the individual tensions and lines of action in the muscles of the quadriceps femoris. Tension bands were used to simulate the five quadriceps femoris muscle group and were controlled by hydraulic actuators.

Biden and O'Connor (Biden and O'Connor, 1990) used the Oxford rig to evaluate the functions of knee ligaments. The Oxford rig simulates flexed knee stance, provides the specimen six DOF and movements are constrained by the structures of the knee and not by the apparatus itself. The knee is loaded in flexion and stability maintained through applied tension on the quadriceps tendon.

An apparatus that can incorporate the main functions of all the above-mentioned designs would be invaluable to the research community. Such a machine needs to incorporate the most pronounced design features and simplify some of the more complex features. The objective of this work was to design and develop a multi-axis biomechanical testing apparatus (MABTA) to examine human, animal and composite knee joints in various physiological positions for validating finite element models, investigating anterior cruciate ligament fixations and exploring the design of total knee prostheses. Specification, evaluation and validation of the apparatus are described below.

2.2 Design Specifications

The specifications for MABTA were unique in that the system was required to allow tri-axial force application (medial-lateral (M-L), anterior-posterior (A-P), proximal-distal (P-D)) while allowing the specimen to be oriented in all three axes of rotation. The apparatus must include the six DOF capabilities and the ability to only constrict the knee by its own soft tissues as seen in the design of the Oxford rig (Biden and O'Connor, 1990). Additionally it was required to implement the ability to apply anterior-posterior and medial-lateral loads through displacement control, to apply a desired flexion-extension, varus-valgus or internal-external rotation to the specimen, and to account for the various types of specimens, whether it is a cadaveric human, animal or composite femur, tibia or a full knee.

Unlike previous apparatii, MABTA does not simulate individual muscles but incorporates an overall loading situation that replicates the sum of all loads applied by the muscles through the application of loads at the joint itself. This particular feature increases the simplicity of the design by excluding the many complicated systems needed for muscle simulation but still providing the physiological loads applied to the joint.

The specifications listed in Table 2.1 were based on existing analyses of the human gait cycle and human knee biomechanics (Harrington, 1976). Loads can be applied in any increment in the P-D, A-P and M-L directions and can be monitored through a LabVIEW (National Instruments Corp, Austin, Texas, USA) program. Desired rotations are adjusted before testing commences. Internal-external (I-E), varus-valgus (V-V) and flexion-extension (F-E) rotations are all adjustable in 1° increments.

Table 2.1: Loads, rotations and translations specifications for MABTA

Loads	Rotations	Translations
4448 N (1000 lb) compression (P-D)	Up to 100° flexion and 50° hyperextension	150 mm (5.9") in P-D direction
2224 N (500 lb) shear (A-P)	± 20° varus/valgus	76 mm (3") in A-P direction
2224 N (500 lb) (M-L)	30° internal/external	76 mm (3") in M-L direction

2.3 Design Features

The design of a six-degree of freedom (DOF) loading frame is a complicated process. In general, MABTA (Figure 2.1) is a quasi-static loading frame. It is placed upon a painted steel frame (Figure 2.1a), with casters to allow mobility. The widest aspect being 0.762 m (30") and the total height being 1.828 m (72"), allowing MABTA to fit through a standard door and be easily moved. Furthermore, as this biomechanical testing system will be used with cadaveric human, animal and composite specimens, the testing apparatus used sealed bearings, stainless steel and aluminum wherever practical to allow chemical sterilization without damaging the integrity of the design.

32
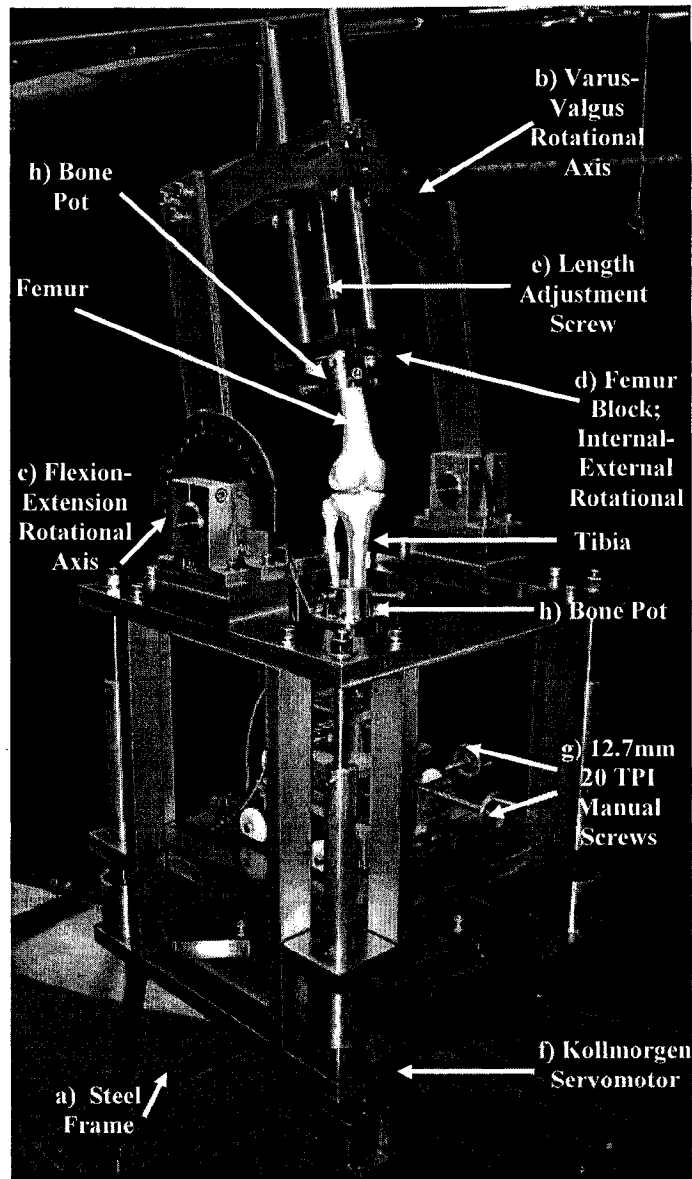
Figure 2.1: Principle MABTA components

The load application is intended to represent a static situation, and as such the desired rotational orientation of the specimen is fixed before the loads are applied. The knee is horizontally inserted into MABTA and is rotated about its approximate centre of rotation. The design of MABTA placed all load application and measurement at the lower end of the apparatus (tibial end); while the upper end of the apparatus (femoral end)

33

controls all three rotational axes of the specimen (I-E, V-V, F-E). This design increases the complexity of the apparatus, particularly at the femoral end, but by separating the axial and rotational displacements it allows for better alignment accuracy of the natural rotational axes of the knee with the rotational axes of the apparatus. This feature avoids constraining the knee through the design of the device but allows for the knee to be naturally constrained by the remaining soft tissues.

A system of rotations within rotations was implemented to allow all three rotational axes on one end of the apparatus. Thus, the I-E rotation occurs within the V-V rotation (Figure 2.1b), which occurs within the F-E rotation (Figure 2.1c). The I-E rotation is accomplished by rotating the femoral bone pot inside the femur block (Figure 2.1d). This rotational precedence was chosen such that the widest range of rotation is the most accessible and easiest to alter since it is the most likely of the three rotations to be adjusted between tests.

Since the reactions of the knee joint between the tibia and the femur are not well understood, the forces on the femoral side of the testing apparatus were difficult to predict. As such, the design of MABTA required a significant safety factor to ensure that failure of any component did not occur. This is particularly important given the long moment arm created by the requirement of the apparatus to accommodate a human specimen from the midshaft of the femur to the midshaft of the tibia. The stiffness of the MABTA frame was estimated at 7321 N/mm (41806 lb/in) by utilizing FE analysis of the design and hand calculations. A length-adjustment screw (Figure 2.1e) on the femoral end and the P-D sliders on the tibial end accommodate specimen lengths up to 508 mm

34

(20"). This length is dependent on the specimen itself and if the specimen can fully immerge in the designed bone pots.

The tibial end of MABTA contains three translational axes for loading. Since these axes must allow displacement, a tri-axial system of sliders was used, with the P-D displacement being accommodated by four solid bearings running on cylindrical axles, while the A-P and M-L displacements are each handled by Super Smart Ball Bushing Pillow Blocks (Model SSUPBO-16, Thomson Industries Inc.) as seen in Figure 2.2b,c.

All loads are measured using an AMTI 6 DOF load cell (MC6-6-2000) (Figure 2.2a) placed between the tibia and the loading system. Loading in the P-D direction is achieved with a 150 mm stroke IDC Motion EC3-B electromechanical actuator and Kollmorgen servomotor (Model AKM42G-BSCN2-02, Figure 2.1f). This allows for precise control of displacement or load through a closed-loop feedback system and requires three-phase 108VAC. The actuator has a repeatability of $\pm$ 0.013mm and a backlash of $\pm$ 0.25mm. The A-P and M-L loads are applied by 12.7 mm (½"), 20 TPI manual screws (Figure 2.1g). These screws can be easily detached from the crossed sliders to allow the entire tibial stage to shift in A-P and M-L directions so that the knee can float to a natural resting position before loads are applied.

35

a) 6 DOF load cell

b) Anterior-Posterior Super Smart Ball Bushing Pillow Blocks

c) Medial-Lateral Super Smart Ball Bushing Pillow Blocks
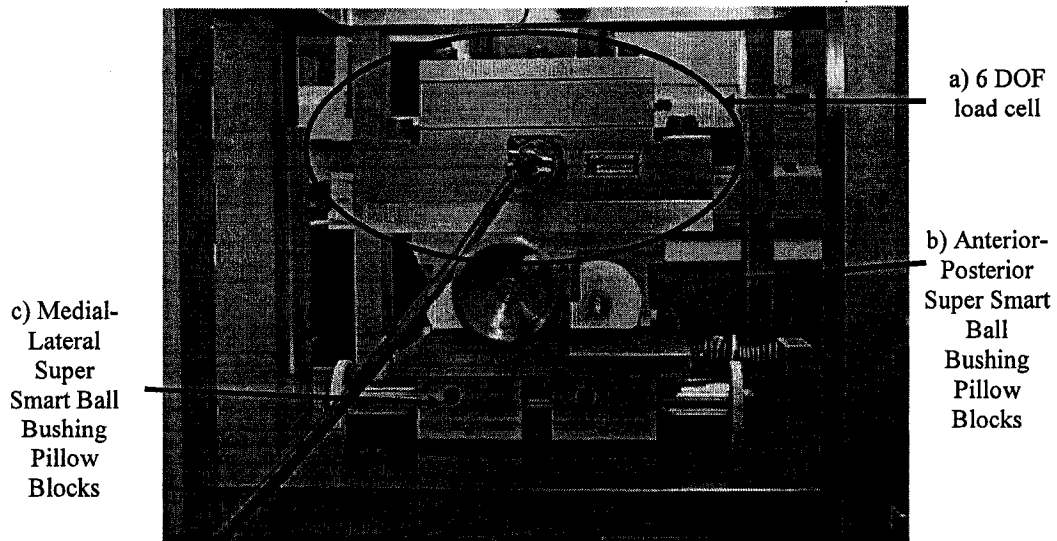
Figure 2.2: AMTI 6 DOF load cell

The distal tibia and proximal femur are fixed using "pots" (Figure 2.1h), which contain three equilateral screws to fix the bone in conjunction with plaster of Paris. The three screws were implemented in the design to aid in the support and alignment of the specimen before the plaster of Paris fully sets.

2.4 MABTA Control and Operation

A data acquisition system was developed in National Instruments (NI) LabVIEW 8.5 to control MABTA and measure the strains along the cortex of bone or any other specimen. The program controls an AMTI signal conditioner (MiniAmp MSA-6) used to measure the loads from the AMTI 6 DOF load cell and the actuator's Kollmorgen servomotor through serial communication and ASCII commands. The program is predominantly based on user input and Boolean comparison functions. Figure 2.3 is a flowchart of the logic used to control loading and to measure the strain along the cortex of a specimen. This logic controls many functions of this program including the

36

application of load from the Kollmorgen servomotor, the recording of load values from the 6 DOF load cell and strain values from the specimen and user inputs such as if the specimen should be loaded axially or transversely or unloaded. Please refer to Appendix B for further details on the developed program.
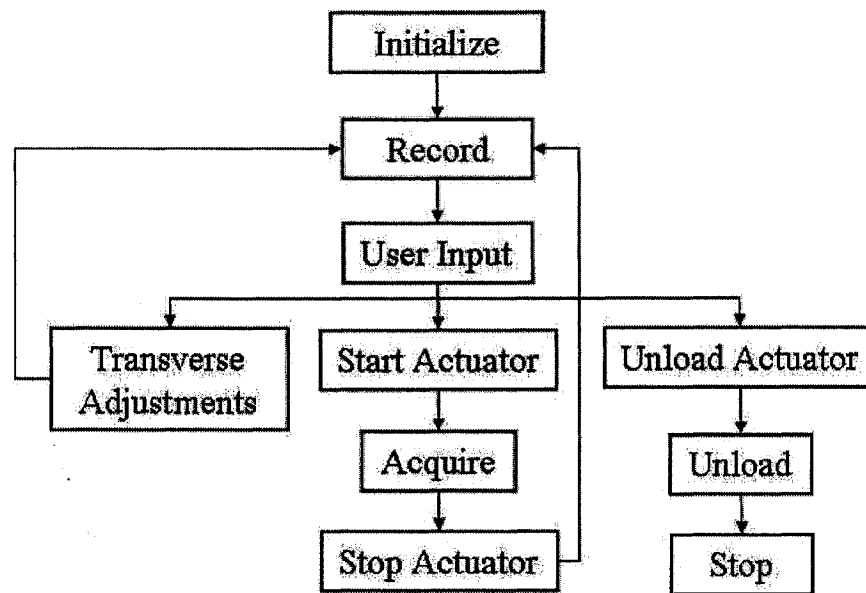
Figure 2.3: Operation and Control Logic. Initialize: zeroes strain gauge and load cell values before specimen is loaded. Record: saves load and strain gauge values at each load increment. User Input: asks user to either input next load value and start the actuator, adjust the transverse load or unload the actuator. Acquire: continuously reads and compares load cell values to user inputted load value; once load cell value equals the desired load value, program stops the actuator.

2.5 Validation of Design

To verify if MABTA meets all objectives and specifications, both known geometry and composite specimens were tested to compare experimental and theoretical strain results. Known geometry and composite specimens were chosen to provide a progression of the theoretical calculations from least complex to most complex and allows for identifying sources of measurement error. In the known geometry experiments, both material properties and specimen dimensions are known and present a relatively simple verification of the main design features. With the composite specimens, material

37

properties are known but geometry can only be measured with a CAD model, adding

complexity to the theoretical calculation and further verifying the success of the design.

2.5.1 Materials and Methods

Two specimens were used in the validation of MABTA's measured results: the

first being a polyvinyl chloride (PVC) pipe of known dimensions (Table 2.2) and the

second being a third generation composite tibia (#3301) and femur (#3303) from Pacific

Research Laboratories, Vashon Island, WA.

Table 2.2: PVC Specimen Dimensions. The measured dimensions are average values. A modulus of elasticity range was provided, as the exact modulus of elasticity for the PVC pipe was not found.

Length, m (in)	0.2198	(8.652)
Inside Diameter, m (in)	0.0258	(1.014)
Outside Diameter, m (in)	0.0334	(1.314)
Area, m^2 (in^2)	3.539×10^{-4}	(5.485×10^{-1})
Moment of Inertia (I), m^4 (in^4)	3.931×10^{-8}	(9.444×10^{-2})
Elastic Modulus[14] Pa (psi)	1.79×10^6	(2.60×10^2)
	4.83×10^9	(7.00×10^5)
Average Elastic Modulus Pa (psi)	2.42×10^9	(3.50×10^5)

The PVC specimen (Figure 2.4) was instrumented with five uniaxial strain gauges

from Micro-Measurements (CEA 13-062-UW-350). Locations of the five uniaxial strain

gauges are presented in Table 2.3.

---

[14] Matweb: Material Property Data
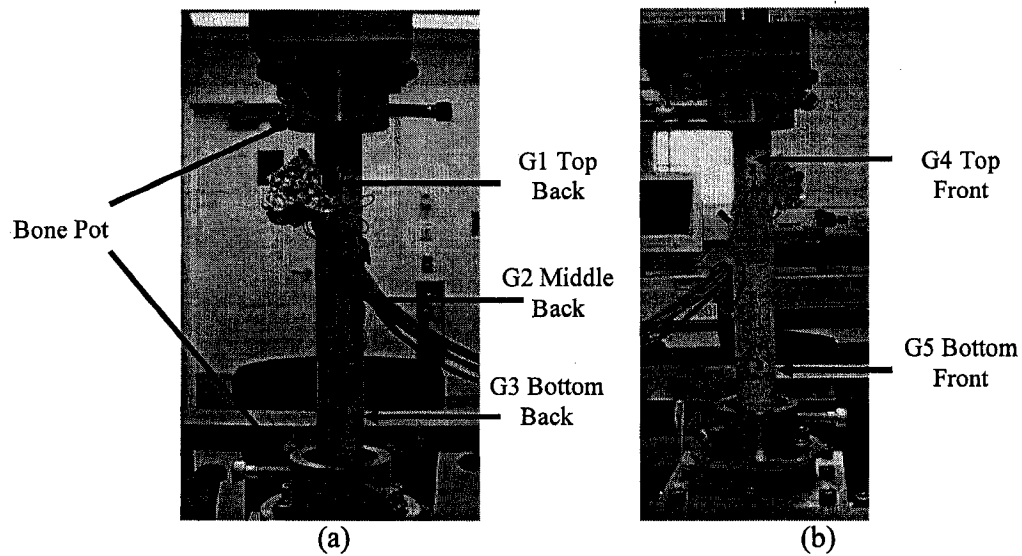
Figure 2.4: PVC pipe instrumented with strain gauges: (a) back of the specimen and (b) front of the specimen

Table 2.3: Strain gauge positions for PVC pipe. All positions were taken with respect to the marble tabletop reference point while piece was vertical with strain gauge 1 nearest to the tabletop.

Specimen	Marble Tabletop Reference Point (mm)	Strain Gauge Position (mm)				
		Back			Front	
		Gauge 1	Gauge 2	Gauge 3	Gauge 4	Gauge 5
PVC	0.00	85	165	245	85	245

The composite tibia (Figure 2.5) and femur (Figure 2.6) were each instrumented with thirteen Omega 45° triaxial-stacked rosettes (SGD-2/350-RY53). Table 2.4 and Table 2.5 indicate the strain gauge position with respect to the centre of the bone pot for the tibia and femur, respectively. Centre of gauge positions were measured using a coordinate measuring machine (CMM, MicroVal, Browne and Sharpe, North Kensington, RI) with an accuracy of 0.001 mm.

39
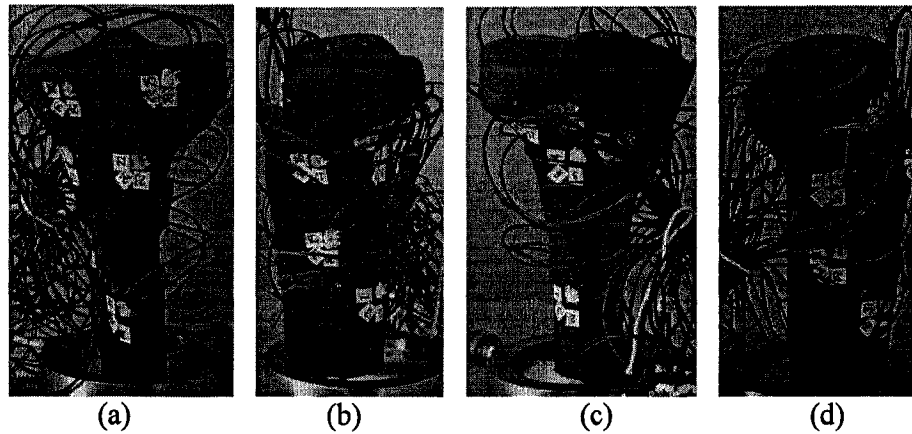
Figure 2.5: The thirteen tibial strain rosette positions: a) Anterior: Rosettes 8-11 b) Lateral: Rosettes 6-7 c) Posterior: Rosettes 1-5 and d) Medial: Rosettes 12-13

Table 2.4: Tibia strain gauge positions with respect to centre of the bottom face of bone pot (all dimensions are in mm)

Rosettes	Gauges	X	Y	Z
1	SG1-3	-6.612	6.810	-75.057
2	SG4-6	-2.849	8.850	-127.176
3	SG7-9	14.955	15.798	-134.340
4	SG10-12	-3.753	14.358	-145.001
5	SG13-15	-19.522	7.000	-139.601
6	SG16-18	-21.288	-13.138	-129.221
7	SG19-21	-16.864	-7.934	-98.486
8	SG22-24	-7.254	-34.554	-130.762
9	SG25-27	-16.533	-27.159	-158.608
10	SG28-30	19.006	-24.616	-154.005
11	SG31-33	22.079	-8.047	-125.825
12	SG34-36	14.687	-7.651	-96.423
13	SG37-39	0.396	-25.347	-73.858

40

Figure 2.6: The thirteen femoral strain rosette positions: a) Anterior: Rosettes 1-4 b) Medial: Rosettes 5-6 c) Posterior: Rosettes 7-11 and d) Lateral: Rosettes 12-13

Table 2.5: Femur strain gauge positions with respect to centre of the bottom face of bone pot (all dimensions are in mm)

Rosettes	Gauges	X	Y	Z
1	SG1-3	-1.202	-24.097	-74.622
2	SG4-6	-0.547	-32.455	-122.579
3	SG7-9	12.509	-44.303	-143.597
4	SG10-12	-24.318	-32.132	-153.054
5	SG13-15	-19.831	-14.950	-102.224
6	SG16-18	-23.365	-14.728	-123.093
7	SG19-21	0.587	0.484	-78.934
8	SG22-24	2.081	-5.060	-126.829
9	SG25-27	-19.545	5.155	-147.140
10	SG28-30	24.730	-0.065	-139.873
11	SG31-33	4.973	-7.239	-164.800
12	SG34-36	21.535	-15.220	-101.474
13	SG37-39	26.126	-21.733	-124.200

The possibility of obtaining the experimental strain results from a digital image correlation (DIC) method was considered. However, it was found that the noise of the system available (Vic-3D, Correlated Solutions®, Columbia, SC, USA) would not satisfy the objectives of a second measurement method for reading strains along the knee joint or

41

individual bones. Nonetheless, the DIC method has good agreement with strain gauges for strain values of 500$\mu\epsilon$ to 1000$\mu\epsilon$ (Simonsen, 2007). See Appendix A for more details.

Using a custom-designed alignment jig, which is designed for 0° flexion, the composite tibia and femur were potted in bone pots. This was done by first securing the tibial and femoral bone pots in the same x-y position with the aid of alignment dowel pins and screws (Figure 2.7). Next, a desirable contact between the two specimens was found. Since there are no soft tissues attached to the composite bone to aid in this contact, the two bones were aligned to achieve stability and to distribute the load across the tibial plateau. Lastly, this position was secured with plaster of Paris. Before either specimen was placed into MABTA, a coaxial alignment indicator was used to align the tibial and femoral bone pot holders to within 0.0127 mm (0.0005"). Since there are no connective tissues attached to the joint, such alignment is important to maintain the desired potted position. For a more detailed description on the use of the alignment jig and coaxial alignment indicator, see Appendix F. For a more detailed description about the alignment jig and coaxial alignment indicator, see Appendix C.
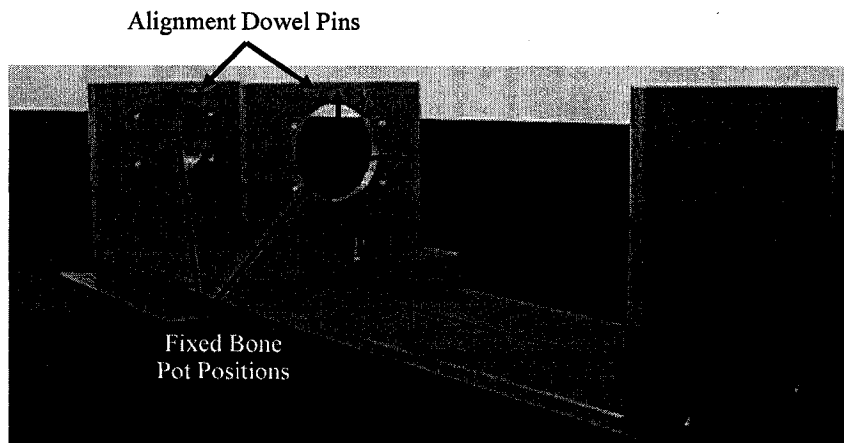
Figure 2.7: Custom-designed alignment jig

2.5.2 Known Geometry Experiments

Two experiments were conducted on a PVC pipe, the first being a compression test in MABTA and the second a compression test in a 500 N MTS Synergie 400 uniaxial testing machine (Model #2700094, MTS Systems Corporation, Eden Prairie, MN, USA). Both tests were conducted to determine if the same experimental strain trends were seen between two different loading devices.

The coaxial alignment indicator protocol detailed in Appendix F was used to align the tibia and femur bone pot holders to within 0.0127 mm. The PVC specimen was inserted into the fitted Delrin® collars (Figure 2.8) and then placed into the bone pots. The fitted Delrin® collars were used to align the specimen in the centre of the bone pots without the use of plaster of Paris, which simplified set up. The bone pots were then carefully inserted into MABTA and actuator was raised[15] until specimen was in position (Figure 2.4). The PVC pipe was then compressed to 889.6 N (200 lb) in 89.0 N (20 lb) increments.

PVC specimen

Fitted Delrin® collars
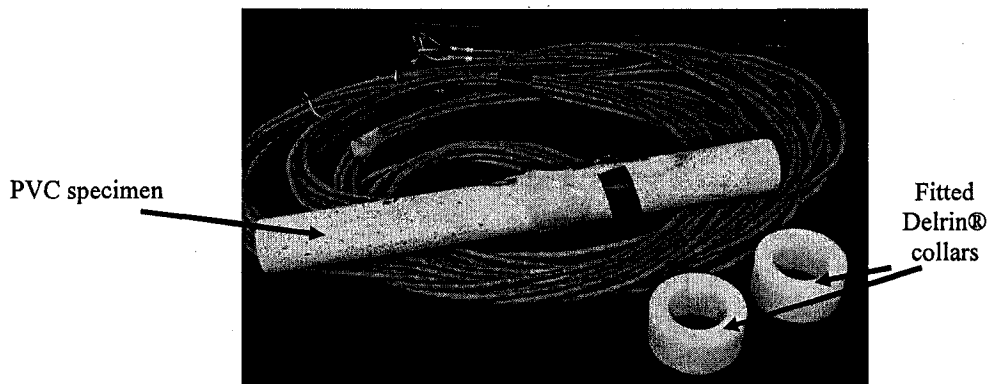
Figure 2.8: PVC specimen with machined Delrin® collars

---

[15] Refer to Appendix E: Windows HyperTerminal to control the actuator

43

For the second known geometry experiment, the specimen was placed into a 500 N MTS Synergie 400 uniaxial testing machine (Model #2700094, MTS Systems Corporation, Eden Prairie, MN, USA) (Figure 2.9a). Loading ends of similar diameter to that of the specimen were chosen to produce the best alignment possible (Figure 2.9b).

MTS machine

PVC specimen

(a)   (b)
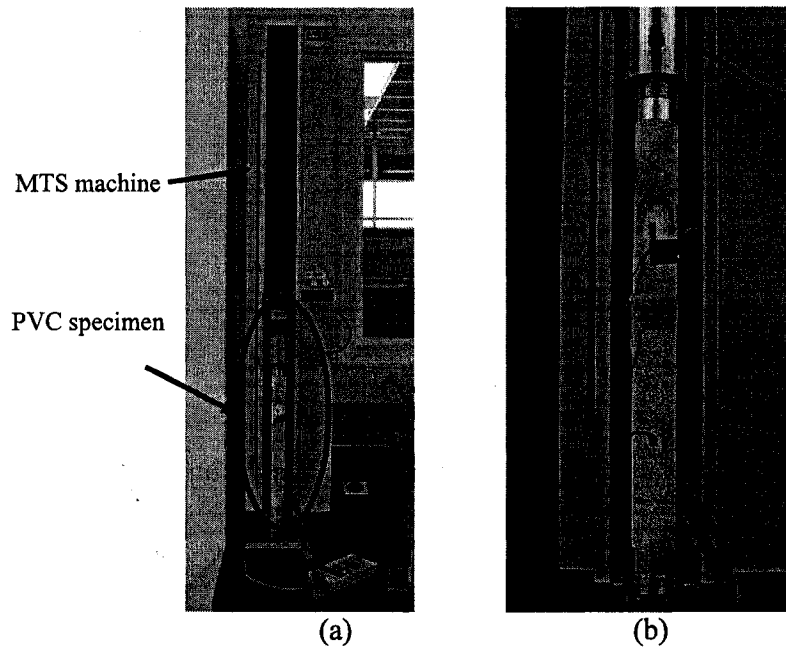
Figure 2.9: (a) MTS Synergie 400 uniaxial testing machine; (b) PVC specimen positioned in MTS machine

Due to the software and load constraints of the MTS Synergie 400, a slightly different loading protocol was used. Once the desired load has been reached, the MTS software automatically unloads the specimen hence requiring four separate tests each with a different final load value. Additionally, the MTS Synergie 400 has a loading capacity of 500 N, slightly half the original load placed on the specimen while in MABTA. To ensure that no damage was done to the MTS Synergie 400, a maximum load of 356 N (~80 lb) was applied to the specimen.

Considering the above-mentioned constraints, four tests were conducted on the PVC specimen with the first test loading the specimen up to approximately 89 N (~20 lb),

44

second test loading to approximately 179 N (~40 lb), third test to approximately 269 N (~60.5 lb) and the final test to approximately 356 N (~80 lb).

2.5.3 Composite Specimen Experiments

Since cadaveric specimens are difficult to obtain, more and more studies are being completed with composite bone specimens. Both the composite tibia and femur provide an appropriate alternative to cadaveric specimens (Cristofolini and Viceconti, 2000; Cristofolini et al., 1996), with the composite femur having much better reproducibility (Cristofolini et al., 1996). However, the composite tibia is more suitable for dominant bending applications than dominant torsion applications (Cristofolini and Viceconti, 2000).

Numerous studies have used composite femurs as substitutes for cadaveric specimens, to investigate the performance of total hip and total knee prostheses and to validate finite element models (Waide et al., 2003; Completo et al., 2007a; Completo et al., 2007c; Papini et al., 2007; Szivek and Gealer, 1991; Heiner and Brown, 2001; Cristofolini et al., 1996) but only a few studies have been completed on the composite tibia (Completo et al., 2007b; Completo et al., 2008; Cristofolini and Viceconti, 2000; Gray et al., 2007). To the author's knowledge this is the first study done where both a composite tibia and femur are loaded simultaneously in compression. Physiological conditions are ignored and only the strains along the cortex of the composite tibia and femur are found based on two point axial loading at the articulating surface.

Before the composite tibia and femur were subjected to compression tests in MABTA, a preliminary test was completed on an epoxy composite block to establish maximum load limits and to ensure no permanent damage would occur to the specimens.

45

This composite block was acquired from Pacific Research Laboratories and has the same material properties as the third generation composite bones. From this preliminary experiment, it was determined that a two-rod custom-made loading jig (Au, 2008) would crack the epoxy surface of the composite bones at a load of 2000 N (450 lb) or 1000 N (225 lb) per rod. Therefore it was decided to place a piece of foam and rubber in between the two joint surfaces to avoid permanent damage.

The DAQ system is limited to 40 input channels, therefore, only the strains on either the tibia or the femur can be measured during a single test. The composite tibia and femur were placed into MABTA and loaded using the experimental protocols outlined in Appendix F.

Three compression tests were completed first on the tibia (Figure 2.10) and then on the femur (Figure 2.11). Both specimens were subjected to a maximum load of 1780 N (400 lb) in 111 N (25 lb) increments. Since the composite specimens did not have adjoining soft tissue, a piece of foam and rubber were placed between the joint to avoid point loading and to prevent the surface damaged experienced during testing of the epoxy composite block.
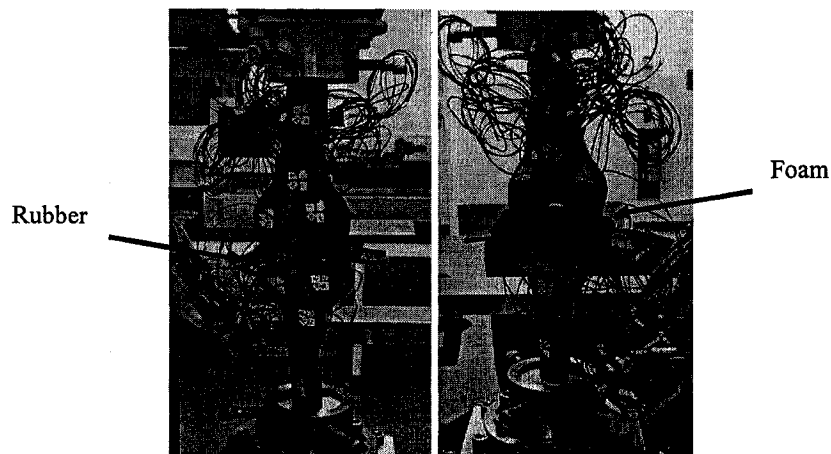
Figure 2.10: Composite tibia compression position
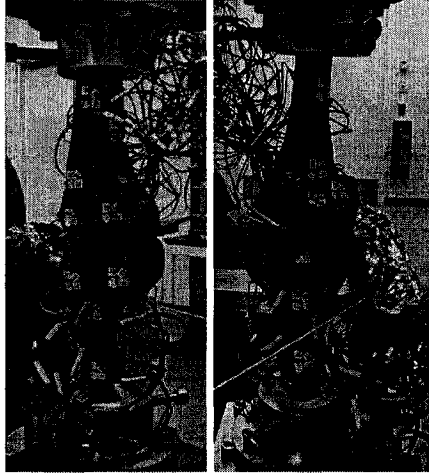
Figure 2.11: Composite femur compression position

2.6 Discussion

2.6.1 Known Geometry Specimen Results

Three compression tests were completed on a PVC pipe while in MABTA. The

PVC pipe was compressed to 889.6 N (200 lb) in 89.0 N (20 lb) increments and produced

the strain results seen in Figure 2.12. This is one representative figure; the other figures

are presented in Appendix G with 18% being the highest percent difference between the

tests.
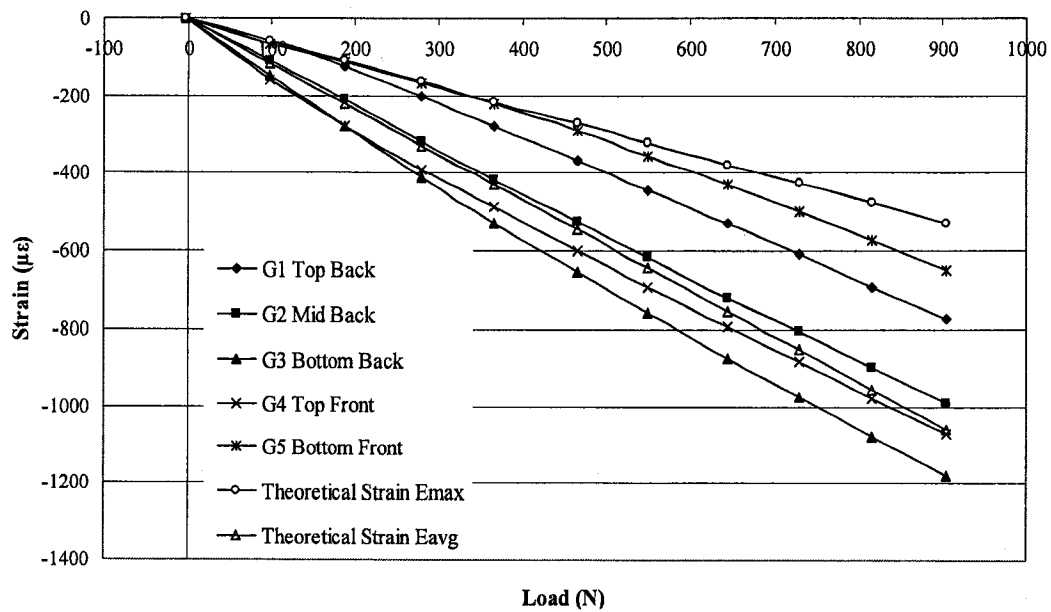
Figure 2.12: MABTA PVC Compression Results. G1 through G5 represent the strain results for gauges 1 through 1. Theoretical strain Emax and theoretical strain Eavg represent the theoretical strains based on Emax and Eavg, respectively. Note the lines are used for visual purposes only.

In theory, if a constant geometry specimen was subjected to pure axial compression along the specimen's central axis, all strain gauge values should be identical. These results indicate the PVC specimen experienced some bending, as the experimental strain values are not consistent across all five gauges. However, the experimental strain values are within the theoretical strain calculations (Figure 2.12). To evaluate if this bending was caused from the apparatus or from the specimen, the same specimen was placed in a 500 N MTS Synergie 400 (Model #2700094, MTS Systems Corporation, Eden Prairie, MN). The results from this test can be seen in Figure 2.13.

48
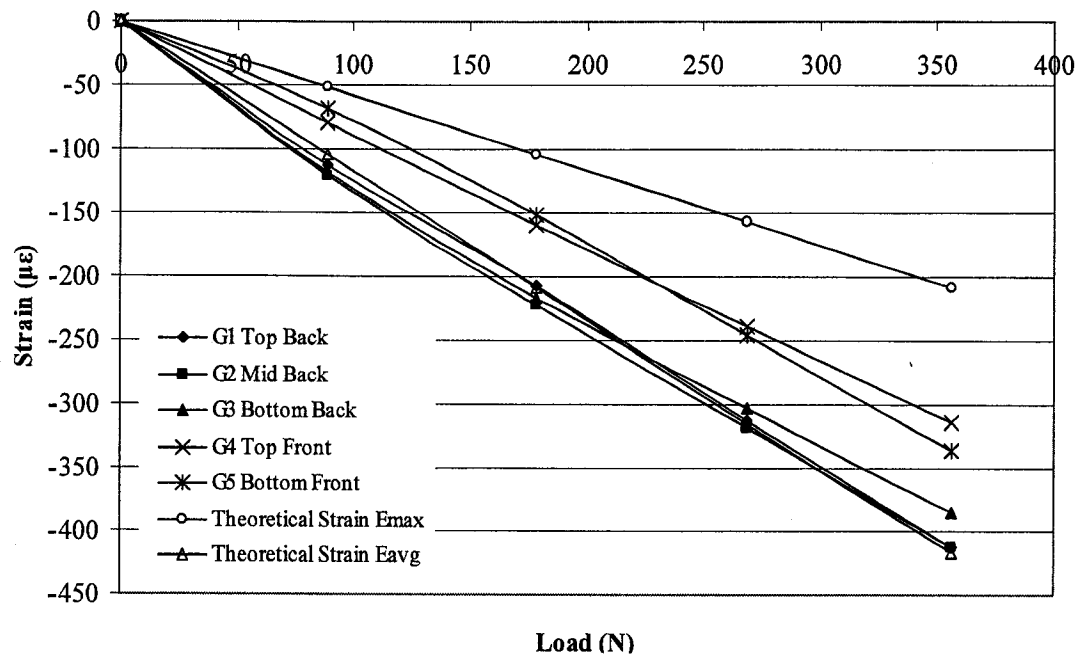
Figure 2.13: PVC strain results for MTS compression test. G1 through G5 represent the strain results for gauges 1 through 1. Theoretical strain Emax and theoretical strain Eavg represent the theoretical strains based on Emax and Eavg, respectively. Note the lines are used for visual purposes only.

Analysis of the results indicates that the PVC piece again experienced bending. Using strength of materials analysis, it was found that if the PVC specimen was misaligned by as little as 1mm or had slightly uneven ends, a strain difference of $100\mu\varepsilon$ would occur between the front and back gauges. This strengthens the argument that MABTA was not the main source of the bending and therefore there is good agreement between experimental and theoretical strain values for the known geometry specimen as the experimental values fall within the theoretical range. For a more detailed description of the experiment, and associated results, see Appendix G.

49

2.6.2 Composite Bone on Bone Experimental Results

The experimental effective von Mises (VM) strain values for the first compression test done on the composite tibia and femur are presented in Figure 2.14 and Figure 2.15, respectively. From these nearly monotonically increasing strains as a function of load results, it is observed that MABTA produces valid strain progression with increasing load. This was noticed across all three compression tests for both the composite tibia and femur.
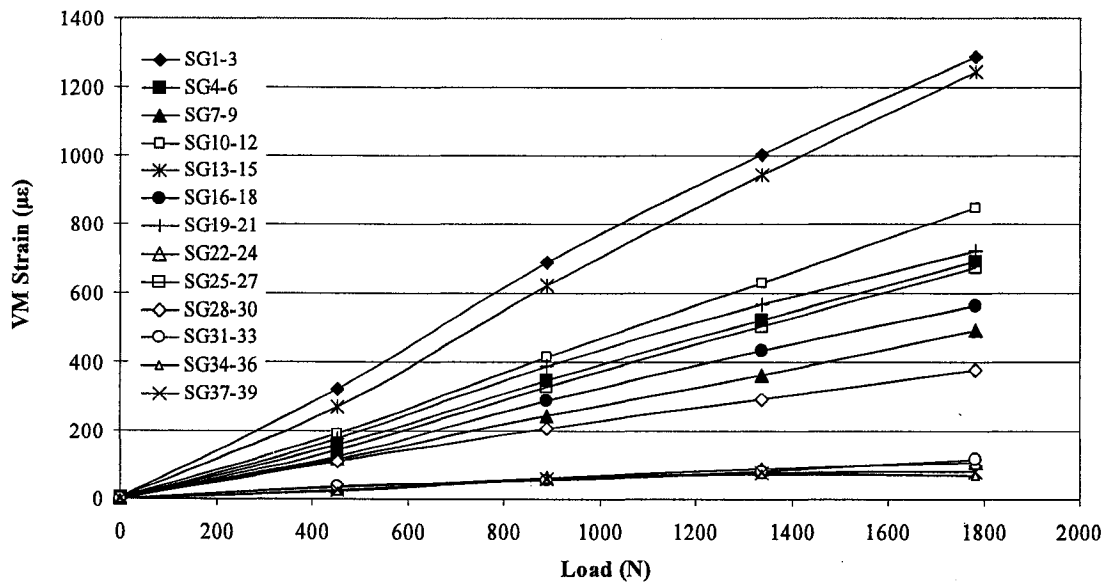
Figure 2.14: Composite tibia experimental von Mises (VM) strain progression. Note the lines are used for visual purposes only.
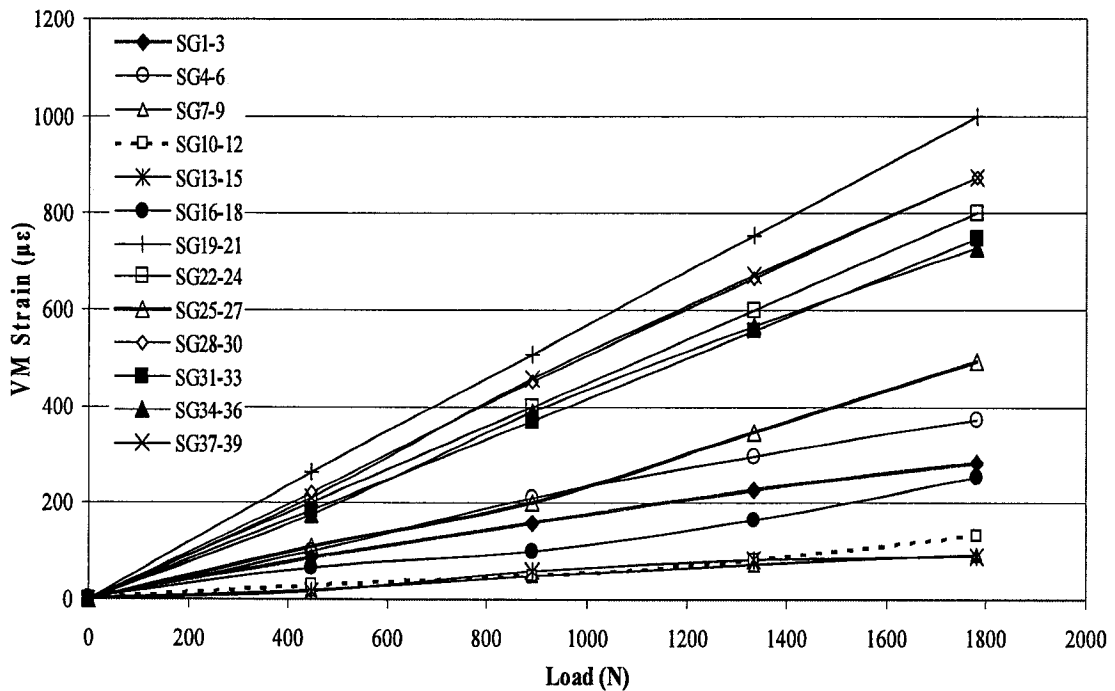
Figure 2.15: Composite femur experimental von Mises (VM) strain progression for test 1. Note the lines are used for visual purposes only.

For both the composite tibia and femur compression tests, highest strain levels occurred at the lowest strain gauge on the posterior side of the specimen (rosette #1 on the tibia and rosette #7 on the femur) and reached well above 1000µε. The smallest strain levels were observed along the medial side of the specimen (rosette #11 and #12 on the tibia and rosette #5 on the femur) in the 45µε to 100µε range. Anatomically, the medial condyle is subjected to higher load (Morrison, 1969), which in turn would produce a higher strain along the medial side of the bone. However, with the composite bones, no connective tissue was attached therefore correct anatomical position and loading are difficult to achieve. The pieces of foam and rubber placed in between the joints to distribute the load across the joint and prevent point loading could have also redistributed the loads towards the lateral side of the specimen.

It was also observed that MABTA can provide repeatable results. Figure 2.16 and Figure 2.17 present the average VM strain and standard deviation of three tests performed on each of the composite tibia and femur, respectively. The highest standard deviation for the composite tibia occurred at SG28-30 with a value of 38με. This rosette is situated on the anterior, medial side of the composite tibia near to the loading contact areas. Higher standard deviation could occur at this position because of variation in loads measured at the load cell between subsequent tests or the repositioning of the foam and rubber combination between subsequent tests. The highest standard deviation for the composite femur occurred at SG19-21 with a value of 32με. This gauge is the lowest strain gauge on the posterior side of the composite femur and again could be affected by the variation in loads measured at the load cell between subsequent tests.
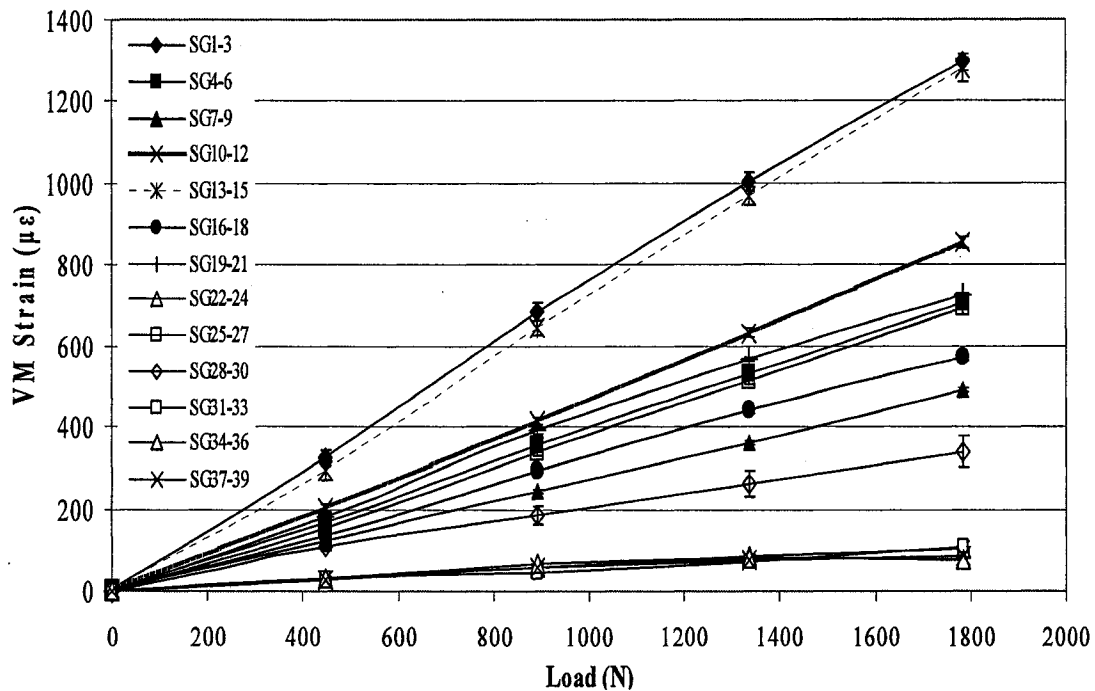
Figure 2.16: Average von Mises (VM) strain and standard deviation for composite tibia. Please note that some of the standard deviation values are too small in comparison with symbol size. Note the lines are used for visual purposes only.

52
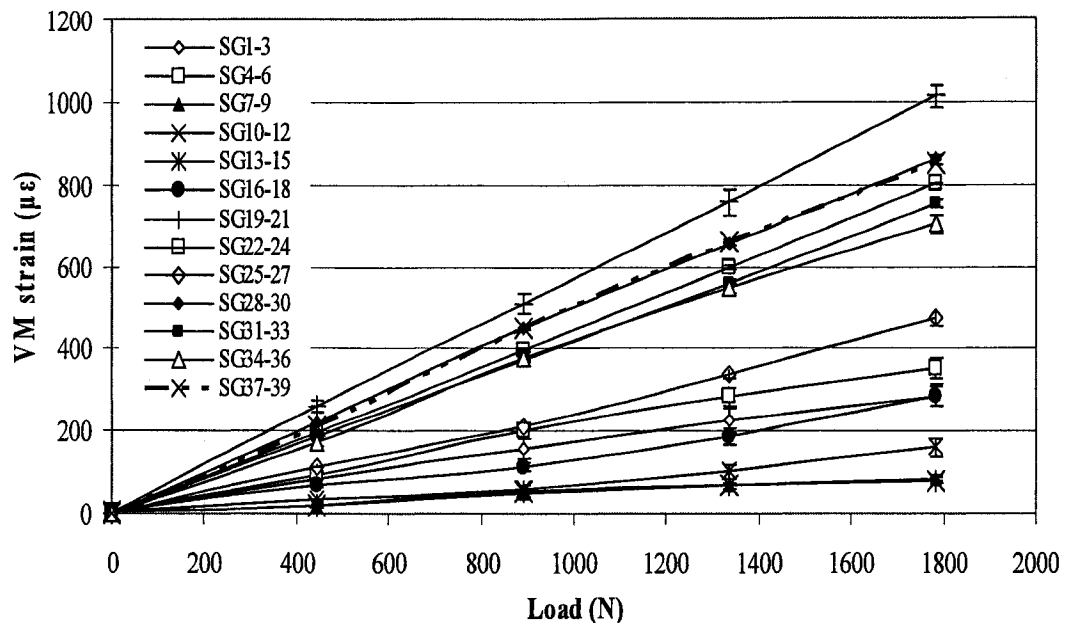
Figure 2.17: Average von Mises (VM) strain and standard deviation for composite femur. Please note that some of the standard deviation values are too small in comparison with symbol size. Note the lines are used for visual purposes only.

Reviewing the experimental VM strain results between the three composite tibia experiments and the three femur experiments, it was found that the experimental results had good repeatability between tests. Small variations in experimental results could be caused by backlash in the lead screws that control the A-P and M-L position of the tibial bone pot. A maximum misalignment of 0.389 mm was measured between tests before the position was reset to zero using the coaxial alignment indicator. Additionally removing and replacing the foam and rubber combination between the joints in a slightly altered position could distribute the load across the condyles differently.

Theoretical and experimental three-dimensional (3D) VM strains were calculated for both the composite tibia and composite femur and are presented in Appendix I. A sample calculation is also presented in Appendix I for the composite tibia, bone on bone loading at 445N. VM strains were used for comparison purposes as it ignores the

53

direction of the strain gauge and therefore allows for comparison of theoretical and experimental strain results. From the mostly axial stress state found at the surface of the specimens as a result of the applied loads, the VM strain results are approximately in line with the longitudinal strain since there is minimal shear from torsional loading. Figure 2.18 and Figure 2.19 present the experimental and theoretical VM strain results at maximum load for the first composite tibia and femur compression test, respectively. Since the loads vary slightly between each test, theoretical and experimental comparisons were done for each individual test. The second and third test results are presented in Appendix H. It should be noted that the theoretical VM strain values are based on the loads measured at the centre of the 6 DOF load cell. Therefore, any effects seen from the distribution of load caused from the placement of the foam and rubber would be included in the measured forces and moments.
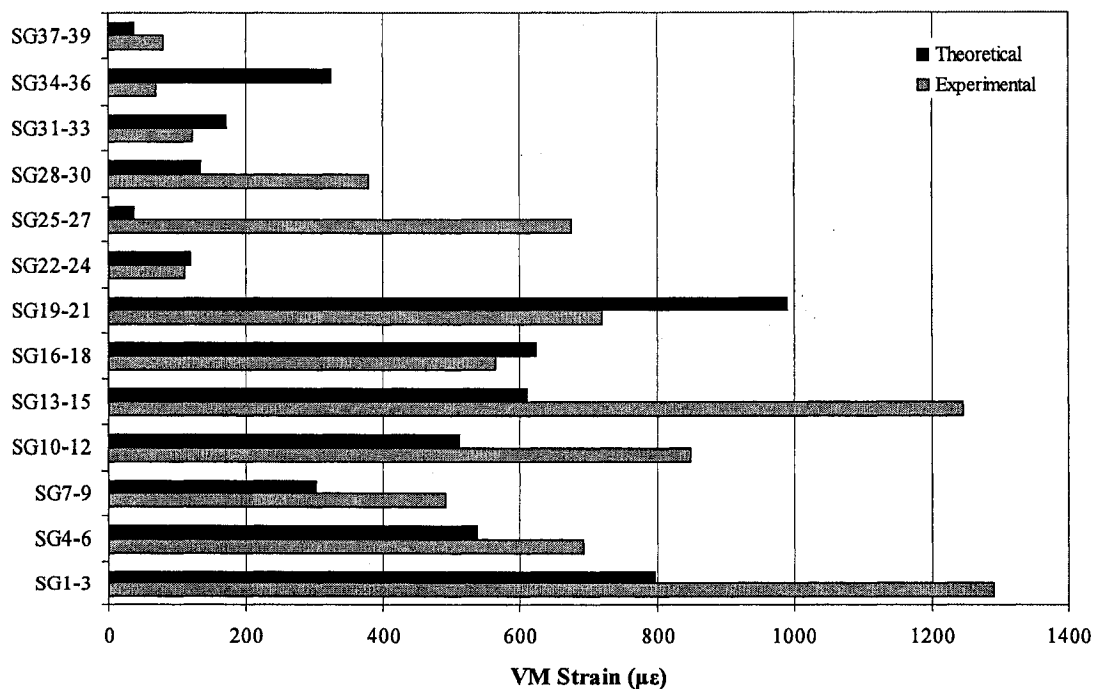
Figure 2.18: Composite tibia first compression test experimental and theoretical von Mises (VM) strain at 1780 N

54
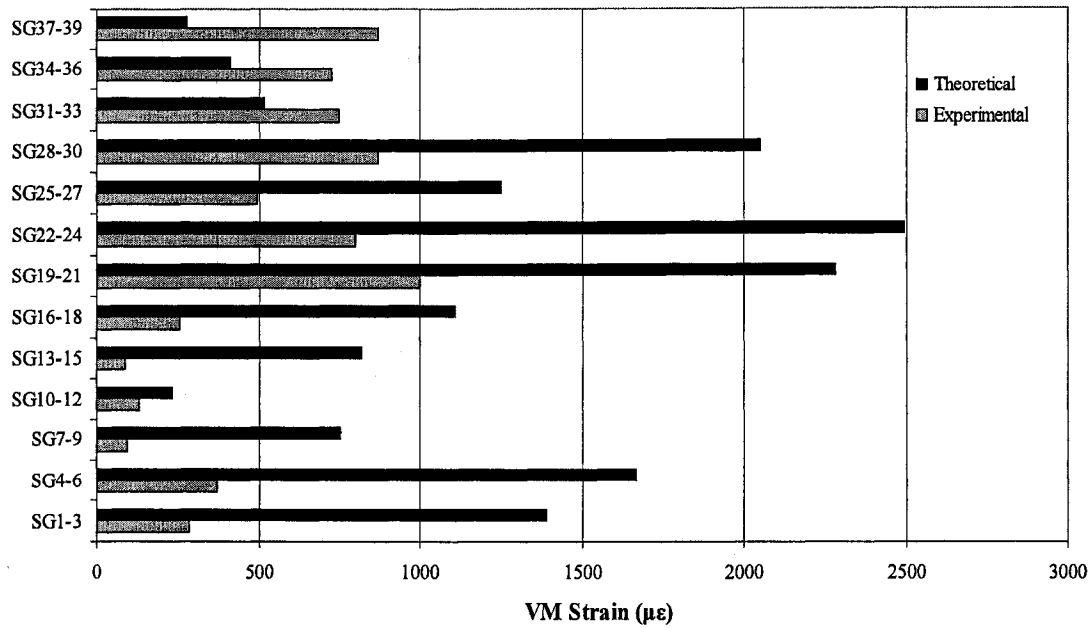
Figure 2.19: Composite femur first compression test experimental and theoretical von Mises (VM) strain at 1780 N

In general, the experimental strain values are higher than the predicted theoretical strain values. Only four strain gauge rosettes have an experimental VM strain lower than the predicted VM strain and occur at strain gauges 16-18, 19-21, 22-24, 31-33 and 34-36. All of these gauges are situated either on the medial or lateral side of the composite tibia with exception of the gauges 22-24 which are located on the tibial tuberosity. This trend change could be explained by the fact that the lateral and medial gauges are near the parting line of the moulded composite tibia, possibly causing a change in the composition and geometry of the bone or a stress concentration near the gauge.

Unlike the composite tibia, the composite femur theoretical VM strain results are generally higher than the experimental VM strain results with exception of gauges 31-33, 34-36, and 37-39. Gauges 31-33 were placed in between the femoral condyles and are most likely affected by loading edge effects as defined by St-Venant's principle. Similarly, gauges 34-39 were placed along the lateral side of the composite tibia near the

55

parting line. The higher experimental results could be explained by an inconsistency in the overall composition and geometry of the composite femur along this line.

The relationship between the experimental and theoretical VM strain values for the composite tibia and femur was determined in Figure 2.20 and Figure 2.22, respectively.
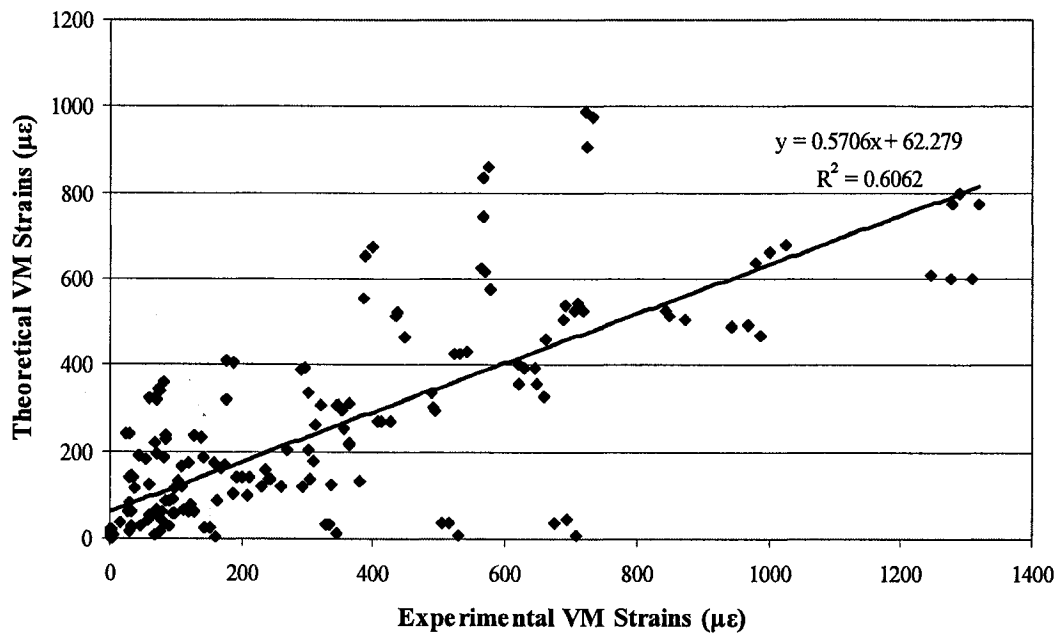
Figure 2.20: Comparison between experimental and theoretical von Mises (VM) strain for composite tibia

A slope of one, an intercept of zero and an R^2 value of 1 represents that there is excellent agreement between experimental and theoretical VM strain results. However, this ideal scenario did not occur in the composite tibia compression test. Instead the composite tibia has a slope of 0.5706 and an R^2 value of 0.6062. This trend suggests that the theoretical results are 0.5706 times lower than the experimental values but the trend has a low correlation coefficient.

Studying Figure 2.20 more closely, it appears that there are two trends. Examining the raw data, it appears that the theoretical values for gauges placed on the lateral side of

the tibia are higher than the experimental values. Removing the lateral gauges from Figure 2.20 produces the results in Figure 2.21, which now indicate that the experimental results for the remaining sides are higher than the theoretical results.
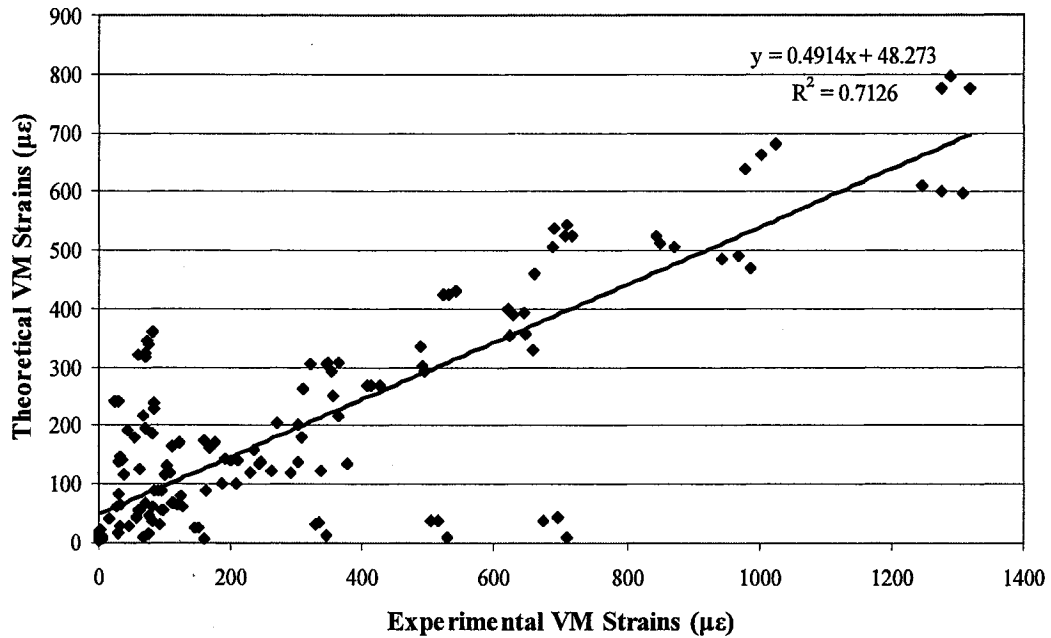
Figure 2.21: Comparison of experimental and theoretical von Mises (VM) strain results for composite tibia. Removed lateral gauges.
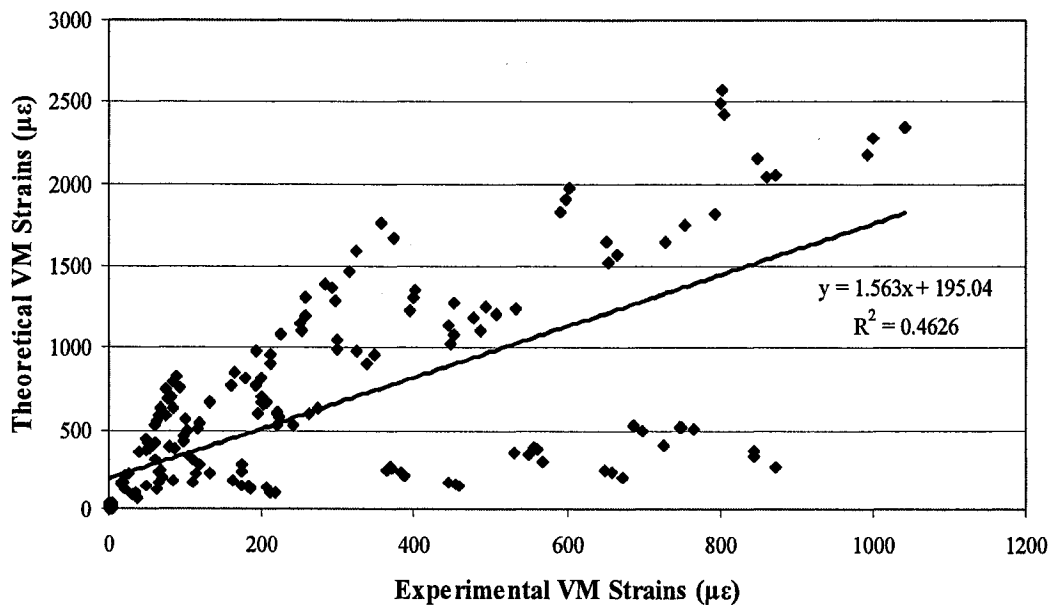
Figure 2.22: Comparison of experimental and theoretical von Mises (VM) strain results for composite femur

57

Similarly, the composite femur did not produce the ideal scenario but instead produced a slope of 1.563 and an R^2 value of 0.4626. The trend suggests that the theoretical results are 1.563 times higher than the experimental values, but the trend has a low coefficient of correlation. Studying Figure 2.22, this graph represents two trends. Examining the raw data, it was found that these trends represent gauges in distinct locations on the femur. Gauges 31-33 located between the two femoral condyles and the gauges on the lateral side of the femur are represented in the lower trend and the remaining gauges are represented in the higher trend. The two sets of gauges were plotted separately in Figure 2.23 and Figure 2.24.
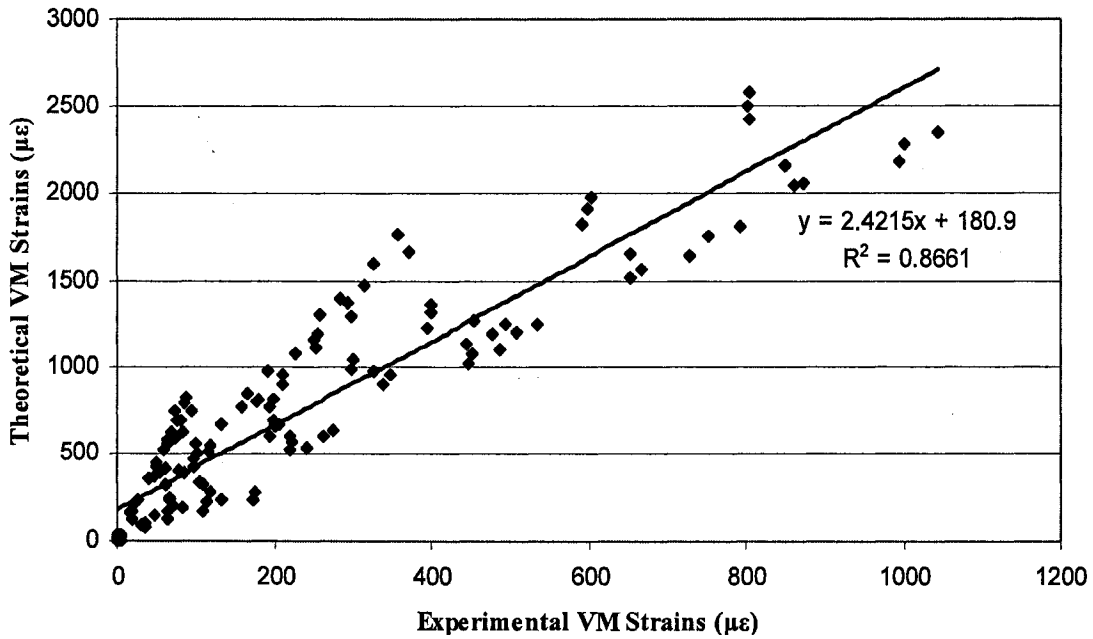
Figure 2.23: Comparison of experimental and theoretical von Mises (VM) strain results for composite femur. Removed gauges 31-39.
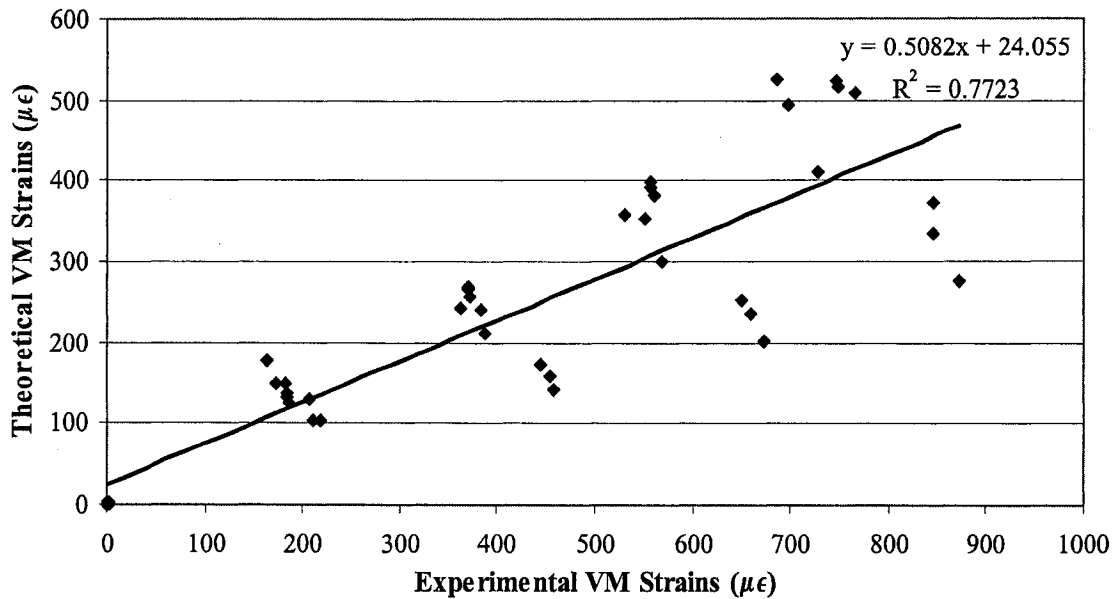
Figure 2.24: Comparison of experimental and theoretical von Mises (VM) strain results for composite femur. Graph only represents gauges 31-39.

From Figure 2.23 it appears that the theoretical values are over predicting the experimental values for the gauges along the front, medial and posterior side of the femur. Similarly, from Figure 2.24 it appears that the experimental values are higher than the theoretical values for the lateral gauges and the gauges between the two femoral condyles, which could be caused by an unaccounted bending moment.

Throughout the experiment and the calculation of the theoretical strain values for the composite bone on bone loading, many assumptions were made that could be sources of difference between the theoretical and experimental VM strain values. Both experimental and theoretical calculations as well as the individual experiments can have the associated errors and are listed below.

Basic assumptions used throughout the theoretical strain calculation are that the material was isotropic, that all loading occurred within the elastic range, and values for the third orthogonal direction were not measured but calculated based on the plane stress

59

state. These assumptions are seen throughout the theoretical strain calculations with the use of Hooke's Law.

Askew and Lewis (Askew and Lewis, 1981) stated that the cortical bone provides most of the loading support. Therefore, for most calculations the cancellous bone can be ignored. For the theoretical strain calculations, both the cancellous and cortical material properties were included in the axial stress equation to evaluate the ratio of the axial load supported by the cortex. It was found that the axial load supported by the cortex was 99.4% of the total load. However, only the cortical bone material properties were used in the bending stress equation, this was justified since the flexural rigidity of the cortical bone was much larger than the flexural rigidity of the cancellous bone (685×10^{12} Nm^2 $>> 1.2 \times 10^{12}$ Nm^2), and it would therefore not play a significant role in the overall flexural stiffness of the bone at any cross section. Additionally, some studies used the tensile elastic modulus (Completo et al., 2007b) instead of the compressive elastic modulus for composite bone studies. For comparative reasons, the tensile elastic modulus was used in this study as well.

All theoretical strains were calculated based on the loads measured at the 6 DOF load cell centre and at the measured strain gauge positions. All geometric properties for the composite bone were taken from a computer aided design (CAD) model of the knee (Au, 2008). If the measured strain gauge positions from the CAD model are slightly different from the actual strain gauge position, then the error between the experimental and theoretical values could be very large. For example, in a best scenario possible where geometry does not change significantly, if the geometry properties were measured approximately 1mm below or 1mm above the actual position of strain gauges 1-3, which

60

are located posteriorly on the shaft of the composite tibia and where no large geometry changes occur, the theoretical longitudinal strains would differ by $10\mu\varepsilon$. This effect could only be amplified if the region of interest was located at a position of large geometric changes.

At the end of each test and before the beginning of another test, specimens were removed from MABTA and alignment of the tibial and femoral bone pot holders was measured to see if the specimen was shifted out of alignment during testing. After each test it was measured that the tibial and femoral bone pot holders were misaligned by a maximum of 0.381 mm in the tibia compression experiments and 0.216 mm in the femur compression experiments. This slight misalignment could be caused from the backlash in the 12.7 mm (1/2"), 20 threads per inch hand screws used to align the bone pot holders and could cause results as discussed in the known geometry testing section to errors in the order of $\pm100\mu\varepsilon$.

All of the above mentioned sources of difference would contribute to possible errors between the theoretical VM strain calculation and the experimental VM strain calculation. Of all these sources of difference, an offset in measurement and a possible variation in coordinate systems between the CAD model and the actual bone would cause the greatest error. A full error analysis was completed on both the experimental and theoretical strain calculations. Theoretical and experimental relative error equations plus a sample calculation using these equations are presented in Appendix I. Figure 2.25 and Figure 2.26 provide the calculated relative error for the both the experimental and theoretical VM strain calculation methods.
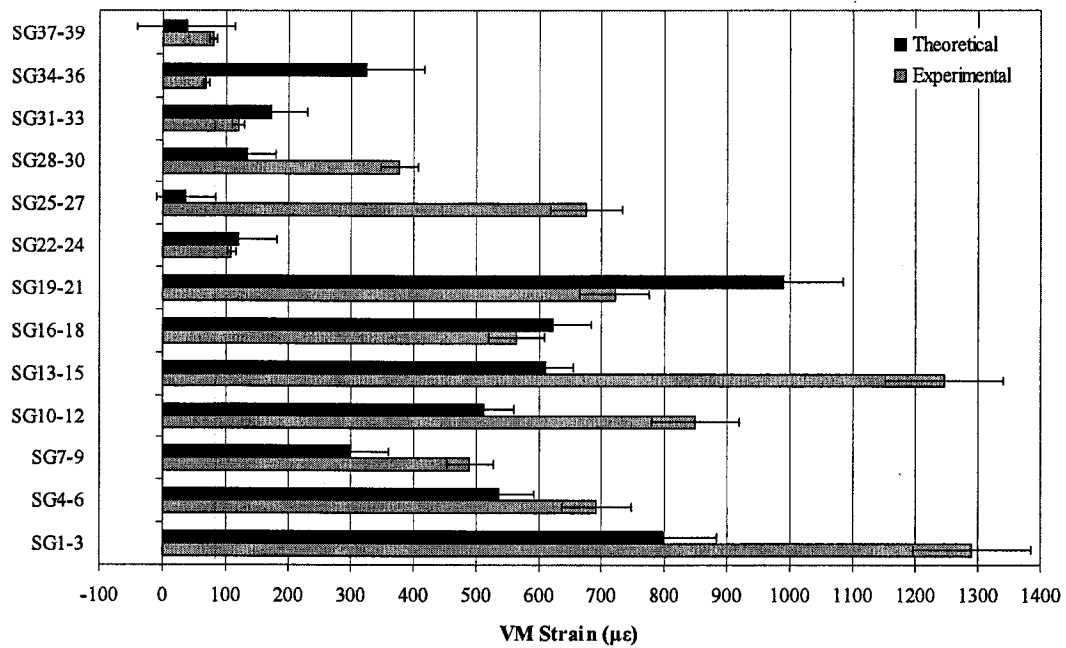
Figure 2.25: Composite tibia experimental and theoretical von Mises (VM) strain with associated error for the first compression test at 1780 N

For the composite tibia, the highest theoretical error and the lowest experimental error occurred at strain gauges 34-36 with values of approximately 95με and 5με, respectively. Similarly, the lowest theoretical error and the highest experimental error occurred at strain gauges 13-15 with an approximate error of 45με and 95με, respectively. The locations of these two rosettes are in areas of complicated geometry. Gauges 13-15 on the composite tibia are located beneath the lateral tibial condyle thus most likely being affected by geometry change, edge effects and load application proximity. Gauges 34-36 are located along the parting line of the composite tibia, where the separate composite halves mate to become one piece. Inconsistent density, composition and geometry may occur along this line thus explaining why the theoretical strain values are overestimating the results. Within the calculated relative error for both the theoretical and experimental

62

strain results, the theoretical strain results predict the experimental results for strain gauges 16-18, 22-24, 31-33 and 37-39.
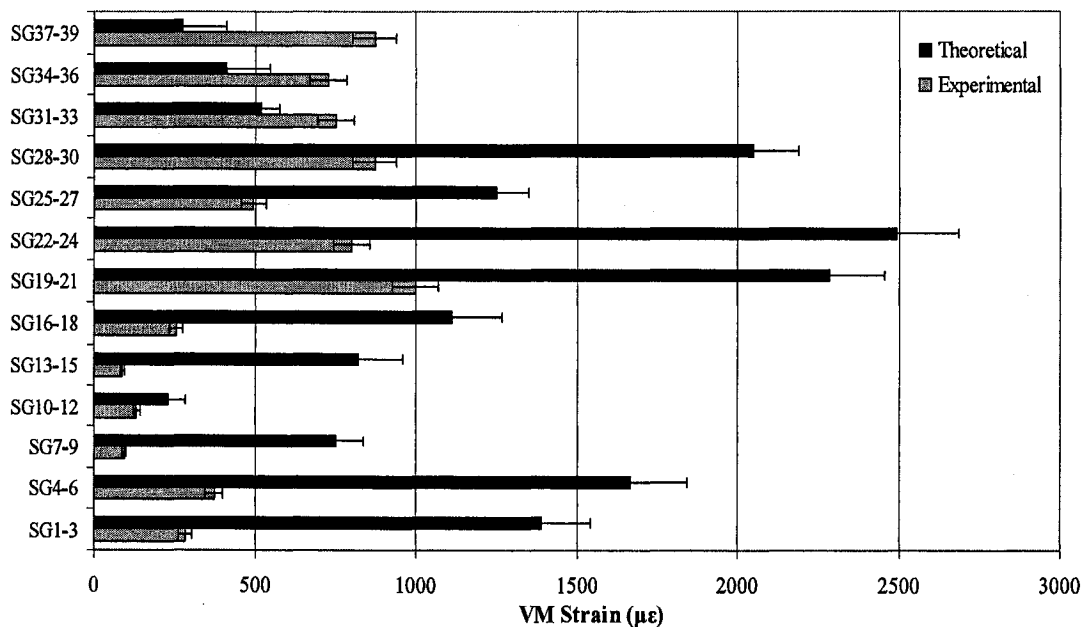
Figure 2.26: Composite femur experimental and theoretical von Mises (VM) error for the first compression test at 1780 N

For the composite femur, the highest theoretical error and the lowest theoretical error occurred at strain gauges 22-24 and 10-12 with values of $206\mu\varepsilon$ and $61\mu\varepsilon$, respectively. The highest experimental error and the lowest experimental error occurred at strain gauges 19-21 and 13-15 with values of $72\mu\varepsilon$ and $6\mu\varepsilon$, respectively. Gauges 10-12 and 13-15 are located on the front medial and the medial side of the composite femur, respectively. These are areas with small geometry changes. Gauges 19-21 and 22-24 are located on the posterior side of the femur. Gauge 19-21 is the lowest strain rosette and could be subjected to stress effects caused by potting. Gauges 22-24 are located where the shaft of the femur starts to widen into the femoral condyles. A small offset in measuring the geometry and location of this strain gauge would account for the large theoretical

63

error. Even with the calculated relative error for both the theoretical and experimental strain results, the theoretical strain results do not predict the experimental results for any strain gauges. For a more detailed description on the composite tibia and femur experiments and the results for the second and third tests, see Appendix H.

2.6.3 Discussion of MABTA Design

MABTA was designed as a multi use apparatus. This particular design enables the user to examine either complete or partial cadaveric human, animal or composite knee specimens (i.e. tibia or femur or both).

The main difference between MABTA and other quasi-static devices mentioned in the literature is that MABTA does not simulate muscles. For example, Whiteside et al. (Whiteside et al., 1987) studied the stability of the knee at various degrees of flexion using the quadriceps muscles. MABTA can study the stability of the knee as well but unlike the apparatus designed by Whiteside et al. the quadriceps muscles are not simulated and are not used to flex or extend the knee joint. Instead the magnitude of the forces applied to the joint by the quadriceps is included in the loading capabilities at the joint. Additionally, flexion-extension angles are adjusted through the F-E rotational axis of MABTA. The one design feature that is similar in both apparatii is that the femur is fixed and the tibia moves around it.

Comparing MABTA to the apparatus described in Bach and Hull (Bach and Hull, 1994), the placement of the specimen into each apparatus is similar. Both machines require that the knee is first inserted horizontally at full extension. Again, the main difference between these two apparatii is that no muscles are simulated with MABTA.

64

Lastly, the Oxford rig discussed in the study by Biden and O'Connor (Biden and O'Connor, 1990) is similar to MABTA in that they both can simulate flexed knee stance, allow for six degrees of freedom and that the movements of the joint is constrained by the structures of the knee and not by the apparatus itself. This feature was implemented in the design of MABTA by allowing the A-P/M-L loading mechanism to easily attach or detach from the entire tibial stage allowing the knee to float to a natural resting position before the loads are applied.

The design of MABTA incorporates several successful features of other published designs plus adds features that make it resemble no other apparatus. Not only can this portable apparatus conduct *in-vitro* experiments on cadaveric human, animal or composite bones with or without soft tissue, this apparatus can examine the design of total knee replacements, ACL fixations and knee joint bracing.

2.7 Conclusions

The multi-axis biomechanical testing apparatus was designed to conduct and measure the strain distribution along the cortex of a composite, animal or human knee joint. This machine has many advantages ranging from measuring loads in all six axes of the joint to allowing the application of load in numerous physiological positions.

From the known geometry experiment with a PVC pipe, it was found that the experimental results had good agreement with the theoretical results. It was found that the specimen was subjected to bending in both MABTA and the MTS Synergie 400 machine, therefore MABTA was not the source of the observed bending. Also theoretical calculations show that a strain difference of $100\mu\epsilon$ would occur between the front and back gauges, if the piece was off centre as little as 1mm or had slightly uneven ends.

65

Again this suggests that MABTA was not the main source of bending and illustrates that there should be even better agreement between experimental and theoretical strain results if the specimen was well manufactured and well aligned. This realization was the source for developing the alignment jig for the bones.

From the composite tibia and femur experimental results it was found that MABTA can provide repeatable strain results between tests. There are numerous sources of difference which explain the weak predicting capabilities of the theoretical strain calculations.

In conclusion, MABTA is a novel and valuable research apparatus. The results of this verification process show that MABTA can be considered an apparatus which exhibits a high experimental standard for composite specimen testing. The design of this machine was a success as it can apply many loading conditions, has good repeatability and with careful set-up can supply accurate and reliable data. As with any custom designed apparatus and budgetary constraints, the design of MABTA has limitations. MABTA may be improved by using electromechanical actuators to load the A-P and M-L directions. Secondly, MABTA is restricted to static testing, as the femoral end of the apparatus must be oriented first and manually fixed. Actuating these rotational axes is possible to create actuation in all six degrees of freedom, but would greatly increase the complexity, size, and cost of the design. Addressing these limitations would improve the apparatus but are not necessary for fulfilling the design objectives.

References

Ahmed, A.M., Burke, D.L., 1983. In-vitro measurement of static pressure distribution in synovial joints – Part II: Retropatellar Surface. Journal of Biomechanical Engineering 105, 226-236.

Askew, M.J, Lewis, J.L., 1981. Analysis of model variables and fixation post length effects on stresses around a prosthesis in the proximal tibia. Transactions of ASME, Journal of Biomechanical Engineering 103, 239-245.

Au A.G., 2008. A comprehensive approach to constructing human bone models: from CT to FE. PhD thesis. University of Alberta.

Bach, J.M., Hull, M.L., 1994. Description and evaluation of a new load application system for in vitro study of ligamentous injuries to the human knee joint. Advances in Bioengineering 128, 283-284.

Biden, E., O'Connor, J., 1990. Experimental Methods Used to Evaluate Knee Ligament Function. In: Daniel et al. eds. Knee Ligaments: Structure, Function, Injury and Repair. New York: Raven Press, Ltd, 135-151.

Bosma, R., Moes, H., Ligterink, D.J., Miehlke, R., 1979. The development of a knee joint simulator. Proceedings of the Institution of Mechanical Engineers 8(3), 177-180.

Burgess, I.C., Kolar, M., Cunningham, J.L., Unsworth, A., 1997. Development of a six station knee wear simulator and preliminary wear results. Proceedings of the Institution of Mechanical Engineers 211 Part H, 37-47.

Chao, E.Y.S., MacWilliams, B.A., Chan, B., 1994. Evaluation of a dynamic joint simulator using a prosthetic knee system. Advances in Bioengineering 28, 281-282.

Completo, A., Fonseca, F., Simões, J.A., 2007a. Experimental validation of intact and implanted distal femur finite element models. Journal of Biomechanics 40, 2467-2476.

Completo, A., Fonseca, F., Simões, J.A., 2007b. Finite Element and experimental cortex strains of the intact and implanted tibia. Journal of Biomechanical Engineering 129, 791-797.

Completo, A., Simões, J.A., Fonseca, F., 2007c. Experimental evaluation of strain shielding in distal femur in revision TKA. Experimental Mechanics, 1-8. (article in press)

Completo, A., Fonseca, F., Simões, J.A., 2008. Strain shielding in proximal tibia of stemmed knee prosthesis: experimental study. Journal of Biomechanics 41, 560-566.

67

Cristofolini, L., Viceconti, M., 2000. Mechanical validation of whole bone composite tibia models. Journal of Biomechanics 33, 278-288.

Cristofolini, L., Viceconti, M., Cappello, A., Toni, A., 1996. Mechanical validation of whole bone composite femur models. Journal of Biomechanics 29(4), 525-535.

Currier, J.H., Duda, J.L., Sperling, D.K., Collier, J.P., Currier, B.H., Kennedy, F.E., 1998. In vitro simulation of contact fatigue damage found in ultra-high molecular weight polyethylene components of knee prostheses. Proceedings of the Institution of Mechanical Engineers 212 Part H, 293-302.

DesJardins, J.D., Walker, P.S., Haider, H., Perry, J., 2000. The use of a force-controlled dynamic knee simulator to quantify the mechanical performance of total knee replacement designs during functional activity. Journal of Biomechanics 33, 1231-1342.

DiAngelo, D.J., Harrington, I.A., 1992. Design of a Dynamic Multi-Purpose Joint Simulator. Advances in Bioengineering 22, 107-110.

Dowson, D., Jobbins, B., O'Kelly, J., Wright, V., 1977. A Knee Joint Simulator. In: Dowson D, Wright V eds. Evaluation of Artificial Joints. London, Great Britain: The Biological Engineering Society, 79-90.

Fujie, H., Sekito, T., Orita, A., 2004. A novel robotic system for joint biomechanical tests: application to the human knee joint. Transactions of the ASME 126, 54-61.

Gray, H.A., Zavatsky, A.B., Taddei, F., Cristofolini, L., Gill, H.S., 2007. Experimental validation of a finite element model of a composite tibia. Journal of Engineering in Medicine 221 Part H, 315-324.

Guess, T.M., Maletsky, L.P., 2005. Computational modelling of a dynamic knee simulator for reproduction of knee loading. Journal of Biomechanical Engineering 127, 1216-1222.

Harrington, I.J., 1976. A bioengineering analysis of force actions at the knee in normal and pathological gait. Bio-Medical Engineering 11(5), 167-172.

Hashemi, J., Chandrashekar, N., Jang, T., Karpat, F., Oseto, M., Ekwaro-Osire, S., 2007. An alternative mechanism of non-contact anterior cruciate ligament injury during jump-landing: In-vitro simulation. Experimental Mechanics 47, 347-354.

Heiner, A.D., Brown, T.D., 2001. Structural properties of a new design of composite replicate femurs and tibias. Journal of Biomechanics 34, 773-781.

Kiguchi, K., Fukuda, T., Koga, Y., Watanabe, T., Terajima, K., Hayashi, T., Sakamoto, M., Matsueda, M., Suzuki, Y., Segawa, H., 1999. Development of a physiological knee motion simulator. Advanced Robotics 13(2), 171-188.

Li, G., Gill, J., Kanamori, A., Woo., S.L.-Y., 1999a. A validated three-dimensional computational model of a human knee joint. Journal of Biomechanical Engineering 121, 657-662.

Li, G., Rudy, T.W., Sakane, M., Kanamori, A., Ma, C.B., Woo, S.L.-Y., 1999b. The importance of quadriceps and hamstring muscle loading on knee kinematics and in-situ forces in the ACL. Journal of Biomechanics 32, 395-400.

Maletsky, L.P., Hillberry, B.M., 1999. Dynamic Control of a Four-Axis, Electrohydraulic Knee Simulator. Proceedings of the ASME Dynamic Systems and Control Division 61, 447-452.

Maletsky, L.P., Hillberry, B.M., 2000. Loading evaluation of knee joint during walking using the next generation knee simulator. Advances in Bioengineering 48, 91-92.

Maletsky, L.P., Hillberry, B.M., 2005. Simulating dynamic activities using a five-axis knee simulator. Journal of Biomechanical Engineering 127, 123-133.

MatWeb: Material Property Data. Online Information Materials Resource. 8 May 2008 < http://www.matweb.com/search/DataSheet.aspx?MatID=78512>.

Morrison, J.B., 1969. Function of the knee joint in various activities. Biomedical Engineering 4(12), 573-580.

Papini, M., Zdero, R., Schemitsch, E.H., Zalzal, P., 2007. The Biomechanics of Human Femurs in Axial and Torsional Loading: Comparison of Finite Element Analysis, Human Cadaveric Femurs, and Synthetic Femurs. Journal of Biomechanical Engineering 129, 12-19.

Paul, I., Rose, R., Simon, S., Radin, E., 1977. The MIT Knee Simulator. In: Dowson D, Wright V eds. Evaluation of Artificial Joints. London, Great Britain: The Biological Engineering Society, 69-77.

Pavlovic, J.L., Kirstukas, S.J., Touchi, H., Bechtold, J.E., Gustilo, R.B., 1994. Dynamic simulation machine for measurement of knee mechanics and intra-articular pressures. Advances in Bioengineering 28, 277-278.

Shaw, J.A., Murray, D.G., 1973. Knee Joint Simulator. Clinical Orthopaedics and Related Research 94, 15-23.

69

Sheshadri, V.B., Rullkoetter, P.J., Hillberry, B.M., 1997. In vitro measurement of the six degree of freedom kinematics of the human knee during simulated gait. American Society of Mechanical Engineers, Dynamic Systems and Control Division DSC 61, 375-379.

Simonsen, M. 19 Dec. 2007. Email Communication.

Szivek, J.A., Gealer, R.L., 1991. Comparison of the Deformation Response of Synthetic and Cadaveric Femora during Simulated One-Legged Stance. Journal of Applied Biomaterials 2, 277-280.

Szklar, O., Ahmed, A.M., 1987. A Simple Unconstrained Dynamic Knee Simulator. Journal of Biomechanical Engineering 109, 247-251.

van Kampen, A., Huiskes, R., 1990. The three-dimensional tracking pattern of the human patella. Journal of Orthopaedic Research 8, 372-382.

Waide, V., Cristofolini, L., Stolk, J., Verdonschot, N., Toni, A., 2003. Experimental investigation of bone remodelling using composite femurs. Clinical Biomechanics 18, 523-536.

Walker, P.S., Blunn, G.W., Broome, D.R., Perry, J., Watkins, A., Sathasivam, S., Dewar, M.E., Paul, J.P., 1997. A knee simulating machine for performance evaluation of total knee replacements. Journal of Biomechanics 30(1), 83-89.

Whiteside, L.A., Kasselt, M.R., Haynes, D.W., 1987. Varus- valgus and rotational stability in rotationally unconstrained total knee arthroplasty. Clinical Orthopaedics and Related Research 219, 147-157.

Wilson, D.R., MacWilliams, B.A., DesJardins, J.D., 1996. In vitro simulation of knee joint mechanics for the validation of biomechanical models. American Society of Mechanical Engineers, Bioengineering Division BED 33, 323-324.

Zachman, N.J., Hillberry, B.M., Kettelkamp, D.B., 1978. Design of a Load Simulator for the Dynamic Evaluation of Prosthetic Knee Joints. American Society of Mechanical Engineers (78-DET-59).

Chapter 3: Experimental Verification of a Proposed Patient Specific Finite Element Knee Model using Composite Femur and Tibia

3.1 Introduction

Finite element (FE) models are frequently used to evaluate the effectiveness of a prosthetic design and to examine problem areas in a particular component without having to create a prototype of the design (Stolk et al., 2002). Experimental validation of these FE models is pertinent before such models can be considered accurate (Stolk et al., 2002).

FE models have been experimentally validated for human anterior cruciate ligaments (Song et al., 2004), cadaveric femurs (Yosibash et al., 2007; Taddei et al., 2006; Schileo et al., 2007; Keyak et al., 1993), a full tibio-femoral joint (Li et al., 1999) and several composite specimens. More and more studies are being completed with composite specimens as cadaveric specimens are difficult to acquire. Both the composite tibia and femur provide an appropriate substitute to cadaveric specimens (Cristofolini and Viceconti, 2000; Cristofolini et al., 1996), with the composite femur having higher reproducibility (Cristofolini et al., 1996). The composite tibia is more suitable for bending-dominant applications rather than torsion-dominant applications (Cristofolini and Viceconti, 2000).

Several studies have used composite bones as substitutes for cadaveric specimens to validate finite element models, some for the femur (Completo et al., 2007a; Stolk et al., 2002; Cheung et al., 2004), others for the tibia (Completo et al., 2007b; Gray et al.,

71

2007). In the composite tibia FE experimental validation studies (Completo et al., 2007b; Gray et al., 2007), the strain was measured along the cortex while vertical point loads were applied sequentially to each of the tibial condyles.

Gray et al. (Gray et al., 2007) conducted axial, bending and torsional tests on the composite tibia. Only the experimental results from the axial loading scenario were used in the validation of the FE model since axial loading is physiologically dominant. The tibial plateau surface was first prepared by creating ten small indentations to ensure good loading contact between bone and rod, followed by the application of a 700 N vertical load to one of the ten different points on the tibial plateau using a tapered steel rod with a 5mm diameter tip. Tests were performed at each of the ten indentation locations.

Completo et al. (Completo et al., 2007b) applied vertical loads to the tibial condyles through a metallic sphere. Each condyle was loaded sequentially with 60% of the load placed on the lateral condyle (1160 N) and 40% of the load placed on the medial condyle (870 N). Using the principal of superimposition a loading state of 3-times body weight (BW) was applied to the specimen.

A principal goal of the patient-specific FE model currently being assessed is for the design of future knee prostheses. The evaluation of the distal composite femur is more applicable, hence the studies completed on the proximal femur (Stolk et al., 2002; Cheung et al., 2004) are not as relevant. Completo et al. (Completo et al., 2007a) experimentally validated a FE model of the distal femur. In this study, separate vertical loads were applied to a metallic sphere, placed on top of an aluminum base bonded to the femoral condyles. Forty percent of the load (870 N) was placed on the medial condyle

72

and 60% of the load (1160 N) was placed on the lateral condyle. The principal of superimposition was used to apply a total load of 3BW to the femur.

The aim of this study is to experimentally verify a patient-specific finite element model of a tibia and femur developed by Au (Au, 2008) using strain results measured from a third generation composite tibia and femur loaded using the multi-axis biomechanical testing apparatus developed at the Department of Mechanical Engineering. In the previous chapter, this apparatus was shown that it can be classified as an apparatus with a high standard for composite specimen experiments.

3.2 Materials and Specimen Preparation

A third generation composite tibia (#3301) and femur (#3303) (Pacific Research Laboratories, Vashon Island, WA) were used in this study. The composite tibia (Figure 3.1) and femur (Figure 3.2) were each instrumented with thirteen Omega 45° triaxial-stacked rosettes (SGD-2/350-RY53). Strain gauges were placed where the most stress effects are seen on the cortex from total knee replacements. These positions are of high importance when designing future knee prostheses therefore were chosen in the verification of the patient-specific FE model.

Table 3.1 and Table 3.2 indicate the strain gauge positions with respect to the centre of the bone pot for the tibia and femur, respectively. Centre of gauge positions were measured using a coordinate measuring machine (CMM, MicroVal, Browne and Sharpe, North Kensington, RI) with an accuracy of 0.001 mm in each direction.

73
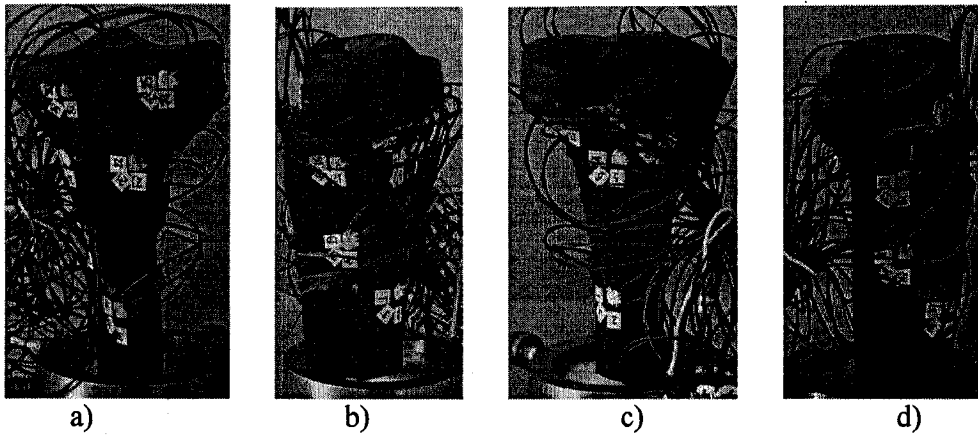
Figure 3.1: The thirteen tibial strain rosette positions: a) Anterior: Rosettes 8-11 b) Lateral: Rosettes 6-7 c) Posterior: Rosettes 1-5 and d) Medial: Rosettes 12-13

Table 3.1: Tibia strain gauge positions with respect to centre of the bottom face of bone pot (all dimensions are in mm)

Rosettes	Gauges	X	Y	Z
1	SG1-3	-6.612	6.810	-75.057
2	SG4-6	-2.849	8.850	-127.176
3	SG7-9	14.955	15.798	-134.340
4	SG10-12	-3.753	14.358	-145.001
5	SG13-15	-19.522	7.000	-139.601
6	SG16-18	-21.288	-13.138	-129.221
7	SG19-21	-16.864	-7.934	-98.486
8	SG22-24	-7.254	-34.554	-130.762
9	SG25-27	-16.533	-27.159	-158.608
10	SG28-30	19.006	-24.616	-154.005
11	SG31-33	22.079	-8.047	-125.825
12	SG34-36	14.687	-7.651	-96.423
13	SG37-39	0.396	-25.347	-73.858

Figure 3.2: The thirteen femoral strain rosette positions: a) Anterior: Rosettes 1-4 b) Medial: Rosettes 5-6 c) Posterior: Rosettes 7-11 and d) Lateral: Rosettes 12-13

Table 3.2: Femur strain gauge positions with respect to centre of the bottom face of bone pot (all dimensions are in mm)

Rosettes	Gauges	X	Y	Z
1	SG1-3	-1.202	-24.097	-74.622
2	SG4-6	-0.547	-32.455	-122.579
3	SG7-9	12.509	-44.303	-143.597
4	SG10-12	-24.318	-32.132	-153.054
5	SG13-15	-19.831	-14.950	-102.224
6	SG16-18	-23.365	-14.728	-123.093
7	SG19-21	0.587	0.484	-78.934
8	SG22-24	2.081	-5.060	-126.829
9	SG25-27	-19.545	5.155	-147.140
10	SG28-30	24.730	-0.065	-139.873
11	SG31-33	4.973	-7.239	-164.800
12	SG34-36	21.535	-15.220	-101.474
13	SG37-39	26.126	-21.733	-124.200

Using a custom-designed alignment jig, the composite tibia and femur were potted in bone pots. This was done by first securing the tibial and femoral bone pots in the same x-y position with the help of alignment dowel pins and screws (Figure 3.3). Next, a desirable contact between the two specimens was found. Since there are no soft tissues attached to the composite bones to aid in this contact, the two bones were aligned

75

to achieve stability and to distribute the load across the tibial plateau. Lastly, this position was secured with plaster of Paris. Before either specimen was placed into MABTA, a coaxial alignment indicator was used to align the tibial and femoral bone pot holders to within 0.0127 mm (0.0005"). For a more detailed description and proper use of the alignment jig and coaxial alignment indicator, see Appendices C and F.
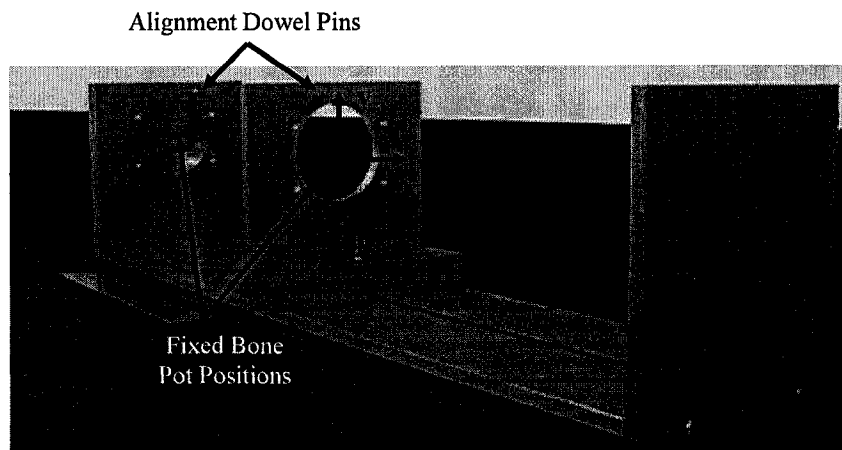
Figure 3.3: Custom-designed alignment jig

3.2.1 Experimental Equipment to Measure Strain along Cortex of Composite Bone

Several pieces of equipment (described in Appendix H) are required to measure the experimental strains along the cortex of composite bone: a personal computer with data acquisition software (National Instruments LabVIEW 8.5) to record strain values, a data acquisition system (SCXI-1000 chassis with two SCXI-1314 and one SCXI-1317 strain gauge terminal blocks, National Instruments) to measure strain values, a signal conditioner (AMTI MiniAmp MSA-6) to measure loads placed on the specimen, MABTA, the custom-made loading jig (Figure 3.4a), two voltmeters (Figure 3.4b) and a Vishay instrument (Figure 3.4c) to measure the load distribution across the aluminum

76

rods of the loading jig (Figure 3.4) and the composite tibia (Figure 3.1) and femur (Figure 3.2) instrumented with strain gauges.
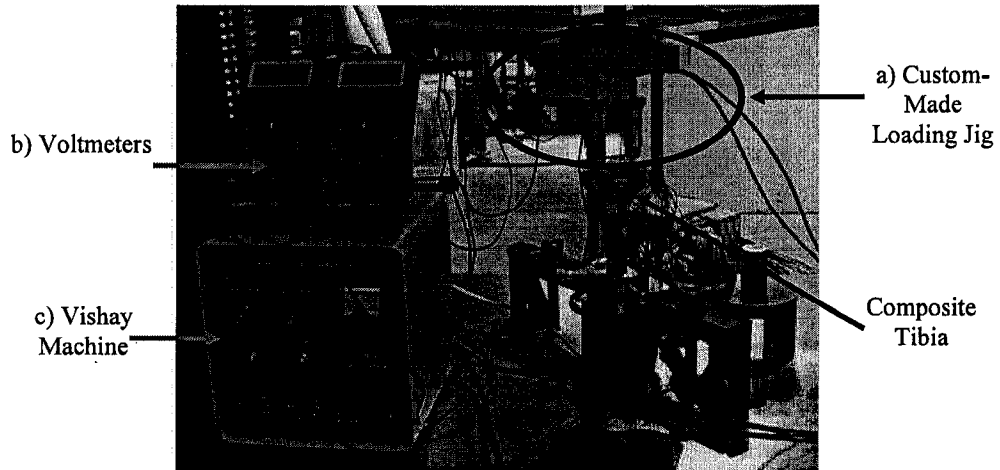
Figure 3.4: Test set up in Instron machine to conduct compression test on composite tibia with custom-made loading jig

To study the validity of the experimental results obtained from tests done in MABTA and to compare those results with a finite element model, a custom made loading jig was designed by Au (Au, 2008) to place two point loads onto the tibial condyles Figure 3.5).
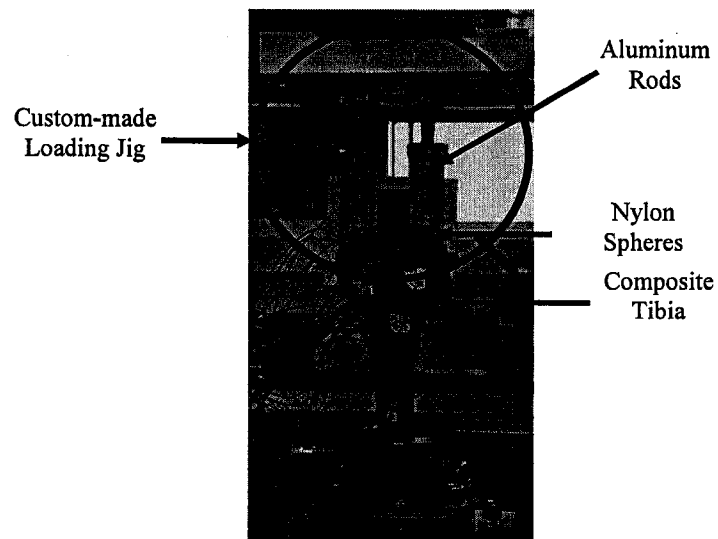
Figure 3.5: Custom-made loading jig in position for composite tibia compression test

77

Unlike the loading mechanisms in previous FE validation studies with a composite tibia (Completo et al., 2007b; Gray et al., 2007), the custom-made loading jig consists of two length adjustable aluminum rods with nylon spheres attached to the ends. These nylon spheres were attached to the end of the loading rods to lower the Hertzian contact stresses between the loading jig and the composite specimen. The aluminum rods can be adjusted in the medial-lateral and proximal-distal directions to account for different sized specimens. Each aluminum rod was instrumented with four CEA strain gauges (CEA 13-062-UW-350) used to measure the load distribution occurring on each condyle. This jig was first inserted into an Instron machine (Model TTK, Norwood, MA, USA) and second into a multi-axis biomechanical testing apparatus (MABTA).

3.2.2 Experimental Set-up

The experimental set-up between the Instron compression test and MABTA compression test varies slightly due to the different components involved and different loading mechanisms. For all compression tests, the custom-made loading jig and the composite specimen were inserted into either the Instron machine (Figure 3.6, Figure 3.7) or MABTA (Figure 3.8). The composite specimen was then loaded to 667.2 N (150 lb) in 222.2 N (50 lb) increments. The strains were recorded at each increment, allowing the program to record for approximately 20 seconds. Further details for the experimental protocols for both the Instron compression test and the MABTA compression tests are presented in Appendix F.

78

Figure 3.6: Positioning nylon spheres on tibial condyles

Foam

Rubber
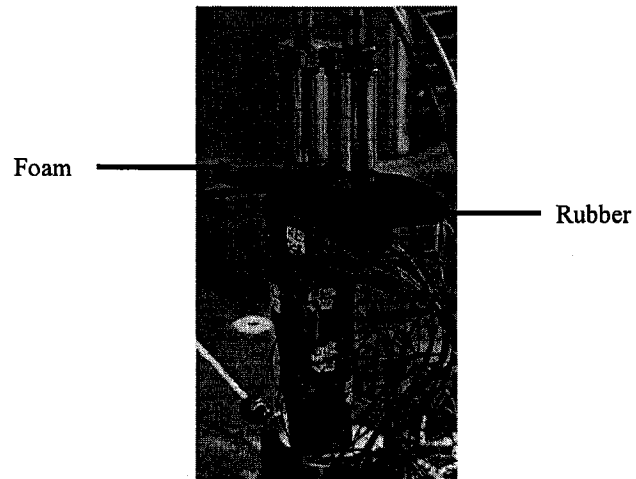
Figure 3.7: Final set-up for composite tibia compression test in Instron machine

79

Composite
Tibia

(a)   (b)
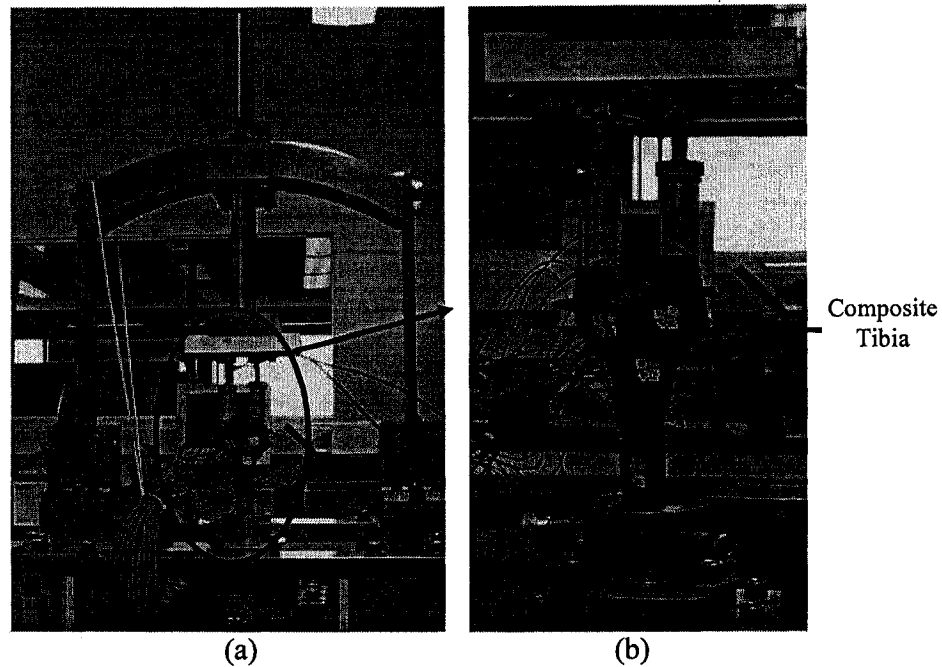
Figure 3.8: (a) Custom-made loading jig installed in MABTA; (b) Magnified view of custom-made loading jig positioned on composite tibia

3.3 Results and Discussion

To verify the patient-specific FE model of the knee, the two-prong loading jig was used to load a third generation composite tibia and femur. Prior to loading the composite bone specimens, it was first used to load a composite block acquired from Pacific Research Laboratories to determine maximum load limits. From this preliminary experiment, it was determined that the jig would crack the epoxy surface of the composite bones at a load of 2000 N (450 lb) or 1000 N (225 lb) per rod, test loads were adjusted in consequence.

80

3.3.1 Experimental Longitudinal Strain Results Verification between Two Separate Loading Mechanisms

To verify the experimental strain results from MABTA, two experiments were conducted: one in MABTA and the other in the Instron machine. Following the experimental protocol described earlier, the third generation composite tibia was first loaded to 667 N (150 lb) in the Instron machine and the test was repeated in MABTA. The measured longitudinal strains for both the Instron and MABTA experiments are presented in Figure 3.9 and the microstrain difference between these two apparatii for each strain rosette is presented in Figure 3.10 and in Figure 3.11 with outliers removed.
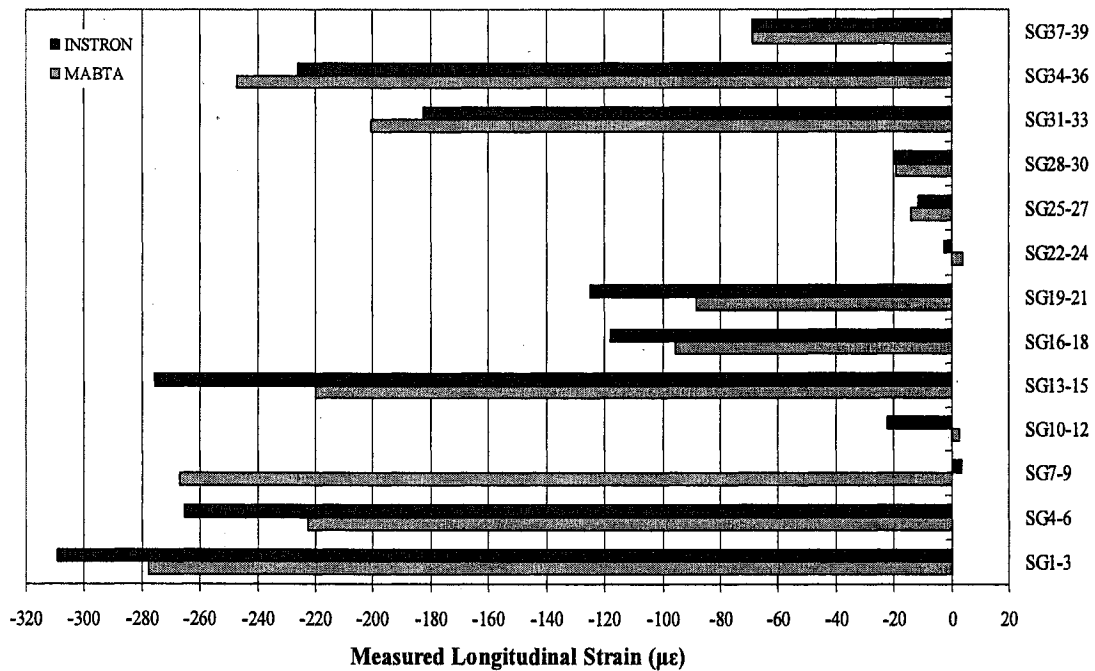
Figure 3.9: Comparison between MABTA and Instron machine composite tibia measured longitudinal strain results at 667 N
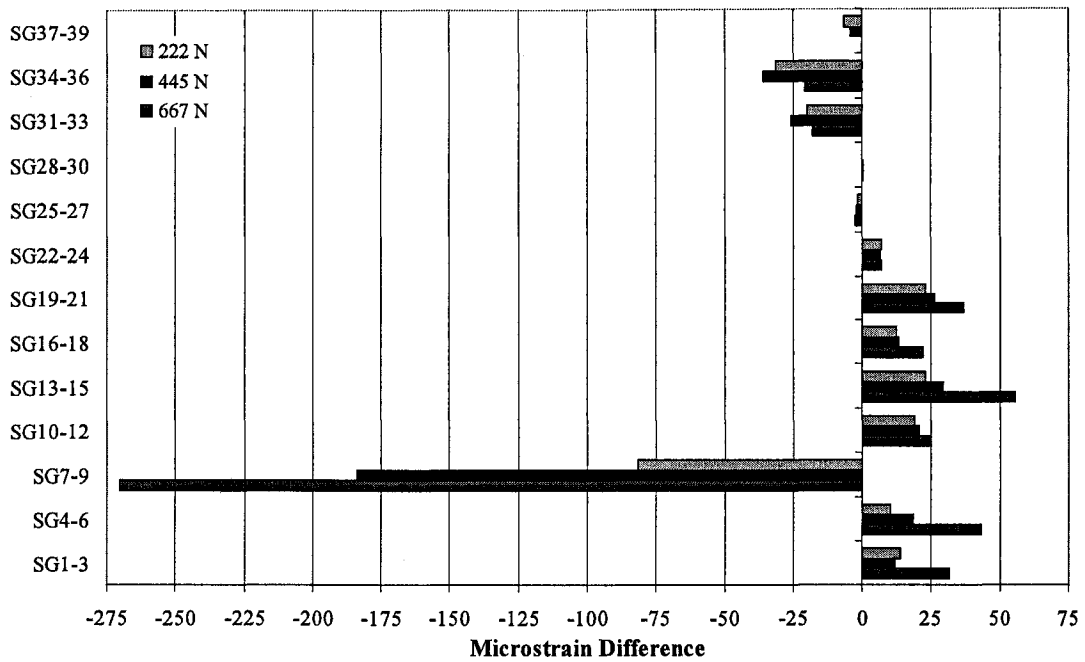
Figure 3.10: Microstrain difference between MABTA and Instron composite tibia measured longitudinal strains for all strain gauge rosettes
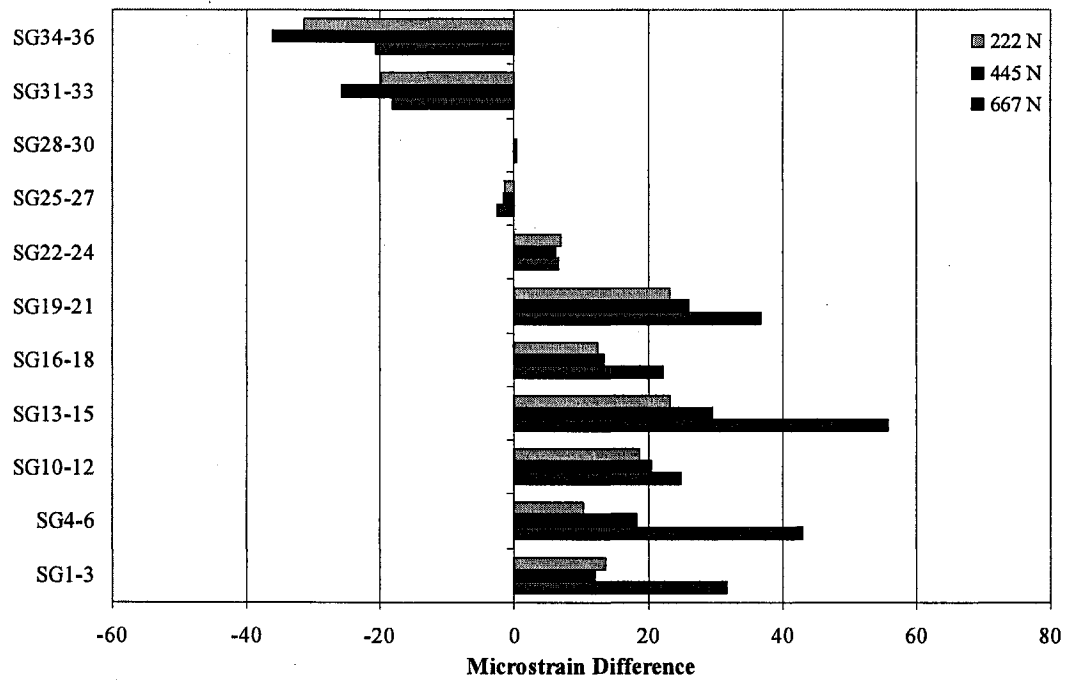
Figure 3.11: Microstrain difference between Instron and MABTA composite tibia measured longitudinal strains (removed SG7-9)

82

It can be seen from Figure 3.9 through Figure 3.11, that MABTA can produce experimental longitudinal strains similar to the Instron machine. Figure 3.10 presents the microstrain difference between the two tests for each strain rosette. From this plot, strain gauges 7-9 have the highest microstrain difference with approximately 270με. This extremely high difference can be attributed to the wiring failure, which occurred during the Instron compression test. Therefore gauges 7-9 were considered outliers and as such were removed from Figure 3.11.

With strain gauges 7-9 removed, the magnitude of the maximum and minimum microstrain difference at maximum load is approximately 56με (SG13-15) and 0.28με (SG28-30), respectively (Figure 3.11). The largest microstrain difference occurs at strain gauges 13-15, which are located beneath the lateral tibial condyle thus most likely being affected by geometry change, edge effects and load application proximity.

Other differences between the experimental results most likely arose from the readjustment of the loading rods onto the composite tibia for the MABTA compression test and the foam and rubber pads, not from the design of the apparatus, strengthening the argument that MABTA can produce valid experimental strain results.

3.3.2 Comparison of Foam and No Foam Loading with Custom-Made Loading Jig and Composite Tibia in MABTA

Following previously described protocols, the composite tibia was loaded to 667.2 N (150 lb) in 222.2 N (50 lb) increments. Initially, to mimic connective and load-bearing tissues attached to the composite tibia, a piece of foam and rubber would be able to better distribute the load across the joint and avoid specimen surface damage. The experiment

83

was repeated with and without foam and the experimental von Mises (VM) strains for

both experiments were determined and are presented in Figure 3.12.
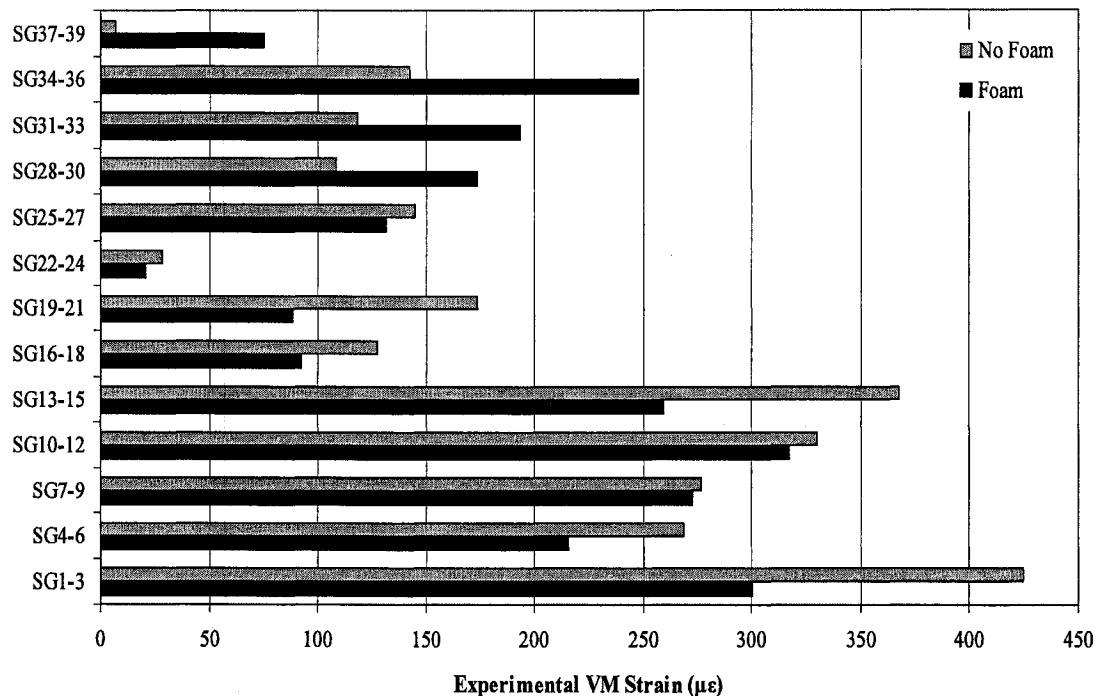
Figure 3.12: Comparison of experimental von Mises (VM) strain for composite tibia at 667 N (150lb) with and without the foam and rubber pieces inserted between loading jig and tibial plateau.

The experimental VM strain values at each rosette in Figure 3.12 show that the

compression test without foam produces higher strains than the one with foam except for

gauges 28 through 39. Using Figure 3.1 and

Table 3.1, these strain gauges are located on the medial and front medial side of

the composite tibia. This phenomenon could have two reasons: the first being that the two

rods of the jig were aligned differently between the two tests and secondly, the position

of the foam could have distributed the load more toward the medial side of the specimen

and reduce the differences in contact pressure seen without the foam.

84

Similarly previous studies (Completo et al., 2007a; Gray et al., 2007; Completo et al., 2007b) applied load directly to the surface of the composite specimen; therefore the experimental verification of the patient-specific FE knee model will only compare strain results from no foam tests. Additionally, for experimental verification of the FE model, the exact loading distribution and contact points are required. In the compression test with the foam, this information would be approximate as the foam creates an unknown load distribution across the joint.

3.3.3 Comparison of Experimental and Predicted von Mises Strain

For verification of the patient-specific FE knee model purposes, a maximum load of 667 N (150 lb) was first applied to the composite tibia followed by the composite femur. In both experiments, two point loads were applied to the condyles of the specimen.

The experimental and predicted FE VM strain results for the composite tibia and femur are presented in Figure 3.13 and Figure 3.14, respectively. VM strains were used for comparison purposes as it ignores the direction of the strain gauge and therefore allows for comparison of FE predicted and experimental strain results. For the mostly axial stress state found at the surface of the specimen as a result of applied loads, the VM strain results are approximately in line with the longitudinal strain since there is minimal shear from torsional loads. Also, it should be noted that all FE results were obtained from Au (Au, 2008).
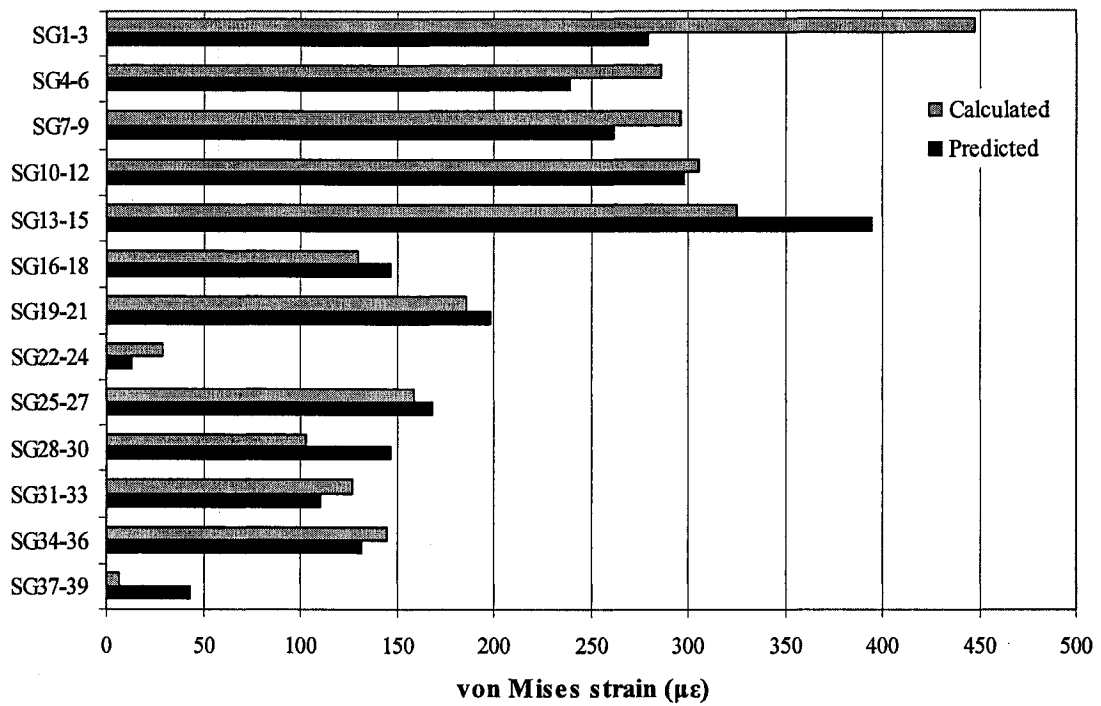
Figure 3.13: Comparison of experimentally calculated and FE predicted von Mises strain for the composite tibia.
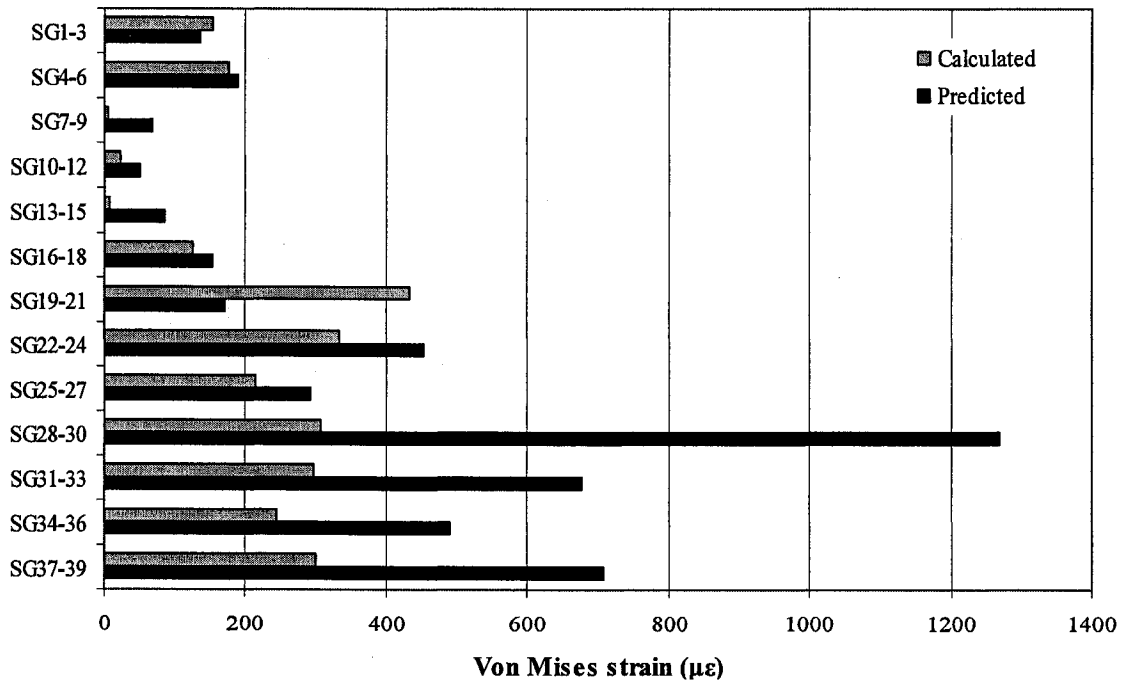
Figure 3.14: Comparison of experimentally calculated and FE predicted von Mises strain for the composite femur.

86

From Figure 3.13 and Figure 3.14, the experimental VM strain results match much better with the predicted results for the composite tibia than for the composite femur. When potting the composite specimens, the main objectives were to create a desirable stability and load distribution for bone on bone loading. With these objectives, the femur was potted at 4° from the vertical axis of MABTA. This slight angle increases the complexity of load application in the FE model thus explaining why the predicted strain results differ more for the femur than the tibia. For instance, at one of the most complicated geometrical areas of the composite femur (strain gauges 28-30, located on the underside of the femoral condyles), the theoretical VM hand calculations, as used in the previous chapter and described in Appendix I, would decrease from 719με to 362με at maximum load if the 4° offset was not included.

Comparing the FE predicted and experimental values for the composite tibia (Figure 3.13), it is observed that the experimentally calculated VM strains at strain gauges 1-3 are approximately 170με larger than the FE predicted VM strains, this is a difference of 38%. Similarly strain gauges 28-30 on the composite femur (Figure 3.14) have a difference of 76% (961.5με) between FE predicted VM strains and experimentally calculated strains. These higher percent differences indicate that these gauges are outliers and were thus removed from the analysis.

Next, a plot comparing the calculated VM strain and FE predicted VM strain was created for both the composite tibia (Figure 3.15) and femur (Figure 3.16).
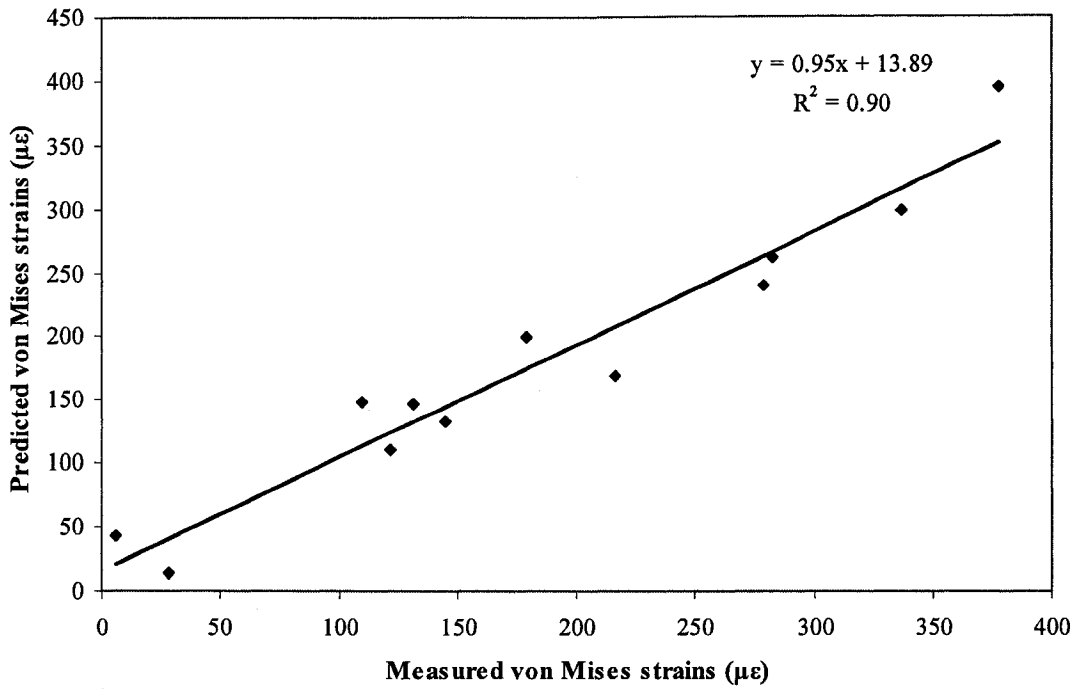
Figure 3.15: Comparison of finite element predicted von Mises strains and calculated von Mises strains at 667 N for composite tibia. Strain gauges 1-3 were considered outliers and thus removed.
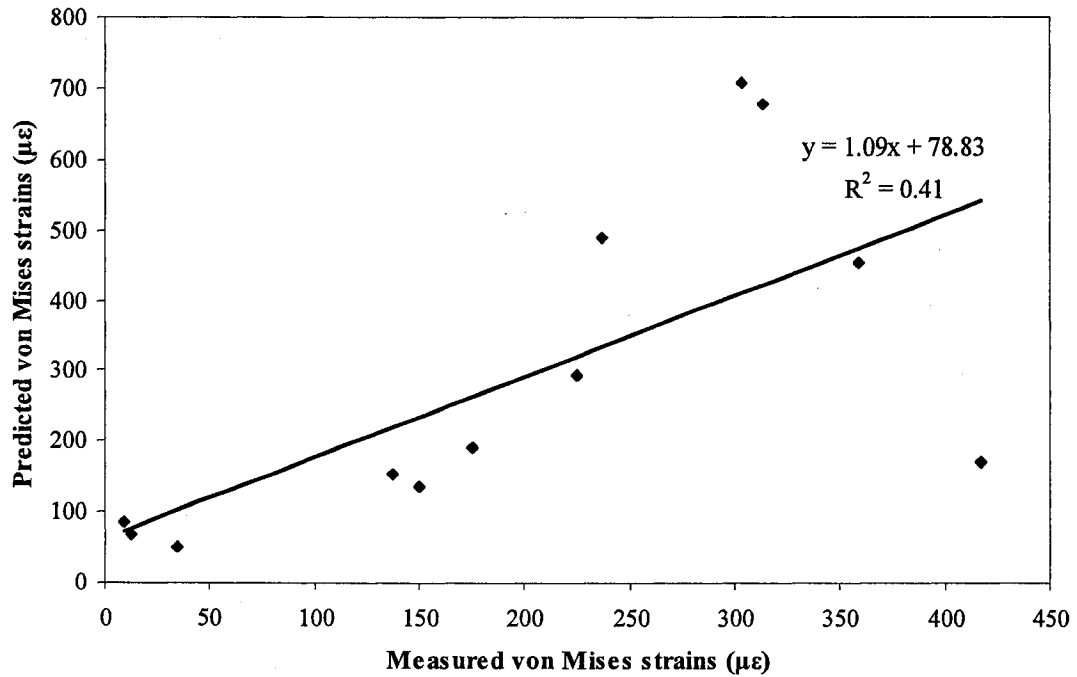
Figure 3.16: Comparison of finite element predicted von Mises strains and calculated von Mises strains at 667 N for composite femur. Strain gauges 28-30 were considered outliers and thus removed.

88

A slope of one, an intercept of zero and an R^2 value of 1 represents that there is perfect agreement between experimental and predicted VM strain results (Gray et al., 2007). The composite tibia plot (Figure 3.15) indicates that the FE VM strain results strongly predict the experimental strain results (slope = 0.95, intercept = 13.89μɛ, R^2 = 0.90). However, the composite femur plot (Figure 3.16) indicates that the FE VM strain results can predict the experimental strain results but not very strongly (slope = 1.09, intercept = 78.83μɛ, R^2 = 0.41). The low regression coefficient for the composite femur FE model could be explained by the 4° angle from the vertical axis.

Both Gray et al. (Gray et al., 2007) and Completo et al. (Completo et al., 2007b) experimentally validated a FE model with a composite tibia. In these two studies the predicted values strongly matched the experimental values. Gray et al. (Gray et al., 2007) found a regression line with a slope of 0.999, an intercept of -6.24μɛ and an R^2 of 0.962 for all axial load cases. Similarly, Completo et al. (Completo et al., 2007b) had a slope of 1.03, an intercept of 7.69μɛ and a R^2 of 0.91. Two main distinctions between the two previous studies and the present study are (1) Gray et al. caused stress effects along the top surface of the tibia by first creating indentations for loading contact and thus excluded the strain results from rosettes which were within 25 mm from the loading point and (2) Completo et al. applied individual point loads and then used the superimposition principal to load specimen to 3BW. In the present study two simultaneous point loads were applied. The individual loading conditions cannot be said to be as representative of the physiological situation of dual loading.

Completo et al. (Completo et al., 2007a) also completed an experimental validation study of the distal femur. In this study two load cases were examined, the first

one being 1160 N on the medial condyle and the second one being 870 N on the lateral condyle. For both of these load cases, the FE values strongly predicted the experimental strain values with slopes of 0.96, small intercepts and R^2 of 0.97 and 0.99 for loading case one and two, respectively. There are two possible sources of difference between the study conducted by Completo et al. (Completo et al., 2007a) and the present study and why the present study did not obtain as strong of a prediction between FE values and experimental values. Firstly, the loads were placed on each of the femoral condyles individually, unlike in the present study where both rods applied loads simultaneously. Secondly, the femur in the present study was potted in such a way to obtain composite tibia and femur bone on bone loading thus creating a 4° angle between the central axis of the femur and the vertical axis of MABTA.

3.4 Conclusions

Through the comparison of experimental longitudinal strains along the cortex of a composite tibia, it was found that the experimental strain results were reproducible between an Instron machine and MABTA. This strengthens the argument that MABTA produces valid experimental results.

Using MABTA, which was shown to have a high standard in experimenting with composite specimens, the FE model in the present study was successfully shown to accurately predict strains for a composite tibia. However, the strains from the composite femur FE model did not predict the experimental strain results as well. It is believed that these results are a factor of the slight offset angle of the femur resulting from the physiologically alignment of the bones that added complexity for the determination of

90

load placement in the FE model. Both the FE model and MABTA are useful tools for examining the strains along the cortex of composite bone.

References

Au A.G., 2008. A comprehensive approach to constructing human bone models: from CT to FE. PhD thesis. University of Alberta.

Completo, A., Fonseca, F., Simões, J.A., 2007a. Experimental validation of intact and implanted distal femur finite element models. Journal of Biomechanics 40, 2467-2476.

Completo, A., Fonseca, F., Simões, J.A., 2007b. Finite element and experimental cortex strains of the intact and implanted tibia. Journal of Biomechanical Engineering 129, 791-797.

Cheung, G., Zalzal, P., Bhandari, M., Spelt, J.K., Papini, M., 2004. Finite Element Analysis of a Femoral Retrograde Intramedullary Nail Subject to Gait Loading. Medical Engineering and Physics 26, 93-108.

Cristofolini, L., Viceconti, M., 2000. Mechanical validation of whole bone composite tibia models. Journal of Biomechanics 33, 278-288.

Cristofolini, L., Viceconti, M., Cappello, A., Toni, A., 1996. Mechanical validation of whole bone composite femur models. Journal of Biomechanics 29(4), 525-535.

Gray, H.A., Zavatsky, A.B., Taddei, F., Cristofolini, L., Gill, H.S., 2007. Experimental validation of a finite element model of a composite tibia. Journal of Engineering in Medicine 221 Part H, 315-324.

Keyak, J.H., Fourkas, M.G., Meagher, J.M., Skinner, H.B., 1993. Validation of an automated method of three-dimensional finite element modelling of bone. Journal of Biomedical Engineering 15 (6), 505-509.

Li, G., Gill, J., Kanamori, A., Woo., S.L.-Y., 1999. A validated three-dimensional computational model of a human knee joint. Journal of Biomechanical Engineering 121, 657-662.

Schileo, E., Taddei, F., Malandrino, A., Cristofolini, L., Viceconti, M., 2007. Subject-specific finite element models can accurately predict strain levels in long bones. Journal of Biomechanics 40, 2982-2989.

91

Song, Y., Debski, R.E., Musahl, V., Thomas, M., Woo., S.L.-Y., 2004. A three-dimensional finite element model of the human anterior cruciate ligament: a computational analysis with experimental validation. Journal of Biomechanics 37, 383-390.

Stolk, J., Verdonschot, N., Cristofolini, L., Toni, A., Huiskes, R., 2002. Finite element and experimental models of cemented hip joint reconstructions can produce similar bone and cement strains in pre-clinical tests. Journal of Biomechanics 35, 499-510.

Taddei, F., Cristofolini, L., Martelli, S., Gill, H.S., Viceconti, M., 2006. Subject-specific finite element models of long bones: An in vitro evaluation of the overall accuracy. Journal of Biomechanics 39, 2457-2467.

Yosibash, Z., Padan, R., Joskowicz, L., Milgrom, C., 2007. A CT-Based High-Order Finite Element Analysis of the Human Proximal Femur Compared to In-vitro Experiments. Journal of Biomechanical Engineering 129, 297-309.

Chapter 4: Preliminary Evaluation of the Applicability of MABTA to Testing of Biological Structures

4.1 Introduction

As discussed in Chapter 2, MABTA was made out of stainless steel and aluminum in order to be corrosion resistant and easily sanitized for use with biological specimens, i.e. human or animal. Most biological tissue testing revolves around determining the material and mechanical properties of soft tissues and bone using various animal or human specimens. The robustness of the design allows for numerous anatomical loading positions and large variations in size and geometry from cows to human. For example, the flexion-extension (F-E) rotational axis can be fixed from 50° hyperextension to 100° flexion to account for the constant F-E rotation seen in many animals and for the daily activities seen in humans.

Animal specimens have often been used as alternatives to human specimens as they are easier to obtain and still provide insight into the structure, properties and behaviour of soft tissues. This chapter aims to demonstrate that MABTA could be used to conduct *in vitro* experiments ranging from static testing of ligaments, articular cartilage, and menisci to finding stress/strain properties along the cortex of bone.

Extensive research has been conducted on the properties of tissues such as ligaments, menisci, articular cartilage and bone of various animals. For example, several studies have been conducted on the biomechanical properties of ligaments and the success of various fixation techniques using rabbits (Woo et al., 1992; Woo et al., 1987; Moon et al., 2006; Grassman et al., 2002, Woo et al., 1990), porcine (Berkson et al.,

93

2006; Kitamura et al., 2003; Nurmi et al., 2004), ovine (Fabbriciani et al., 2005; Tapper et al., 2008) and bovine (Pioletti et al., 1999; Spalazzi et al., 2006) specimens.

Animals have also been used in understanding the material properties, failure and repair of the menisci in porcine (Barber et al., 2004), ovine (von Lewinski et al., 2006) and bovine (Maes and Donahue, 2006; Proctor et al., 1989; Villegas et al., 2007) specimens.

Additionally, the properties, contact surface and degradation of articular cartilage has been studied in rabbits (Serink et al., 1977; Clark et al., 1999; Radin et al., 1984; Reimann, 1973) and bovine (Verteramo and Seedhom, 2007; Sasazaki et al., 2006; de Visser et al., 2008) specimens.

Most studies with bovine bone focus on the material and mechanical properties of this specimen. For instance, the effects of tensile damage (Kotha and Guzelsu, 2003), fatigue (Moore and Gibson, 2003), fracture toughness (Lucksanasombool et al., 2001; Yan et al., 2006; Norman et al., 1995; Yan et al., 2008) and yield strains (Chang et al., 1999; Kopperdahl and Keaveny, 1998) have all been studied using bovine bone.

However, studies on the measurement of strain along the cortex of a bovine tibia are lacking. Studies, although, have been completed where either static or cyclic loads were applied to other types of animal tibias. For example, Fukuda et al. (Fukuda et al., 2000) investigated the propagation of impact load through a porcine tibia and Grover et al. (Grover et al., 2007) studied the effects of static and cyclic asymmetric loads applied to five ovine proximal tibia growth plates.

In the present study a bovine tibia and femur were loaded simultaneously in compression and strains were measured along the cortex of the bovine tibia. The

94

objective of this work was to evaluate the applicability of MABTA to biological structures, evaluate its capabilities in a different loading configuration and determine if this apparatus can be classified as an apparatus with a high standard for experimenting with biological tissues.

4.2 Experimental Materials and Methods

A right bovine tibia and femur, obtained from a local abattoir (Parkland Packers Slaughterhouse, Stony Plain, AB, Canada), were used to determine how applicable MABTA is for testing biological structures. Removed of all soft tissues, the bovine tibia was instrumented with thirteen Omega 45° triaxial-stacked rosettes (SGD-2/350-RY53) as presented in Figure 4.1. Table 4.1 presents the strain gauge positions with respect to the centre of the bottom face of the bone pot. Gauge positions were first measured using a coordinate measuring machine (CMM, MicroVal, Browne and Sharpe, North Kensington, RI) and then plotted in a computer aided design (CAD) model of the bovine knee obtained from CT imaging (Au, 2008) for future comparisons between finite element and experimental results.

| (a) | (b) | (c) | (d) |
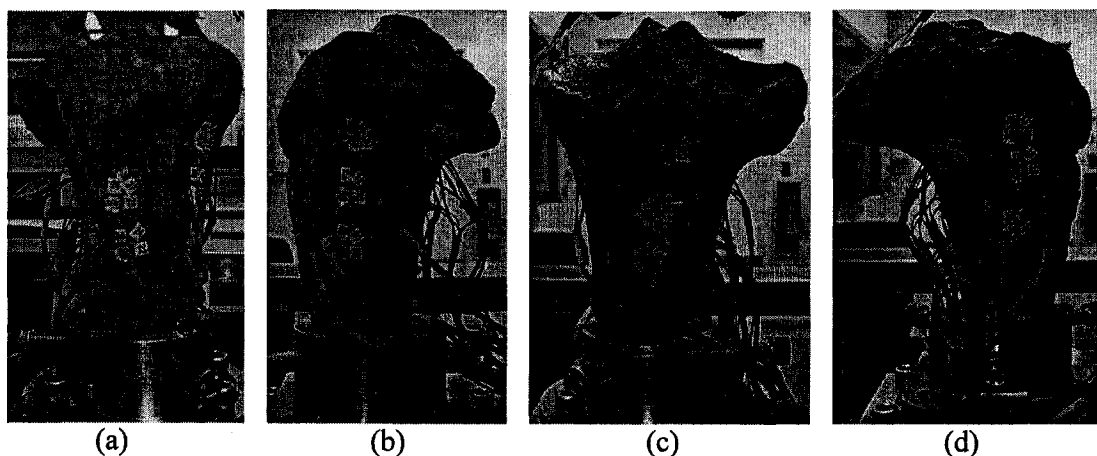
Figure 4.1: The thirteen tibial strain rosette positions: a) Anterior: Rosettes 8-9 b) Medial: Rosettes 10-13 c) Posterior: Rosettes 1-3 and d) Lateral: Rosettes 4-7

95

Table 4.1: Bovine tibia strain gauge positions with respect to centre of the bottom face of bone pot (all dimensions are in mm)

Rosettes	Gauges	X	Y	Z
1	SG1-3	7.507	-3.383	-111.392
2	SG4-6	2.954	-0.431	-91.178
3	SG7-9	8.702	-3.861	-133.335
4	SG10-12	38.724	-19.453	-120.908
5	SG13-15	17.274	-32.458	-83.297
6	SG16-18	15.330	-42.665	-107.455
7	SG19-21	17.964	-44.978	-124.574
8	SG22-24	-6.516	-56.792	-72.960
9	SG25-27	-3.940	-67.638	-92.313
10	SG28-30	-32.401	-27.271	-80.602
11	SG31-33	-33.287	-33.121	-103.053
12	SG34-36	-36.819	-34.919	-126.022
13	SG37-39	-36.806	-1.455	-130.481

Using a custom-designed alignment jig, the bovine tibia and femur were potted in bone pots (Figure 4.2). This was done by first securing the tibial and femoral bone pots in the same x-y position with the aid of alignment dowel pins and screws (Figure 4.3) and then fixing the position of the bones in the pots with plaster of Paris. For a more detailed description about the alignment jig and how to properly use it, see Appendix C and F, respectively.

Figure 4.2: Alignment and potting of the bovine tibia and femur into custom-designed alignment jig

96

Alignment Dowel Pins
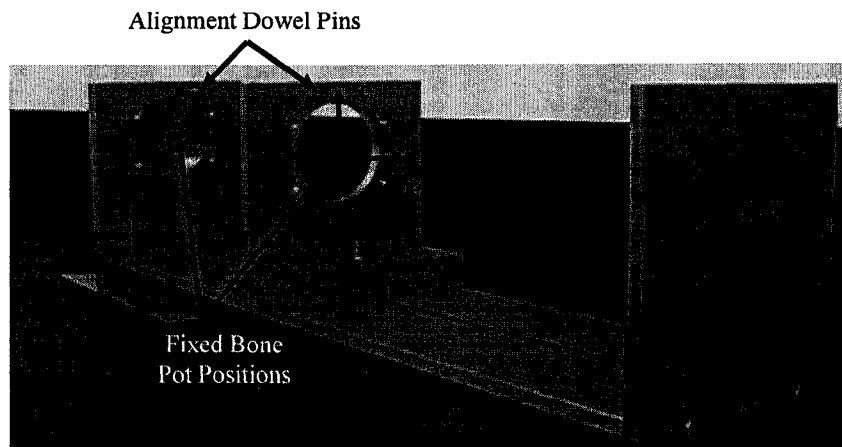
Figure 4.3: Custom-designed alignment jig

Unlike the human knee joint, the bovine stifle joint is constantly rotated about the flexion-extension (F-E) axis (Figure 4.4). For this reason the bovine femur was placed superior to the tibia and rotated to an F-E angle of 45° (Figure 4.5) in MABTA.
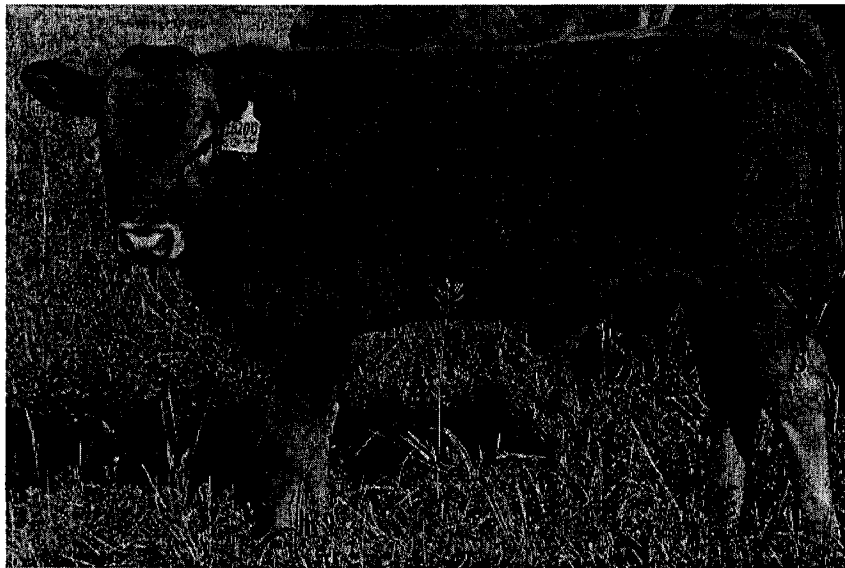
Figure 4.4: Bovine bull calf; indicating hind limb anatomy[16]. With 'A' being the femoral condyles, 'B' the hip joint, 'C' the bovine stifle which is analogous to a knee joint and 'D' the tarsal joint which is analogous to an ankle joint.

---

[16] Reproduced from http://www.gelbviehworld.com/more.ecs/show/478/0/244/27/none/0/149/0/ with permission from Alf Epp and Gayle Smith

97
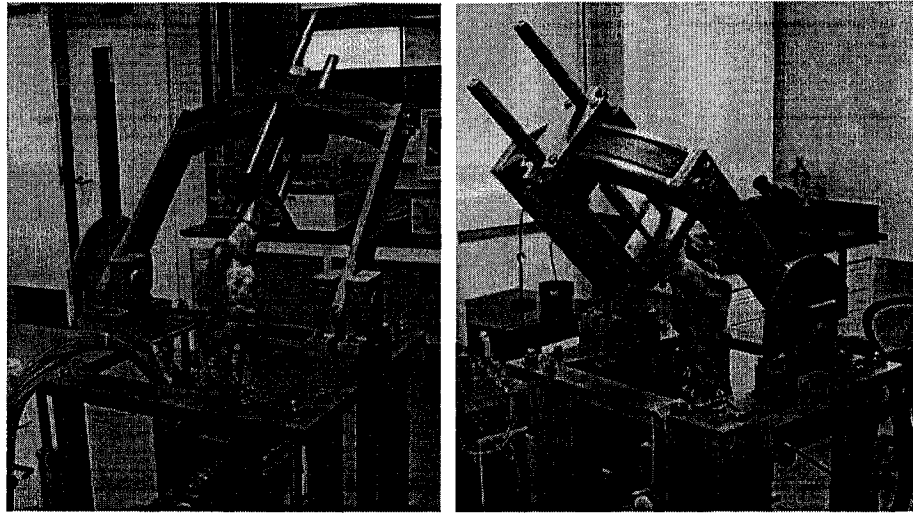
Figure 4.5: Position of bovine tibia and femur bone on bone compression experiment

All biological materials display some viscoelastic behaviour (Reilly and Burstein, 1974), which is characterized by a deformation rate dependent relationship between load and deformation (Viceconti et al., 1992). Viscoelasticity exhibits two behaviours, namely, creep and stress relaxation; both of which must be addressed when conducting bone experiments. Due to these viscoelastic properties the bovine tibia was conditioned by first preloading to 890 N (200 lb) and then allowing the load to relax. This process was repeated five to seven times until it was noticed that the load no longer rapidly decreased after loading due to stress relaxation. This set of conditioning cycles was repeated prior to the start of each test which involved loading the specimen in 111 N (25 lb) increments until a maximum load of 1780 N (400 lb) was reached. The experimental strains were measured along the cortex of the bovine tibia (Figure 4.6). Strains were recorded for 30 seconds at each load increment in order to observe the drift in strain values as the bone relaxes. This experiment was repeated three times. A recovery time of 5 minutes was

allowed between subsequent tests in order to recover from any creep deformations that were induced by the loading. Discussion of recovery time effect is presented later.
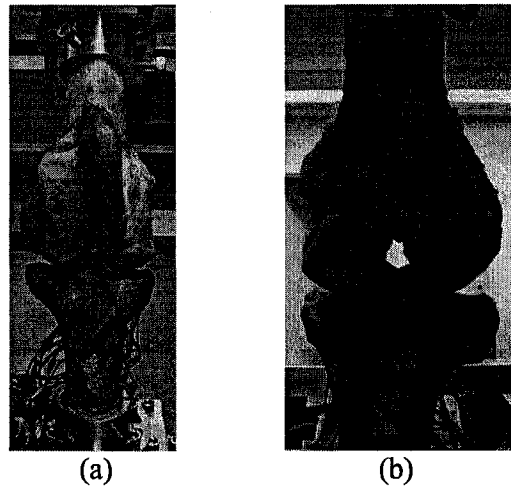
Figure 4.6: Bovine tibia compression loading position; (a) anterior (b) posterior

In previous composite bone on bone tests, the specimens were completely removed from MABTA at the end of each test to measure any alignment changes that may have occurred during loading. This was possible because MABTA was positioned at 0° flexion for the composite bones which are based on human geometry. Since the alignment jig and coaxial alignment indicator were used during setup, the specimens could be accurately repositioned after removal. However, the bovine stifle joint is always rotated about the F-E axis, as shown in Figure 4.4. With the F-E axis rotated to 45°, the coaxial alignment indicator could not be used to align the tibial and femoral bone pot holders. Instead the anterior-posterior and medial-lateral translational axes were used to align the tibia beneath the femoral condyles. With this procedure the specimens were aligned relative to each other and not to MABTA and so it would be difficult to accurately reposition the specimens after removal. Therefore the specimens were not removed at the end of each test to have consistent testing conditions.

99

4.3 Theoretical Methods

To evaluate if MABTA can provide reasonable and accurate experimental results, theoretical strain calculations were completed at each strain rosette. These calculations used strength of materials analysis, geometric properties from Au (Au, 2008) and the forces measured at the 6 DOF load cell to determine the theoretical principal strains. Calculus was used to determine the error in the theoretical and experimental strain calculations. Both the theoretical and experimental strain calculations and their associated error calculations are shown in Appendix I.

These calculations assumed that the material was transverse isotropic (Reilly and Burstein, 1974), that all loading occurred within the elastic range and the response was linear in this region.

Askew and Lewis (Askew and Lewis, 1981) stated that the cortical bone provides most of the loading support. Therefore, for most calculations the cancellous bone can be ignored. The elastic properties (Reilly and Burstein, 1975) used in the theoretical strain calculations, which have 5% errors, are presented in Table 4.2.

Table 4.2: Elastic properties of bovine haversian femoral compact bone. E' and E are the modulus of elasticity for longitudinal and transverse specimens, respectively. v' and v are the Poisson's ratio for longitudinal and transverse specimens, respectively.

Elastic Properties	Bovine Haversian Femoral Compact Bone
E' (GPa)	22.6
E (GPa)	10.2
v'	0.36
v	0.51

100

4.4 Bovine Bone on Bone Loading: Tibia Compression Discussion

The experimental longitudinal strain values for the first test are provided in Figure 4.7. From this plot, it is observed that the strain results from most gauges are nonlinear which could be attributed to complex geometry around some of the gauges. It can also be seen that not all strains increase with load. For example, strain gauges 4-6 and 37-39 reach a maximum value and then decline. Since these relationships are consistent across all three experiments, this suggests that MABTA is showing good repeatability. The results from the second and third run of the experiment can be found in Appendix J.
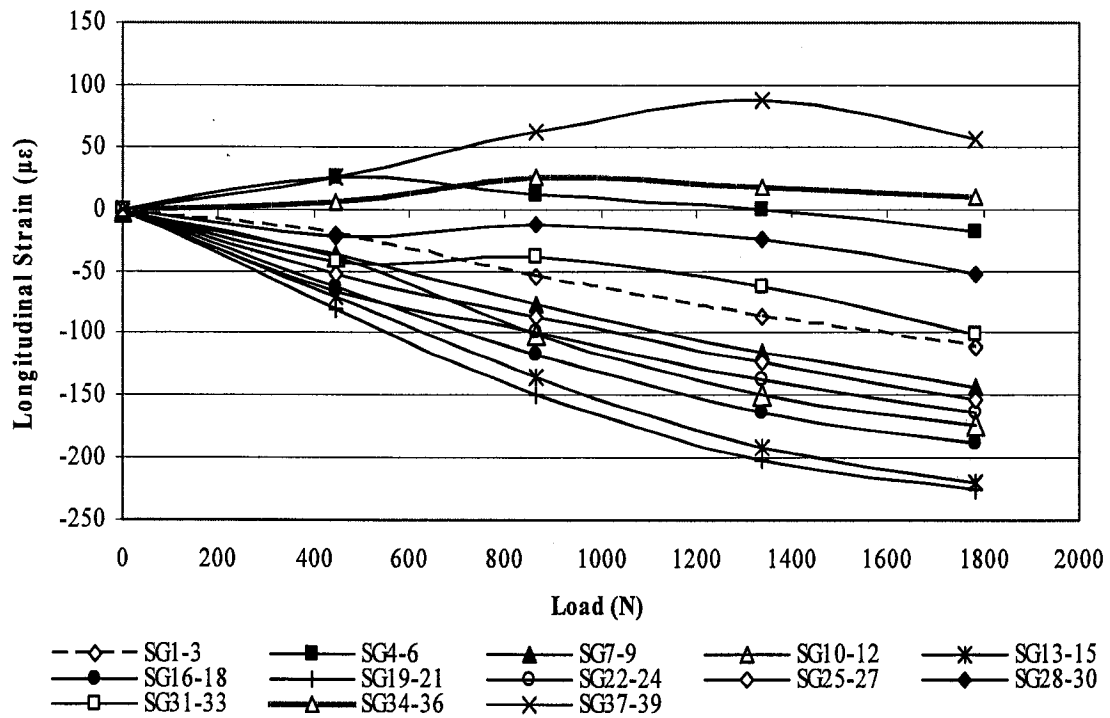
Figure 4.7: Experimental longitudinal strains along bovine tibia for test one at 1780 N. Note lines are used for visual purposes only.
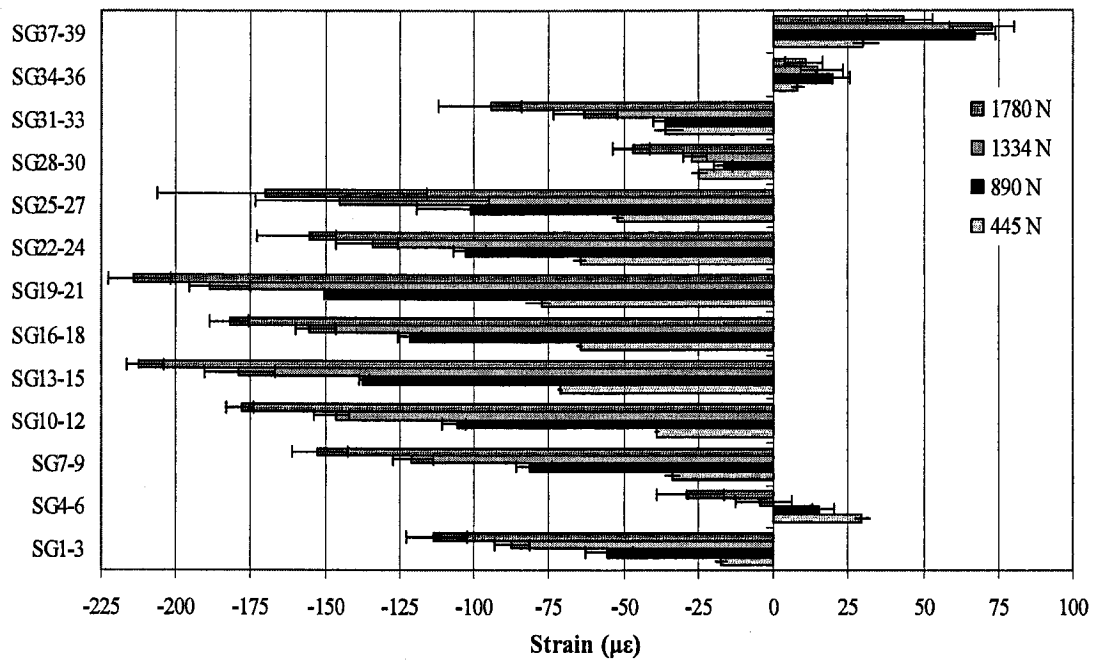
Figure 4.8: Average longitudinal strain with range of values from all three tests

The longitudinal strain was measured at each strain gauge rosette for every load increment; this was done for all three tests. The experimental strain range is the maximum difference between the strain values of a rosette across all tests at a particular load increment. Ideally, this range should be zero for a perfectly repeatable experiment. The average longitudinal strain with the strain range for all rosettes was plotted in Figure 4.8, the strain range alone was plotted in Figure 4.9 and the percentage of the experimental strain range to the average longitudinal strain was plotted in Figure 4.10.

102
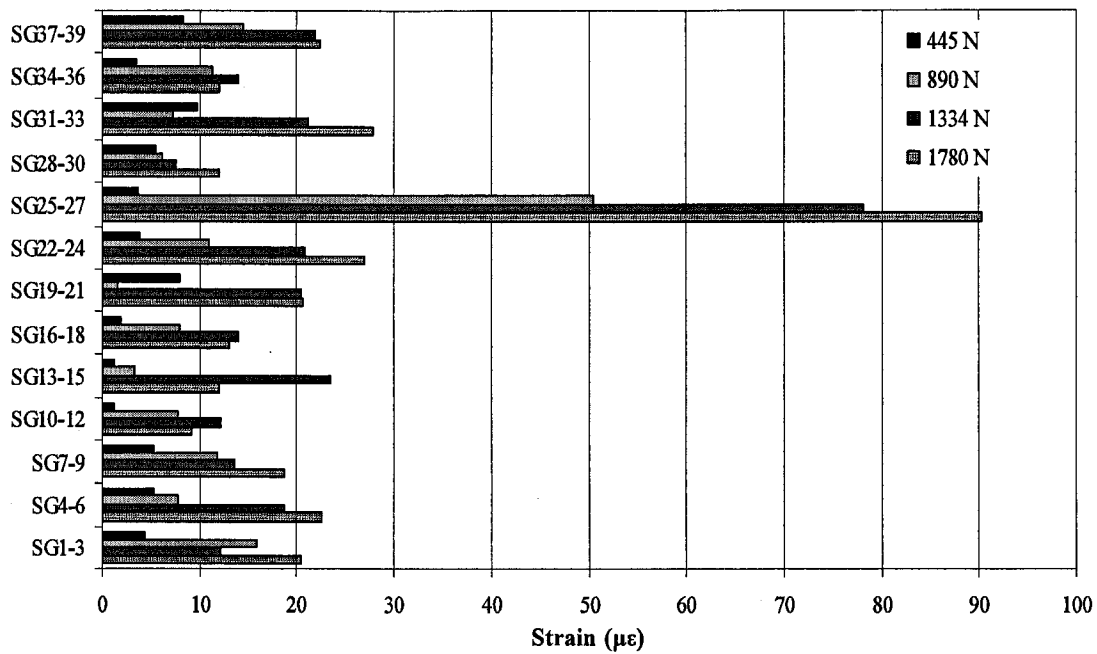
Figure 4.9: Experimental strain range between all tests for load increments of 445N, 890N, 1334N and 1780N.

The largest strain range across all rosettes for loads 890 N to 1780 N occurs at strain gauges 25-27. The range, load increment and maximum and minimum strain for this gauge are presented in Table 4.3.

Table 4.3: Maximum and minimum strain and the corresponding range in experimental values for strain gauges 25-27

Load Applied (N)	Maximum Strain ($\mu\epsilon$)	Minimum Strain ($\mu\epsilon$)	Strain Range ($\mu\epsilon$)
445	-49.73	-53.37	3.65
870	-83.33	-133.77	50.44
1334	-116.67	-194.87	78.2
1780	-133.40	-223.73	90.33

The variation between forces measured at the load cell (Table 4.4) and the resulting differences in moments applied to the bone is one possible explanation for this large strain range. The forces Fx, Fy, and Fz apply loads in the medial-lateral (M-L), anterior-posterior (A-P) and proximal-distal (P-D) directions, respectively.

Table 4.4: Mean and standard deviation of Fx, Fy and Fz calculated from all three tests at each load increment

Load Increment (N)	Fx (N)		Fy (N)		Fz (N)	
	Mean	Standard Deviation	Mean	Standard Deviation	Mean	Standard Deviation
0	-1.45	0.00	-0.48	0.84	0.00	0.00
445	-18.34	3.01	-217.75	5.23	445.62	0.00
890	-20.75	3.34	-382.27	16.76	883.77	15.44
1334	-19.79	3.34	-546.78	6.04	1350.88	17.05
1780	-23.65	7.97	-699.21	15.39	1783.42	1.62

Strain gauges 25-27 are the topmost gauges located on the anterior side of the bovine tibia (Figure 4.1a) and therefore have a large moment arm between gauge location and load application. These gauges would be especially affected by the variation in Fy. For instance, using the theoretical longitudinal strain calculation presented in Appendix I, the theoretical longitudinal range at 1780 N was calculated to be 59$\mu\varepsilon$, which is in the same order of magnitude as the experimental range of 90$\mu\varepsilon$. This shows that the variation in load between subsequent tests is a significant source of difference between the experimental values for subsequent tests.

The strain range progressively increased as the load increased for six out of the thirteen rosettes (strain gauges 4-6, 7-9, 22-24, 25-27, 28-30 and 37-39). This observation is arbitrary as when comparing between four out the six rosettes, the minimum and maximum strains occur at different tests. For instance, Table 4.5 provides the occurrence of minimum and maximum strains for gauges 4-6 and 7-9. However, for gauges 22-24 and 25-27, which are the respective lowest and topmost gauges on the anterior side of the bovine tibia, the minimum and maximum strains occur at the same tests, i.e. minimum strain occurs at test 2 and maximum strain occurs at test 3. As stated above, the variation in Fy would greatly affect gauges 25-27 but since the spread in Fy does not increase as the load increment increases, it is believed that this is a coincidental observation.

104

Table 4.5: Example illustrating the difference in occurrence between minimum and maximum strain for gauges 4-6 and 7-9

	Load Applied (N)	Occurrence of Minimum Strain	Occurrence of Maximum Strain
SG4-6	445	Test 1	Test 3
	870	Test 1	Test 3
	1334	Test 1	Test 3
	1780	Test 1	Test 3
SG7-9	445	Test 1	Test 2
	870	Test 2	Test 1
	1334	Test 2	Test 1
	1780	Test 2	Test 1
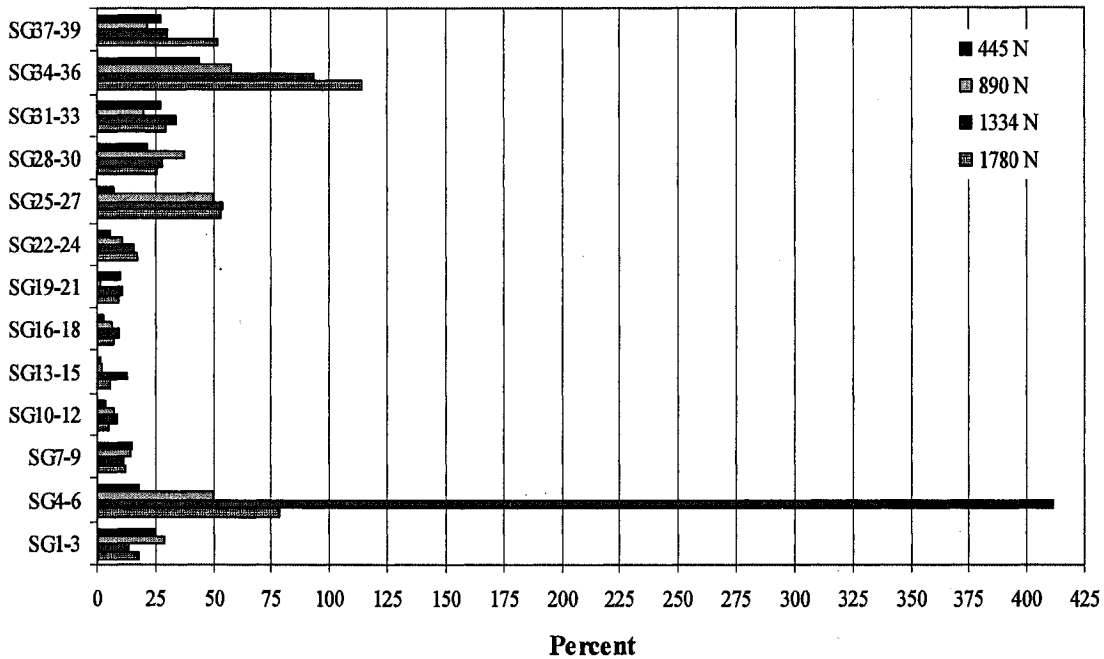
Figure 4.10: Percentage of the experimental strain range to the average strain across all three tests for all strain rosettes

The percentage of the experimental strain range to the average longitudinal strain is presented in Figure 4.10. The highest percentage occurs at strain gauges 4-6, followed by 34-36 and then 25-27. From Figure 4.8, it can be seen that gauges 4-6 have both tensile and compressive strain readings with an average strain of approximately -5με and an experimental strain range of approximately 19με and gauges 34-36 have strains less

105

than 25µε at all load increments. Therefore the large percentages seen at these two rosettes are a result of miniscule strain readings. The next highest percentage occurs at gauges 25-27 with a value of 53%. As discussed above, it is believed that this high strain range and percentage can be attributed to the variation in loads measured at the load cell.

Even though saline solution was applied to the specimen during testing, the difference between the measured experimental strain values for each test could also be attributed to the change in properties as bone dehydrates throughout subsequent tests (Evans and Lebow, 1951). Additionally, as mentioned in the review article by Carter and Spengler, the "sustained loading of cortical bone produces a gradual increase in deformation with time" (Carter and Spengler, 1978, pg 198).
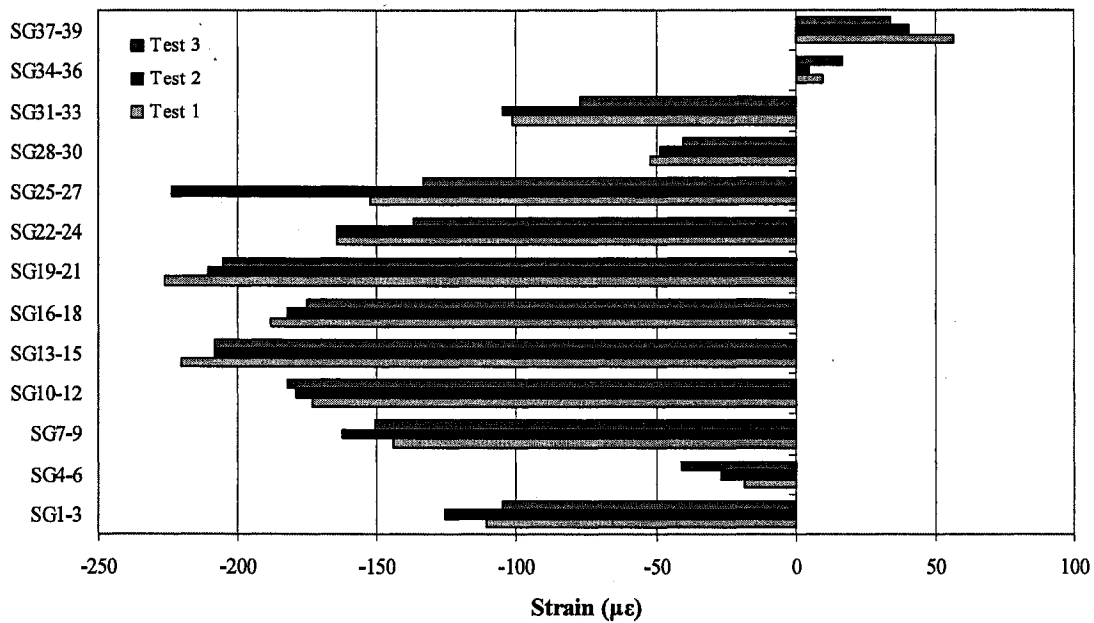
Figure 4.11: Sequence of longitudinal strain results at maximum load

The sequence of strain through subsequent experiments was analyzed and is presented in Figure 4.11. From this plot, it is observed that strain gauges 4-6 and 10-12 continually increase in longitudinal strain throughout the experiments while gauges 16-18, 28-30 and 37-39 continually decrease in longitudinal strain. However, gauges 13-15 and 22-24 have the same experimental values for two out of the three tests. All other gauges have no trend and appear to be unaffected by subsequent testing.

Grover et al. (Grover et al., 2007) allowed a recovery time of 1000 seconds when static and cyclic asymmetric loads were applied to five ovine proximal tibia growth plates. However, Currey (Currey, 1965) reported that a portion of creep deformations may be recovered during unloading. In addition, Joo et al. (Joo et al., 2007) reported that a 10 minute recovery time for tensile damage in human cortical bone is a reasonable minimal recovery time for cross-study comparisons. Additionally, it was found that as much as 90% of the non-permanent strain or stress was recovered within 10 minutes (Joo et al., 2007). The bovine specimen in the present study was allowed to recover for five minutes before the subsequent test began, therefore, the increase and decrease of strain throughout experimentation for the five rosettes could have been caused by insufficient recovery time. It was found in Joo et al. (Joo et al., 2007) that a time of 5 minutes would correspond to the recovery of approximately 83% of non-permanent strain for human cortical bone.

Table 4.6 provides the transverse and longitudinal experimental strains as well as the calculated first and second principal strains for the first test. Please see Appendix I for the first and second principal strain calculations. It was observed that the direction of the longitudinal strains, ε_L, matches with the direction of the second principal strain, ε_2, when

the bone is in compression (strain gauges 1-33 show negative strain) and to the direction of the first principal strain, ε_1, when the bone is in tension (strain gauges 34-39 show positive strain). It was noticed that the direction of the first principal strain, ε_1, did not match the direction of the transverse strain, ε_T, for gauges 31-33, which is located on the medial side of the bovine tibia. This pattern was seen across all three experiments. Large geometry changes are not evident at this rosette location and the strain measured in the longitudinal direction matches the direction of the second principal strain across all tests. The unexpected results could be caused from the transverse gauge itself. Viceconti et al. (Viceconti et al., 1992) describe that in general, cortical bone has 5% to 30% porosity, which is similar for dog, bovine, monkey and human specimens (Gong et al., 1964), and thus it is possible for moisture to penetrate under the strain gauge, leading to imprecise measurements (Viceconti et al., 1992).

Table 4.6: Comparing the transverse and longitudinal experimental strain values to the first and second principal strains for test 1 at maximum load. Bold face values indicate which directions match while bone is in compression.

Gauges	Experimental Strain ($\mu\varepsilon$)			
	ε_T	ε_L	ε_1	ε_2
SG1-3	-31.778	**-110.967**	-24.646	**-118.098**
SG4-6	14.496	**-18.435**	32.087	**-36.026**
SG7-9	-23.141	**-144.133**	-19.696	**-147.578**
SG10-12	4.688	**-173.167**	27.762	**-196.240**
SG13-15	6.104	**-220.367**	35.032	**-249.294**
SG16-18	133.634	**-188.067**	149.751	**-204.183**
SG19-21	187.333	**-226.267**	187.634	**-226.567**
SG22-24	-39.883	**-164.167**	-39.023	**-165.027**
SG25-27	-117.700	**-152.633**	-105.618	**-164.715**
SG28-30	3.823	**-52.040**	92.607	**-140.825**
SG31-33	-28.611	**-101.500**	57.659	**-187.770**
SG34-36	**-87.888**	9.804	21.389	**-99.472**
SG37-39	**-40.807**	56.410	56.887	**-41.284**

108

To determine if MABTA can produce reasonable strain values for soft tissue specimens, theoretical strain calculations and their associated errors were calculated as described in Section 4.3 and Appendix I. The theoretical principal strains were calculated based on the theoretical strains and then compared to the principal strains calculated using experimental values. The comparisons between the theoretical and experimental first and second principal strains for test 1 are shown in Figure 4.12 and Figure 4.13, respectively. The average experimental principal strain values for all three tests were not compared to the average theoretical principal strain values because the loads at each increment varied between tests (Table 4.4). The theoretical principal strain value would possibly be the same, if it was calculated at maximum load for tests one through three and then averaged, or if the load was averaged and then used to calculate the theoretical principal strain. However, it is uncertain that the experimental strain values measured at maximum load for tests one through three would accurately correspond to the strains measured at the average load. For this reason, the experimental and theoretical principal strain values for each test are compared independently.

109
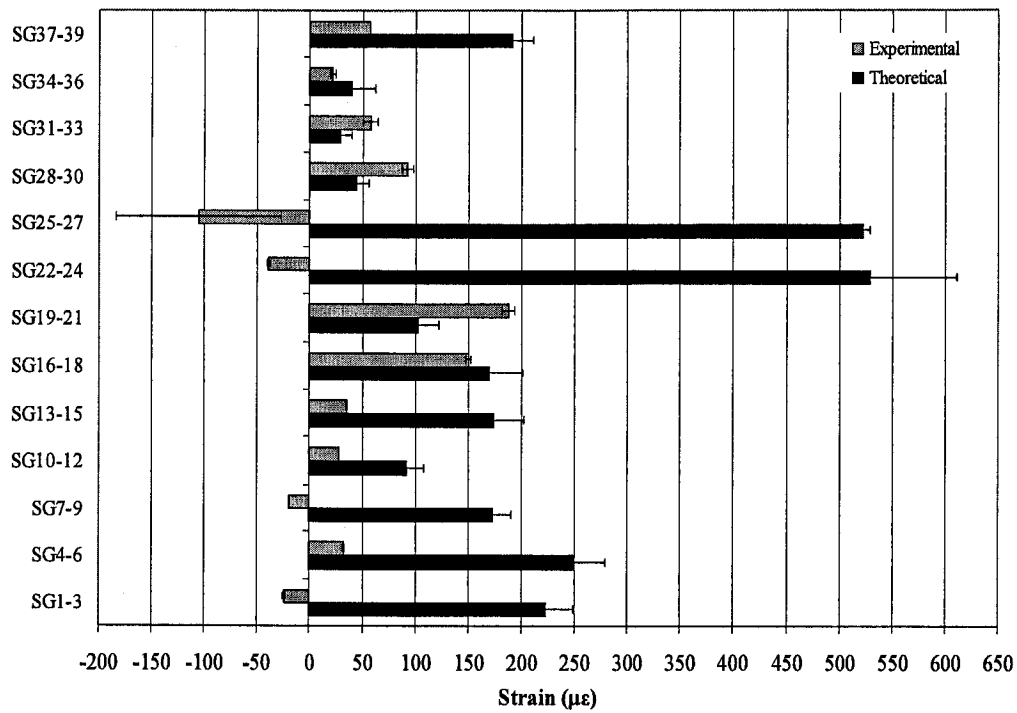
Figure 4.12: Comparison of first principal strains for test 1 at maximum load. Error bars represent the calculated theoretical and experimental error.

From Figure 4.12 it can be seen that the theoretical first principal strains differ from the experimental first principal strains for eleven out of the thirteen rosettes. Specifically, strain gauges 1-3, 7-9, 22-24 and 25-27 are reading compressive strains while theoretical strains are predicting tensile strains. However, for gauges 16-18 and 34-36, the experimental first principal strains fall within the calculated theoretical error, found in Appendix I. These results are consistent across all three tests. The comparison of the theoretical and experimental first principal strains for the second and third tests can be seen in Appendix J.

110
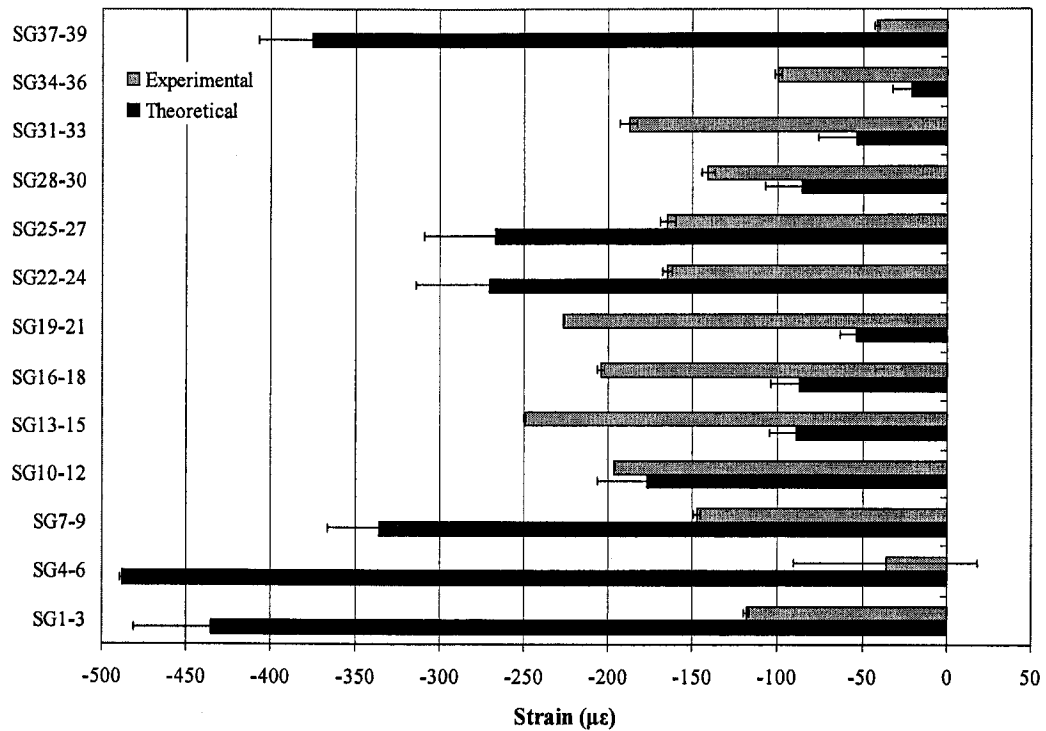
Figure 4.13: Comparison of second principal strains for test 1 at maximum load. Error bars represent the calculated theoretical and experimental error.

Figure 4.13 shows that the theoretical second principal strains are larger than the experimental second principal strains for five out of the thirteen rosettes. Also no significant trends are seen as the experimental second principal strains only fall within the calculated theoretical error, found in Appendix I, for gauges 10-12 for test 1, gauges 25-27 for test 2 and gauges 28-30 for test 3.

Possible sources of difference between theoretical and experimental strain calculations as well as experimental strain results measured between subsequent tests are as follows. As mentioned in Section 4.3, assumptions used throughout the theoretical strain calculation are that the material was transversely isotropic (Reilly and Burstein, 1974), cortical bone provides most of the loading support (Askew and Lewis, 1981), all

111

loading occurred within the elastic range and the response was linear in this region. These assumptions are seen throughout the theoretical strain calculations.

All theoretical strains were calculated based on the loads measured at the 6 DOF load cell centre and at the measured strain gauge positions. All geometric properties for the bovine tibia were taken from a computer aided design (CAD) model of the bovine knee (Au, 2008) created from CT images. If the measured strain gauge positions from the CAD model are slightly different from the actual strain gauge position, then the error between the experimental and theoretical values could be very large. For example, if the geometric constants (area, moments of inertia) of strain gauges 7-9, which are located between the tibial condyles, were measured approximately 1mm below or 1mm above the actual position along the tibia, the theoretical longitudinal strains would differ by 20$\mu\epsilon$.

After the completion of previous compression tests with a composite tibia and femur, a maximum misalignment of 0.381 mm and 0.216 mm, respectively, was measured between the tibial and femoral bone pot holders. It is believed that this misalignment was caused from the backlash in the 12.7 mm (1/2"), 20 threads per inch hand screws used to align the bone pot holders. Since the bovine tibia and femur were aligned relative to each other and not relative to MABTA as described in Section 4.2 Experimental Materials and Methods, the specimens were not removed at the end of each test. Although no measurements were possible, it is very probable that a misalignment similar to the one seen in the composite bone experiments could have occurred during the bovine test. The backlash in the screws could allow a change in the relative positions of the tibia and femur between or during tests. This is a possible explanation for experimental differences between subsequent tests.

Experimenting with soft tissues creates more possible sources of error. As shown in the study by Evans and Lebow (Evans and Lebow, 1951), dehydration of the specimen greatly affects the material properties. Even though saline solution was regularly applied throughout specimen preparation and testing, air-drying can increase the average ultimate tensile strength by as much as 31.3%, the modulus of elasticity by as much as 17.6% and the hardness by as much as 54.3% (Evans and Lebow, 1951).

Lastly, strain gauge protection is an important factor when working with biological tissues. Cortical bone can have a porosity of 5% to 30% (Viceconti et al., 1992); therefore, it is possible for moisture inside the bone to migrate to the surface and damage the bond between gauge and specimen (Viceconti et al., 1992). If moisture penetrated the bond between gauge and specimen at any of the rosettes, the measured strains would not represent the actual strain occurring at that position.

4.5 Conclusion

A bovine tibia and femur were inserted into MABTA and loaded to a maximum load of 1780 N to examine the applicability of this novel apparatus to biological structures. The first and second experimental principal strains correctly matched the directions of the experimental longitudinal and transverse strains for all gauges except 31-33. Strains varied between tests but it was shown that this variability was most likely caused by the spread in load values at each load increment. Other differences could be attributed to the effects from the surrounding environment, insufficient recovery time or the subsequent testing of the specimen.

Due to complicated bone geometry and biological material behaviour, theoretical calculations poorly predict experimental strain calculations as the theoretical first

113

principal strains consistently matched with the experimental principal strains for only two rosettes; it is believed that such discrepancies have been explained.

Theoretical strain calculations do not provide the necessary information needed to conclude that MABTA can produce reasonable and accurate experimental results. Bone is a complex material, both in structure and in geometry and thus a finite element bovine model would be best suited for comparison purposes and is needed to fully verify that this apparatus can be used for such structures.

From the results of the preliminary evaluation with biological tissues, it is concluded that MABTA did not fill all the requirements needed to be acknowledged as an apparatus with a high standard for experimenting with biological tissues, specifically the ability of the specimens to be accurately repositioned when removed from MABTA. However in the present, preliminary study it was shown that MABTA can be adjusted to account for different anatomical positions.

The following issues need to be addressed before this apparatus can be fully accepted as an apparatus with a high experimental standard for testing with biological tissues. First, decrease the variation in load seen between tests. It is suggested to include a proportional, integral, derivative (PID) controller so that more precise and consistent load increments can be achieved between subsequent tests. Second, increase the recovery time between experiments so that stress relaxation and creep in the specimen does not affect later results. Third, implement a method to lock the tibial stage and remove the backlash from the existing 12.7 mm (1/2"), 20 threads per inch hand screws. Additionally, modify the existing alignment jig in order to accurately align and pot animal knee joints that are constantly rotated about the F-E axis. Lastly, modify MABTA

to include digital read outs along the A-P and M-L translational axes. These digital read outs, which are used for aligning machined components on milling machines, would simplify and provide a method of accessing if the alignment of the specimens is changing during experiments as well as allow proper repositioning of the specimens. The idea behind the digital read out is that once a specific position is fixed, the digital read out would be used to zero this alignment position and so if the specimens were removed from MABTA, this exact position can be replicated by realigning the specimens following the dimensions provided by the digital read out. These modifications would increase the repeatability of the experimental procedure for such specimens, allow for the removal and accurate reposition of the specimens after experiments, and to measure if any alignment changes has occurred. With these suggestions, MABTA would become a much more useful and reliable tool in studying biological structures.

References

Askew, M.J, Lewis, J.L., 1981. Analysis of model variables and fixation post length effects on stresses around a prosthesis in the proximal tibia. Transactions of ASME, Journal of Biomechanical Engineering 103, 239-245.

Au A.G., 2008. A comprehensive approach to constructing human bone models: from CT to FE. PhD thesis. University of Alberta.

Barber, F.A., Herbert, M.A., Richards, D.P., 2004. Load to failure testing of new meniscal repair devices. The Journal of Arthroscopic and Related Surgery 20(1), 45-50.

Berkson, E., Lee, G.H., Kumar, A., Verma, N., 2006. The effect of cyclic loading on rotated bone-tendon-bone anterior cruciate ligament graft constructs. The American Journal of Sports Medicine 34(9), 1442-1449.

Carter, D.R., Spengler, D.M., 1978. Mechanical Properties and Composition of Cortical Bone. Clinical Orthopaedics and Related Research 135, 192-217.

Chang, W.C.W., Christensen, T.M., Pinilla, T., Keaveny, T.M., 1999. Uniaxial yield strains for bovine trabecular bone are isotropic and asymmetric. Journal of Orthopaedic Research 17 (4), 582-585.

Clark, J.M., Norman, A.G., Kääb, M.J., Nötzli, H.P., 1999. The surface contour of articular cartilage in an intact, loaded joint. Journal of Anatomy 195, 45-56.

Currey, J.D., 1965. Anelasticity in bone and echinoderm skeletons. Journal of Experimental Biology 43, 279-292.

de Visser, S.K., Crawford, R.W., Pope, J.M., 2008. Structural adaptations in compressed articular cartilage measured by diffusion tensor imaging. Osteoarthritis and Cartilage 16, 83-89.

Evans, F.G., Lebow M., 1951. Regional Differences in Some Physical Properties of the Human Femur. Journal or Applied Physiology 3(9), 563-572.

Fabbriciani, C., Mulas, P.D., Ziranu, F., Deriu, L., 2005. Mechanical analysis of fixation methods for anterior cruciate ligament reconstruction with hamstring tendon graft. An experimental study in sheep knees. The Knee 12, 135-138.

Fukuda, Y., Takai, S., Yoshino, N., Murase, K., Tsutsumi, S., Ikeuchi, K., Hirasawa, Y., 2000. Impact load transmission on the knee joint-influence of leg alignment and the role of meniscus and articular cartilage. Clinical Biomechanics 15, 516-521.

Grassman, S.R.M., McDonald, D.B., Thornton, G.M., Shrive, N.G., Frank, C.B., 2002. Early healing processes of free tendon grafts within bone tunnels is bone-specific: a morphological study in a rabbit model. The Knee 9, 21-26.

Gong, J.K., Arnold, J.S., Cohn, S.H., 1964. Composition of trabecular and cortical bone. The Anatomical Record 149 (July), 325-331.

Grover, J.P., Vanderby, R., Leiferman, E.M., Wilsman, N.J., Noonan, K.J., 2007. Mechanical behaviour of the lamb growth plate in response to asymmetrical loading: A model for Blount Disease. Journal of Pediatric Orthopaedics 27 (5), 485-492.

Joo, W., Jepsen, K.J., Davy, D.T., 2007. The effect of recovery time and test conditions on viscoelastic measures of tensile damage in cortical bone. Journal of Biomechanics 40, 2731-2737.

Kitamura, N., Yasuda, K., Yamanaka, M., Tohyama, H., 2003. Biomechanical comparisons of three posterior cruciate ligament reconstruction procedures with load-controlled and displacement-controlled cyclic tests. American Journal of Sports Medicine 31, 907-914.

Kopperdahl, D.L., Keaveny, T.M., 1998. Yield strain behaviour of trabecular bone. Journal of Biomechanics 31, 601-608.

116

Kotha, S.P., Guzelsu, N., 2003. Tensile damage and its effects on cortical bone. Journal of Biomechanics 36, 1683-1689.

Lucksanasombool, P., Higgs, W.A.J., Higgs, R.J.E.D., Swain, M.V., 2001. Fracture toughness of bovine bone: influence of orientation and storage media. Biomaterials 22, 3127-3132.

Maes, J.A., Haut Donahue, T.L., 2006. Time dependent properties of bovine meniscal attachments: Stress relaxation and creep. Journal of Biomechanics 39, 3055-3061.

Moon, D.K., Woo, S.L-Y., Takakura, Y., Gabriel, M.T., Abramowitch, S.D., 2006. The effects of refreezing on the viscoelastic and tensile properties of ligaments. Journal of Biomechanics 39, 1153-1157.

Moore, T.L.A., Gibson, L.J., 2003. Fatigue of bovine trabecular bone. Journal of Biomechanical Engineering 125, 761-768.

Norman, T.L., Vashishth, D., Burr, D.B., 1995. Fracture toughness of human bone under tension. Journal of Biomechanics 28 (3), 309-320.

Nurmi, J.T., Sievänen, H., Kannus, P., Järvinen, M., Järvinen, T.L.N., 2004. Porcine tibia is a poor substitute for human cadaver tibia for evaluating interference screw fixation. American Journal of Sports Medicine 32, 765-771.

Pioletti, D.P., Rakotomanana, L.R., Leyvraz, P.-F., 1999. Strain rate effect on the mechanical behaviour of the anterior cruciate ligament-bone complex. Medical Engineering & Physics 21, 95-100.

Proctor, C.S., Schmidt, M.B., Whipple, R.R., Kelly, M.A., Mow, V.C., 1989. Material properties of the normal medial bovine meniscus. Journal of Orthopaedic Research 7 (6), 771-782.

Radin, E.L., Martin, R.B., Burr, D.B., Caterson, B., Boyd, R.D., Goodwin, C., 1984. Effects of mechanical loading on the tissues of the rabbit knee. Journal of Orthopaedic Research 2, 221-234.

Reilly, D.T., Burstein, A.H., 1974. The mechanical properties of cortical bone: a review. Journal of Bone and Joint Surgery 56-A (5), 1001-1002.

Reilly, D.T., Burstein, A.H., 1975. The elastic and ultimate properties of compact bone tissue. Journal of Biomechanics 7, 393-405.

Reimann, I., 1973. Experimental osteoarthritis of the knee in rabbits induced by alteration of the load-bearing. Acta Orthopaedica Scandinavia 44, 496-504.

Sasazaki, Y., Shore, R., Seedhom, B.B., 2006. Deformation and failure of cartilage in the tensile mode. Journal of Anatomy 208, 681-694.

Serink, M.T., Nachemson, A., Hansson, G., 1977. The effect of impact loading on rabbit knee joints. Acta Orthopaedica Scandinavica 48, 250-262.

Spalazzi, J.P., Gallina, J., Fung-Kee-Fung, S.D., Konofagou, E.E., Lu, H.H., 2006. Elastographic Imaging of Strain Distribution in the Anterior Cruciate Ligament and at the Ligament – Bone Insertions. Journal of Orthopaedic Research Oct, 2001-2010.

Tapper, J.E., Fukushima, S., Azuma, H., Sutherland, C., Marchuk, L., Thornton, G.M., Ronsky, J.L., Zernicke, R., Shrive, N.G., Frank, C.B., 2008. Dynamic in vivo three-dimensional (3D) kinematics of the anterior cruciate ligament/medial collateral ligament transacted ovine stifle joint. Journal of Orthopaedic Research May, 660-672.

Viceconti, M., Toni, A., Giunti, A., 1992. Strain gauge analysis of hard tissues: factors influencing measurements. In: Little, E.G. ed. Experimental Mechanics. Technology Transfer Between High Tech Engineering and Biomechanics. Amsterdam, Netherlands: Elsevier, 177-184.

Verteramo, A., Seedhom, B.B., 2007. Effect of a single impact loading on the structure and mechanical properties of articular cartilage. Journal of Biomechanics 40, 3580-3589.

Villegas, D.F., Maes, J.A., Magee, S.D., Haut Donahue, T.L., 2007. Failure properties and strain distribution analysis of meniscal attachments. Journal of Biomechanics 40, 2655-2662.

von Lewinski, G., Stukenborg-Colsman, C., Ostermeier, S., Huschler, C., 2006. Experimental measurement of tibiofemoral contact area in a meniscectomized ovine model using a resistive pressure measuring sensor. Annals of Biomedical Engineering 34 (10), 1607-1614.

Woo, S.L.-Y., Hollis, J.M., Roux, R.D., Gomez, M.A., Inoue, M., Kleiner, J.B., Akeson, W.H., 1987. Effects of knee flexion on the structural properties of the rabbit femur-anterior cruciate ligament-tibia complex (FATC). Journal of Biomechanics 20(6), 557-563.

Woo, S.L.-Y., Newton, P.O., MacKenna, D.A., Lyon, R.M., 1992. A comparative evaluation of the mechanical properties of the rabbit medial collateral and anterior cruciate ligaments. Journal of Biomechanics 25(4), 377-386.

Woo, S.L.-Y., Peterson, R.H., Ohland, K.J., Sites, T.J., Danto, M.I., 1990. The effects of strain rate on the properties of the medial collateral ligament in skeletally immature

118

and mature rabbits: A biomechanical and histological study. Journal of Orthopaedic Research 8, 712-721.

Yan, J., Clifton, K.B., Mecholsky, J.J., Reep, R.L., 2006. Fracture toughness of manatee rib and bovine femur using a chevron-notched beam test. Journal of Biomechanics 39, 1066-1074.

Yan, J., Daga, A., Kumar, R., Mecholsky, J.J., 2008. Fracture toughness and work of fracture of hydrated, dehydrated, and ashed bovine bone. Journal of Biomechanics 41, 1929-1936.

Chapter 5: Thesis Summary

Knee injuries and knee replacements are on the rise and are no longer only being performed on the elderly but on the general public who wish to remain active. Anterior cruciate ligament (ACL) reconstruction and total knee replacement (TKR) are two of the most studied and frequent knee surgeries. A multi-axis biomechanical testing apparatus (MABTA) was developed that allows the testing of complete or partial human, animal or composite specimens for (1) ACL fixation device performance, (2) long bones in the lower limb for general stress/strain analysis, (3) future TKR prostheses, (4) accuracy of FE models, and (5) knee bracing.

5.1 MABTA

MABTA is a six-degree of freedom (DOF) quasi-static loading frame designed and developed to conduct *in vitro* experiments on cadaveric human, animal and composite specimens. MABTA features three rotational axes: flexion-extension (F-E), varus-valgus (V-V) and internal-external (I-E) as well as three translational load applications: proximal-distal (P-D), medial-lateral (M-L) and anterior-posterior (A-P). Loading is limited to 4448 N (1000 lb) compression in the P-D direction and to $\pm$ 2224 N (500 lb) in the A-P and M-L directions. All loads are measured with an AMTI MC6-6-2000 six DOF load cell. A Kollmorgen servomotor and an IDC Motion EC3-B electromechanical actuator with a stroke of 150 mm are used to supply the P-D compressive load. All components of the apparatus are controlled with National Instruments LabVIEW.

120

The design of MABTA incorporates several successful features of other published designs plus adds features that make it resemble no other apparatus. The main difference between MABTA and other quasi-static devices mentioned in the literature is that MABTA does not simulate muscles. Instead the magnitude of the forces applied to the joint by the quadriceps is included in the loading capabilities at the joint. Additionally, flexion-extension angles are adjusted through the F-E rotational axis of MABTA and not through the use of the simulated muscles as in the study conducted by Whiteside et al., 1987.

Similar features between MABTA and other quasi-static devices: (1) a fixed femur and mobile tibia (Whiteside et al., 1987), (2) the knee is inserted horizontally at full extension (Bach and Hull, 1994), (3) the ability to simulate flexed knee stance (Biden and O'Connor, 1990), (4) allowing for six degrees of freedom (Biden and O'Connor, 1990), and (5) the movements of the joint is constrained by the structures of the knee and not by the apparatus itself (Biden and O'Connor, 1990). All of these devices are used to examine ligaments or ligamentous injuries.

Dynamic knee simulators and MABTA both examine similar features of the knee, whether it be wear, fit or design of knee prostheses or the attempt to reproduce daily activities. Since MABTA is still in the development stage of the design, the current experiments conducted with MABTA do not include TKR components unlike the studies conducted with dynamic knee simulators (Shaw and Murray, 1973; DesJardins et al., 2000; Burgess et al., 1997; Walker et al., 1997). Instead MABTA has conducted experiments with a known geometry PVC pipe and complete and partial composite and bovine specimens.

121

5.2 Verification of MABTA

It was thought that Vic-3D, a digital image correlation (DIC) method from Correlated Solutions®, could be used as a second strain measurement method for more complicated geometries and for materials on which it has been shown problematic to bond strain gauges such as the knee joint cortex; it was shown not to meet the requirements. As a result only strain gauges were used throughout all experiments.

A PVC pipe of known geometry and a third generation composite tibia and femur from Pacific Research Laboratories were used to verify the mechanical design of MABTA. All specimens were instrumented with strain gauges, inserted into MABTA and compressed.

For the known geometry experiment a PVC pipe was inserted into MABTA and into a 500 N MTS Synergie 400 (Model #2700094, MTS Systems Corporation, Eden Prairie, MN). Both experimental results indicated that the PVC pipe was subjected to bending as all gauges along the piece measured different strain values. Since this occurred in both apparatii, it was concluded that the specimen was deformed and errors were not caused by the MABTA design.

To verify the device for more complex shapes experimental and theoretical results based on strength of materials mechanics were compared. Differences were expected, as the classical approach cannot be directly applied to such a complex structure with accuracy, this is why FEA models are developed; however, the comparison was expected to provide proper trends and an indication of the system capabilities. From the composite tibia and femur experimental results it was found that MABTA can be considered an

122

apparatus with a high standard in providing reasonable strain results and good repeatability between tests for the composite specimens.

Theoretical and experimental effective von Mises (VM) strains were calculated for both the composite tibia and femur compression experiments. Through regression analysis, a slope of 0.5706, an intercept of 62.28με and an R^2 value of 0.6062 for the composite tibia and a slope of 1.563, an intercept of 195.04με and an R^2 value of 0.4626 for the composite femur indicates that the theoretical strain calculations are able to predict the experimental strain calculations but not very strongly, which was expected and an indication that the device works well.

A full error analysis was completed on both the theoretical and experimental strain results for the composite tibia and femur. With this calculated relative error, the theoretical strain results predict the experimental results for strain gauges 16-18, 22-24, 31-33 and 37-39 on the composite tibia. For the composite femur, even with the calculated relative error for both the theoretical and experimental strain results, the theoretical strain results do not predict the experimental results for any strain gauges.

For the composite tibia, the highest theoretical error and the lowest experimental error occurred at strain gauges 34-36. Similarly, the lowest theoretical error and the highest experimental error occurred at strain gauges 13-15. The locations of these rosettes for the composite tibia are in areas of complex geometry. Gauges 13-15 on the composite tibia are located beneath the lateral tibial condyle thus most likely being affected by geometry change, edge effects and load application proximity. Gauges 34-36 are located along the parting line of the composite tibia, where the separate composite halves mate to become one piece. Inconsistent density, composition and geometry may occur along the

parting line thus explaining why the theoretical strain values are overestimating the results.

For the composite femur, the highest theoretical error and the lowest theoretical error occurred at strain gauges 22-24 and 10-12. The highest experimental error and the lowest experimental error occurred at strain gauges 19-21 and 13-15. The lowest error in the composite femur occurs in areas with small geometry changes. Gauges 10-12 and 13-15 are located on the front medial and the medial side on the composite femur, respectively. For the highest error, gauges 19-21 and 22-24 are located on the posterior side of the femur. Gauge 19-21 is the lowest strain rosette and could be subjected to stress effects caused by potting. Gauges 22-24 are located where the shaft of the femur starts to widen into the femoral condyles. Small offset in measuring the geometry and location of the strain gauge would account for the large theoretical error.

5.3 Verification of FE model with composite tibia and femur

A patient-specific finite element (FE) model of a composite tibia and femur (Au, 2008) was experimentally validated using MABTA. A third generation composite tibia and femur were inserted into MABTA and loaded with two point loads from a custom-made loading jig. Experimentally calculated von Mises (VM) strain values were compared to the predicted VM strain values from the FE model using regression analysis. A slope of 0.95, an intercept of $13.89\mu\varepsilon$, and an R^2 value of 0.90, indicate that the FE VM strains strongly predict the experimental strain results for the composite tibia. However, the regression line for the composite femur has a slope of 1.09, an intercept of $78.83\mu\varepsilon$, and an R^2 of 0.41 indicating that the FE VM strain results can predict the experimental

124

strain results but not as strong. These results show that the FEA models are better predictors than classical strength of materials methods for complex shape specimens as well for tissues that are not isotropic or homogeneous. It is thought that the composite femur results can be explained by the offset angle between the femur vertical axis and the vertical axis of MABTA. This slight angle increases the complexity for the determination of the exact loading position in the FE model.

5.4 Preliminary Experimentation with Biological Specimens

Since this machine was designed and developed to conduct *in vitro* experiments on cadaveric human and animal knee joints, a bovine tibia and femur obtained from a local abattoir and removed of all soft tissues were inserted into MABTA. Unlike the human knee joint, the bovine stifle joint is always at an F-E angle. As a result, the bovine femur was inserted into MABTA superior to the tibia and rotated to an F-E angle of 45°.

First and second principal strains were calculated using the strains measured along the cortex of the bovine tibia. It was found that the first and second experimental strain correctly matched the directions of the experimental longitudinal and transverse strains for all strain gauges except gauges 31-33 for all tests. It is uncertain why the direction of the first principal strain, ε_1, did not match the direction of the transverse strain, ε_T, for this rosette, which is located on the medial side of the bovine tibia.

Experimental strains varied between tests; the largest variation in the experimental longitudinal strains occurred at strain gauges 25-27 at 890 N, 1334 N and 1780 N. The variation between forces measured at the load cell and the resulting difference in moments applied to the bone is one possible explanation for this large strain

125

range and for the spread in results between subsequent tests. Effects from the surrounding environment, subsequent testing of the specimen and insufficient recovery time are other possibilities.

Theoretical and experimental principal strains as well as their associated errors were calculated. The theoretical principal strains predicted experimental principal strains for strain gauges 16-18 and 34-36 on the composite tibia for all tests and gauges 10-12 for test 1, gauges 25-27 for test 2 and gauges 28-30 for test 3 on the composite femur.

The theoretical strain calculations do not provide the necessary information needed to conclude that MABTA can produce reasonable and accurate experimental results with biological specimens. FE analysis is needed to fully verify that this apparatus can be used for such structures. At this time, MABTA has the potential to be used for such objectives as it can be adjusted to account for different anatomical positions. For more in depth biological specimen testing, MABTA needs to undergo further development.

References

Au A.G., 2008. A comprehensive approach to constructing human bone models: from CT to FE. PhD thesis. University of Alberta.

Bach, J.M., Hull, M.L., 1994. Description and evaluation of a new load application system for in vitro study of ligamentous injuries to the human knee joint. Advances in Bioengineering 128, 283-284.

Biden, E., O'Connor, J., 1990. Experimental Methods Used to Evaluate Knee Ligament Function. In: Daniel et al. eds. Knee Ligaments: Structure, Function, Injury and Repair. New York: Raven Press, Ltd, 135-151.

Burgess, I.C., Kolar, M., Cunningham, J.L., Unsworth, A., 1997. Development of a six station knee wear simulator and preliminary wear results. Proceedings of the Institution of Mechanical Engineers 211 Part H, 37-47.

DesJardins, J.D., Walker, P.S., Haider, H., Perry, J., 2000. The use of a force-controlled dynamic knee simulator to quantify the mechanical performance of total knee replacement designs during functional activity. Journal of Biomechanics 33, 1231-1342.

Shaw, J.A., Murray, D.G., 1973. Knee Joint Simulator. Clinical Orthopaedics and Related Research 94, 15-23.

Walker, P.S., Blunn, G.W., Broome, D.R., Perry, J., Watkins, A., Sathasivam, S., Dewar, M.E., Paul, J.P., 1997. A knee simulating machine for performance evaluation of total knee replacements. Journal of Biomechanics 30(1), 83-89.

Whiteside, L.A., Kasselt, M.R., Haynes, D.W., 1987. Varus-valgus and rotational stability in rotationally unconstrained total knee arthroplasty. Clinical Orthopaedics and Related Research 219, 147-157.

Chapter 6: Conclusions, Recommendations and Future Work

6.1 Conclusions

MABTA is a novel and valuable research apparatus with six degrees of freedom. It was further developed to conduct *in vitro* experiments on complete or partial cadaveric human, animal and composite specimens. MABTA has three rotational axes: flexion-extension, varus-valgus and internal-external as well as three translational load applications: proximal-distal (P-D), medial-lateral (M-L) and anterior-posterior (A-P). Loading is limited to 4448 N compression in the P-D direction and to ± 2224 N in the A-P and M-L directions.

A data acquisition program to control and monitor all integrated components plus record the strain distribution along the cortex of a composite and bovine tibia and femur was developed in National Instruments LabVIEW 8.5. Protocols for specimen preparation, experimentation with complete or partial composite and bovine bones, and for using the designed alignment jig and coaxial alignment indicators were developed.

Through experiments with a known geometry polyvinyl chloride (PVC) pipe and a composite tibia and femur, MABTA has good repeatability, supplies accurate and reliable data and is able to verify a finite element model of a composite tibia and femur. The design of this apparatus was successful for these specimens. However, such conclusions are not realistic with the bovine tibia and femur preliminary experiments. The theoretical strain calculations do not provide enough information to conclude that MABTA can produce reasonable and accurate experimental results with biological

128

specimens. Thus FE analysis is needed to fully verify the experimental results for such complicated structures.

As previously mentioned a primary objective of this project is to develop MABTA into an apparatus with a high standard for experimenting with composite and biological tissues. Through the verification process, it has been shown that MABTA can produce accurate and reliable results with composite specimens. Through the ability of MABTA to load bone on bone, loading jig on bone and the ability to experiment with a known geometry specimen and composite and bovine specimens, MABTA has been shown to be a very versatile apparatus. As illustrated in the bovine tibia experiments, MABTA can accommodate the necessary physiological loading conditions needed for such specimens. However, further development is needed before MABTA can be considered a high standard for experimenting with biological tissues.

6.2 Recommendations and Future Work

Since this is a newly developed apparatus, further improvements can be made to the apparatus itself and to its incorporated components. These improvements will ensure that MABTA becomes a high experimental standard for testing biological tissues.

From a design stand point, MABTA may be improved by using electromechanical actuators to load the A-P and M-L directions. Additionally, implementing digital read outs to the A-P and M-L translational directions to allow the repositioning of biological specimens between subsequent tests.

From a control perspective, the program could incorporate a proportional, integral, derivative (PID) controller to improve the consistency in load increments

129

between subsequent experiments. Secondly, the ability to load and unload arbitrarily should be incorporated into the LabVIEW program so that future experiments do not need to load consecutively. Thirdly, all tasks dealing with MABTA should be added to the program. Currently, Windows HyperTerminal is used to control the actuator prior to the actual test. This should be included into the main program so that only one program is needed to run the apparatus.

Since this apparatus will be conducting experiments mostly on soft tissue specimens, a preload function should be added. This function should be able to ask the user for a specific preload value, how long to preload the specimen and then implement it.

Lastly, the strain gauges are recorded for no set amount of time; this time is user dependent. A function should be included which questions the user for a specific time so the user can be attentive to the specimen itself and not concentrating on how long the strain values have been recorded.

MABTA is a useful device which can be used to examine known geometry structures through to biological structures. With the above suggestions, MABTA will continue to increase its applicability to many biomechanical functions.

Appendix A: Digital Image Correlation

Digital image correlation (DIC) is a commercial, full field, non-contact strain measurement method that functions on modern digital image technology (Adeeb and Horsley, 2006). This method measures the surface displacement by correlating a point on an image of the unloaded object to a point on an image of the loaded object (Chen et al., 2005).

VIC-3D, software included with the Correlated Solutions system, measures the strain from images taken from two cameras (Figure A.1). The use of two cameras enables the user to measure full field strain, displacements and the shape of the object in three dimensions (Correlated Solutions). A reference image is taken prior to specimen loading and subsequent images are taken at each load increment. The strain is then calculated from the change in displacement from one image to another.
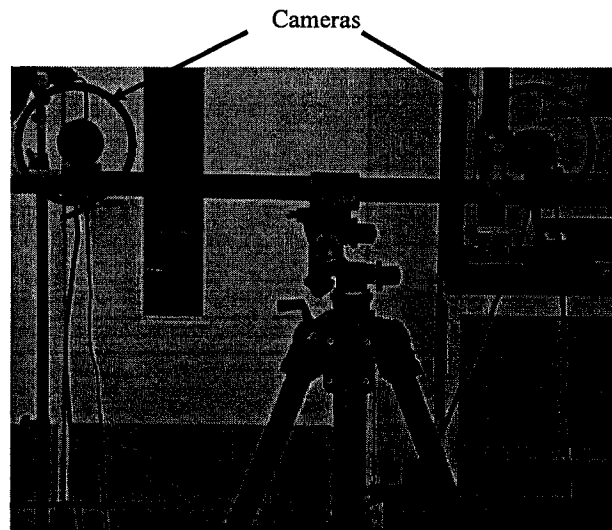
Figure A.1: Digital Image Correlation System

In order for the DIC method to measure the strain from the reference image to all subsequent images, the specimen surface must have contrasting speckles. This was done

by applying a white base coat followed by air brushing black speckles. All paint used was Games Workshop Citadel Colour water based acrylic paint (Games Workshop, Nottingham, UK). The speckle pattern can be seen on a copper pipe in Figure A.2 and on a PVC pipe in Figure A.3.

Front
Strain
Gauges

Back Strain
Gauges

(a)   (b)
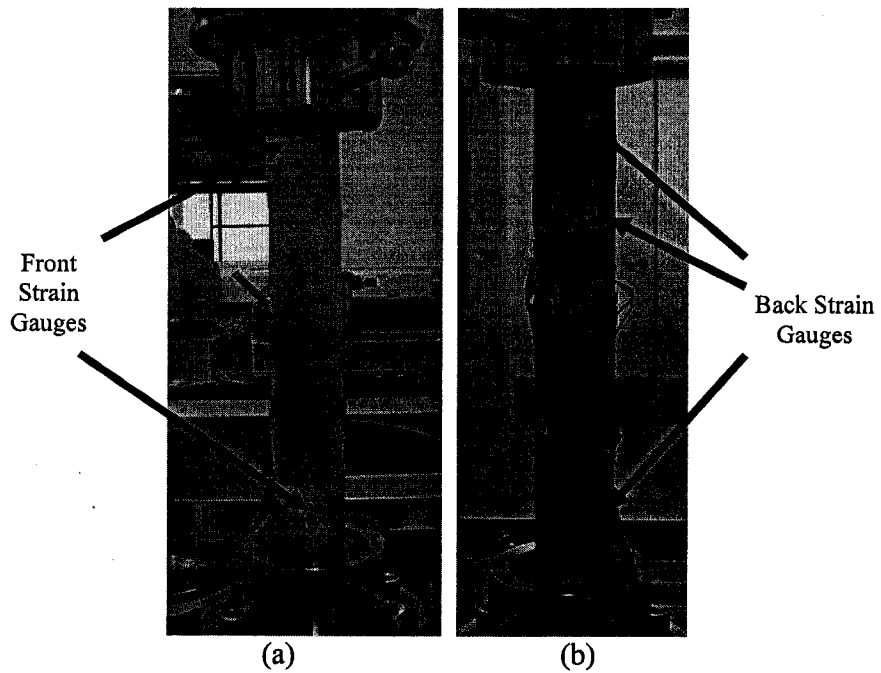
Figure A.2: Copper specimen a) Speckling on front of specimen and b) strain gauges on back of specimen
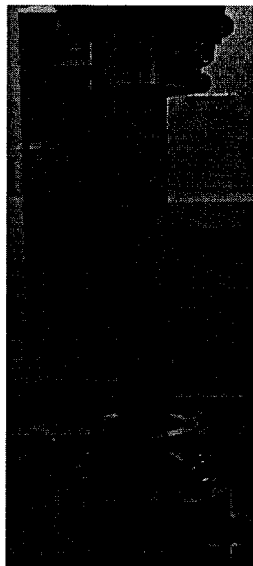
Figure A.3: Speckled PVC pipe

132

A.1 Instron and DIC Testing

To verify repeatability, accuracy and applicability of the DIC system from Correlated Solutions®, two specimens were speckled, strain gauged, placed into an Instron machine (Model TTK, Norwood, MA, USA) and subjected to three consecutive compression tests. The Instron machine has a maximum load capacity of 50,000 lb but for this experiment, the load cell was calibrated to 1000 lb full scale. For comparison purposes the Correlated Solutions® system was used to measure the strain along the front of the specimens and strain gauges were used to measure the strain along the back of the specimens.

A.1.1 Specimens and Specimen Preparation

A PVC and copper specimen were used to test the capabilities of the DIC method from Correlated Solutions® because of their availability, size, cost and simplicity for theoretical calculations. Both specimens were cut down to better reflect the length of an animal joint to be used in future tests. The dimensions associated with both the PVC and copper specimens are presented in Table A.1.

Table A.1: Specimen Dimensions for Comparison of DIC and Strain Gauge Results

Specimen	Length		Inside Diameter		Outside Diameter	
	mm	inch	mm	inch	mm	inch
Copper	208.00	8.189	32.08	1.263	35.00	1.378
PVC	219.761	8.652	25.76	1.014	33.38	1.314

The specimens were carefully secured into the bone pots, refer to Chapter 2 for description, and a height gauge was used to locate the exact position of the strain gauges for both the PVC (Table A.2) and copper (Table A.3). The distances were measured when the specimen was potted in the bone pots and placed in a vertical position (Figure A.2) on

133

a marble tabletop. The tabletop was used as the reference point (0.00 mm) and all distances were measured from this point. Care was taken when strain gauges were applied and aligned 180° by a technician. Three strain gauges were placed on the back of the PVC specimen with two gauges in front (Figure A.4) and five strain gauges were placed on the back of the copper specimen, with two gauges in front (Figure A.5). The specimen was then speckled between the two front gauges (Figure A.2a). Originally, the PVC specimen was used for preliminary testing purposes and the copper specimen was the main specimen. At the time of specimen preparation, the pipes were two independent specimens and would not be compared; so the difference in the number of strain gauges was irrelevant.

Table A.2: Strain gauge positions for PVC pipe

Specimen	Marble Tabletop Reference Point (mm)	Strain Gauge Position (mm)				
		Back			Front	
		Gauge 1	Gauge 2	Gauge 3	Gauge 4	Gauge 5
PVC	0.00	85	165	245	85	245

Front   Back
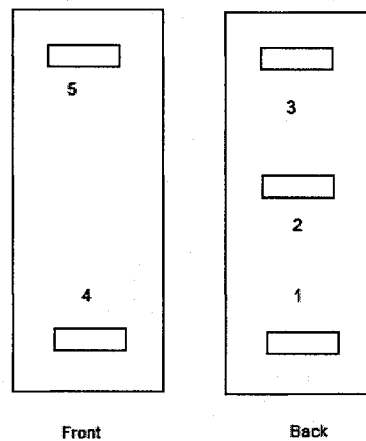
Figure A.4: PVC pipe strain gauge positions

134

Table A.3: Strain gauge positions for copper pipe

Specimen	Marble Tabletop Reference Point (mm)	Strain Gauge Position (mm)						
		Back					Front	
		Gauge 1	Gauge 2	Gauge 3	Gauge 4	Gauge 5	Gauge 6	Gauge 7
Copper	0.00	248	208	159	110	70	70	247
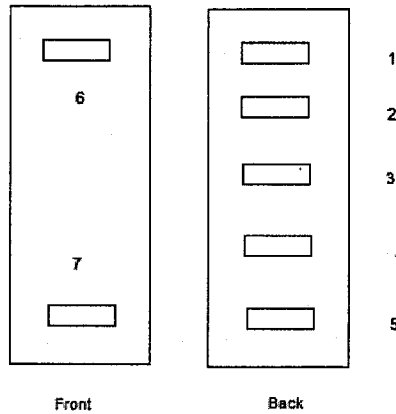
Figure A.5: Copper pipe strain gauge positions

A.1.2 PVC and Copper Tests

The PVC specimen was loaded to a maximum load of 200 lb (889 N). Each end was inserted into fitted Delrin® collars inside the bone pots and placed vertically in the Instron machine. Figure A.4 and Table A.2 provide the location of the strain gauges placed on the PVC pipe.

The copper specimen was subjected to a maximum load of 800 lb. One Delrin® collar was placed around the bottom of the copper specimen and then inside the bone pot. A self-aligning head was inserted into the Instron and was used to apply loads to the top portion of the specimen to avoid the possibility of bending the specimen. Figure A.2 and Figure A.5 illustrate the strain gauge positions.

During testing of the Copper specimen, strain gauge errors were received from LabVIEW regarding strain gauges #2 and #5. All wires were properly inserted into the

135

data acquisition system and no damage was seen at the gauge; nonetheless these gauges were eliminated from the test because of the error readings. This was not critical as there were sufficient redundant gauges to obtain sufficient information from the tests. The strain gauge values at maximum load for both the PVC and copper specimens are presented in Table A.4. Both the PVC and copper strain results are consistent across all three tests.

Table A.4: PVC and copper strain gauge results at maximum load (all values are in microstrain)

Specimen		Test		
		1	2	3
PVC	Gauge 1	-742.26	-753.20	-758.86
	Gauge 2	-912.30	-916.26	-920.22
	Gauge 3	-1083.79	-1084.00	-1084.89
	Gauge 4	-990.88	-991.46	-990.98
	Gauge 5	-691.43	-697.53	-701.24
Copper	Gauge 1	-334.54	-335.80	-339.04
	Gauge 3	-257.38	-257.12	-260.80
	Gauge 4	-207.26	-206.00	-209.04
	Gauge 6	-42.63	-43.82	-45.00
	Gauge 7	-221.84	-221.00	-220.52

If the specimens were subjected to pure axial compression, the strain would be the same everywhere if there are no edge effects. The strain gauge results in Table A.4 illustrate that the PVC specimen experienced bending. It was found that Gauge #1 (back bottom gauge) recorded a smaller strain value than Gauge #4 (front bottom gauge). The opposite was found for the top front and back gauges; Gauge #3 (back top gauge) recorded a larger strain value than Gauge #5 (front top gauge). It is thought this could have occurred from the piece being slightly shifted. For example, the top could have been loaded on the front side and the bottom being loaded on the backside.

136

Similarly, it was recognized that bending occurred along the copper pipe as the strain values are not consistent and Gauges #1 and #6 do not provide similar results. Given that the strain values for Gauges #2 and #5 were not recorded it is unknown if the same bending pattern occurred in this specimen as seen in the PVC specimen.

To analyse the DIC strain results, an area of interest was chosen 180° from gauge #2 on the PVC specimen and 180° from gauge #4 on the copper specimen. In theory, if no bending occurred, the DIC results should be comparable to gauge #2 for the PVC specimen and gauge #4 for the copper specimen. Table A.5 provides the DIC strain results for the PVC and copper specimens for the three tests at maximum load.

Table A.5: DIC strain results at maximum load for PVC and copper specimens

| Test | DIC Strain Results ($\mu\varepsilon$) | |
	PVC	Copper
1	-819.61	-300.97
2	-728.98	-196.99
3	-933.25	-217.57

The strain gauge and DIC results for all three tests were plotted for both the PVC (Figure A.6) and copper (Figure A.7) specimens. Analysing the PVC compression results in Table A.4 and Figure A.6, the strain gauge results are very repeatable from test to test. However, Table A.5 and Figure A.6 illustrate that the PVC DIC results vary between all tests.

137
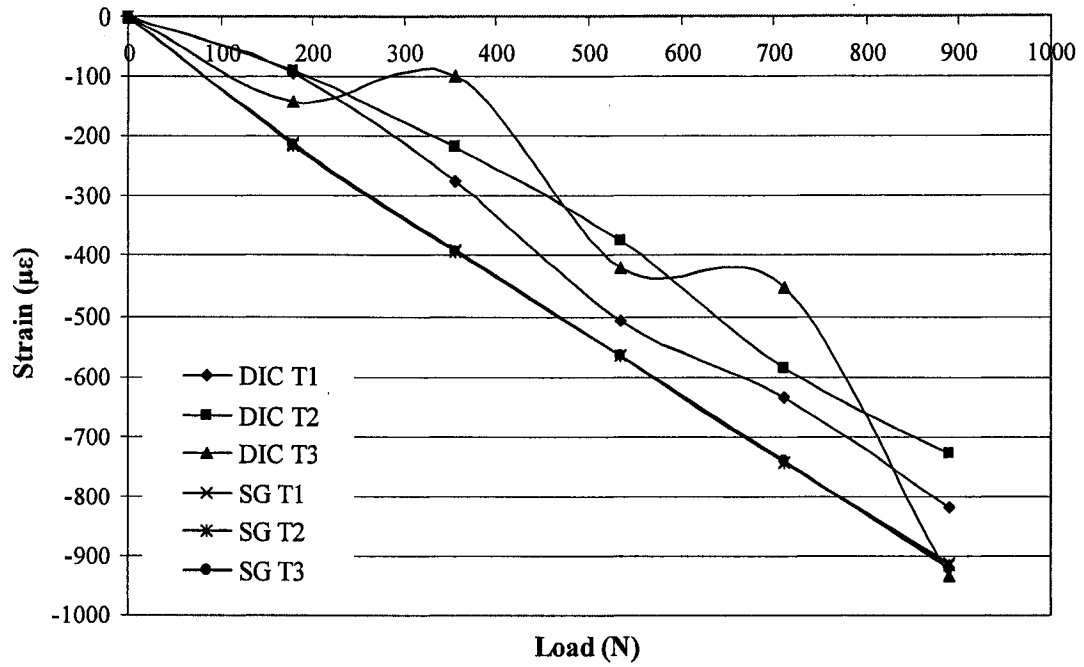
Figure A.6: DIC and strain gauge #2 results for the PVC specimen. Note lines are used for visual purposes only.
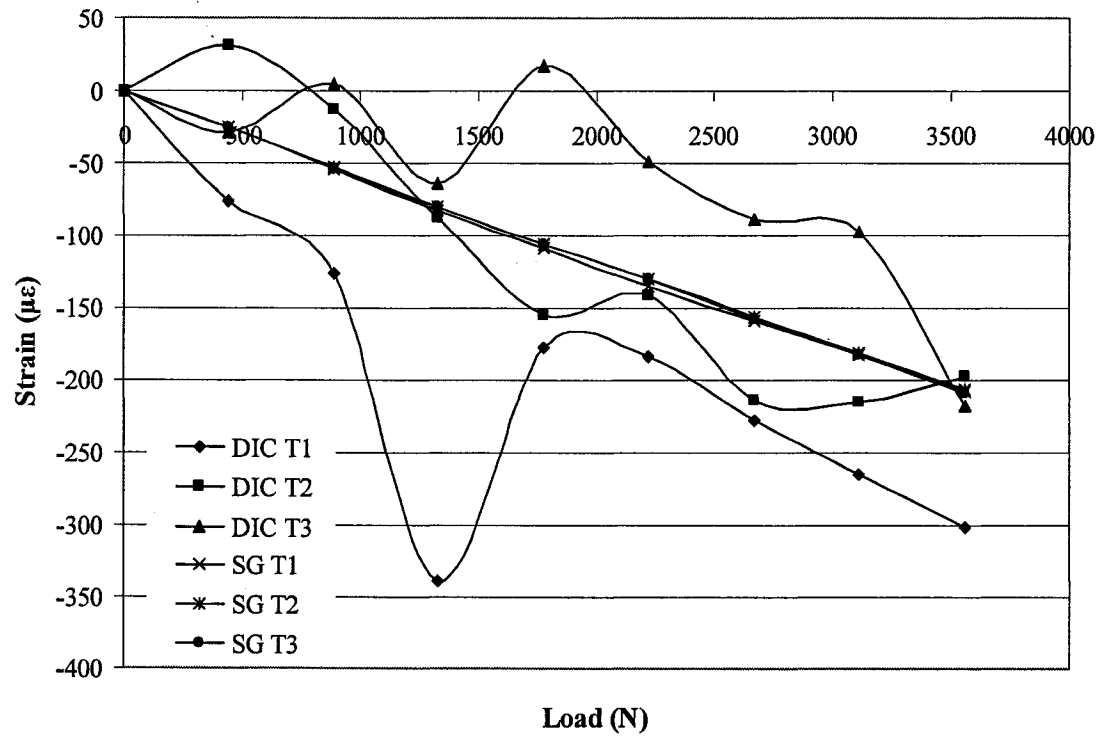
Figure A.7: DIC and strain gauge #4 results for copper specimen. Note lines are used for visual purposes only.

138

Similar to the PVC test, the strain gauge results appear to be consistent and repeatable between each test but the camera strain results show a much higher variability (Figure A.7). It is thought that the non-linearity of the DIC results for the copper pipe can be attributed to the noise in the camera system, which can be as little as ± 50µε or as large as ± 300µε for strains less than 1000µε (Simonsen, 2007).

A.1.3 Conclusions from Instron Results

Analysis of the results shows that the strain gauge data for both pipes are consistent between all three tests however this was not the case for the DIC results. It was found that the PVC pipe, which had strains ranging from -700µε to -1000µε, did not vary as much as the copper pipe which had strains ranging from -50µε to -340µε. After consultation with the company, Correlated Solutions®, it was concluded that this variation was caused by the noise in the camera strain system. The noise occurs in a strain range from -50µε to -150µε and can be as little as ± 50µε or as large as ± 300µε for strains less than 1000µε (Simonsen, 2007).

Since the goal of using this system was for a second measurement method for reading strains along the knee joint, the noise of this system will be a major issue. Previous studies indicate that strains on the knee can range from 0 to -270µε (Bourne et al., 1984a) and -11 to -333µε (Reilly et al., 1982), which are within the specified noise range. It is therefore not recommended to use this system for this application.

References

Adeeb, S., Horsley, D., 2006. Local stress-strain response of an axial X100 girth weld under tensile loading using digital image correlation. Proceedings of IPC 2006 International Pipeline Conference.

Chen, T.Y., Lee, C.H., Chen, Y.-C., Shih, K.-L., 2005. A Study of Mechanical Behavior of Bellows by Digital Image Correlation and Strain Gages. Proceedings of the 2005 SEM Annual Conference and Exposition on Experimental and Applied Mechanics, 395-399.

Correlated Solutions. Correlated Solutions, Inc. – Digital Image Correlation. 11 Aug. 2008. <http://www.correlatedsolutions.com/index.php?option=com_content&task=view&id=13&Itemid=26>.

Bourne, R.B., Finlay, J.B., Papdopoulos, P., Rorabeck C.H., Andreae, P., 1984a. In vitro strain distribution in the proximal tibia. Clinical Orthopaedics and Related Research 188, 285-291.

Reilly, D., Walker, P.S., Ben-Dov, M., Ewald, F.C., 1982. Effects of tibial components on load transfer in the upper tibia. Clinical Orthopaedics and Related Research 165, 273-282.

Simonsen, M. 19 Dec. 2007. Email Communication.

Appendix B: Data Acquisition System

A data acquisition system was developed in National Instruments (NI) LabVIEW 8.5 (National Instruments Corp, Austin, Texas, USA) to control and measure the strains along the cortex of bone. The program records 39 strain values while controlling an AMTI signal conditioner (MiniAmp MSA-6) for an AMTI six-degree of freedom load cell (MC6-6-2000) and a Kollmorgen servomotor (Model AKM42G-BSCN2-02) through serial communication and ASCII commands (Table B.1).

Table B.1: Serial Communication ASCII Commands

Component	ASCII Commands	Description
Servomotor	EN	Enable actuator
	LOAD	Loads set-up information
	SAVE	Saves information into controller memory
	COLDSTART	Restarts the controller
	J .3	Move actuator up at a speed of 0.3mm/min
	J -.3	Move actuator down at a speed of 0.3mm/min
	STOP	Stop actuator movement
	DIS	Disable actuator
Signal Conditioner	Q	Starts signal conditioner
	R	Stops signal conditioner
	S	Autozero signal conditioner

The program is predominantly based on user input and Boolean comparison functions. Before the program executes, the user is recommended to set a maximum load value; this check was implemented to avoid the possibility of the user incorrectly entering an excessive load value. Once the program is running an ASCII command is sent to the load cell to zero the load values and all strain values along the specimen are passed into a built in LabVIEW function that automatically zeroes the strain values. These zeroed values are then recorded. Next the program moves onto the user input state. The user is

141

asked to enter the next desired load value and whether to start the actuator, unload the actuator or adjust transverse loads (Figure B.1). Once the user has finished entering the desired load value and has chosen the subsequent state, the program compares the entered load value to the maximum load value entered at the beginning of the program. If this load value is greater than the maximum load, the program will ask that another value will be entered and will not continue until this maximum value is within an acceptable range for the hardware used (1000 lb) or for the specific specimen tested (400 lb). Depending on the state chosen the program will continue to run until the user has either specified to unload the actuator or to permanently stop the program. It is recommended that the program be stopped only after the actuator has been fully unloaded. The front panel of the program can be seen in Figure B.1 and a flowchart of the logic described can be seen in Figure B.2.

142
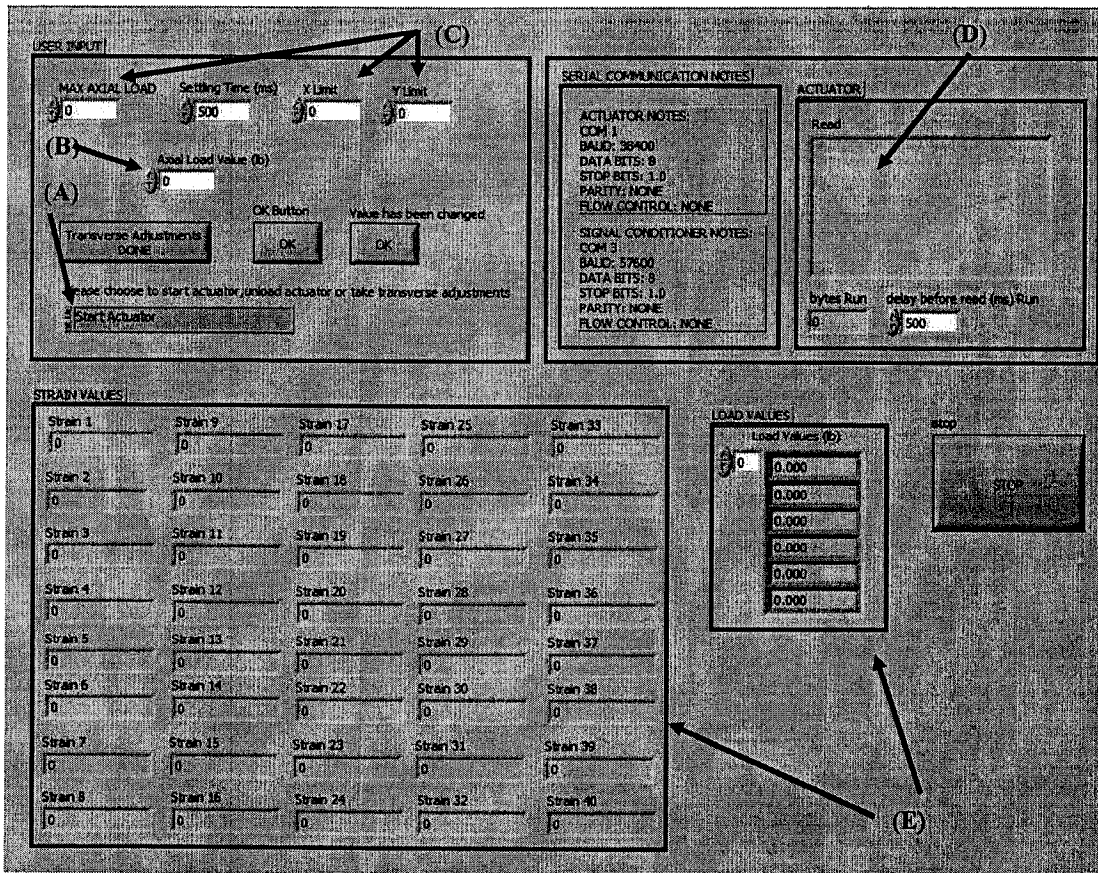
Figure B.1: LabVIEW Front Panel where (A) Choose nest state, (B) Enter next load value (C) User specified limits, (D) Serial communication acknowledgement and (E) Strain and load output.
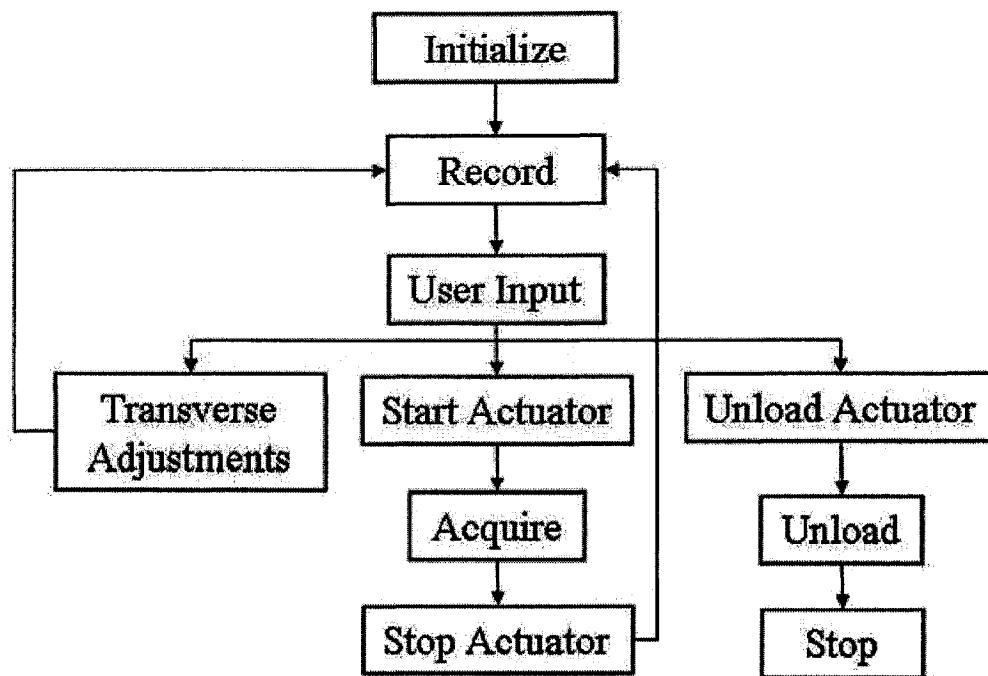
Figure B.2: Flowchart of LabVIEW Logic

The following is a more detailed, step-by-step description of the program developed to test the knee joint. Descriptions of several LabVIEW terms are presented throughout Section B.1 LabVIEW Logic.

B.1 LabVIEW Logic

1. Reads serial port information for the actuator
2. Initializes the global Stop button to false (stops the sub vi "RUN SC")
3. Initializes the local Stop button to false (stops the main program)
4. Calls the sub vi "RUN SC"
   a. "RUN SC" converts the offset binary values sent from the signal conditioner into pounds (lb)
5. Reads that the program starts at the Initialize State
6. Starts while loop
7. Checks if the Enum Constant "Initialize" is equal to the Enum constant "Stop"
   Where Enum constant is an enumerated data type that allows the program to cycle through a list of strings
   a. If equal then program stops
   b. Else program continues

144

8. Check the Boolean value sent into each state.
    a. If true, the program stops
    b. If false, the program continues with logic
9. Initialize State
    a. Reads MABTA DAQ Comp Tibia Task
    b. Nulls the strain gauges on the bone
    c. Sends a True command to the Global auto zero variable which sends a true value to the "RUN SC" sub vi to auto zero the 6 DOF load cell
    d. Sends a True command to the Global read variable which sends a true value to the "RUN SC" sub vi to continuously read the values from the signal conditioner
    e. Reads the load values from the global load values variable and displays on main program front panel in Load Values Array
    f. Read Boolean value from main while loop
        i. If true, program stops
        ii. Else program moves to the 'Record' state
10. Program moves to main while loop
    a. Checks if Enum Constant equals Stop
        i. If Stop then program is finished
        ii. Else program continues
11. Record State
    a. For loop that reads each value in the Global load values array
        i. Iterates 6 times to go through all 6 channels listed in the array
    b. Sends values to a measurement file
    c. Reads the strain values from MABTA DAQ Comp Tibia task
    d. Waits for a user specified settling time
    e. Sends strain values to another measurement file
    f. Read Boolean value from main while loop
        i. If true, program stops
        ii. Else program moves to the 'User Input' state
12. Program moves to main while loop
    a. Checks if Enum Constant equals Stop
        i. If Stop then program is finished
        ii. Else program continues
13. User Input
    a. Displays a dialog box that says: "Please enter next load value and indicate next action: Start Actuator, Unload Actuator, or Transverse load adjustments." User must press OK.
    b. While loop that waits for front panel activity
        i. Once user has enter the next load value and action, they must press OK
        ii. Program will not continue until the "OK" or "STOP" button has been pressed
            1. If Stop button is pushed then a True is sent to the case structure used to determine the next state.
            2. Program goes to Stop state and program ends

3. If Ok is pushed then a true is sent, the while loop is stopped and the program continues
   c. Starts while loop that checks the load value entered by the user
      i. If this value is greater than the maximum load value entered by the user:
         1. Message is displayed that says: "Next axial load value has exceeded the maximum capacity of the machine, please change your load value!"
         2. Starts while loop that waits for front panel activity
         3. Program will not continue unless user has changed the load value to less than the specified maximum load and then pushed the "OK" button with the label that says "Value has been changed"
      ii. If value is less than the maximum load entered by the user:
         1. While loop ends and the program continues
   d. Reads the Enum constant value entered by the user and goes to specified state:
      i. Start Actuator
      ii. Unload Actuator
      iii. Transverse Adjustments
   e. Read Boolean value from main while loop
      i. If true, program stops
      ii. Else program moves to the specified state

14. Program moves to main while loop
   a. Checks if Enum Constant equals Stop
      i. If Stop then program is finished
      ii. Else program continues

15. Start Actuator
   a. ASCII command to enable (EN) and move actuator (J .3) is written to serial port
   b. Enters flat sequence (method to enforce order of operations) and waits for a specified time
   c. Reads the ASCII command
   d. Read Boolean value from main while loop
      i. If true, program stops
      ii. Else program moves to the "Acquire" state

16. Program moves to main while loop
   a. Checks if Enum Constant equals Stop
      i. If Stop then program is finished
      ii. Else program continues

17. Acquire State
   a. Enters into a while loop
      i. While loop will continue until axial load value read in the Load Values array equals to the specified load value entered by the user
      ii. Fx and Fy values are checked against a limit

146

b. Send a True command to the Global read variable which sends a true value to the "RUN SC" sub vi to continuously read the values from the signal conditioner

c. Reads the load values from the global load values variable and displays on main program front panel in Load Values Array

d. Reads MABTA DAQ Comp Tibia task

e. Display strain readings onto front panel

f. Once axial load value equals to specified load value or STOP button is pushed, while loop stops

g. Read Boolean value from main while loop
  i. If true, program stops
  ii. Else program moves to the "Stop Actuator" state

18. Program moves to main while loop
  a. Checks if Enum Constant equals Stop
    i. If Stop then program is finished
    ii. Else program continues

19. Stop Actuator
  a. ASCII command to stop (STOP) is written to serial port
  b. Enters flat sequence and waits for a specified time
  c. Reads the ASCII command
  d. Read Boolean value from main while loop
    i. If true, program stops
    ii. Else program moves to the "Record" state

20. Program moves to main while loop
  a. Checks if Enum Constant equals Stop
    i. If Stop then program is finished
    ii. Else program continues

21. Record (see point 11 for detailed description of this state)

22. Program moves to main while loop
  a. Checks if Enum Constant equals Stop
    i. If Stop then program is finished
    ii. Else program continues

23. User Input (see point 13 for detailed description of this state)

24. Program moves to main while loop
  a. Checks if Enum Constant equals Stop
    i. If Stop then program is finished
    ii. Else program continues

25. Transverse Adjustments
  a. Dialog box: "Please adjust transverse load values, user must press OK
  b. Enters while loop, while loop will end once the "DONE" or "STOP" button is pressed
  c. Send a True command to the Global read variable which sends a true value to the "RUN SC" sub vi to continuously read the values from the signal conditioner
  d. Reads the load values from the global load values variable and displays on main program front panel in Load Values Array

    e. Reads MABTA DAQ Comp Tibia task

    f. Display strain readings onto front panel

    g. Compares Fx, Fy and Fz values in Load values array to specified limits

    h. Read Boolean value from main while loop

        i. If true, program stops

        ii. Else program moves to the "Record" state

26. Program moves to main while loop

    a. Checks if Enum Constant equals Stop

        i. If Stop then program is finished

        ii. Else program continues

27. Record (see point 11 for detailed description of this state)

28. Program moves to main while loop

    a. Checks if Enum Constant equals Stop

        i. If Stop then program is finished

        ii. Else program continues

29. User Input (see point 13 for detailed description of this state)

30. Program moves to main while loop

    a. Checks if Enum Constant equals Stop

        i. If Stop then program is finished

        ii. Else program continues

31. Unload Actuator

    a. ASCII command to unload (J -.3) is written to serial port

    b. Enters flat sequence and waits for a specified time

    c. Reads the ASCII command

    d. Read Boolean value from main while loop

        i. If true, program stops

        ii. Else program moves to the "Unload" state

32. Program moves to main while loop

    a. Checks if Enum Constant equals Stop

        i. If Stop then program is finished

    b. Else program continues

33. Unload State

    a. Send a True command to the Global read variable which sends a true value to the "RUN SC" sub vi to continuously read the values from the signal conditioner

    b. Reads the load values from the global load values variable and displays on main program front panel in Load Values Array

    c. Reads MABTA DAQ Comp Tibia task

    d. Display strain readings onto front panel

    e. Compares Fz values in Load values array to 0

        i. Once load value is less than or equal to 0 or the STOP button is pushed the while loop is stopped

    f. Read Boolean value from main while loop

        i. If true, program stops

        ii. Else program moves to the "Stop" state

34. Program moves to main while loop

148

       a. Checks if Enum Constant equals Stop
         i. If Stop then program is finished
       b. Else program continues

35. Stop State
       a. Send a True command to the Global Stop variable which sends a true value to stop the "RUN SC" sub vi
       b. ASCII command to stop (STOP) and disable (DIS) the actuator is written to serial port
       c. Enters flat sequence and waits for a specified time
       d. Reads the ASCII command
       e. Read Boolean value from main while loop
         i. If true, program stops
         ii. Else program moves to the "Stop" state

36. Program moves to main while loop
       a. Checks if Enum Constant equals Stop
       b. Program is finished

149

Appendix C: Design of Two Alignment Devices

Alignment of a mounted specimen in a testing machine requires considerable attention when trying to validate experimental results with theoretical calculations. This is especially important for specimens of irregular geometry, such as composite and animal bones. When validating a machine or a finite element model through theoretical calculation and/or experimental results, it is essential that the specimens are well aligned and this alignment is known and consistent throughout all experiments. If a specimen has a slight misalignment from a previous experiment, the results are not easily comparable thus means to ensure proper alignment and repeatability is required.

Since all soft tissue has been removed from the specimens, alignment is no longer done by the connective tissues but through instruments and experimental protocols. To guarantee that the desired contact position between the tibia and femur is maintained throughout potting and transporting to MABTA, an alignment jig was designed and a coaxial alignment indicator was used. The design and limitations of each device are explained in detail.

C.1 Alignment Jig

The alignment jig (Figure C.1) was designed to consistently align, secure and pot both the tibia and femur of either the composite or bovine bone into the bone pots. The primary specimen potting objective was that the bone pots be at a fixed position. When transferring the potted specimens to MABTA, it was designed that if the tibia and femur bone pot holders are aligned then the specimens are in the same position as when potted. The second objective of the alignment jig is that once the pots are secured into their fixed

150

position, the specimens are adjusted to recreate the most natural contact between the tibia and femur within the given situation. Once this contact has been achieved, bones are potted.
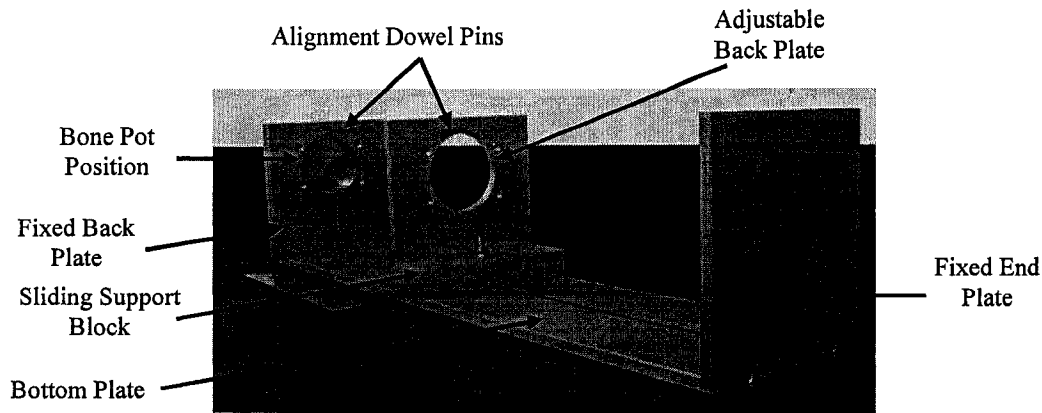
Figure C.1: Alignment Jig

C.1.1 Design of Alignment Jig

The alignment jig was designed to adjust for both the composite and bovine tibia and femur. Since bovine bones are much larger than the composite bones, the jig was designed to adapt to both types of specimens.

The alignment jig (Figure C.1) consists of a bottom plate, fixed back plate, an adjustable back plate, two alignment dowel pins, a sliding support block and a fixed end plate. The material and dimensions of each component are listed in Table C.1.

Table C.1: Dimensions and material information for alignment jig components

Component	Length		Width		Height		Material
	inch	mm	inch	mm	inch	mm	
Bottom Plate	27.00	685.80	6.0	152.40	0.375	9.53	Aluminum
Fixed Back Plate	0.75	19.05	6.0	152.40	6.0	152.40	Aluminum
Adjustable Back Plate	0.375	9.53	6.0	152.40	6.0	152.40	Aluminum
Fixed End Plate	0.25	6.35	6.0	152.40	6.375	161.93	Aluminum
Sliding Support Block	2.00	50.80	6.0	152.40	1.0	25.40	Aluminum

The fixed back plate and fixed end plate are bolted to the bottom plate. The adjustable back plate is bolted to the sliding support block and both components slide along a 6.35 mm (¼") wide, 381 mm (15") long T-slot. A 6.35 mm (¼") dowel pin and a 6.35 mm (¼") shoulder bolt were placed on the bottom of the adjustable back plate and sliding support block, respectively, to maintain alignment while the piece is sliding into position. Additionally, the shoulder bolt is used to fix the adjustable back plate once a desired length has been chosen. The bone pots are secured into the fixed back plate and the adjustable back plate through four stainless steel screws and a dowel pin. The dowel pin was added to the design to ensure that the bone pots are parallel to the top of the end plates and are not potted with an unknown rotation. As described in Appendix G, a misalignment of 1 mm can cause a strain difference of 100με between front and back gauges. A fixed end plate was included in the design so that the alignment jig could be placed vertical on either end (Figure C.2) during bone potting procedures. Lastly, all components of the alignment jig were anodized to prevent corrosion in a biological fluid environment.

Figure C.2: Alignment Jig Standing on Fixed End Plate

152

C.1.2 Alignment Limitations

The alignment jig was used to produce well-aligned specimens. To verify the suitability of the jig designed for its alignment capabilities, the jig was placed into a Coordinate Measuring Machine (CMM, Figure C.3), accurate to 0.001 mm, to measure the jig's alignment limitations.
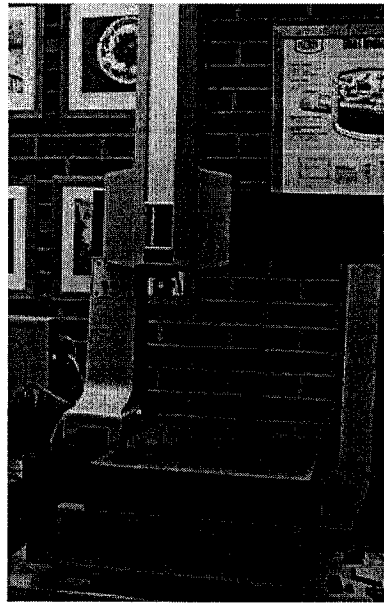
Figure C.3: CMM machine (MicroVal, Brown and Sharpe, North Kensington, RI)

153
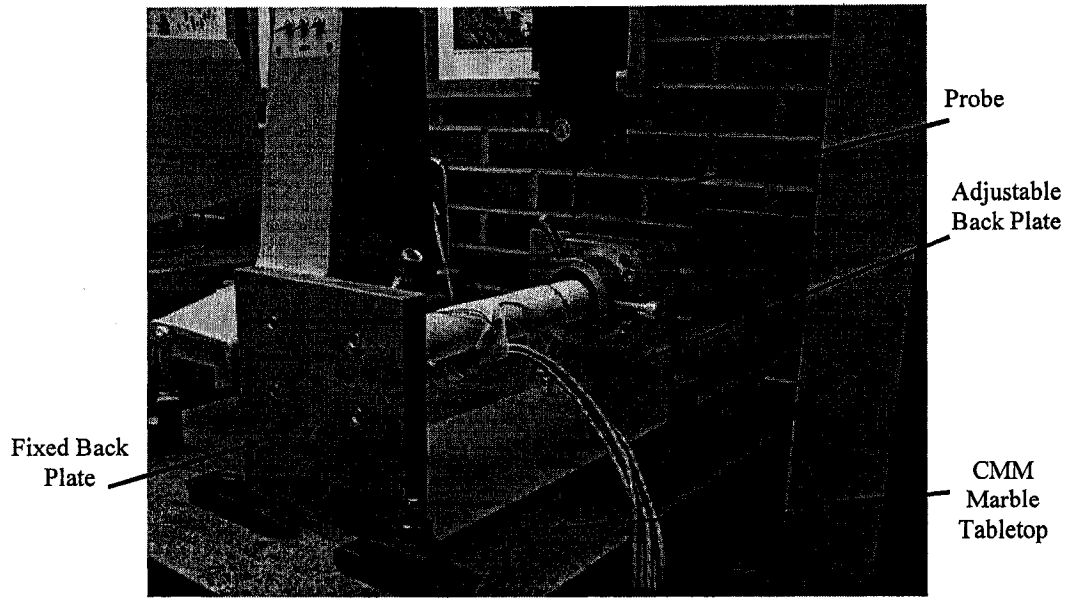
Figure C.4: Alignment jig with PVC specimen mounted in place in CMM

The alignment jig was placed into the CMM machine (Figure C.4) with the fixed back plate at the front of the marble table. The system's coordinate system is as shown in Figure C.4. The probe was used to measure the x-coordinate of the front and back corners of the jig and was adjusted until the jig was parallel with the y-axis of the machine. The coordinate of each corner of the fixed back plate was recorded and used to find the x-coordinate centre of the jig. This x-coordinate was then fixed and used to measure the variation in heights along the length of each component starting at the fixed back plate and moving towards the adjustable back plate (Table C.2). From Table C.2 it was noticed that the largest variation occurred across the bottom plate (0.054 mm), first bone pot (0.026 mm) and the PVC specimen (0.024 mm), however all variation was found to be less than 0.1 mm and could be caused from anodizing. Referring to Appendix G, a misalignment of 0.1 mm can cause a strain difference of approximately $12\mu\varepsilon$ difference

154

between front and back gauges. This possible source of error is minimal when compared to all the other sources when experimenting with biological specimens.

Table C.2: Height variation through length of each component (all dimensions are in mm)

	Max Height	Min Height	Difference
Fixed Back Plate	-214.755	-214.759	0.004
Bone Pot 1	-229.393	-229.419	0.026
PVC Pipe	-248.922	-248.946	0.024
Bone Pot 2	-229.497	-229.498	0.001
Adjustable Back Plate	-214.823	-214.825	0.002
Bottom Plate	-367.208	-367.262	0.054

Next the variation across the width of the fixed and adjustable back plates was measured (Table C.3). The largest variation occurred across the adjustable back plate (0.091 mm). This variation could be due to the adjustability of the plate; only one shoulder bolt is used to secure the plate in position, therefore, slight variation in the heights could occur between the centre of the plate where it is fixed and the ends of the plate. Additionally, the anodizing of the alignment jig could cause slight variations in height across individual components.

Table C.3: Height variation across the width of each component (all dimensions are in mm)

	Max Height	Min Height	Difference
Fixed Back Plate	-214.756	-214.761	0.005
Adjustable Back Plate	-214.763	-214.854	0.091

To determine how aligned the two pots are with respect to each other (main function of jig), the height at the highest position on both bone pots was measured when the alignment jig was in an upright position and when it was rotated 90° (Table C.4). When the alignment jig was in the upright position (Figure C.4), a 0.068 mm difference

155

in height was measured. This difference increased slightly to 0.128 mm when the jig was rotated 90°.

Table C.4: Height variation between bone pots (all dimensions in mm)

	Upright Position		Rotated 90°	
	Bone Pot 1	Bone Pot 2	Bone Pot 1	Bone Pot 2
x	249.610	250.586	303.611	304.461
y	-367.971	-75.179	-356.534	-76.636
z	-229.394	-229.462	-264.244	-264.116
Difference	0.068		0.128	

Lastly it was determined if the fixed and adjustable back plates were parallel (Table C.5). Theoretically, if two vectors are parallel, the dot product of the two vectors will be of equal magnitude to the multiplication of the magnitudes of the vectors ($\vec{a} \cdot \vec{b} = |\vec{a}||\vec{b}|$). Coordinates were measured and recorded along the width and length of the plate. The cross product was used to find an orthogonal vector to these two perpendicular lines for each back plate. Next the dot product of the two orthogonal vectors was found to conclude if the two plates are parallel ($\theta = 0°$ or $180°$).

From Table C.5 it can be seen that the fixed and adjustable plates are parallel as the magnitude of the dot product and the multiplication of the magnitudes produced an angle of 180° ($\theta = \cos^{-1}\left(\dfrac{\vec{a} \cdot \vec{b}}{|\vec{a}||\vec{b}|}\right)$).

Table C.5: Cross product and dot product results

		Cross Product			Dot Product	Multiplication of Magnitudes	Angle (degrees)
		i	j	k			
Upright Position	Fixed Plate	0.000	0.000	-365.417	-48069.3	48069.3	180.0
	Adjustable Plate	0.000	0.000	131.546			
Rotated 90	Fixed Plate	0.000	0.000	432.595	-96583.8	96583.8	180.0
	Adjustable Plate	0.000	0.000	-223.266			

156

From the CMM measurements, it can be concluded that the alignment jig is well aligned and thus to be used to align composite and bovine specimens accurately as all variations were less than 0.13 mm. The protocol on how to place and align specimens in the alignment jig can be found in Appendix F, section F.2.

C.2 Coaxial Alignment Indicator
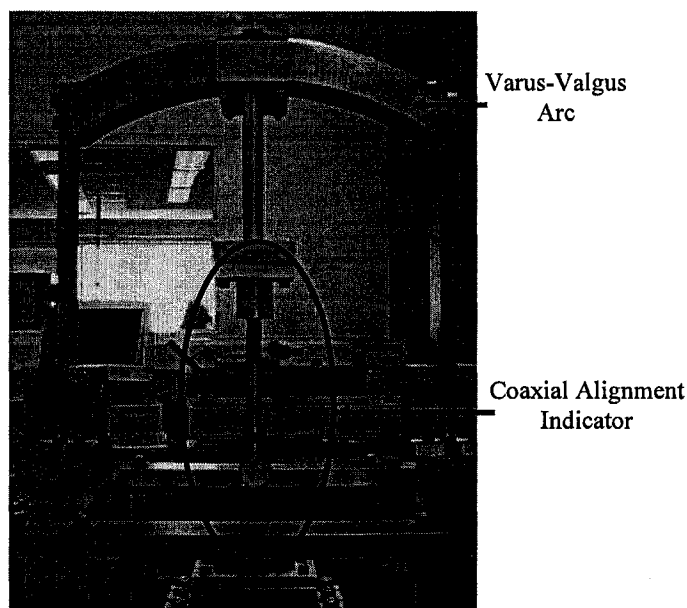
Figure C.5: Coaxial Alignment Indicator in MABTA

The coaxial alignment indicator (Figure C.5) was designed to align the tibia and femur bone pot holders. In the design process of MABTA it was decided that the femur is to be fixed into position in the centre of the varus-valgus arc with the tibia moving relative to the femur. It is with the coaxial alignment indicator that the tibia bone pot holder can be positioned directly below the femur bone pot holder. Using the alignment jig and the coaxial alignment device, the tibia and femur maintain the desired contact determined during potting.

157

C.2.1 Design of Coaxial Alignment Indicator

The coaxial alignment indicator (Figure C.6) was designed to bolt to the femur bone pot holder and rotate about its axis to align the tibia bone pot holder relative to the femur. This design consists of a coaxial indicator (Jewel 6, Links), a 25.4 mm (1") steel shaft, connecting plate and ball bearings.
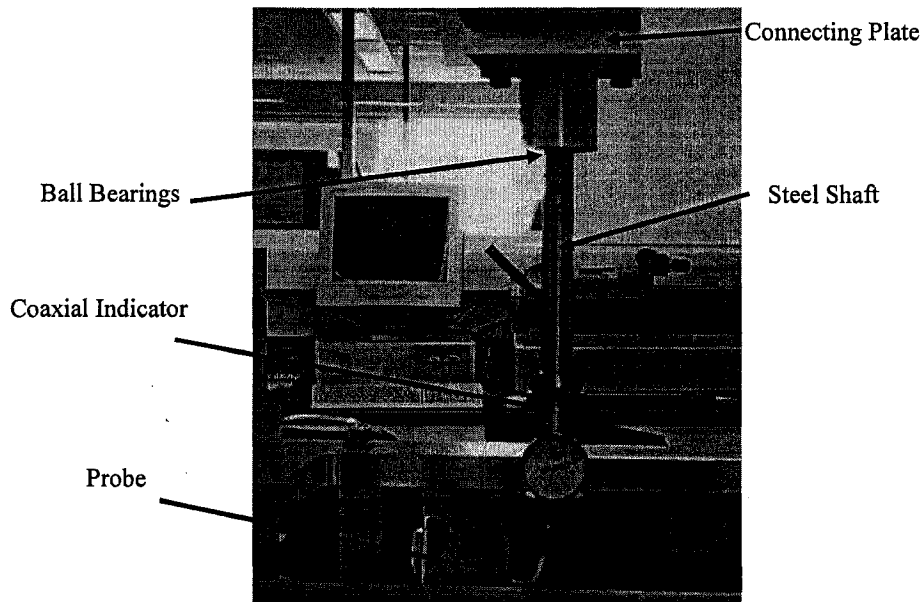
Figure C.6: Components of coaxial alignment indicator

C.2.2 Alignment Limitations

The coaxial alignment indicator is a suitable method to align the femur and tibia bone pot holders as the tibia and femur bone pot holders can be aligned within one division (0.0127mm, 0.0005") on the dial face. The connecting plate is bolted into the femur bone pot holder and the indicator rotates about its own axis. The probe of the coaxial alignment indicator rests on the inside of the bone pot holder. When the shaft is rotated, the hands of the dial face rotate indicating if the two components are aligned.

It is very difficult and tedious to get an alignment better than one division since the hand cranks are attached to 12.7 mm (½"), 18-8 stainless steel lead screws with a

158

pitch of 20 threads per inch. The pitch size limits the amount of adjustability and alignment accuracy as the load platform translates 1.27mm (0.05") in the x or y direction with each turn of the hand crank. The protocol on how to use the coaxial alignment indicator can be found in Appendix F: Experimental Protocols, section F.5: Coaxial Alignment Indicator Protocol.

C.3 Conclusion

As proven in Appendix G, alignment is an essential component and if hindered could influence the verification of experimental results with theoretical results. Using the designed alignment devices, acceptable alignment can be achieved and maintained throughout testing.

159

Appendix D: Calibration

In general, calibration is a process of comparing the output of a measuring device to a range of known inputs (Hall et al., 2006). Calibration is very common among experimental work and must be done using a known gold standard. A set of standard weights (8.9 N (2lb), 22.2 N (5lb), 35.5 N (8lb), 111.2 N (25lb) and 222.4 N (50lb)) were used to calibrate the load platform and later the six degree of freedom load cell of MABTA.

D.1 Preliminary Load Cell Design Calibration

In the preliminary design, MABTA used a custom-made load cell to measure the medial-lateral (M-L), anterior-posterior (A-P) and proximal-distal (P-D) applied loads. This custom-made load cell consisted of three platforms connected by two sets of aluminum U-shaped channels (Figure D.1). Ideally these channels resist deflection in one axis while allowing deflection in another axis. Strain gauges were applied on the surface of the small aluminum U-shaped channels and measured the M-L shear and A-P shear. A separate axial load cell placed on the top load platform measures the P-D load.

U-shaped
Channels
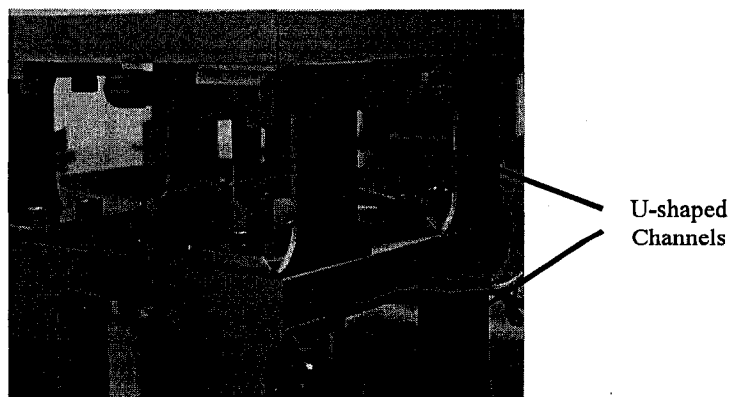
Figure D.1: Custom-made load cell

160

Cross talk or off axis loading, which is an issue found in most load cells, can cause errors in the measurement readings. It is possible when applying a P-D load or transverse load, longitudinal or transverse deflection will occur and thus provide a false reading in the shear or axial measurements. It is believed that the problem of cross talk can be calibrated out and so numerous calibration tests were conducted.

Initially strain gauges were applied to each U-shaped channel on the custom-made load platform. Four transverse weight tests, one for each direction of the load cell, were completed on the load platform to see how the individual platforms would respond when load was applied in the opposite direction. Various combinations of 8.9 N (2lb), 22.2 N (5lb), 35.5 N (8lb), 111.2 N (25lb) and 222.4 N (50lb) weights were applied to the top and bottom of the aluminum cylinder. A maximum weight of 453.7 N (102 lb) was applied to the apparatus. Schematics of the four loading directions and positions can be seen in Figure D.2 though Figure D.5.
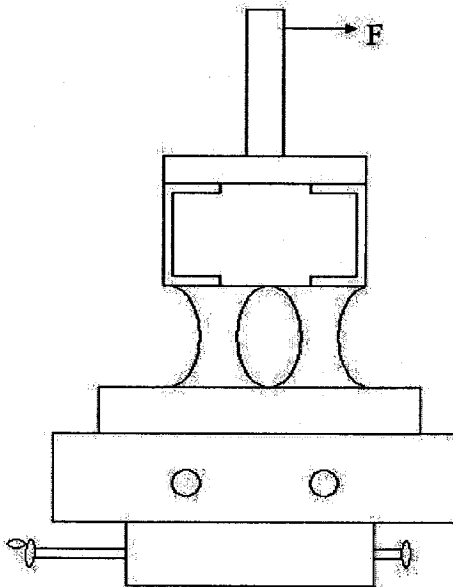
Figure D.2: Loading direction of first test (0 degrees)

161
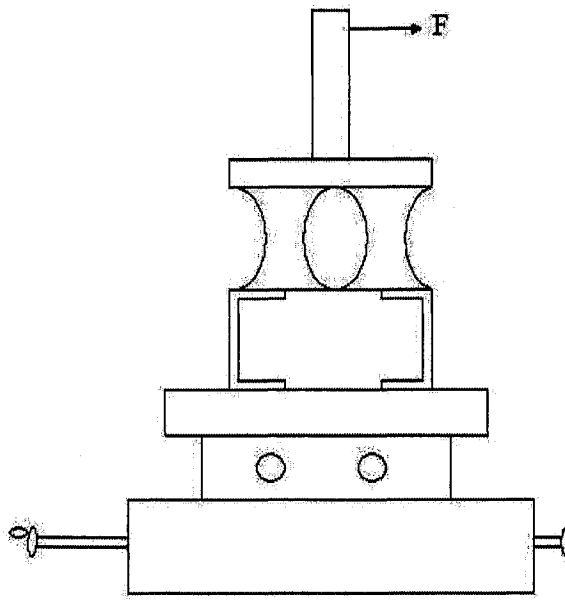
Figure D.3: Loading direction of second test (90 degrees)
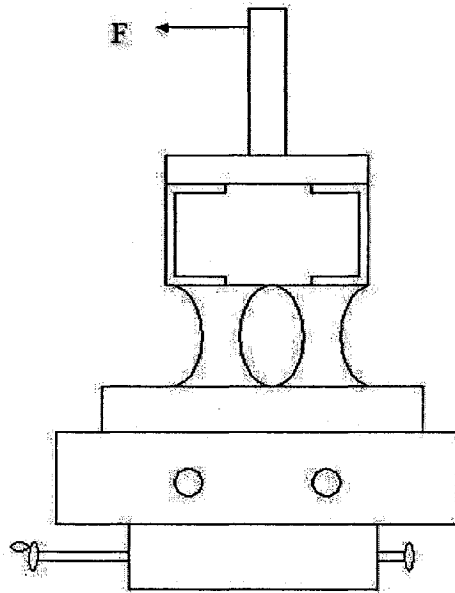
Figure D.4: Loading direction of the third test (180 degrees)

162
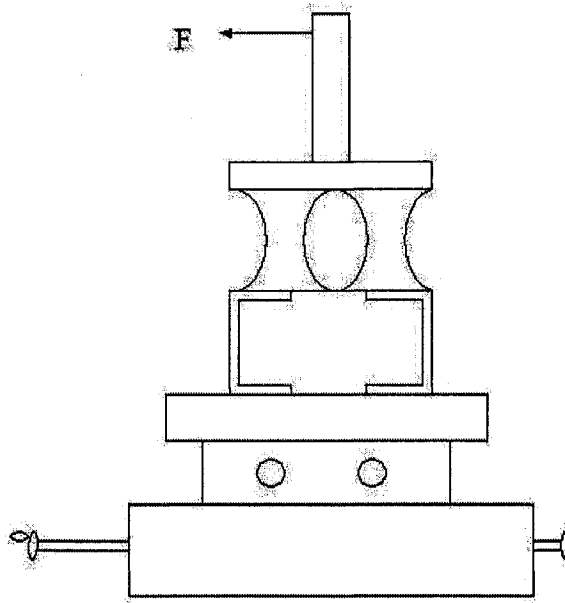
Figure D.5: Loading direction of fourth test (270 degrees)

From these preliminary tests (Figure D.6 and Figure D.7), it was observed that very little differences occurred if the load was applied at the top or the bottom of the aluminum cylinder. Additionally, slight off axis loading was noticed between the top and bottom load platforms.

The top and bottom outputs represent the voltage being read by the top and bottom load platforms. Figure D.6 represents the load voltage relationship when the load was applied to the top load platform at the top of the aluminum cylinder.

163
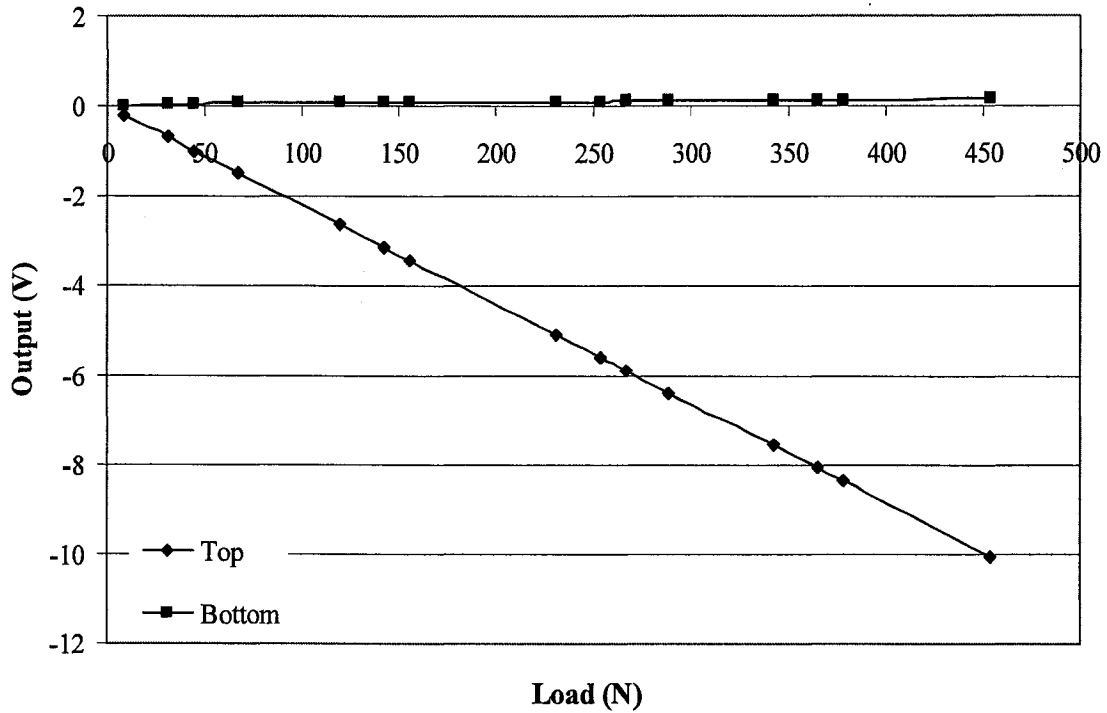
Figure D.6: Voltage output when load applied to top platform at the top of the aluminium cylinder (Position 1: 0 degrees). Note lines are used for visual purposes only.

For these tests, the top load platform is showing a linear relationship between load and output while the bottom load platform seems to be reading slight off axis loading along the 0 V line. Figure D.7 represents the load voltage relationship when the load was applied to the bottom load platform at the top of the aluminum cylinder.

164
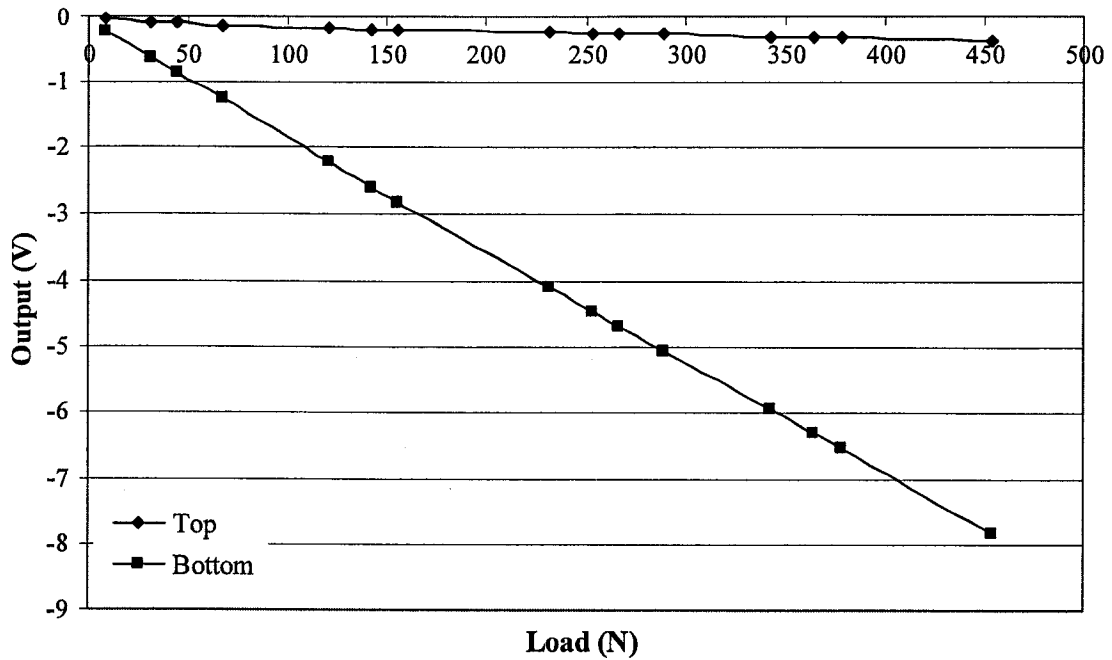
Figure D.7: Voltage output when load applied to bottom platform at the top of the aluminium cylinder (Position 2: 90 degrees). Note lines are used for visual purposes only.

The bottom load platform is providing a linear relationship between the load and output while the top load platform is reading slight off axis loading. With this test, the off axis loading is a little more evident than in the first position.

To understand how MABTA responds to a purely axial test, it was placed into the Instron machine (Model TTK, Norwood, MA, USA) located in the Mechanical Engineering machine shop. MABTA was loaded in 444.8 N (100 lb) increments until 4448 N (1000 lb) compression (Figure D.8). From this test, it was noticed that the top and bottom outputs are not reading consistently throughout loading and unloading.

165
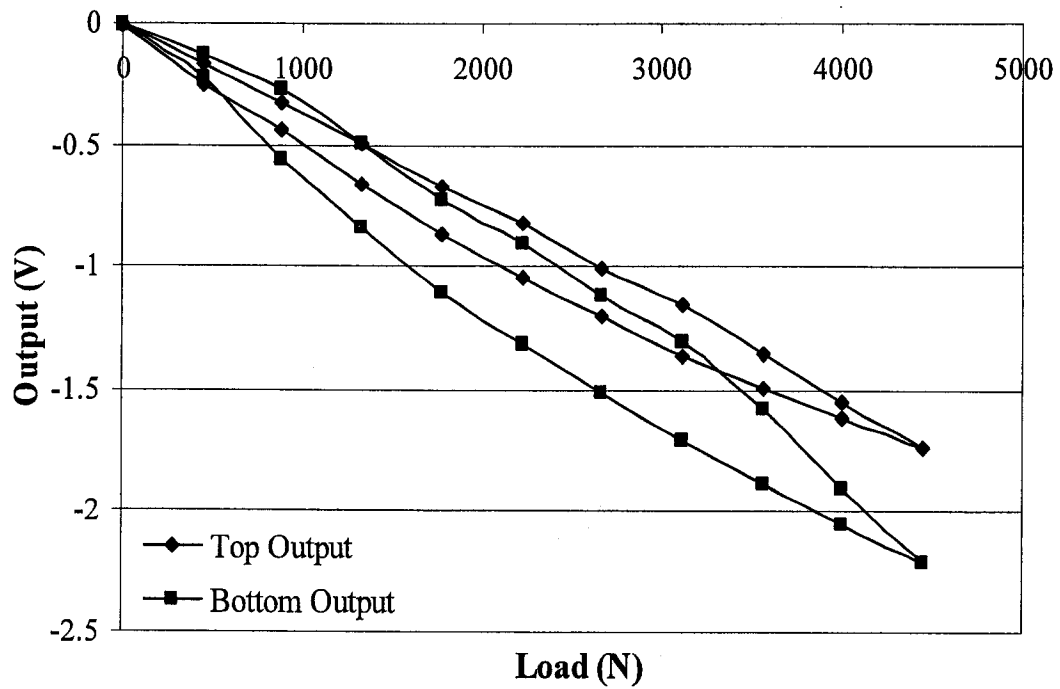
Figure D.8: Axial load placed on MABTA. Note lines are used for visual purposes only.

The above tests were repeated to ensure that the results are accurate and were not influenced by controllable, outside factors and all results were consistent. Also the off axis loading was measured when the load was applied at 0°, 90°, 180° and 270°.
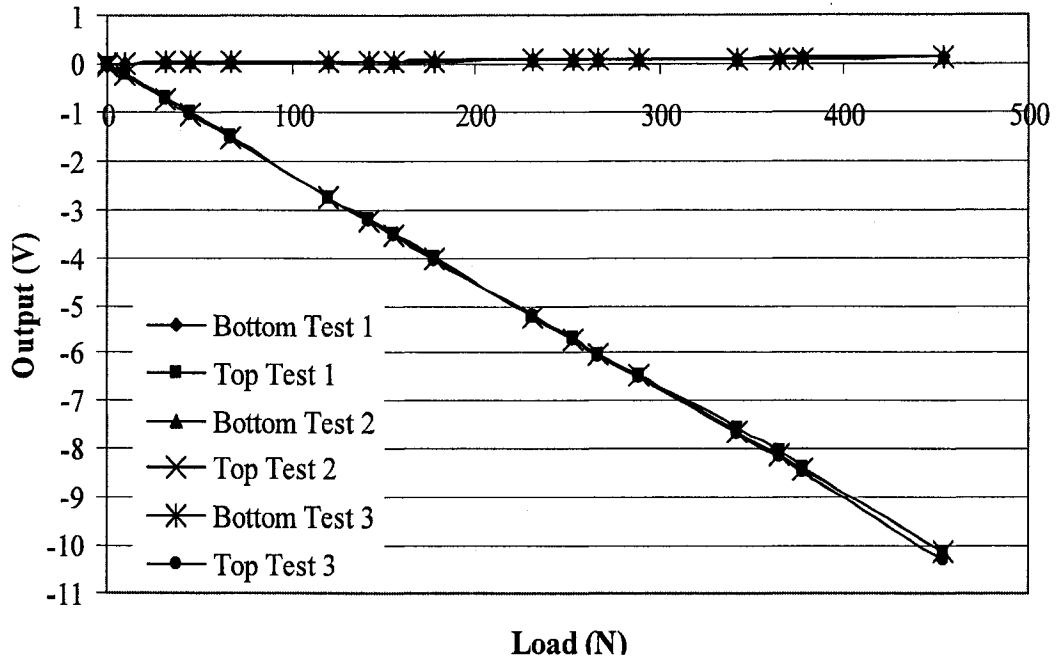
Figure D.9: Voltage output when load applied to top platform at the top of the Al cylinder (0°). Note lines are used for visual purposes only.
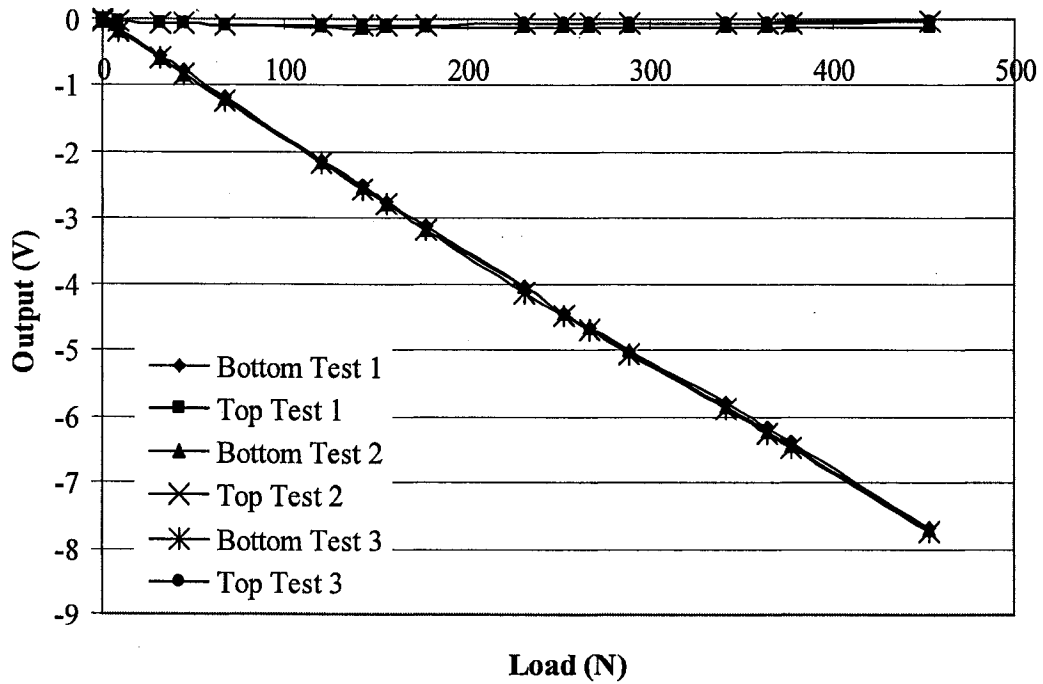
Figure D.10: Voltage output when load applied to bottom platform at the top of the aluminium cylinder (90°). Note lines are used for visual purposes only.

167
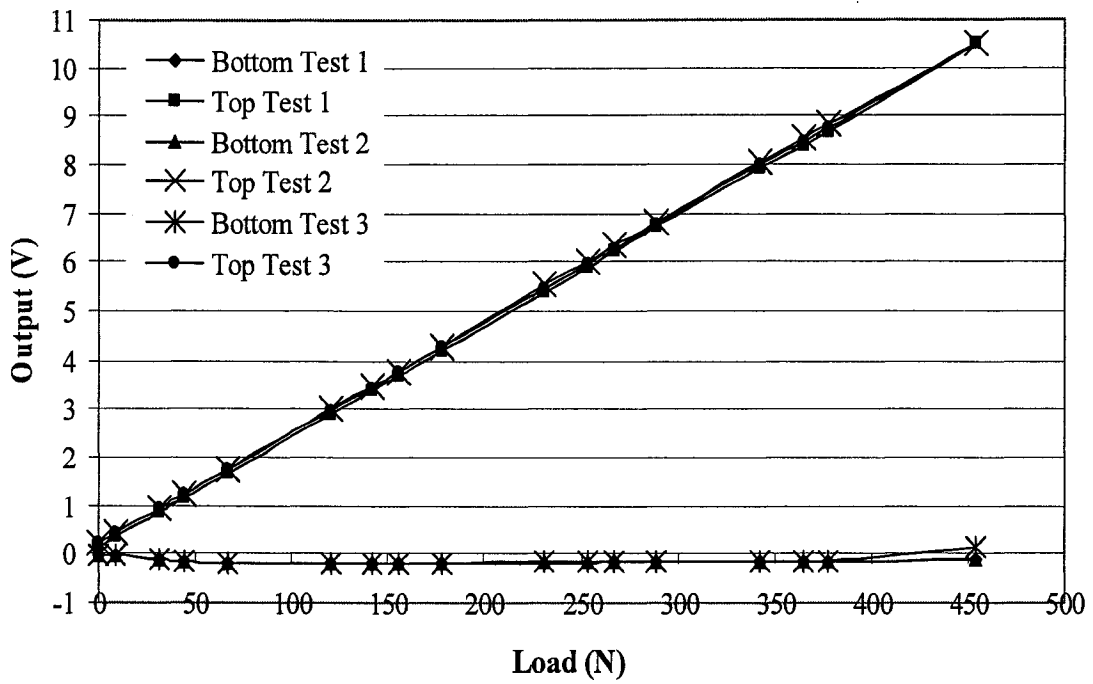
Figure D.11: Voltage output when load applied to top platform at the top of the Al cylinder (180°). Note lines are used for visual purposes only.
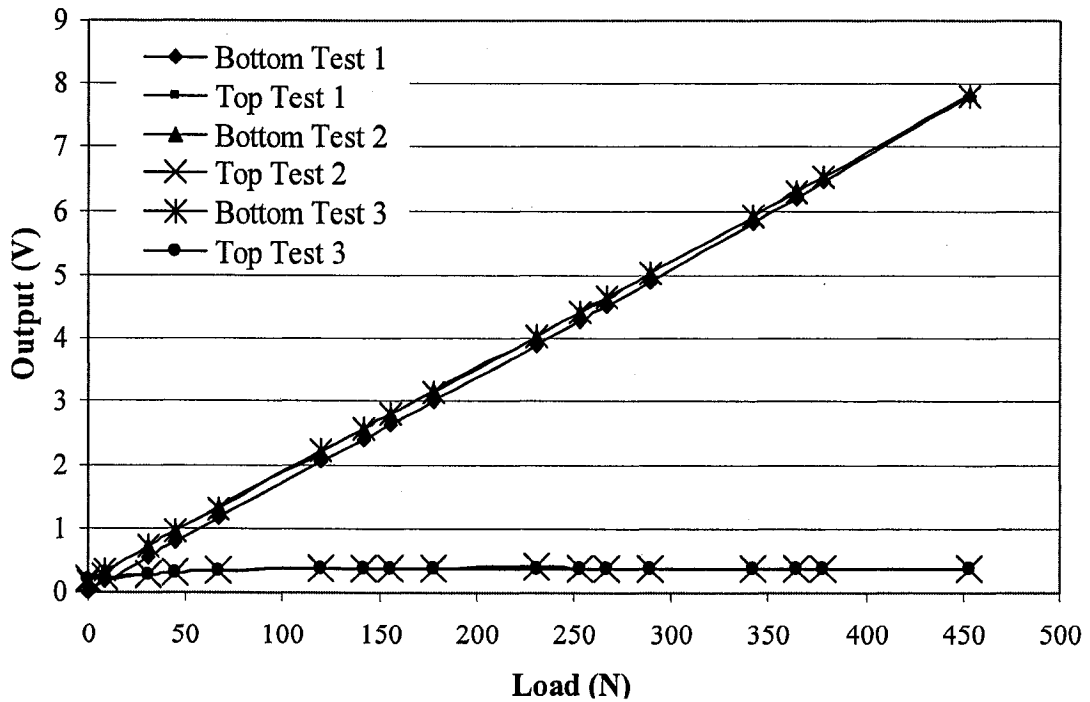
Figure D.12: Voltage output when load applied to bottom platform at the top of the aluminium cylinder (270°). Note lines are used for visual purposes only.

168

Figure D.9 through Figure D.12 illustrate good loading repeatability and consistency for all positions and as observed in the previous tests, the cross talk is minimal. However, when comparing the fourth loading position (270°) to the other loading positions, more cross talk was observed which could have been caused through slight misalignment in the application of the loads when changing loading directions.
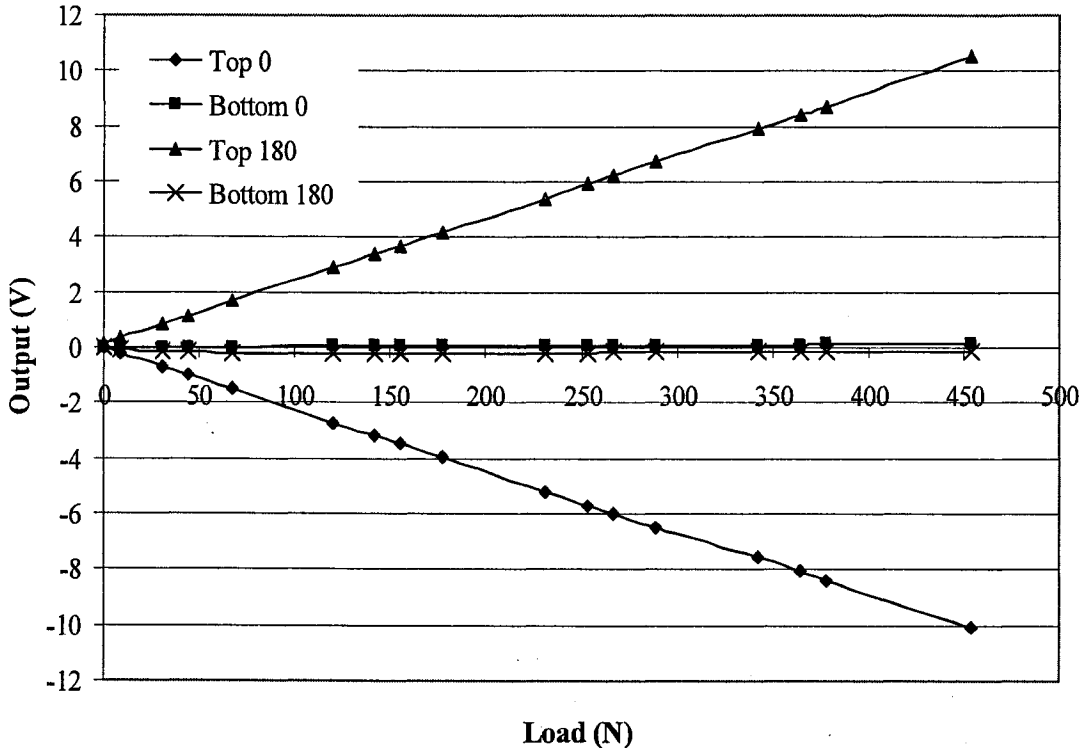
Figure D.13: Load positions 0 and 180 degrees with load applied to top platform. Note lines are used for visual purposes only.

Figure D.13 combines the results for the 0° and 180° loading positions. Both directions provide a linear relationship between load and output voltage. Even though both directions have an output magnitude just above 10V, the 180° testing position has a slightly higher value than the 0° testing position.

169
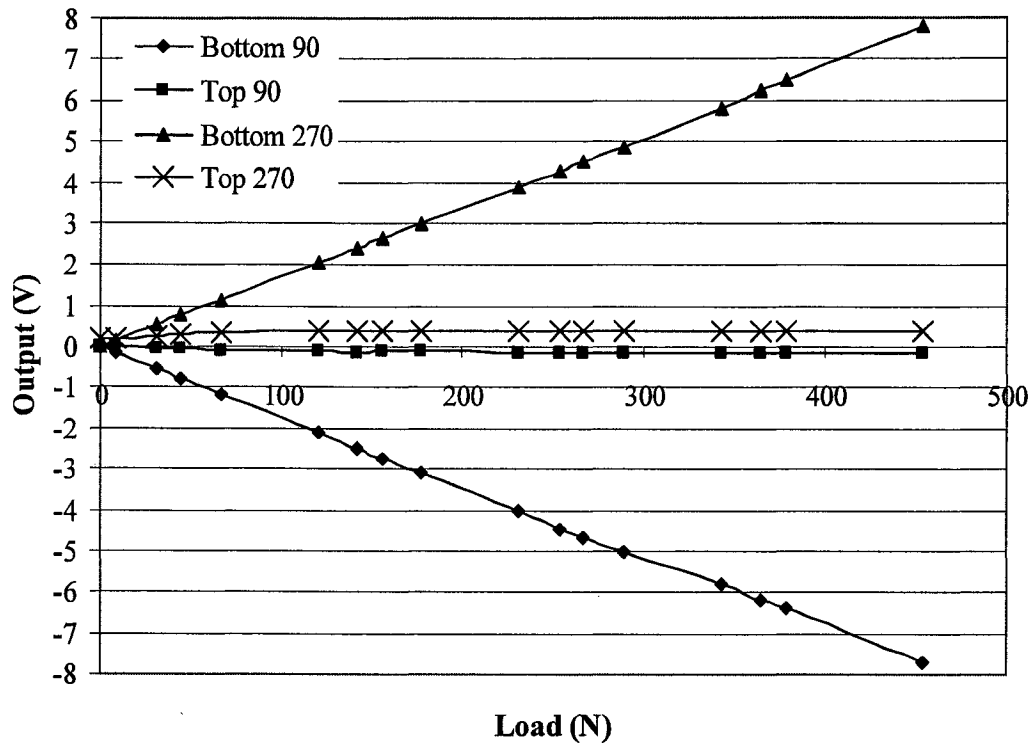
Figure D.14: Load positions 90 and 270 degrees with load applied to bottom platform. Note lines are used for visual purposes only.

Figure D.14 combines the results for the 90° and 270° loading positions. Both directions provide a linear relationship between load and output voltage and have output magnitudes slightly lower than 8V.

Transverse loading of the custom-made load cell is repeatable and consistent between tests. Additionally similar results were obtained between opposite directions (i.e. 0° and 180° and 90° and 270°). However axial loading on the load platform created unexpected and conflicting results.

D.2 Calibration of Modified Load Platform

Since the top and bottom platforms provided conflicting output when applied with axial load, the load platform design was modified. A cantilever beam (44.50 mm tall,

170

12.73 mm wide and 0.83 mm thick) instrumented with four strain gauges was installed in the centre of the load platform (Figure D.15). Theoretically, the strain gauges on the cantilever beam only measure shear loads applied to MABTA and ignore axial loads. This design was used to calibrate the axial and transverse load platform (Figure D.16 through Figure D.20) using the same procedure utilized to calibrate the original load platform.
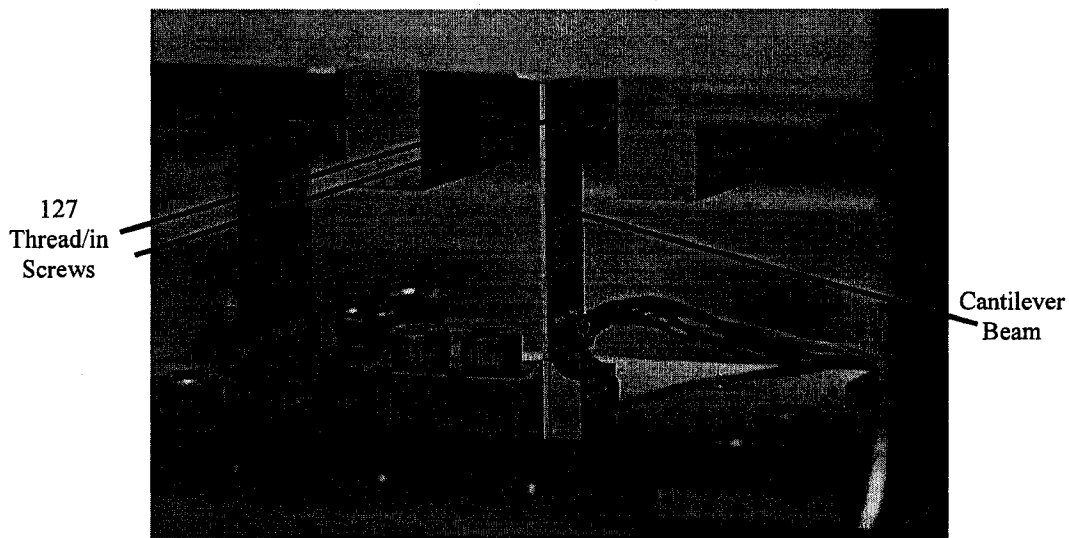
Figure D.15: Cantilever Beam added to custom-made load cell

Figure D.16 through Figure D.20 provide the calibration curves used in the data acquisition program. Figure D.16 presents the calibration curve and its associated calibration equation for the axial load cell. Since each direction of the load cell had a slightly different calibration curve, an average of the slope from the equations for the 0° (Figure D.17) and 180° (Figure D.19) directions and the 90° (Figure D.18) and 270° (Figure D.20) directions were taken and used in the data acquisition program. Equations (1) and (2) are the calibration equations used in the data acquisition program for the 0°-180° direction and 90°-270° direction, respectively, where x is the measured voltage and y is the corresponding load in pounds (lb).

171

$$y = 1.91185x10^{-5}x \tag{1}$$

$$y = 1.85149x10^{-5}x \tag{2}$$

Additionally before any confidence could be placed on the DAQ strain measurements, hand calculations were done to find the strain based on voltage readings. As seen in Figure D.17 through Figure D.20, the theoretical strain values (noted V-S) agreed well with the measured strain results (noted LVTC and LVBC).

Load (lb)
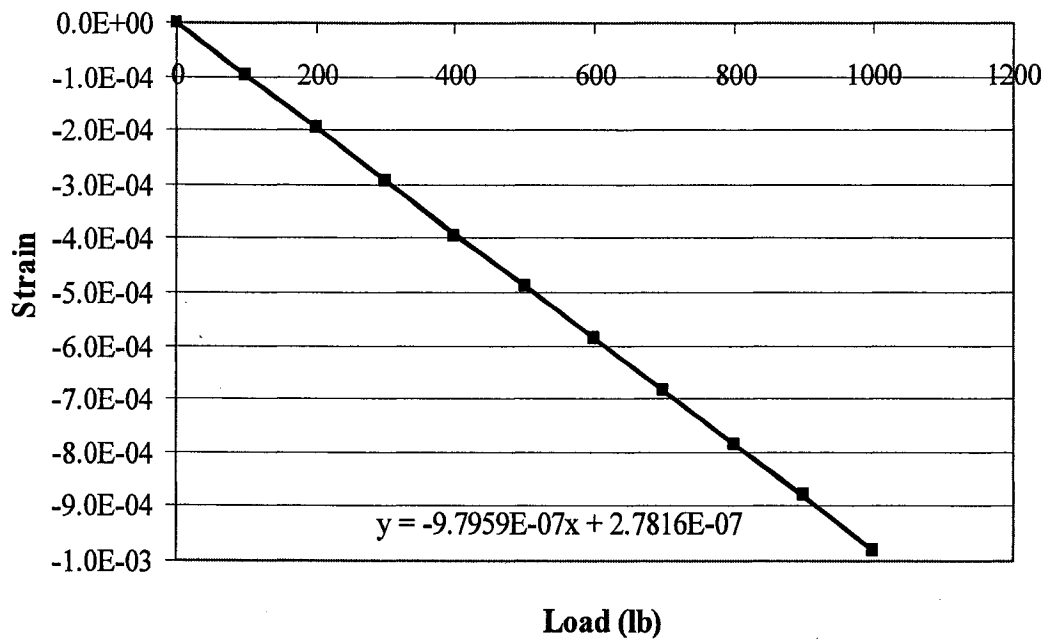
Figure D.16: Axial Load Cell Calibration Curve. Note lines are used for visual purposes only.

172
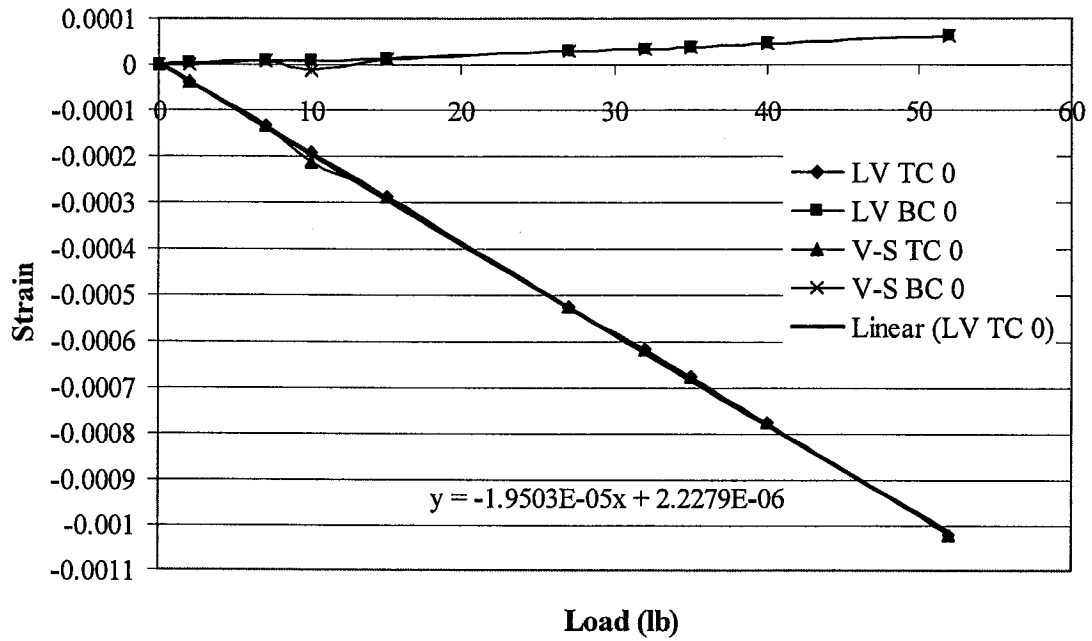
Figure D.17: Top platform calibration curve (0 degrees) where LVTC 0 and LVBC 0 are the LabVIEW measured strain results for the top and bottom cantilever beams and V-S TC 0 and V-S BC 0 are the calculated strain results for the 0 degree position. Note lines are used for visual purposes only.
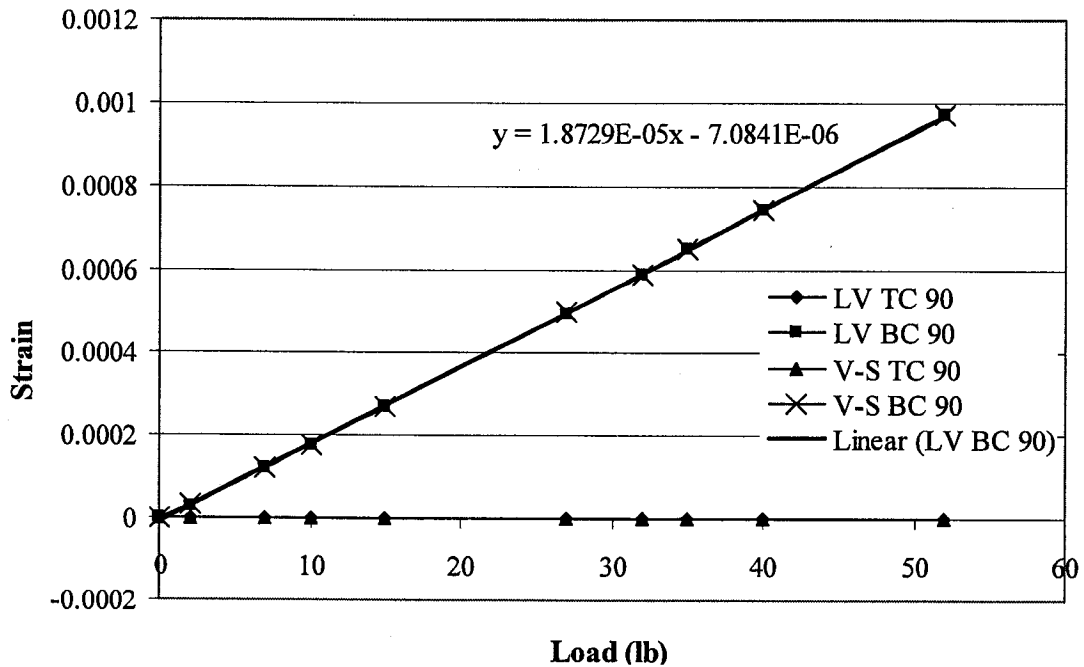
Figure D.18: Bottom calibration curve (90 degrees) where LVTC 90 and LVBC 90 are the LabVIEW measured strain results for the top and bottom cantilever beams and V-S TC 90 and V-S BC 90 are the calculated strain results for the 90 degree position. Note lines are used for visual purposes only.

173
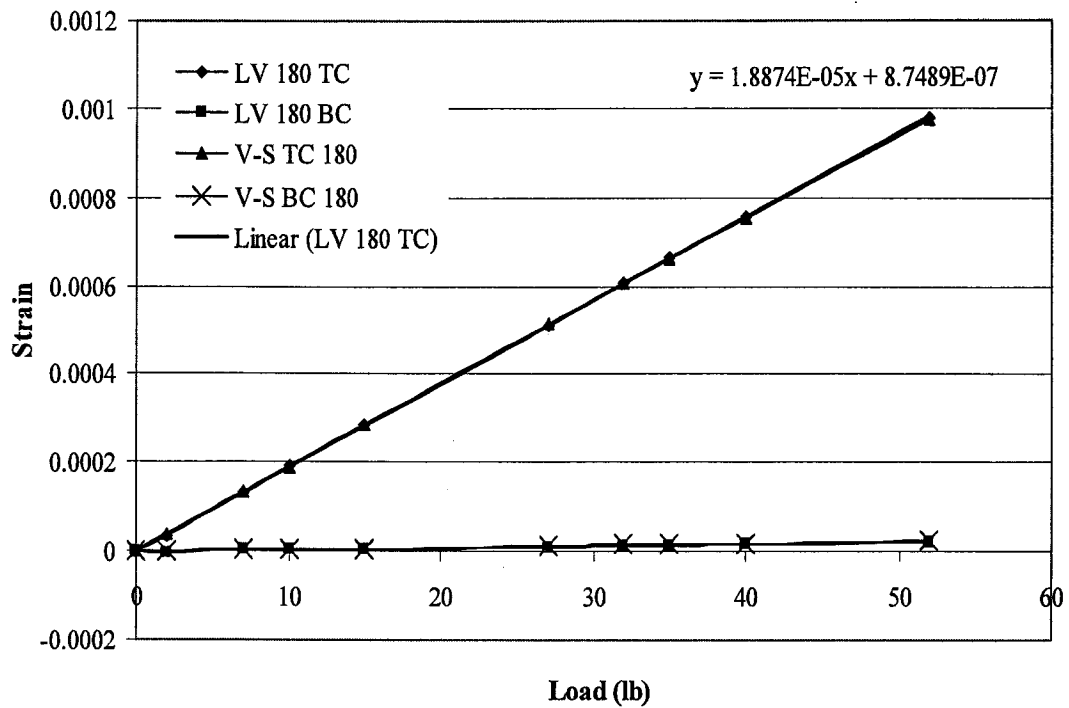
Figure D.19: Top platform calibration curve (180 degrees) where LVTC 180 and LVBC 180 are the LabVIEW measured strain results for the top and bottom cantilever beams and V-S TC 180 and V-S BC 180 are the calculated strain results for the 180 degree position. Note lines are used for visual purposes only.
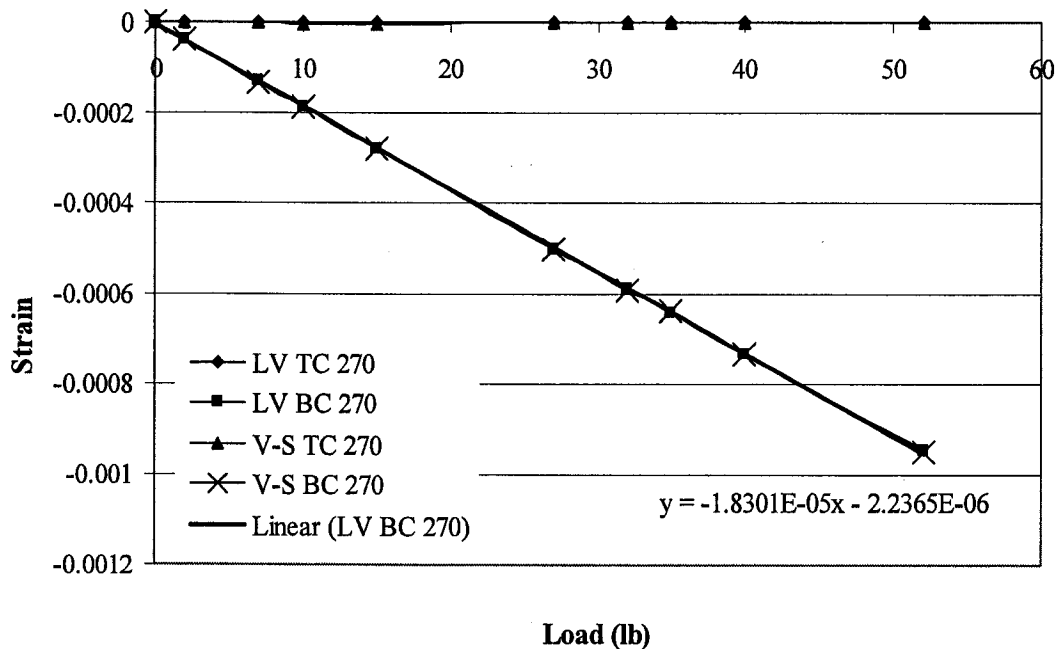
Figure D.20: Bottom calibration curve (270 degrees) where LVTC 270 and LVBC 270 are the LabVIEW measured strain results for the top and bottom cantilever beams and V-S TC 90 and V-S BC 270 are the calculated strain results for the 270 degree position. Note lines are used for visual purposes only.

174

D.3 Combined Transverse and Axial Loads

One of the many functions of MABTA is the ability to apply both axial and transverse loads to a specimen. This function was investigated with a PVC pipe and the below procedure was followed to place the specimen into MABTA:

- Backed screws off of cantilever beams

- Carefully aligned top and bottom bone pots

- Placed PVC specimen into Delrin® collars and inserted into MABTA

- Carefully tightened screws around cantilever beams so as not to place any bias on load measurements

D.3.1 Axial Load Followed by Transverse Load

Five tests were completed on each top and bottom cantilever beam with a total of ten tests. Axial loads of 0, 111.2 N (25 lb), 222.4 N (50 lb), 333.6 N (75 lb) and 444.8 N (100 lbs) were initially applied; once axial load was reached a transverse load of 44.5 N (10lb) was applied in 8.9 N (2lb) increments.

Tests 1 through 5 (Figure D.21 to Figure D.25) represent the data acquired from adjusting the hand crank that controlled the top cantilever beam to a maximum load of 44.5 N (10 lbs) once an initial axial load was applied.

175
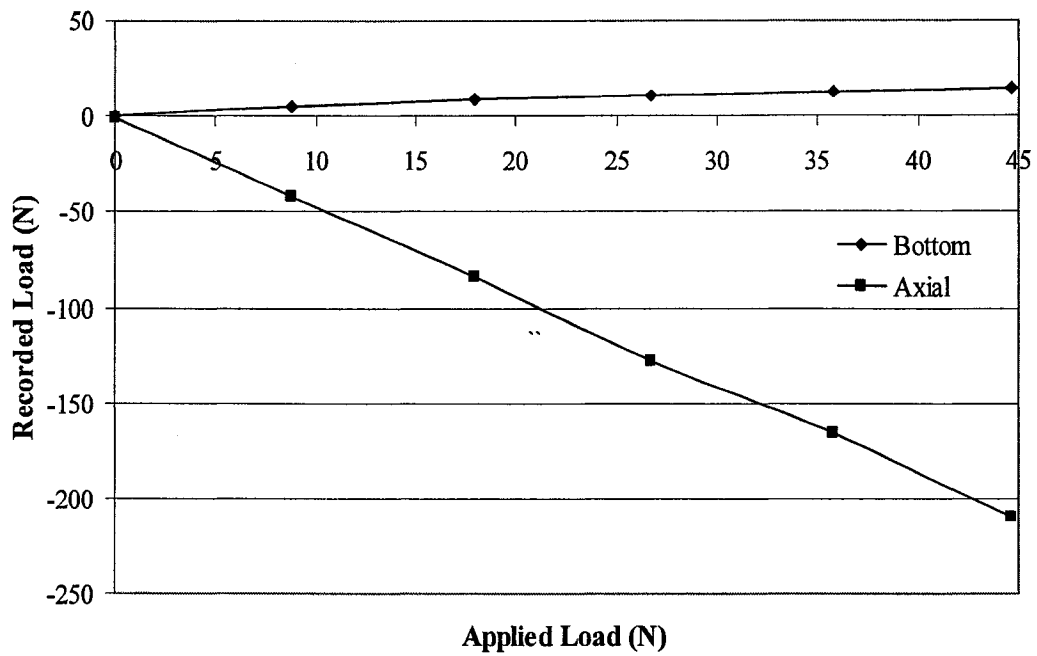
Figure D.21: Transverse weights applied to top platform Test 1, initial axial load of 0 N where bottom and axial indicate the load measured on the bottom cantilever beam and axial load cell. Note lines are used for visual purposes only.
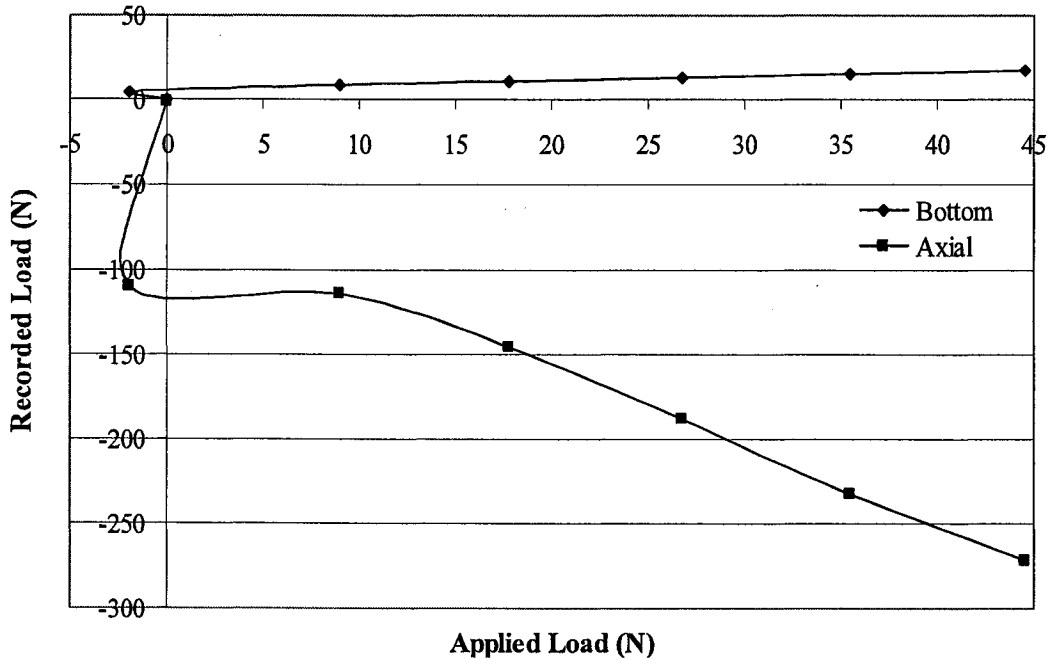
Figure D.22: Transverse weights applied to top platform Test 2, initial axial load of 111.2 N (25 lb) where bottom and axial indicate the load measured on the bottom cantilever beam and axial load cell. Note lines are used for visual purposes only.

176
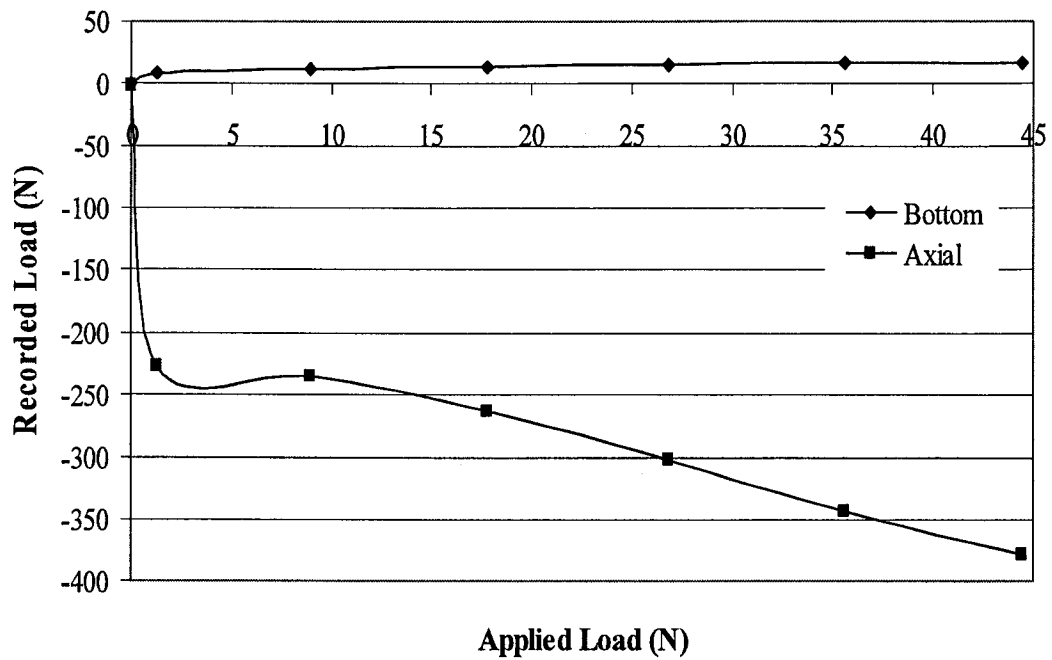
Figure D.23: Transverse weights applied to top platform Test 3, initial axial load of 222.4 N (50 lb) where bottom and axial indicate the load measured on the bottom cantilever beam and axial load cell. Note lines are used for visual purposes only.
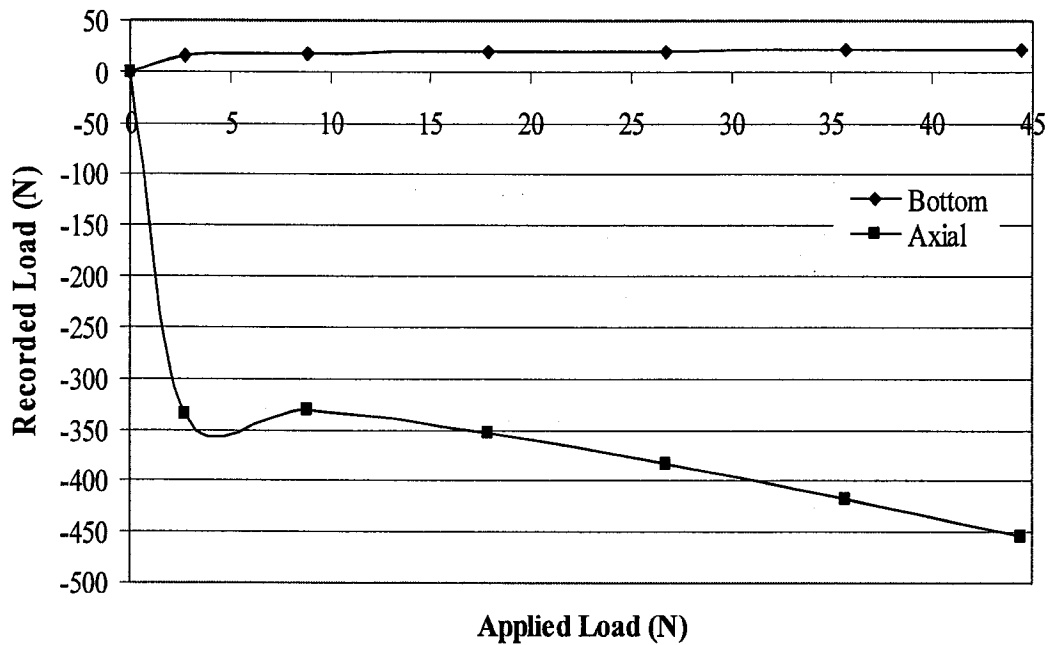
Figure D.24: Transverse weights applied to top platform Test 4, initial axial load of 333.6 N (75 lb) where bottom and axial indicate the load measured on the bottom cantilever beam and axial load cell. Note lines are used for visual purposes only.

177
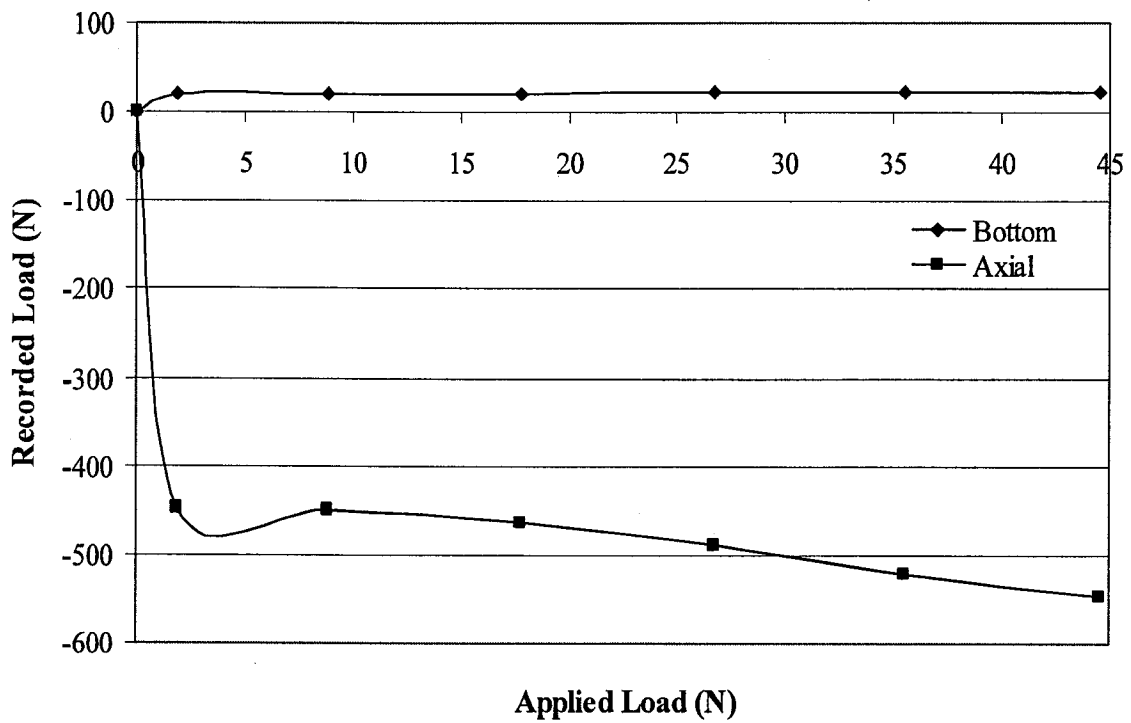
Figure D.25: Transverse weights applied to top platform Test 5, initial axial load of 444.8 N (100 lb) where bottom and axial indicate the load measured on the bottom cantilever beam and axial load cell. Note lines are used for visual purposes only.

Tests 6 through 10 (Figure D.26 to Figure D.30) represent the data acquired from adjusting the hand crank that controlled the bottom cantilever beam to a maximum load of 44.5 N (10 lb) once an initial axial load was applied.
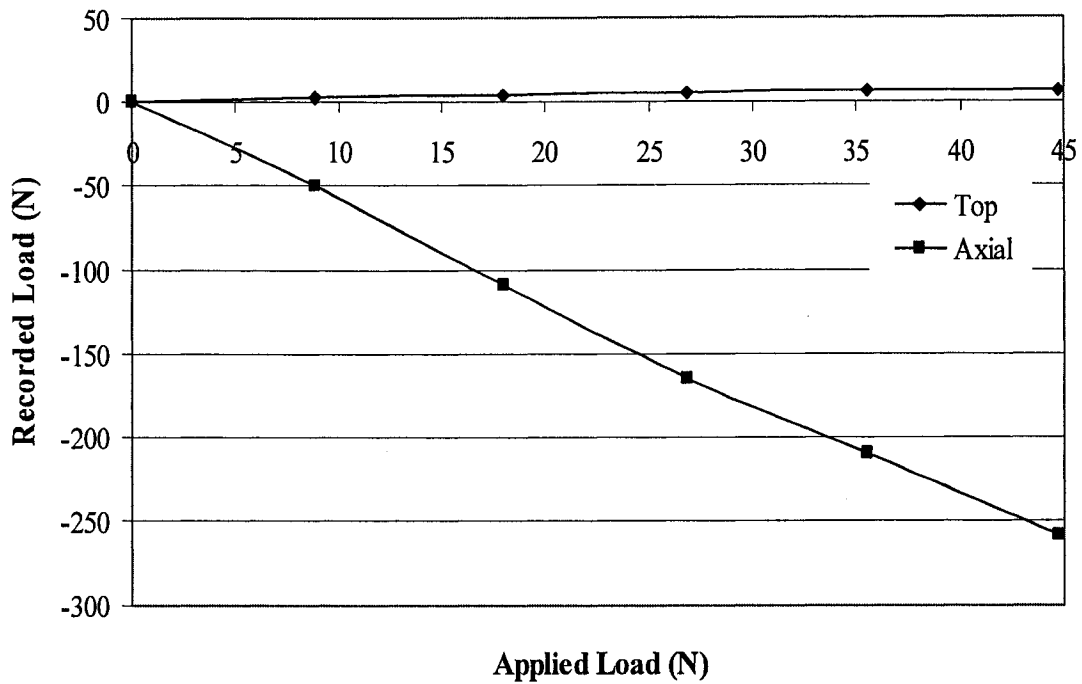
Figure D.26: Transverse weights applied to bottom platform Test 6, initial axial load of 0 N where top and axial indicate the load measured on the top cantilever beam and axial load cell. Note lines are used for visual purposes only.
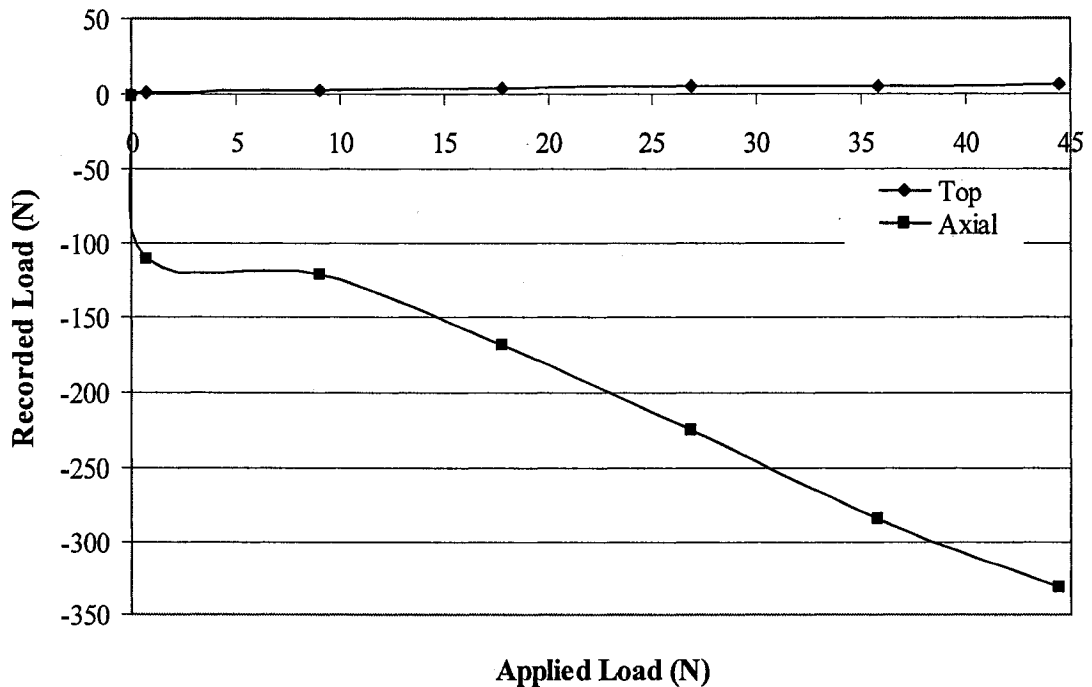
Figure D.27: Transverse weights applied to bottom platform Test 7, initial axial load of 111.2 N (25 lb) where top and axial indicate the load measured on the top cantilever beam and axial load cell. Note lines are used for visual purposes only.

179
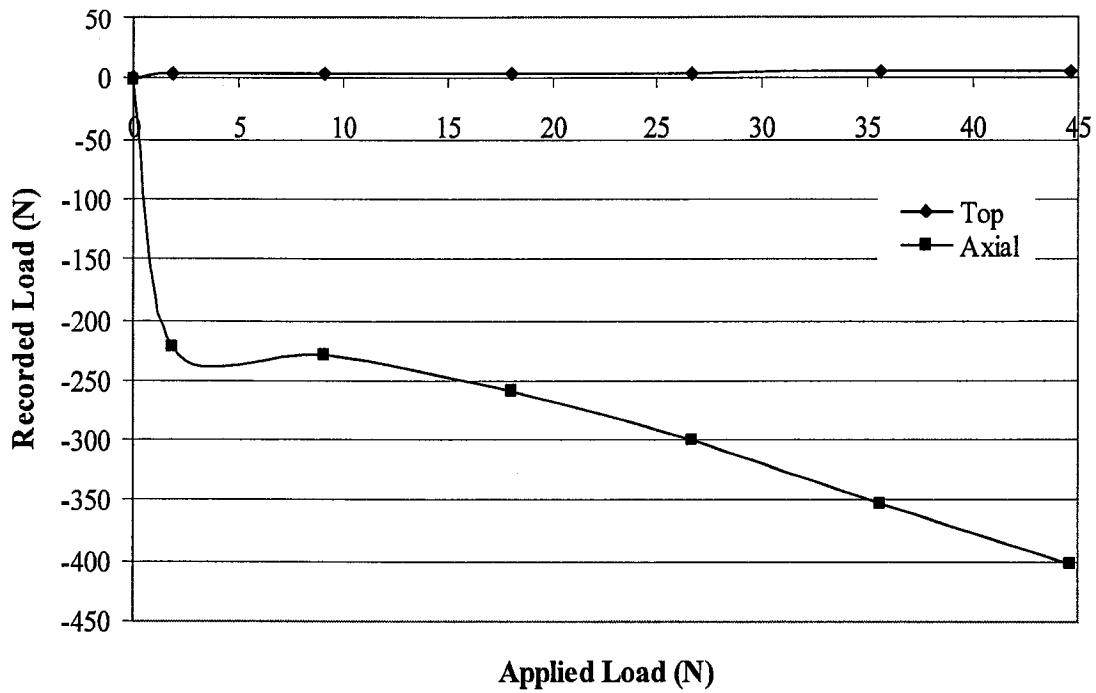
Figure D.28: Transverse weights applied to bottom platform Test 8, initial axial load of 222.4 N (50 lb) where top and axial indicate the load measured on the top cantilever beam and axial load cell. Note lines are used for visual purposes only.
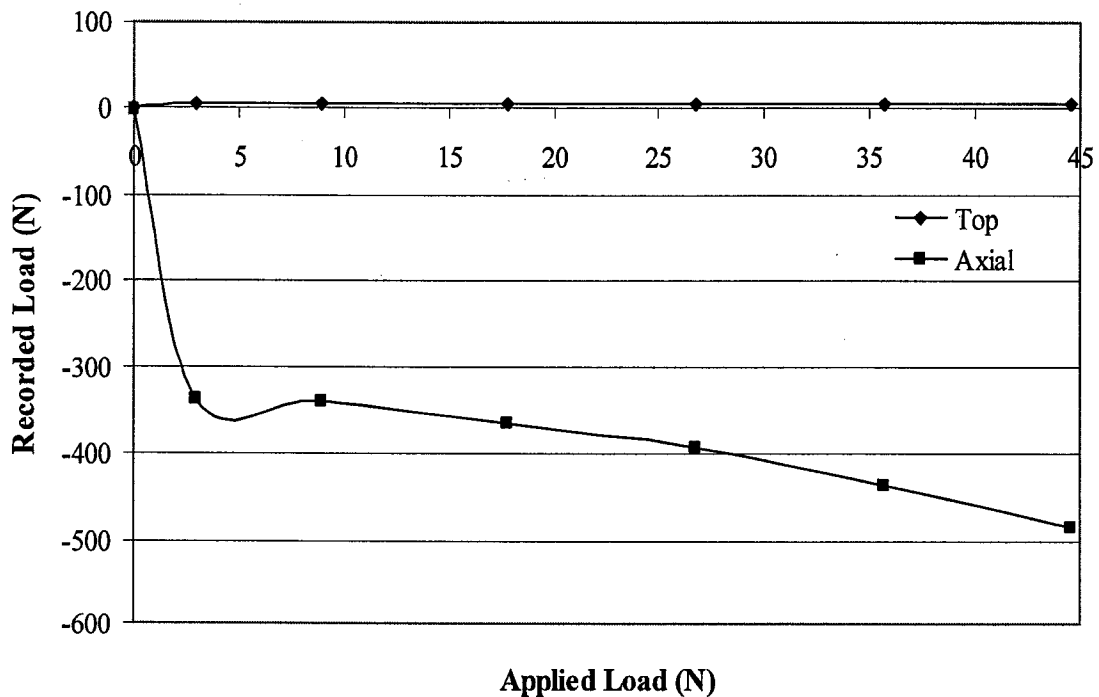
Figure D.29: Transverse weights applied to bottom platform Test 9, initial axial load of 333.6 N (75 lb) where top and axial indicate the load measured on the top cantilever beam and axial load cell. Note lines are used for visual purposes only.

180
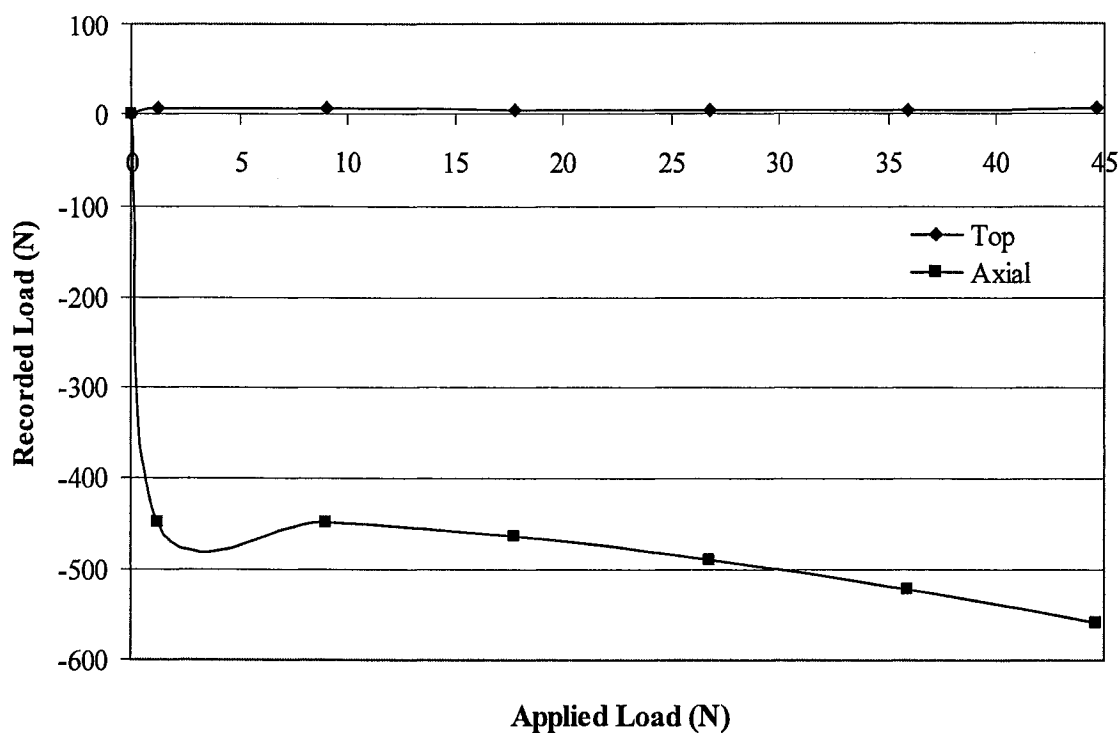
Figure D.30: Transverse weights applied to bottom platform Test 10, initial axial load of 444.8 N (100 lb) where top and axial indicate the load measured on the top cantilever beam and axial load cell. Note lines are used for visual purposes only.

In each of the above tests it was found that as the transverse load increased the axial load increased.

D.3.2 Transverse Load Followed by Axial Load

The same tests were repeated to investigate if the axial load increased because of the order of load application. The procedure to place the PVC specimen in MABTA listed in the previous section was used. Four tests were completed on the PVC specimen, two in the direction of the top cantilever beam and two in the direction of the bottom cantilever beam. A maximum transverse load of 44.5 N (10 lb) was applied in 8.9 N (2 lb) increments. Once the maximum transverse load was achieved the PVC specimen was loaded axially.

181
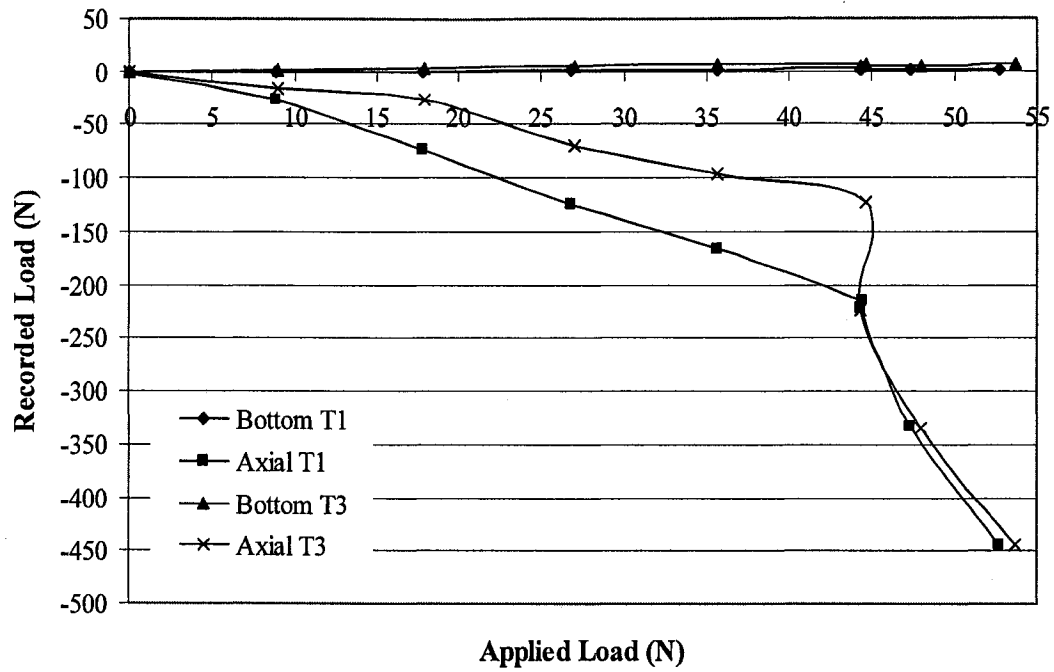
Figure D.31: Transverse weights applied to top platform followed by application of axial load where Bottom T1 and Axial T1 indicate the load measured on the bottom cantilever beam and axial load cell for test one and Bottom T3 and Axial T3 indicate the load measured on the bottom cantilever beam and axial load cell for test three. Note lines are used for visual purposes only.
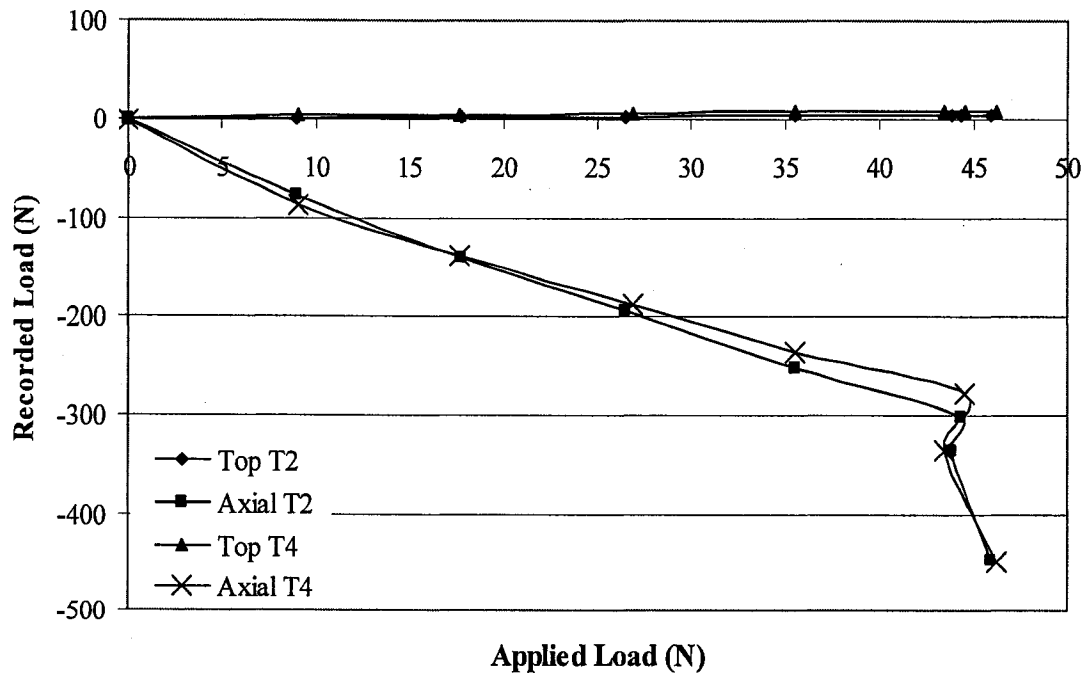
Figure D.32: Transverse weights applied to bottom platform followed by application of axial load where Top T2 and Axial T2 indicate the load measured on the top cantilever beam and axial load cell for test two and Top T4 and Axial T4 indicate the load measured on the top cantilever beam and axial load cell for test four. Note lines are used for visual purposes only.

182

Again it was observed that as the transverse load was applied, the axial load increased. However, the order of load application did not affect the final loading results as much as the previous loading order. For example in Figure D.31, the application of 44.5 N (10 lb) transverse load caused an axial load of approximately 125 N (Test 3) and approximately 225 N (Test 1). After the application of axial loads to a compressive load of 444.8 N, the transverse load only increased to 47 N.

D.3.3 Axial Load Cell Response to Transverse Load Application

Since the axial load cell was strictly designed to handle only axial loads, it is thought that the recording of axial load could be caused from the axial load cell itself. To determine how the load cell reacts to transverse loads, weights were placed transversely in both directions at two distances. First the cable was at a distance near the top of the load cell (Figure D.33) and second at a distance above the load cell (Figure D.34).
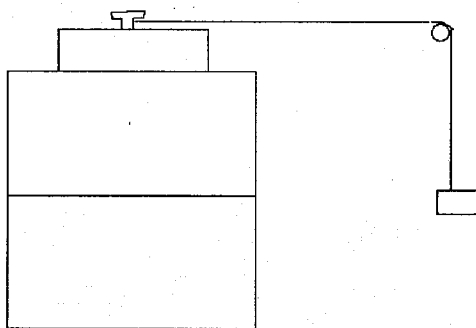
Figure D.33: Application of weights to cause no moment
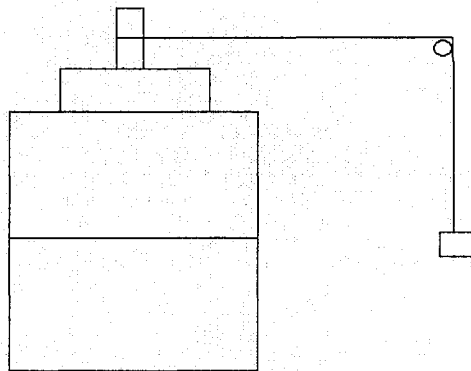
Figure D.34: Application of weights to cause moment

Applied Load (N)
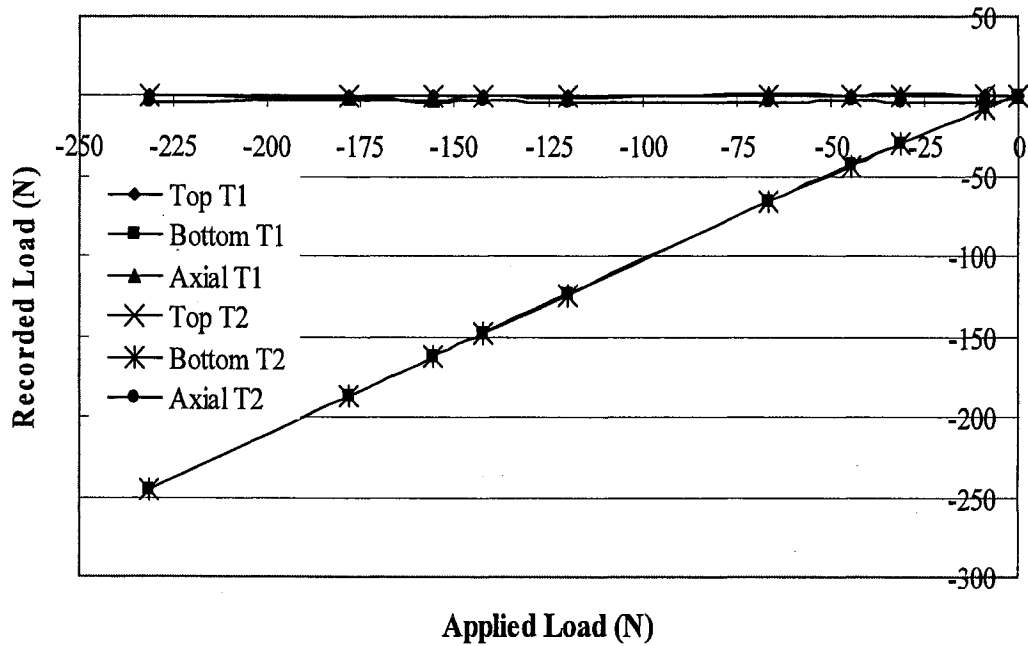
Figure D.35: Top transverse and axial load as a function of applied transverse loads to bottom platform with no moment where Top T1, Bottom T1, Axial T1, Top T2, Bottom T2, and Axial T2 represent the measured top cantilever beam load, the bottom cantilever beam load and the axial load for tests one and two. Note lines are used for visual purposes only.

184
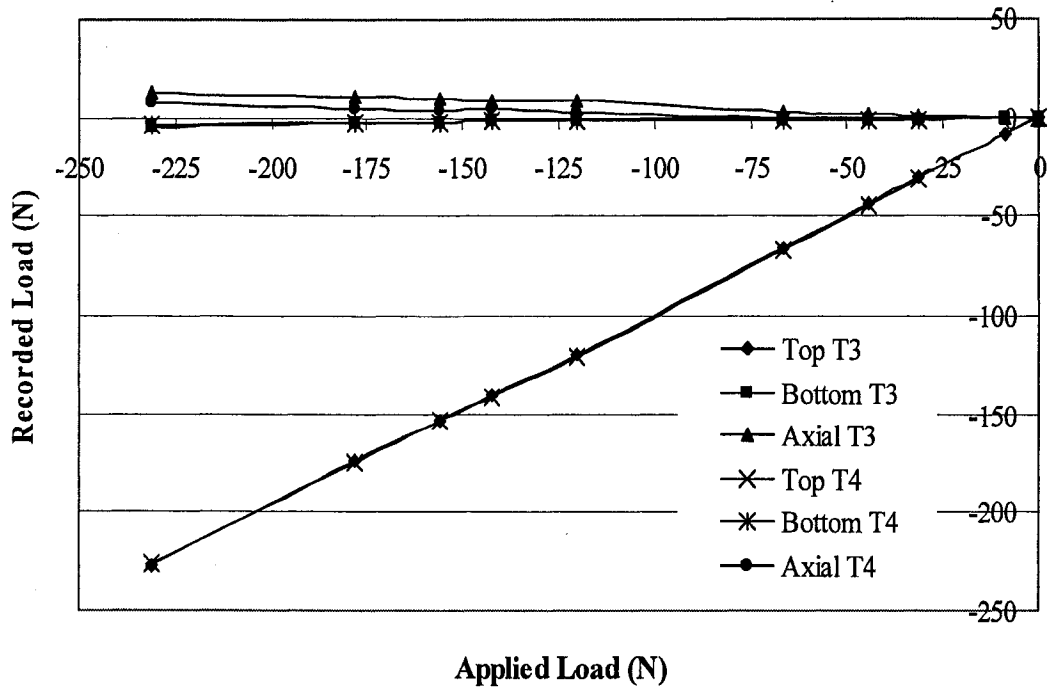
Figure D.36: Bottom transverse and axial load as a function of applied transverse loads to top platform with no moment where Top where Top T3, Bottom T3, Axial T3, Top T4, Bottom T4, and Axial T4 represent the measured top cantilever beam load, the bottom cantilever beam load and the axial load for tests three and four. Note lines are used for visual purposes only.

Figure D.35 and Figure D.36 show that if the transverse load is applied near the load cell, axial load is not significantly affected. It is believed that the 8.9 N (2 lb) of axial load recorded in the top beam direction (Figure D.36) was due to misalignment of the wire; this was adjusted for test 4 and the load was decreased.

185
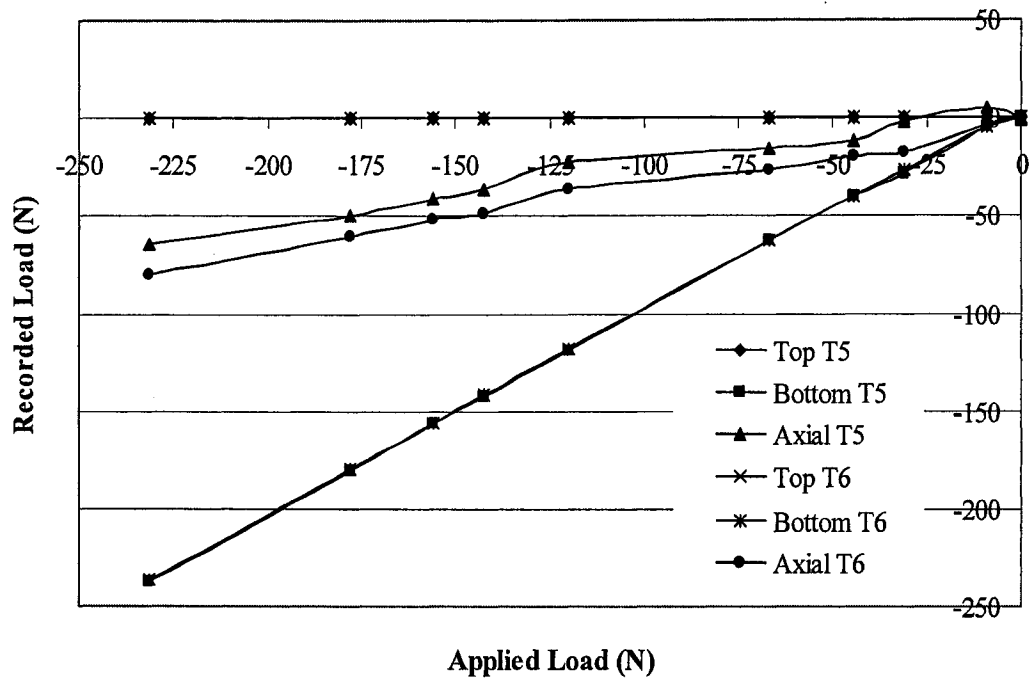
Figure D.37: Top transverse and axial load as a function of applied transverse loads to bottom platform with moment where Top T5, Bottom T5, Axial T5, Top T5, Bottom T5, and Axial T5 represent the measured top cantilever beam load, the bottom cantilever beam load and the axial load for tests five and six. Note lines are used for visual purposes only.
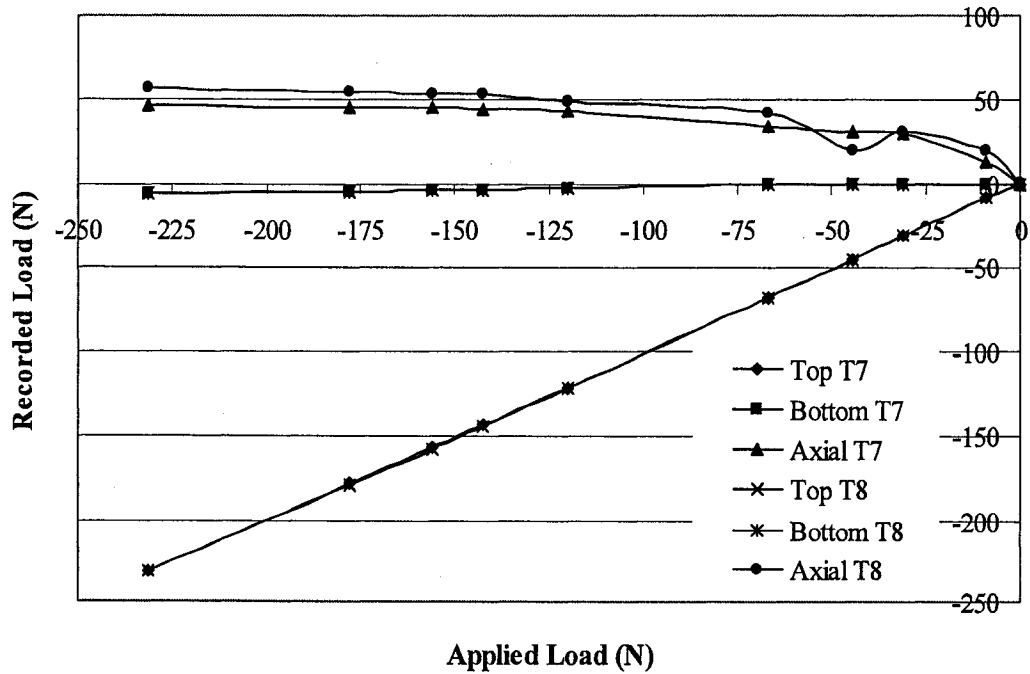
Figure D.38: Bottom transverse and axial load as a function of applied transverse loads to top platform with moment where Top T7, Bottom T7, Axial T7, Top T8, Bottom T8, and Axial T8 represent the measured top cantilever beam load, the bottom cantilever beam load and the axial load for tests seven and eight. Note lines are used for visual purposes only.

186

Figure D.37 and Figure D.38 indicate that the axial load cell records axial load when transverse loads are applied at a distance above the load cell. This signifies that the axial load cell is affected by moments and could give inaccurate readings for tests when both transverse and axial loads are applied. From the above test results, it was decided that the custom-made load platform could no longer be used to obtain reasonable and accurate results.

D.4 Six Degree of Freedom Load Cell Calibration

A six-degree of freedom (DOF) load cell from AMTI (MC6-6-2000, Figure D.39) was installed into MABTA and replaced the custom-made load cell. Axial and transverse tests were completed to verify the calibration of the load cell.
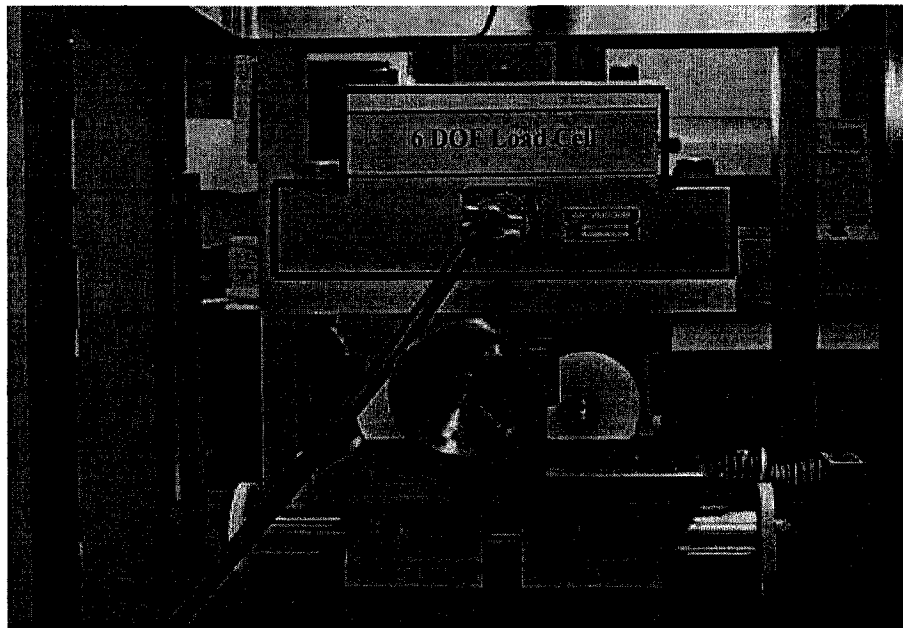
Figure D.39: AMTI 6 DOF Load Cell

187

D.4.1 Axial Calibration

Standard weights were placed on top of the 6 DOF load cell to check axial calibration. Figure D.40 presents the applied load and measured load relationship. From this graph it can be seen that there is good consistency between the value of the standard applied weight and the measured value. However, slight variations occurred, several recorded loads read 4.4 N higher than the actual applied load which could have been caused by slight misalignment of the weights and/or from their irregular shapes.
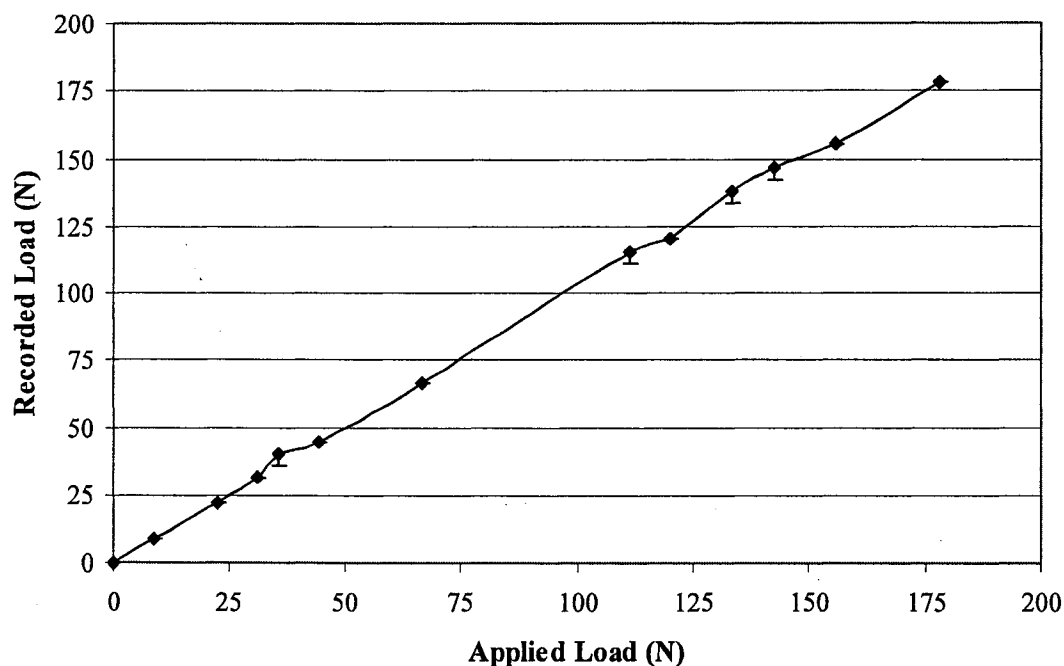
Figure D.40: Axial Calibration Check. Note lines are used for visual purposes only.

D.4.2 Transverse Calibration

To check the calibration of the x and y directions of the 6 DOF load cell, standard weights were placed on a custom made calibration jig (Figure D.41). Since the 6 DOF load cell is much wider than the custom-made load platform, transverse loads could not be applied directly above the top of the load cell. Instead the PVC specimen was placed

188

into the bone pot and actuator moved until the specimen almost touched the femur bone

pot holder to achieve the smallest moment arm distance (~7.5cm) as possible (Figure

D.42, Figure D.43).
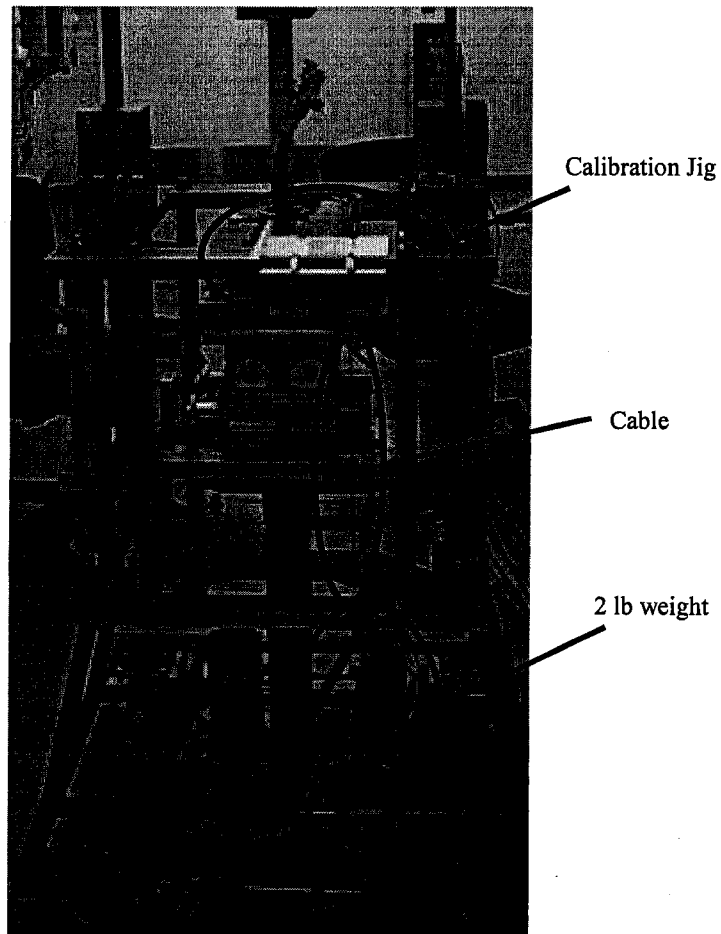
Figure D.41: Components of transverse calibration tests

189
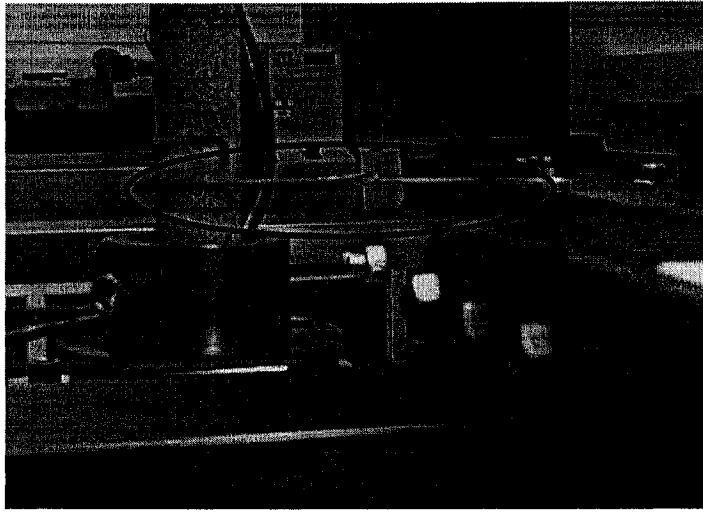
Figure D.42: Position of cable for transverse calibration tests (*x*-direction)
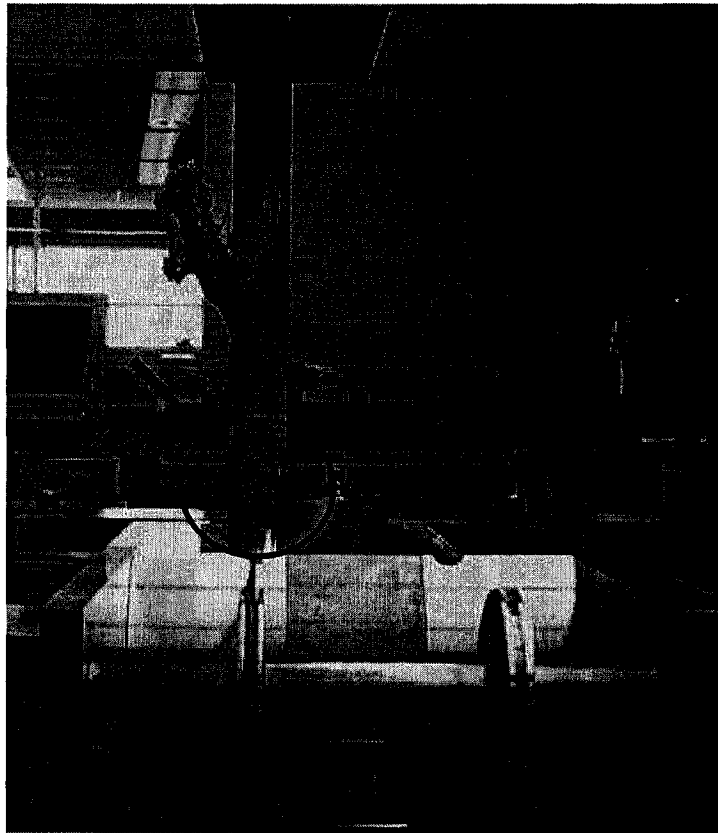
Figure D.43: Position of cable for transverse calibration tests (*y*-direction)

190

Transverse loads of 0 N, 8.9 N (2 lb), 31 N (7 lb), 44.5 N (10 lb), 66.7 N (15 lb), 120 N (27 lb), 142.3 N (32 lb), 155.7 N (35 lb), 177.9 N (40 lb) and 231.3 N (52 lb) were applied and measured on all four sides of the load cell. Two tests were completed per side. Figure D.44 through Figure D.47 represent the relationship between transverse loads being applied either in the x or y direction and the reaction of the remaining axes.

The first and second tests were completed in the negative x direction (Figure D.44). For the first test, transverse loads were not applied purely in the x-direction so approximately 22.2 N (5 lbs) of load in the y-direction was recorded at maximum transverse load. The alignment of the cable was readjusted and the test was redone. The second test shows near zero off axis reading for both the axial direction and the opposite transverse direction. The recorded loading in the x-direction matched well with the applied loading; slight disagreement occurred at the 31 N (7 lb) and 44.5 N (10lb) load where the first test recorded 35.5 N (8 lb) instead of 31 N (7 lb) and the first and second test both recorded 48.9 N (11 lb) instead of 44.5 N (10lb).
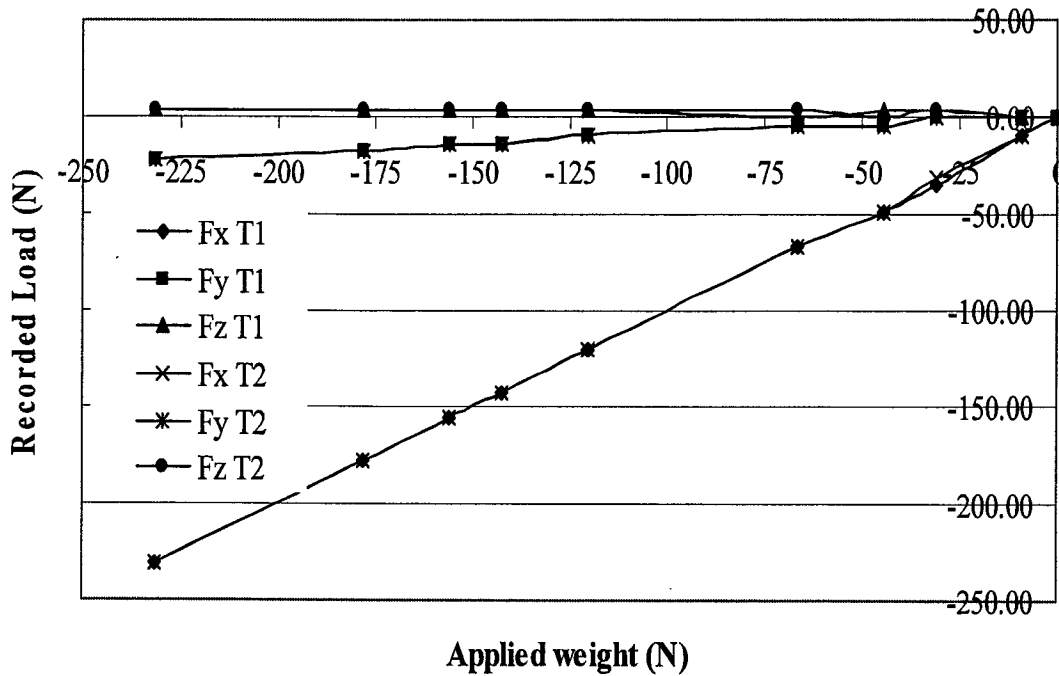
Figure D.44: Application of transverse loads in the negative x direction (0°) where Fx T1, Fy T1, Fz T1, Fx T2, Fy T2 and Fz T2 are the forces in the *x*, *y*, and *z* direction for tests one and two. Note lines are used for visual purposes only.

The third and fourth tests were completed in the negative *y*-direction (Figure D.45). The forces in the *y* direction show good agreement between the applied and recorded load with the exception of the third test recording 4.4 N (1 lb) lower for the 44.5 N (10 lb) and 66.7 N (15 lb) loads. Off axis loading was minimal with the force in the *x*-direction occasionally recording 4.4 N (1 lb) of load. This could be contributed to slight misalignment of the cable.

192
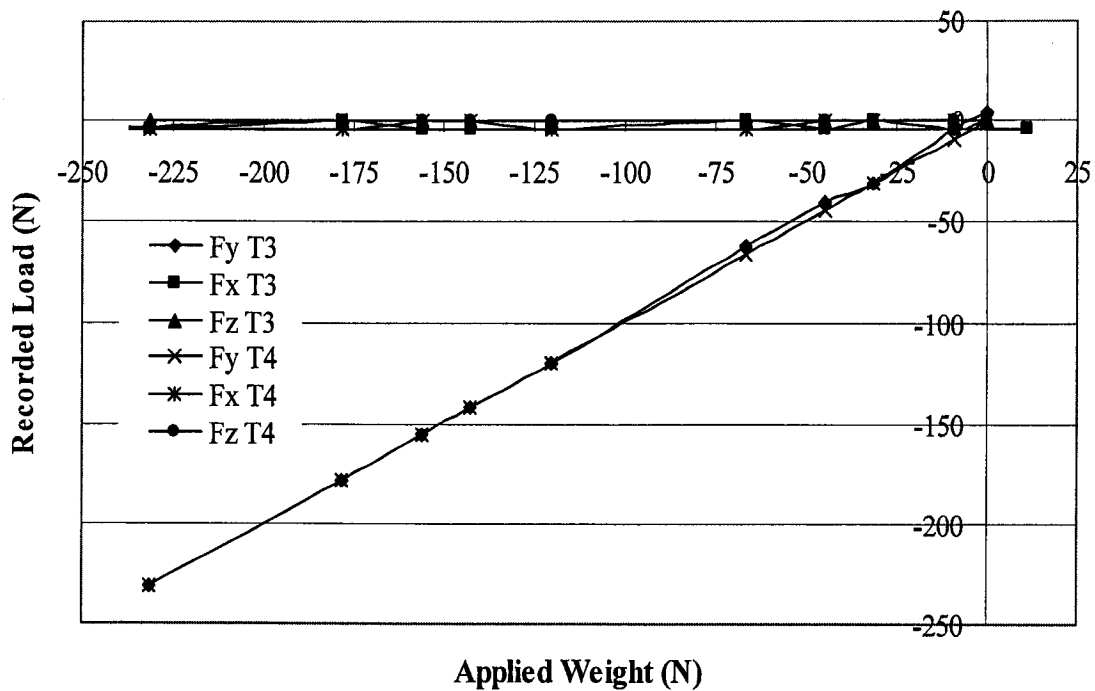
Figure D.45: Application of transverse loads in the negative y direction (90°) where Fx T3, Fy T3, Fz T3, Fx T4, Fy T4 and Fz T4 are the forces in the x, y, and z direction for tests three and four. Note lines are used for visual purposes only.

The fifth and sixth tests were completed in the positive x-direction (Figure D.46).

Good agreement occurred between the applied load and the recorded load. Off axis

loading was more significant in this direction than the previous tests but as seen in the

first test, if the cable was slightly misaligned the off axis loading was noticeable.

193
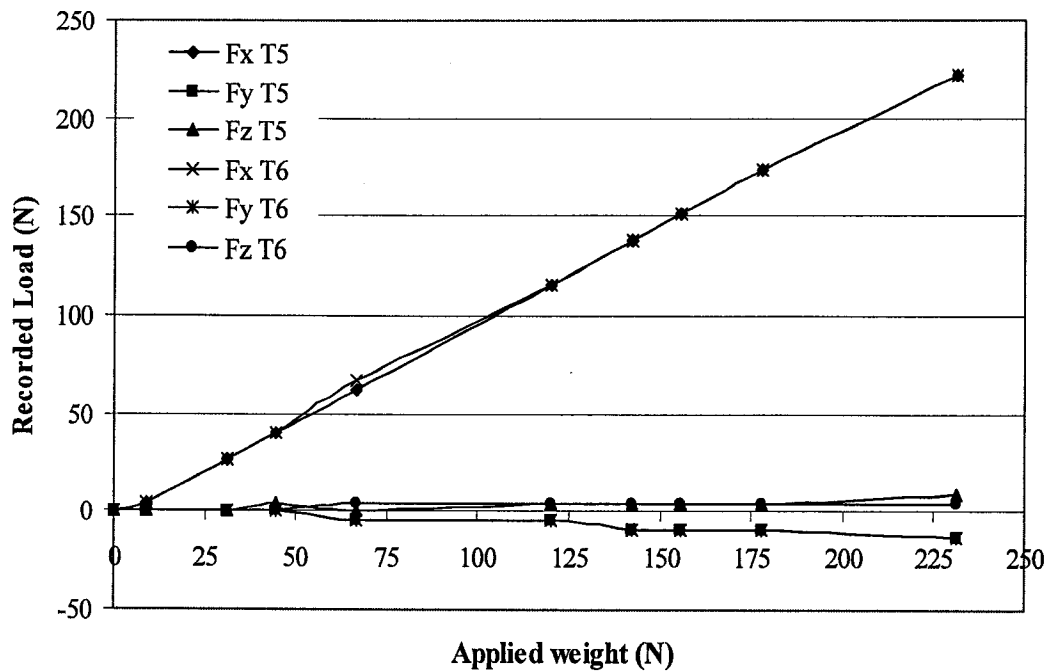
Figure D.46: Application of transverse loads in the positive x direction (180°) where Fx T5, Fy T5, Fz T5, Fx T6, Fy T6 and Fz T6 are the forces in the *x*, *y*, and *z* direction for tests five and six. Note lines are used for visual purposes only.

The last two tests were completed in the positive *y* direction (Figure D.47). Again good agreement occurred between the recorded load and the applied load with a slight disagreement at 177.9 N (40 lb) where instead test 7 recorded 182.4 N (41 lb).

194
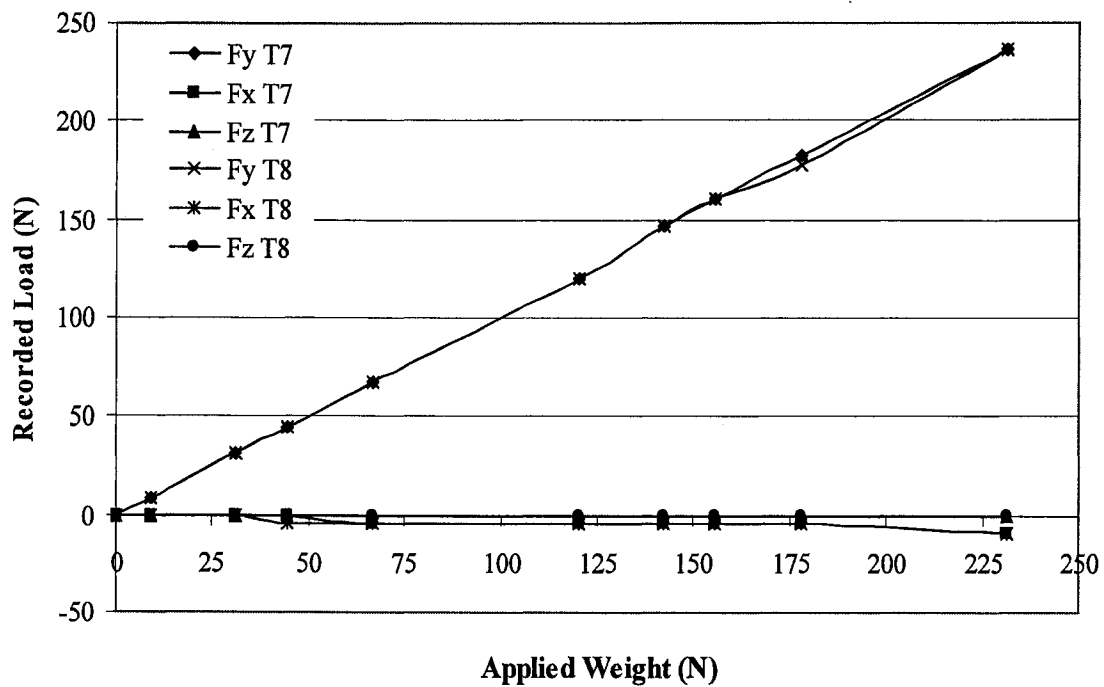
Figure D.47: Application of transverse loads in the positive y direction (270°) where Fx T7, Fy T7, Fz T7, Fx T8, Fy T8 and Fz T8 are the forces in the *x*, *y*, and *z* direction for tests seven and eight. Note lines are used for visual purposes only.

D.5 Conclusion

Each small design modification slightly improved the error results but installation of the 6 DOF load cell immensely improved the error that was seen throughout all previous calibration tests. According to the manual, the 6 DOF load cell can predict loads with errors less than 1% at full load and have less than 2% cross talk. The verification of the 6 DOF load cell calibration was successful. Minimal disagreement was found between applied and recorded load. If disagreement occurred it had a maximum magnitude of 4.4 N (1 lb) difference. Off axis loading was noticed but this proves that alignment is an essential component of testing and that the load cell has great sensitivity to change in loads.

195

References

Hall, J.L., Sundararajan, S., Naim, M., 2006. Instrument Statics. In: Kutz, Myer, eds. *Mechanical Engineers' Handbook - Instrumentation, Systems, Controls, and MEMS*. 3rd ed. John Wiley & Sons. Online version available at: <http://knovel.com.login.ezproxy.library.ualberta.ca/web/portal/browse/display?_EXT_KNOVEL_DISPLAY_bookid=1531&VerticalID=0>.

Appendix E: Windows HyperTerminal

Windows HyperTerminal is an easy, user-friendly program to control serial communication devices outside of LabVIEW. This program is used to move the servomotor before and after the alignment of the femur and tibia bone pot holders and to move the specimen into position before the experiment begins. Below is a detailed description on how to open and run Windows HyperTerminal. Once set-up is complete, the ASCII commands (Table E.1) can be used to control the servomotor as shown in Figure E.1.

a. Go to Start menu
b. Select Run
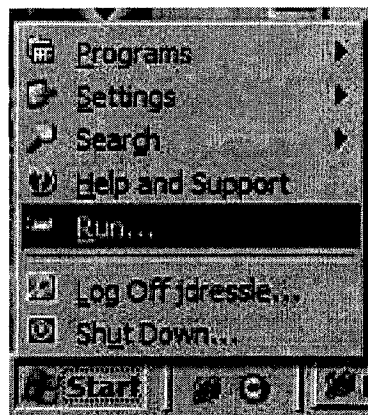
c. Type in "hypertrm"
d. Press OK
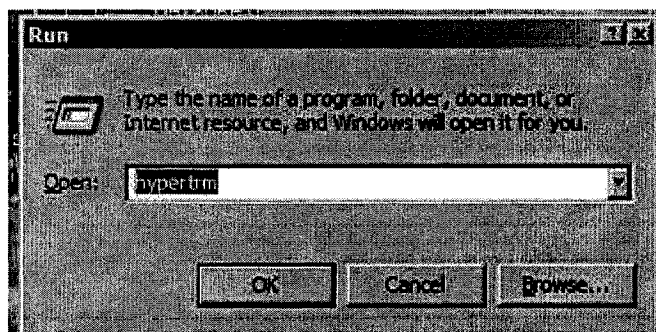
e. Press cancel
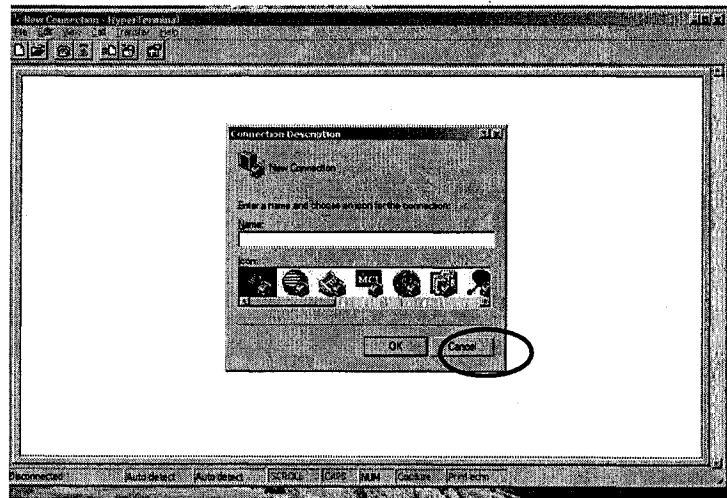
f. Select File
g. Select Properties
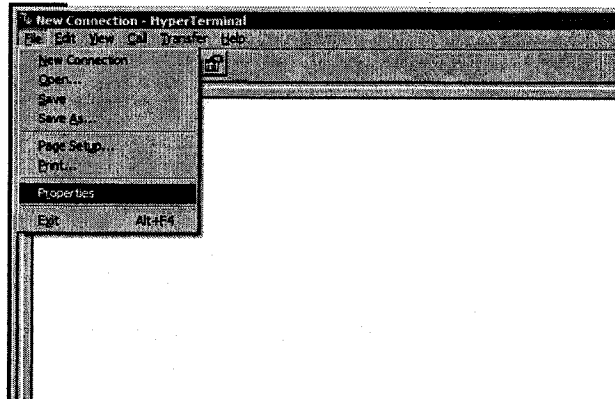
h. Choose port: COM 1
i. Press Configure

198
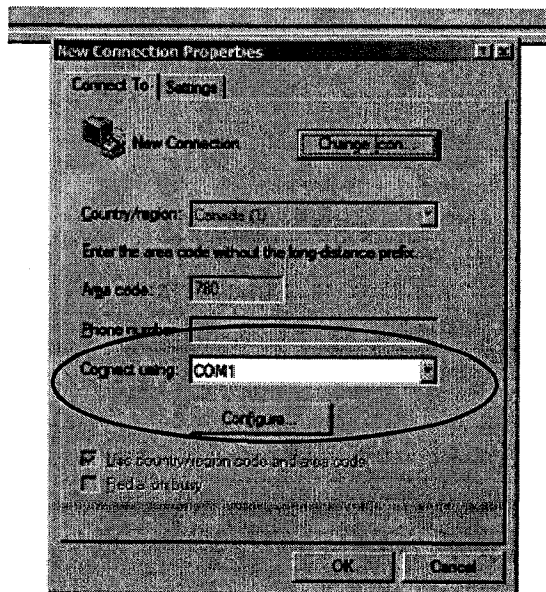
j.   Select Configure

k.   Make sure the following port settings are used:

i.   Bits/second = 38400
ii.   Data bits = 8
iii. Parity = none
iv.   Stop bits = 1
v.   Flow control = none

l.   Select OK
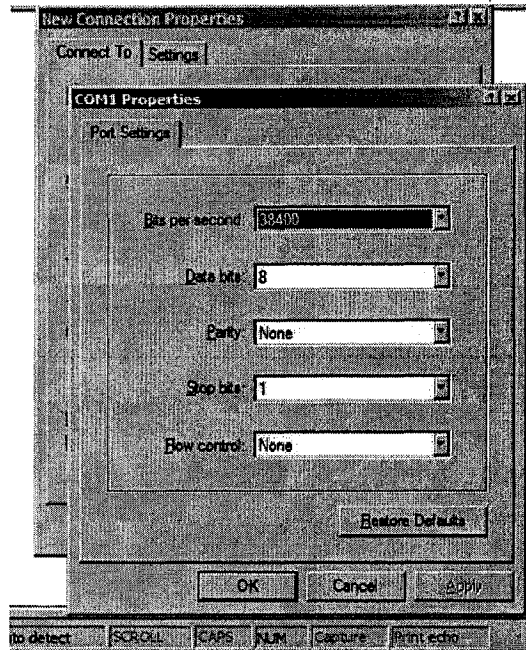
m.   Select Settings
n.   Press ASCII Set-up

199
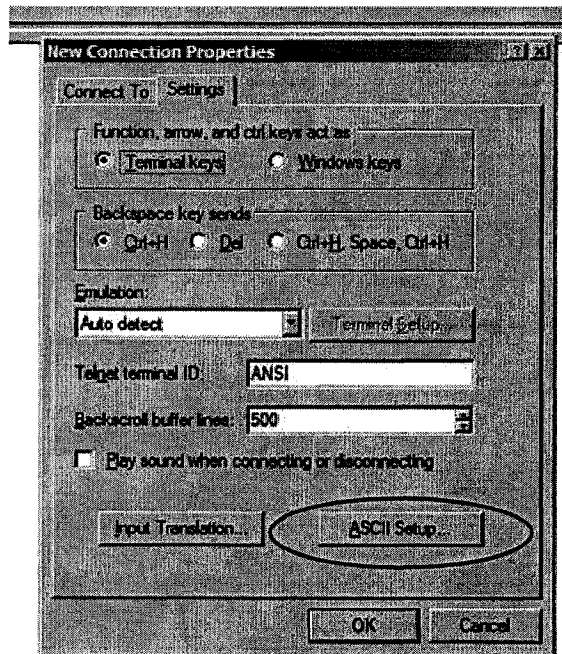
o. Select "Echo typed characters locally"
p. OK
q. OK
r. Set-up is now complete!
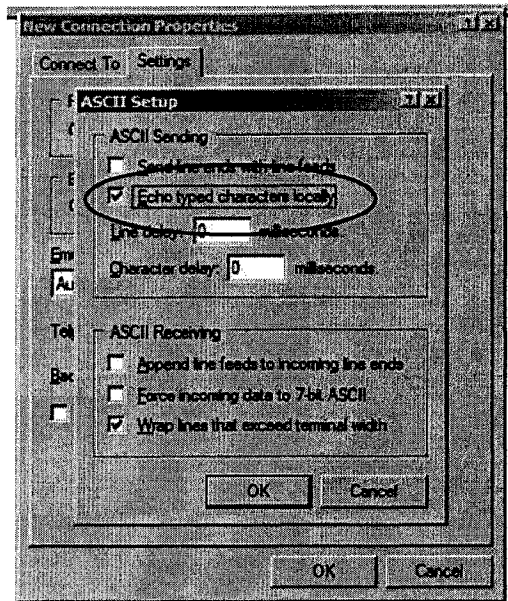
Table E.1: Servomotor ASCII Commands

ASCII Commands	Description
EN	Enable actuator
LOAD	Loads set-up information
SAVE	Saves information into controller memory
COLDSTART	Restarts the controller
J 1	Move actuator up at a speed of 1 mm/min
J -1	Move actuator down at a speed of 1 mm/min
STOP	Stop actuator movement
DIS	Disable actuator

200
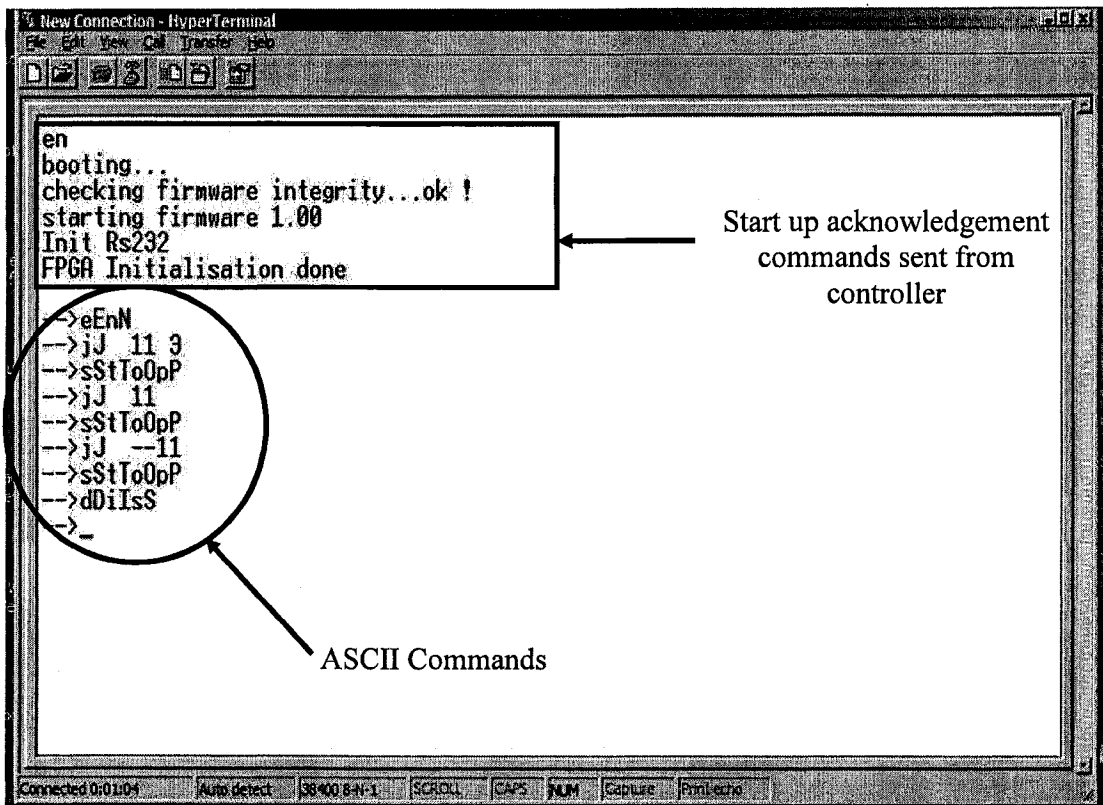
Figure E.1: Windows HyperTerminal screen. Lower case letters indicate the commands typed into Windows HyperTerminal and the upper case letters are the echoed command from Windows HyperTerminal indicating command acknowledgement.

Appendix F: Experimental Protocols

Experimental protocols are needed to reproduce what other experimenters have done previously and to provide future experimenters knowledge on how to repeat certain tasks. The following appendix details for future users, the experimental protocols developed for elements of the systems that must be standardized or controlled. Specifically, for finding the longitudinal axis of a specimen, potting the specimens in the alignment jig, measuring the strain gauge and ball bearing position in the CMM, using the coaxial alignment indicator to align the tibia and femur bone pot holders and the procedure used to test the specimens are all outlined in this appendix and were followed for each specimen.

F.1 Finding Specimen Longitudinal Axis

Listed below is the protocol used to find the longitudinal axis of the composite and bovine tibias and femurs.

1. Place specimen dorsal side down with distal end of tibia and proximal end of femur at front of CMM machine

2. Measure and record x, y, z coordinates of points A and B of the distal end of the specimen (Figure F.1)

3. Find midpoint between the two coordinates and mark on specimen with marker

4. Measure and record x, y, z coordinates for C and D sides of the proximal end of specimen (Figure F.1)

5. Find midpoint between the two coordinates and mark on specimen

6. Using string, secure one end to the marked midpoint of the distal end and the other end to the marked midpoint of the proximal end. It should be noticed that this line is vertical.

7. Using a plumb line, mark the direction of the neutral axis for each strain gauge
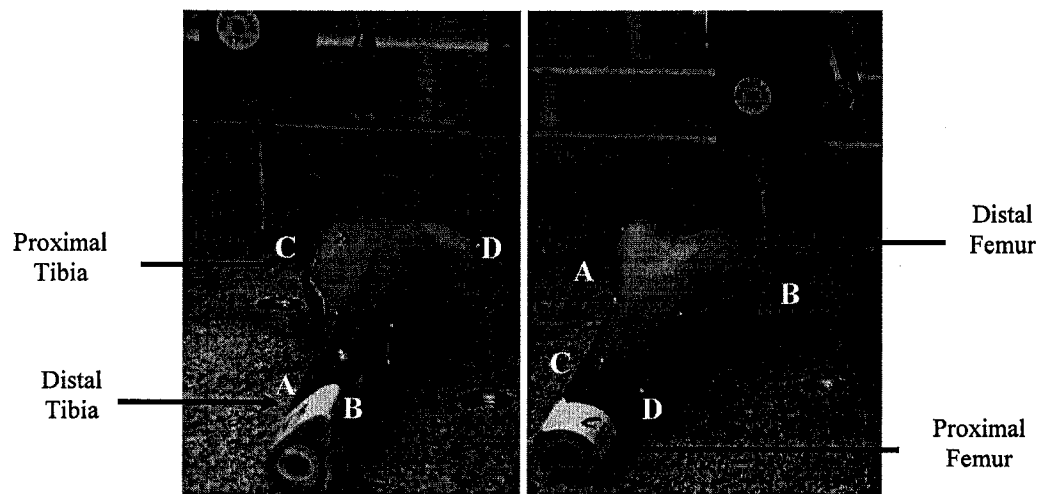
Figure F.1: Placement of composite bones in CMM to find longitudinal axis; a) tibia; b) femur

F.2 Potting Specimens in Alignment Jig

Listed below are the steps of the protocol used to pot the composite and bovine specimens into the alignment jig. Figure F.2 shows the different components needed to pot the bones in the alignment jig.

203
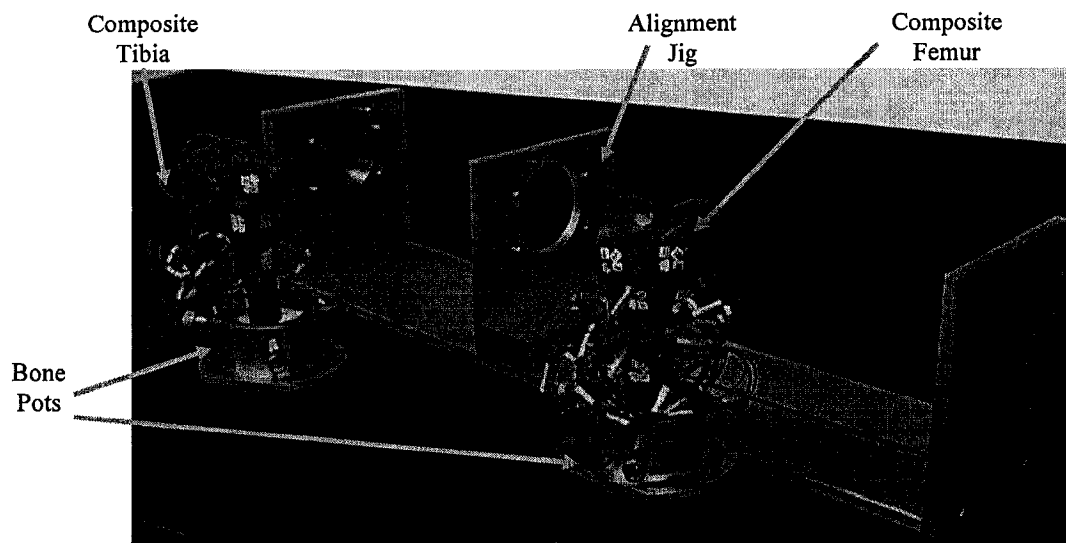
Figure F.2: Alignment jig and composite tibia and femur

1. Place and bolt bone pots into provided positions (Figure F.3)

2. Place proximal end (shaft) of femur and distal end (shaft) of tibia into bone pots (Figure F.4)

3. Hold joint end while tightening screws around shaft

4. Be careful not to include strain gauge wires into potting area

5. Move adjustable back plate until tibial plateau and femoral condyles are touching

6. Align femoral condyles on tibial plateau until the desirable surface contact and stability is achieved. Try to avoid possible point loading from the intercondylar notch of the tibia.

7. Readjust adjustable back plate if needed to obtain contact described in point 6.

8. Search for a second opinion on contact and position of joint. Since there are no soft tissue present on either the composite or bovine specimens, the best contact and position of joint was chosen based on the contact which provided the most stability and distributed the load as best as possible for lower stress.

204

9. Prepare plaster of Paris

    a. Fill cup with water

    b. Continuously add bone cement until a slight layer of cement cannot be dissolved

    c. Stir plaster (Do not stir too much as the more it is stirred the quicker it will set)

    d. Pore into bone pots

10. Place alignment jig on one end (Figure F.5)

11. Pour plaster into pot

12. Allow plaster to set for 2-3 hours

13. Turn alignment jig on other end

14. Mix up another batch of bone cement following steps 9a through d

15. Pour plaster into pot and allow to set

Once fully set, measure the strain gauge and ball bearing positions in the coordinate measuring machine (CMM) following the provided protocol in Section F.4 Measuring Strain Gauge and Ball Bearing Positions.
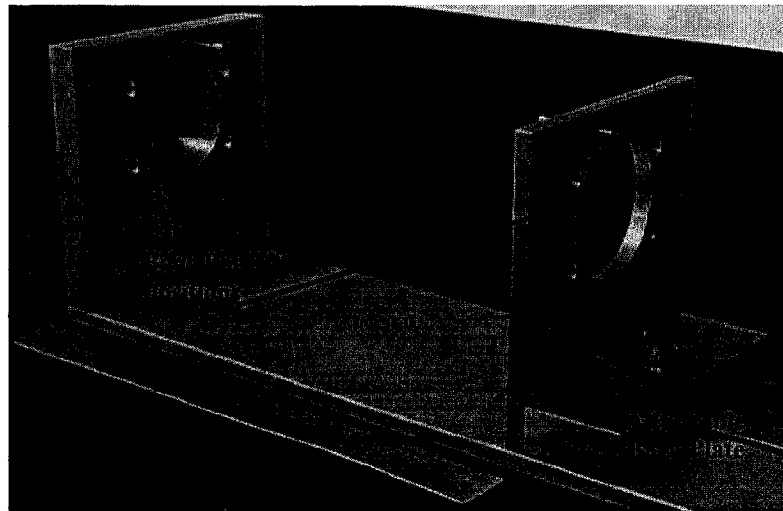
Figure F.3: Alignment Jig
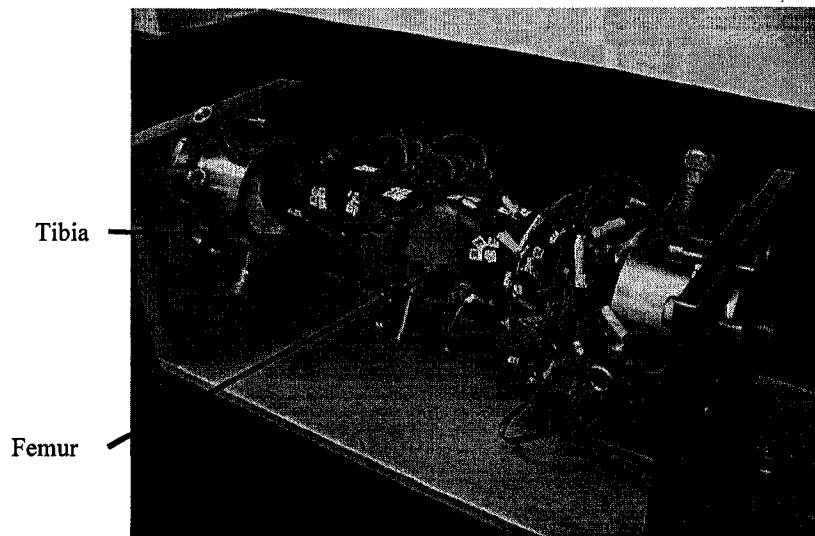
Figure F.4: Composite tibia and femur being potted in alignment jig
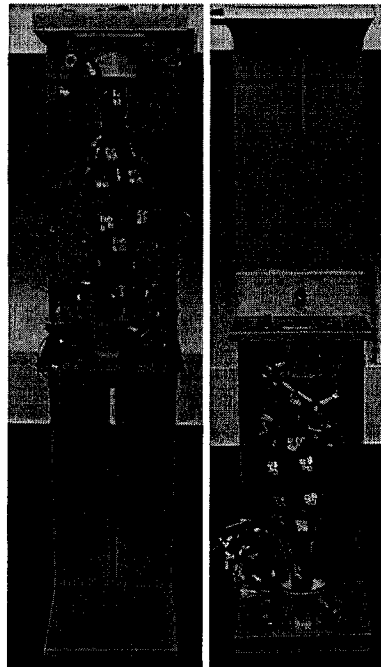
Figure F.5: Place jig on end to pot specimens

F.3 CMM Start Up Procedure

The coordinate measuring machine (CMM), Figure F.6, measures the x, y, z

coordinate of any point up to the third decimal place of a millimetre (0.001mm). Each

206

time the CMM is used, the start up procedure described below, provided by the

manufacturer of the CMM, should be followed.
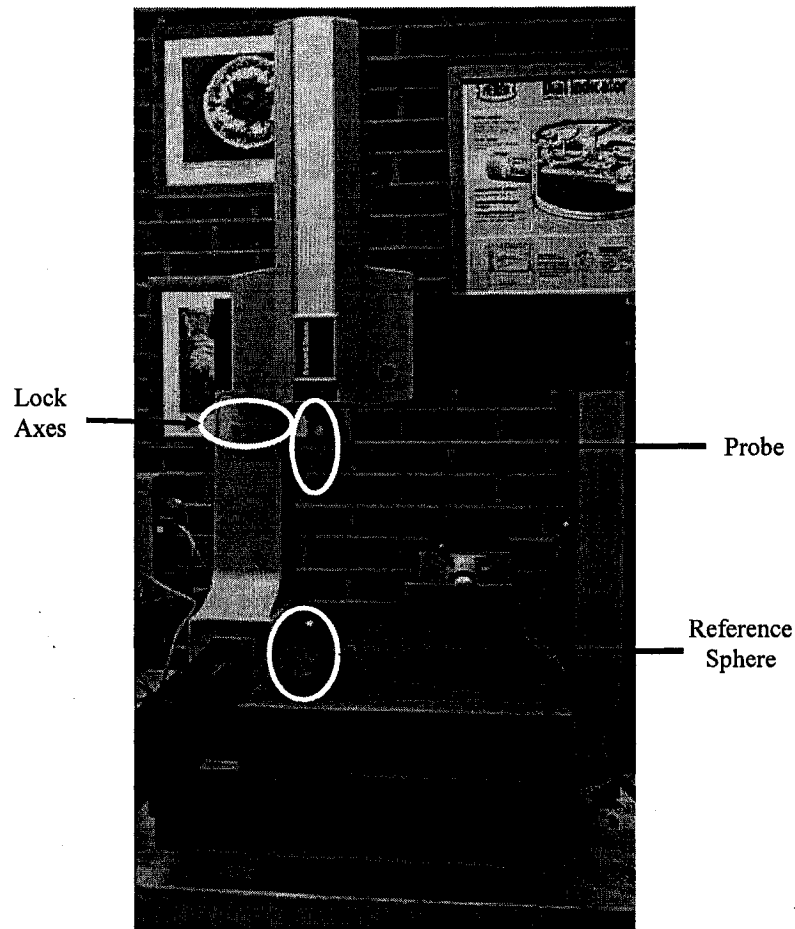
Figure F.6: Various components of the coordinate measuring machine

1. Turn the air supply on at its source to a pressure of 55 psi.

2. Turn on electronic cabinet and computer monitor, choose preferred language.

3. Verify the system by the following steps:

A. Place machine at home position – unlock the axis switch, move the machine to

the upper left corner.

B. Lock the axis, to use a language other than English select one with the light

pen. Touch the pen to the screen where 'Done' displays. The menu will change.

207

C. Place the reference sphere under the machine and move the Z rail above the sphere. Lower it until the bottom fits securely on top of the sphere. Move the rail up.

D. Install the proper tip to the probe and the probe to the Z rail, tightening the clamp on the right side. Attach the electronic connector on the left side to the probe on the right side. Press 'Done', qualification menu will display on the screen.

E. Turn on the probe interface and the pickle so that the probe and the pickle will light.

F. Qualify the tip by hitting the sphere, using the picture on the screen. Four hits are required. Then press 'Done'. The AXES screen will display.

4. Press MICRO MEASURE and choose from the main menu the measurement needed. Use HELP if needed.

5. Once complete, turn off power bar and air pressure.

F.4 Measuring Strain Gauge and Ball Bearing Positions

The strain gauge and ball bearing positions provide essential information needed to find the theoretical strain values, to reproduce the loading conditions in a finite element model and to determine the specific specimen geometry at that particular position. The following procedure was used to measure the strain gauge and ball bearing position with respect to a reference point on the bone pot.

1. Place specimen dorsal side down into alignment jig

2. Align the long axis of the alignment jig to be parallel with the y-axis of the CMM machine.

     a. Record x, y, z coordinate of left front corner of alignment jig (Figure F.7)

     b. Record x, y, z coordinate of left back corner of alignment jig (Figure F.7)

     c. Readjust alignment jig until x-coordinates difference are within 0.5 mm

     d. Record x, y, z coordinates of right front and back corner to ensure proper alignment (Figure F.7)

3. Record x, y, z coordinate of reference point, repeat three times so an average can be taken

4. Record the x, y, z coordinates for each available strain gauge and ball bearing on the top surface, take each point three times

5. Remove specimen and place dorsal side up (Figure F.8)

6. Once specimen is secure, repeat steps 2a-d to ensure alignment jig is parallel to y-axis

7. Ensure that top edge of bone pot is parallel to top of adjustable back plate (Figure F.9)

     a. Record z coordinate of top, left side of bone pot

     b. Record z coordinate of top, right side of bone pot and compare to previous measurement

     c. Adjust bone pot and continue to record z coordinate until both ends read nearly the same position

8. Repeat steps 3 and 4

9. Repeat procedure as many times as necessary

10. To get the vector position, subtract the reference point from each strain gauge and ball bearing
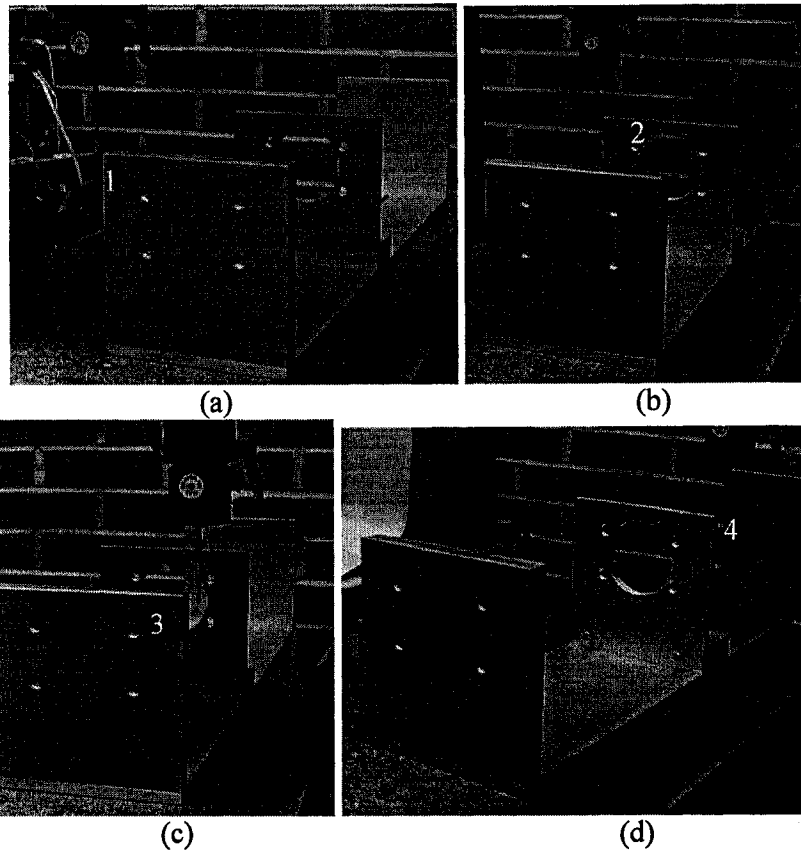
Figure F.7: Aligning alignment jig in CMM machine; a) measuring front, left corner; b) measuring back, left corner; c) measuring front, right corner; d) measuring back, right corner
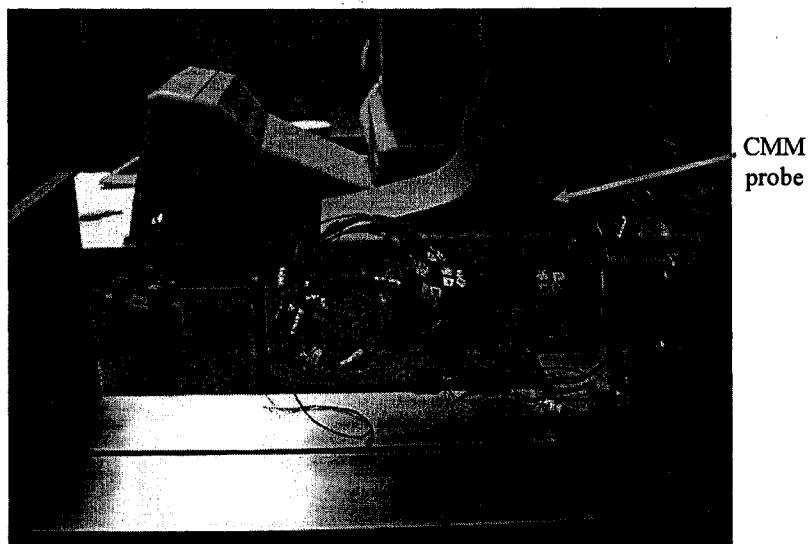
Figure F.8: Composite tibia dorsal side up in alignment jig

210

Top Edge
of Back
Plate

Top Edge
of Bone Pot
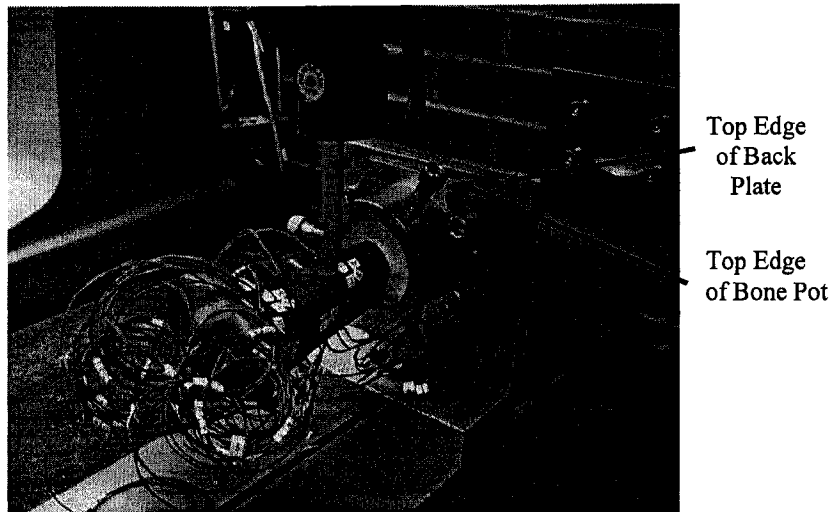
Figure F.9: Composite tibia in alignment jig

F.5 Coaxial Alignment Indicator Protocol

The protocol used to align the femur and tibia bone pot holders is as follows:

1. Secure coaxial alignment indicator into femur block (Figure F.10). If necessary move actuator down, using Appendix E: Windows HyperTerminal, so as not to damage indicator when placing into MABTA.

2. Move actuator up slowly until probe of coaxial indicator is resting near the middle of the bone pot holder

3. Grip the black metal bar in one hand to steady the movement of the dial face and rotate the shaft in other hand (Figure F.10)

4. Adjust either the x or y direction using the hand cranks (Figure F.11)

5. Place indicator along y axis (axis coming out of front of machine)

6. Adjust the 0° mark to overlap the dial hand

7. Alignment is completely off when the hands rotate around the dial face numerous times. If this occurs, count number of times the dial hand has passed the 0° mark.

211

8. Adjust one hand crank at a time to decrease the number of times the dial hand has passed the 0° mark

9. Check indicator for alignment

10. Continue to alternately adjust the x and y directions until indicator reads adjustment within 1°

11. Once aligned move actuator down, be careful not to damage probe during actuator movement. It is recommended to hold the probe away from the edge until no longer inside bone pot holder.

12. Once actuator has moved down enough, remove coaxial alignment indicator from femur block.

13. Careful not to bump hand cranks while removing device.
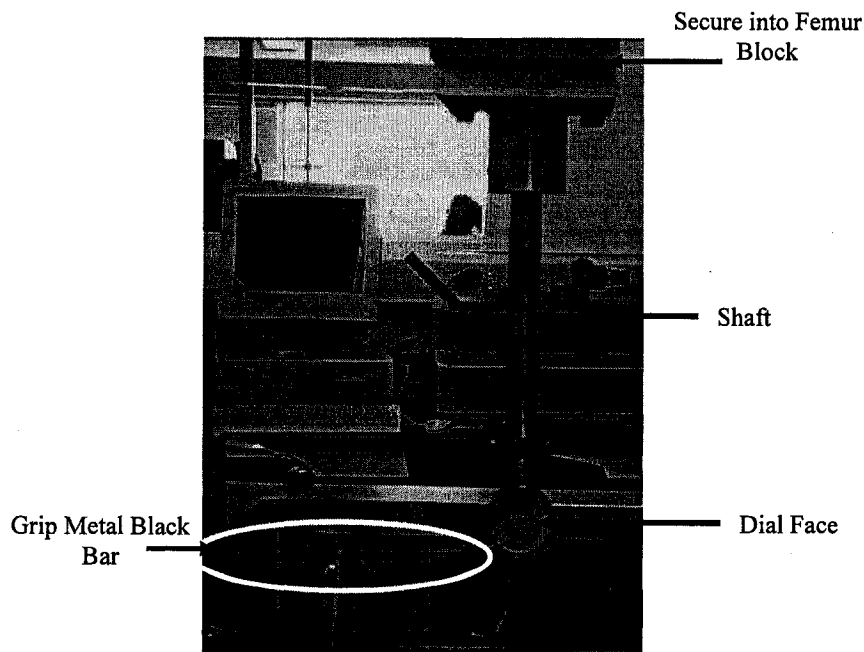
Figure F.10: Coaxial Alignment Indicator Components

212

Hand crank to adjust y direction

Hand crank to adjust x direction
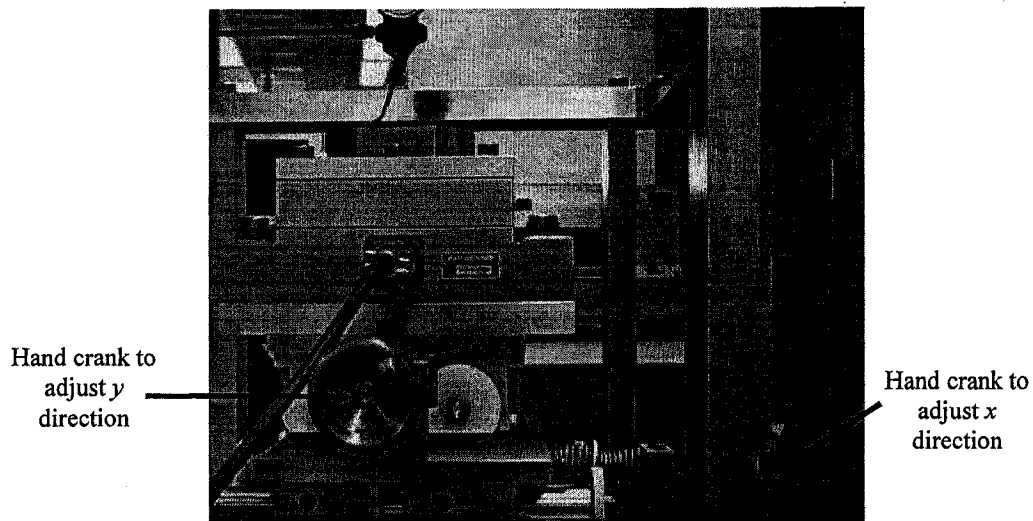
Figure F.11: MABTA hand crank directions

F.6 Composite Bone on Bone Testing Procedure

The experimental procedure used to measure the strain along the cortex of the composite bone for bone on bone testing is as follows.

1. Ensure all of the following components are near by:

   a. Specimens: composite tibia and femur

   b. Pieces of foam and rubber to place between specimens

   c. Coaxial alignment indicator and associated protocol

   d. Windows HyperTerminal protocol

   e. Alignment dowel pins

2. Turn on MiniAmp MSA-6 signal conditioner, let it warm up for at least an hour before experiment. If doing numerous tests, leave signal conditioner on continuously.

3. Plug in power supply and controller to run the actuator

4. Turn on data acquisition (DAQ) module

213

5. Follow Windows HyperTerminal directions in Appendix E to move actuator into position to align femur and tibia bone pot holders.

6. Secure coaxial alignment indicator into femur block and follow coaxial alignment indicator protocol in Appendix F, Section F.5.

7. Once aligned, move actuator down using Windows HyperTerminal and remove coaxial alignment indicator from femur block

8. Place specimens into MABTA,

    a. Align femur pot at the zero degree mark indicated on bottom side of femur block (Figure F.12), tighten bolts

    b. Set tibia into bone pot holder and place dowel pin to ensure proper alignment, tighten bolts

9. Move actuator up using the protocol described in Appendix E: Windows HyperTerminal and the provided ASCII commands

10. Stop actuator once tibia and femur are approximately 2.5 cm away from contact

11. Place rubber on tibial plateau and foam between rubber and femoral condyles (Figure F.13).

12. Move actuator up until femoral condyles slightly compressing foam

13. Open LabVIEW program: 'Experimental Program for MABTA.vi'

14. Ensure all strain gauge connections are complete and information such as gauge factor, acquisition rate and number of samples are inputted into DAQ task

15. Change measurement file information so as to indicate test and date for both signal conditioner and strain gauge values

214

16. Start LabVIEW program and follow program instructions found in Appendix B: Data Acquisition System

17. Precondition foam/rubber combination to 889 N (200 lb)

18. Let specimen relax for a minute and then reload to 889 N (200 lb)

19. Repeat step 18 until load is no longer decreasing (~7 times)

20. Load specimen until 1780 N (400 lb) in 111 N (25 lb) increments

21. Once maximum load has been reached, unload specimen to 0 N (0 lb).

22. Once testing complete, unplug controller and power supply and shut off DAQ

Figure F.12: Experimental Equipment
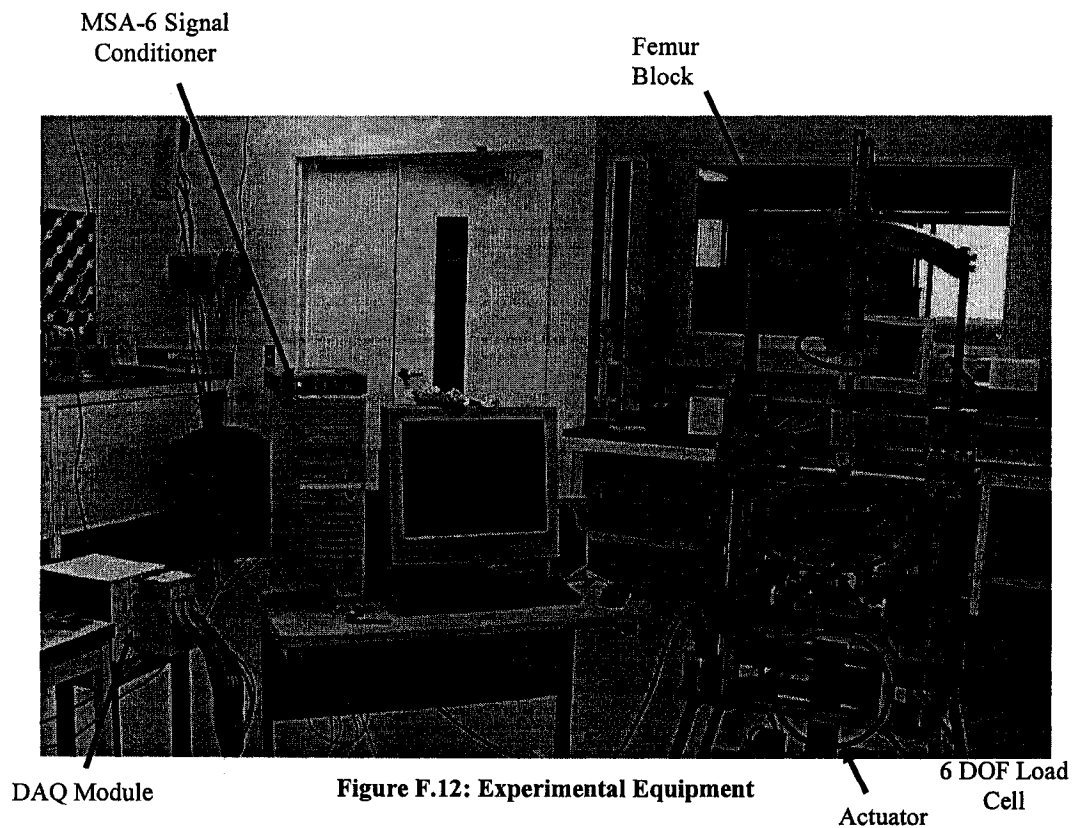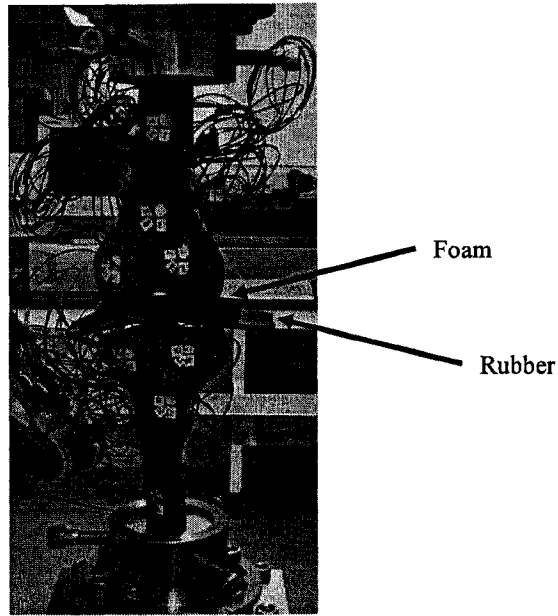
Figure F.13: Placement of tibia and femur before compression test

F.7 Composite Tibia, Custom-Made Loading Jig and Instron Machine

Testing Procedure

Since this experiment was conducted in the Instron machine, a separate experimental protocol was required.

1. Secure custom-made loading jig into Instron machine

2. Place composite tibia/bone pot arrangement vertically into Instron machine

3. Secure bone pot into position with bolts

4. Lower custom-made loading jig until rods are approximately 5mm away from tibial condyles

5. Adjust rods for the best contact in the middle of the condyles (Figure F.14)

216

6. Raise custom-made loading jig, place rubber and foam pieces in between jig and composite bone (Figure F.15)

7. Load composite tibia to 667.2 N (150 lb) in 222.2 N (50 lb) increments

8. Record strains at each increment, allowing the program to record for approximately 10 seconds

9. Repeat experiment three times

Figure F.14: Positioning nylon spheres on tibial condyles
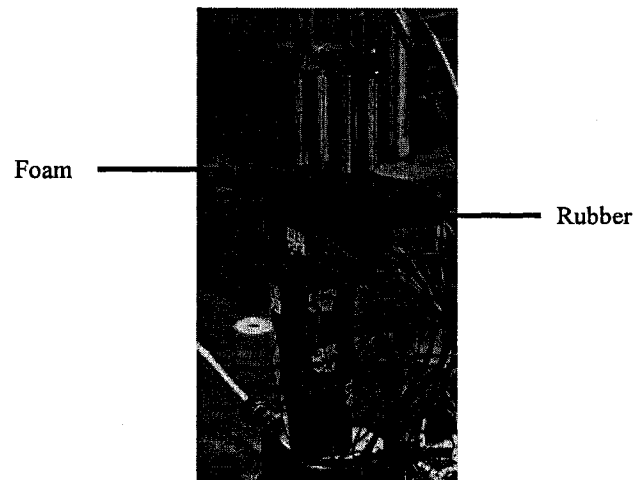
Figure F.15: Final set-up for composite tibia compression test in Instron machine

F.8 Composite Tibia, Custom-Made Loading Jig and MABTA Testing Procedure

The experimental procedure used to measure the strain along the cortex of the composite tibia using the custom-made loading jig is as follows. For comparison purposes, the loading contact points used in the Instron compression test were used in the composite tibia, custom-made loading jig and MABTA compression test. For this reason the experimental protocol was slightly modified from the procedure used in the Instron compression test and the experimental protocol used for bone on bone loading.

1. Ensure all of the following components are near by:

    a. Composite tibia

    b. Pieces of foam and rubber to place between specimens, if being used

    c. Custom-made loading jig

    d. Windows HyperTerminal protocol

2. Turn on MiniAmp MSA-6 signal conditioner, let it warm up for at least an hour before experiment. If doing numerous tests, leave signal conditioner on continuously.

3. Plug in power supply and controller to run the actuator

4. Turn on data acquisition (DAQ) module

5. Follow Windows HyperTerminal directions in Appendix E to move actuator into position to align femur and tibia bone pot holders.

6. Secure custom-made loading jig into MABTA (Figure F.16b)

7. Place composite tibia into MABTA (Figure F.16)

8. Raise the actuator until the custom-made loading jig and the composite tibia are approximately one inch apart

9. Rotate tibia until contact loading points from Instron test are under loading rods

10. Secure bone pot into position with bolts

11. Lower custom-made loading jig until rods are nearly touching the tibial condyles

12. Adjust rods to replicate the contact positions created from the Instron experiment.

13. Lower actuator, place rubber and foam pieces in between jig and composite bone

14. Load composite tibia to 667.2 N (150 lb) in 222.2 N (50 lb) increments

15. Record strains at each increment, allowing the program to record for approximately 10 seconds

(a)   (b)
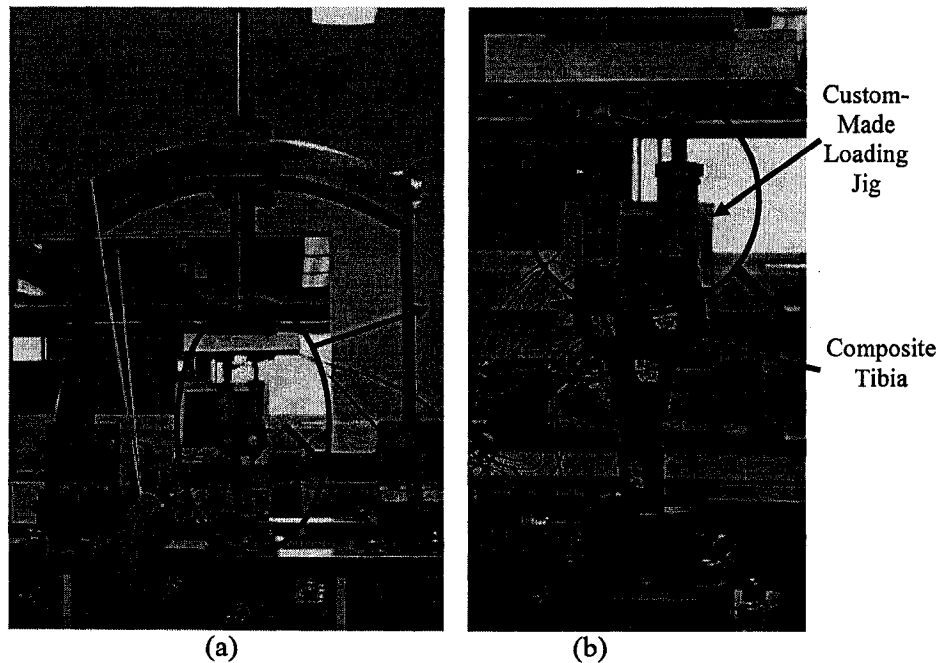
Figure F.16: (a) Custom-made loading jig installed in MABTA; (b) Magnified view of custom-made loading jig positioned on composite tibia

219

F.9 Composite Femur, Custom-Made Loading Jig and MABTA

The experimental procedure used to measure the strain along the cortex of the composite femur using the custom-made loading jig is as follows. The experimental protocol was slightly modified from the composite tibia, custom-made loading jig compression test with MABTA and the experimental protocol used for bone on bone loading.

1. Ensure all of the following components are near by:

    a. Composite femur

    b. Pieces of foam and rubber to place between specimens, if being used

    c. Coaxial alignment indicator and associated protocol

    d. Custom-made alignment jig

    e. Windows HyperTerminal protocol

    f. Alignment dowel pins

2. Turn on MiniAmp MSA-6 signal conditioner, let it warm up for at least an hour before experiment. If doing numerous tests, leave signal conditioner on continuously.

3. Plug in power supply and controller to run the actuator

4. Turn on data acquisition (DAQ) module

5. Follow Windows HyperTerminal directions in Appendix E to move actuator into position to align femur and tibia bone pot holders.

6. Secure coaxial alignment indicator into femur block and follow coaxial alignment indicator protocol in Appendix F, Section F.5.

220

7. Once aligned, move actuator down using Windows HyperTerminal and remove coaxial alignment indicator from femur block

8. Secure custom-made loading jig into MABTA (Figure F.17a)

9. Place composite femur into MABTA (Figure F.17)

10. Raise the actuator until the custom-made loading jig and the composite femur are approximately one inch apart

11. Secure bone pot into position with bolts

12. Lower custom-made loading jig until rods are nearly touching the femoral condyles

13. Adjust rods to contact the centre of the femoral condyles

14. Lower actuator, place rubber and foam pieces in between jig and composite femur

15. Load composite femur to 667.2 N (150 lb) in 222.2 N (50 lb) increments

16. Record strains at each increment, allowing the program to record for approximately 10 seconds

221
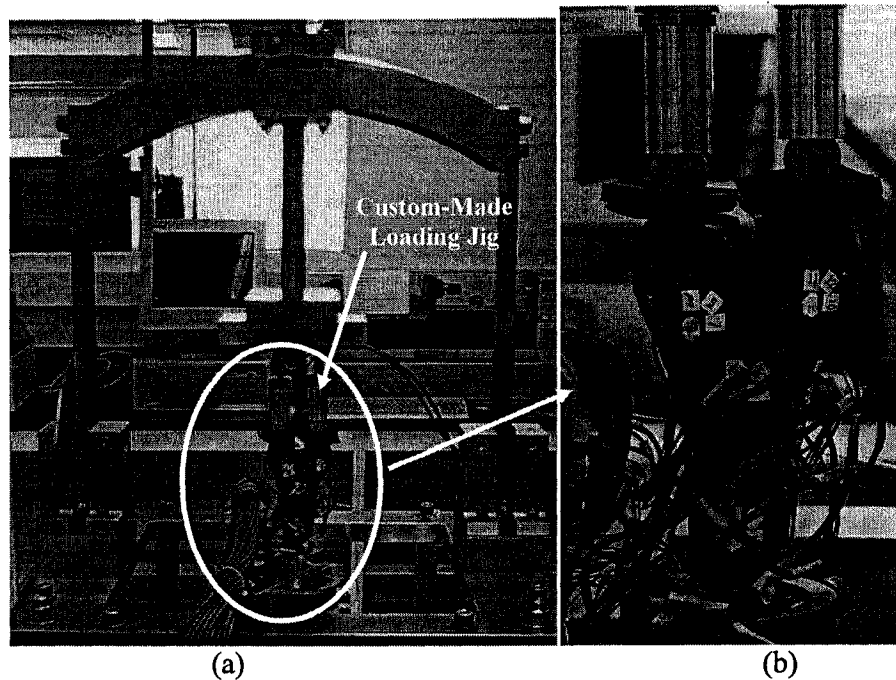
Figure F.17: (a) Custom-made loading jig installed in MABTA with composite femur; (b) Magnified view of custom-made loading jig positioned on composite femur

F.10 Bovine Bone on Bone Testing Procedure

The experimental procedure used to measure the strain along the cortex of the bovine bone is as follows. Please follow steps 1 through 5 in Section F.6 Composite Bone on Bone Testing Procedure to prepare MABTA and all other components for the testing of bovine bone.

1. Ensure all of the following components are near by:

   a. Bovine tibia and femur

   b. Windows HyperTerminal protocol

   c. Alignment dowel pins

222

2. Turn on MiniAmp MSA-6 signal conditioner, let it warm up for at least an hour before experiment. If doing numerous tests, leave signal conditioner on continuously.

3. Plug in power supply and controller to run the actuator

4. Turn on data acquisition (DAQ) module

5. Follow Windows HyperTerminal directions in Appendix E to move actuator into position to align femur and tibia bone pot holders.

6. Place specimens into MABTA,

   a. Align femur pot at the zero degree mark indicated on bottom side of femur block (Figure F.12), tighten bolts

   b. Rotate F-E axis of MABTA to 45 degrees

   c. Set tibia into bone pot holder

   d. Move actuator up using the protocol described in Appendix E: Windows HyperTerminal and the provided ASCII commands. Stop actuator once specimens are close enough for alignment

   e. Using MABTA's x and y hand cranks, align the tibial condyles beneath the femoral condyles

   f. Once specimens are aligned in the x and y directions, continue to move actuator up until specimens are approximately 0.5 cm away from contact

7. Open LabVIEW program: 'Experimental Program for MABTA.vi'

8. Ensure all strain gauge connections are complete and information such as gauge factor, acquisition rate and number of samples are inputted into DAQ task

223

9. Change measurement file information so as to indicate test and date for both signal conditioner and strain gauge values

10. Start LabVIEW program and follow program instructions found in Appendix B: Data Acquisition System

11. Precondition bovine bone to 889 N (200 lb)

12. Let specimen relax for a minute and then reload to 889 N (200 lb)

13. Repeat step 8 until load is no longer decreasing (~7 times)

14. Load specimen until 1780 N (400 lb) in 111 N (25 lb) increments

15. Once maximum load has been reached, unload specimen to 0 N (0 lb)

16. Allow specimen to recover for 5 minutes

17. Repeat experiment three times

18. Once testing complete, unplug controller and power supply and shut off DAQ

Appendix G: Known Geometry Experiments

G.1 Introduction

Prior to performing experiments using specimens such as composite and bovine bones, which interject possible sources of variability related to their complex geometry and inconsistent materials properties, it is an appropriate research and validation strategy to perform tests on specimens of known geometry and properties.

G.2 Materials

A cylindrical, polyvinyl chloride (PVC) specimen with known dimensions and material properties (Table G.1) was used as a validation for MABTA's measured results. It should be noted that the modulus of elasticity was obtained from MatWeb, an online materials database (MatWeb). Unfortunately, for this specimen the actual modulus of elasticity value is unknown, therefore a range was established using the minimum and maximum values.

Table G.1: Dimensions and material properties of the PVC specimen

Length, m (in)	0.2198	(8.652)
Inside Diameter, m (in)	0.0258	(1.014)
Outside Diameter, m (in)	0.0334	(1.314)
Area, m^2 (in2)	3.539×10^{-2}	(5.485×10^{-1})
Moment of Inertia (I), m^4 (in^4)	3.931×10^{-4}	(9.444×10^{-2})
Modulus of Elasticity Pa (psi)	1.79×10^6	(2.60×10^2)
	4.83×10^9	(7.00×10^5)

G.3 Methods

Two experiments were conducted on a PVC pipe, the first being a compression test in MABTA and the second a compression test in a 500N MTS Synergie 400 uniaxial testing machine (Model #2700094, MTS Systems Corporation, Eden Prairie, MN, USA). Both tests were conducted to determine if the same experimental strain trends were seen between two different loading devices.

G.3.1 Compression of PVC Specimen in MABTA

The coaxial alignment indicator protocol detailed in Appendix F, section F.5 was used to align the tibia and femur bone pot holders to within 0.0127 mm. The PVC specimen was inserted into the fitted Delrin® collars (Figure G.1) and then placed into the bone pots. The fitted Delrin® collars were used to align the specimen in the centre of the bone pots. Bone pots were then carefully inserted into MABTA and actuator was moved up[17] until specimen was in position (Figure G.2).

PVC specimen

Fitted Delrin® collars
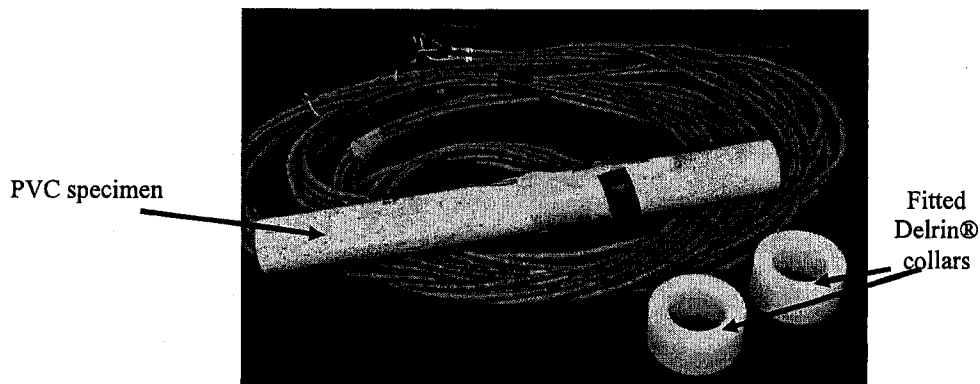
Figure G.1: PVC specimen with machined Delrin® collars

---

[17] Refer to Appendix E: Windows HyperTerminal to control the actuator

226
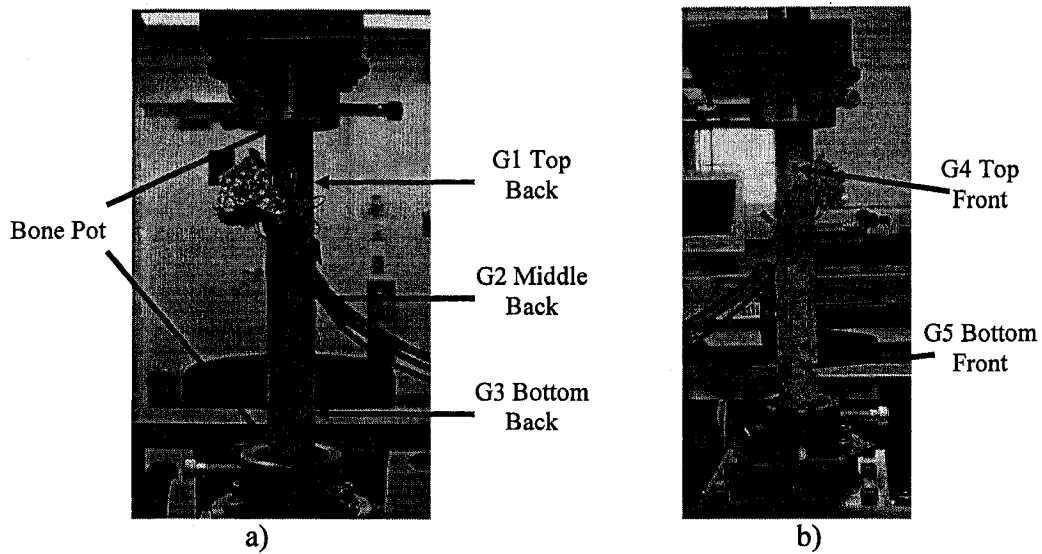
Figure G.2: PVC pipe instrumented with strain gauges: a) back of the specimen and b) front of the specimen

Four tests were completed on the PVC specimen; all tests compressed the specimen to a maximum load of 890 N (200 lb) with three of those tests loading in 89 N (20 lb) increments and one test loading in 178 N (40 lb) increments. Prior to the beginning of the tests, it was noticed that two strain gauges, G3 and G5, had wiring failure and as a result no data was collected on these locations. Table G.2 presents the maximum strain values for all four compression tests.

Table G.2: Maximum Strain Values from PVC compression test in MABTA

Test	Maximum Load (lb)	Maximum Load (N)	Strain (με)		
			G1 Top Back	G2 Mid Back	G4 Top Front
1	200.73	892.89	-820.46	-996.74	-974.78
2	202.25	899.65	-835.52	-1014.16	-982.32
3	200.99	894.04	-845.82	-992.68	-963.74
4	201.62	896.85	-835.26	-982.26	-981.88

227
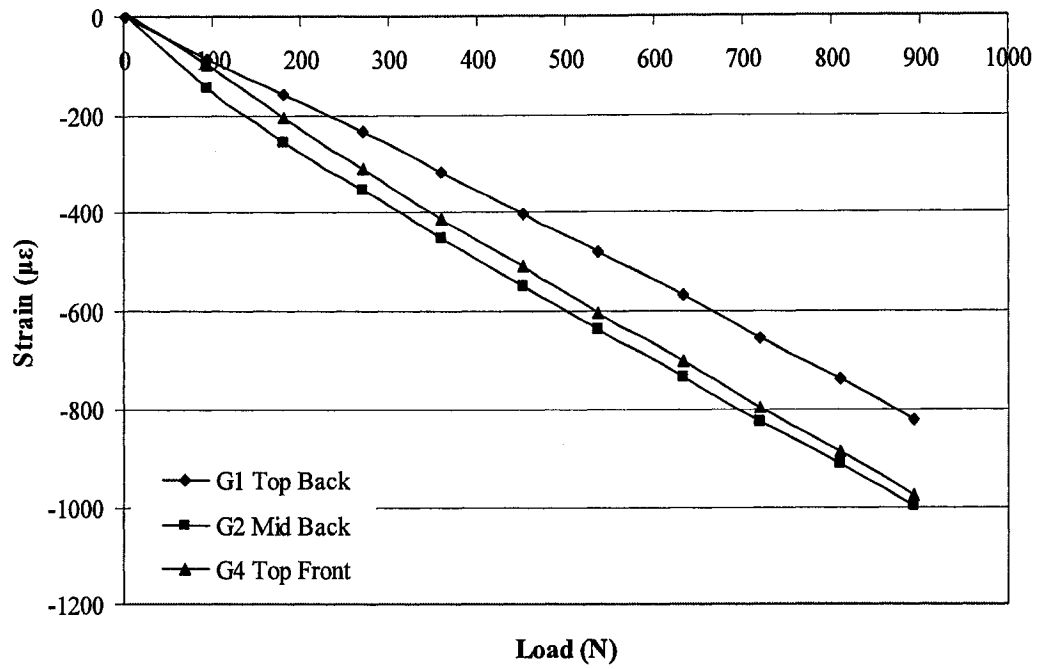
Figure G.3: Strain results from the first PVC specimen compression test in MABTA. G1, G2 and G4 are the specimen's strain gauge readings in the specified locations. Note lines are for visual purposes only.
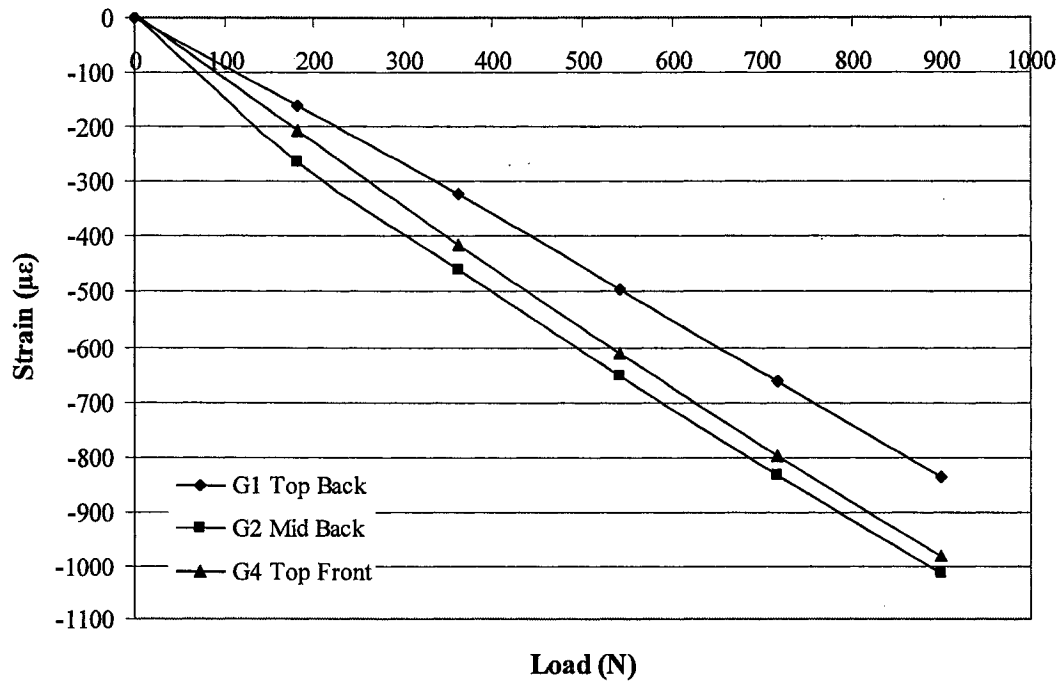
Figure G.4: Strain results from the second PVC specimen compression test in MABTA. G1, G2 and G4 are the specimen's strain gauge readings in the specified locations. Note lines are for visual purposes only.

228
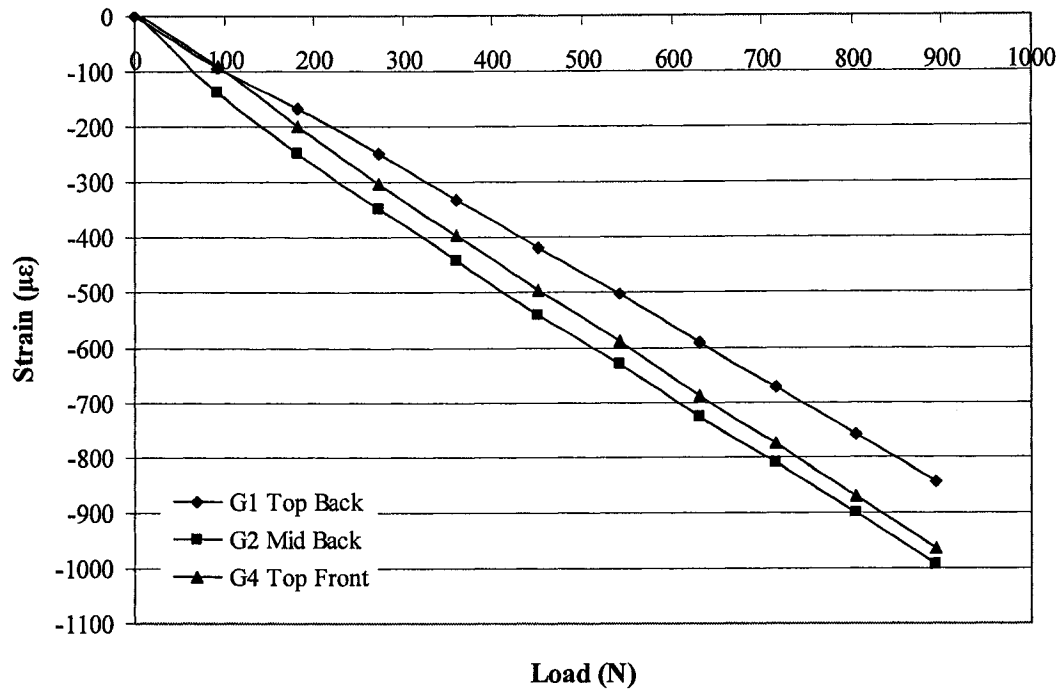
Figure G.5: Strain results from the third PVC specimen compression test in MABTA. G1, G2 and G4 are the specimen's strain gauge readings. Note lines are for visual purposes only.
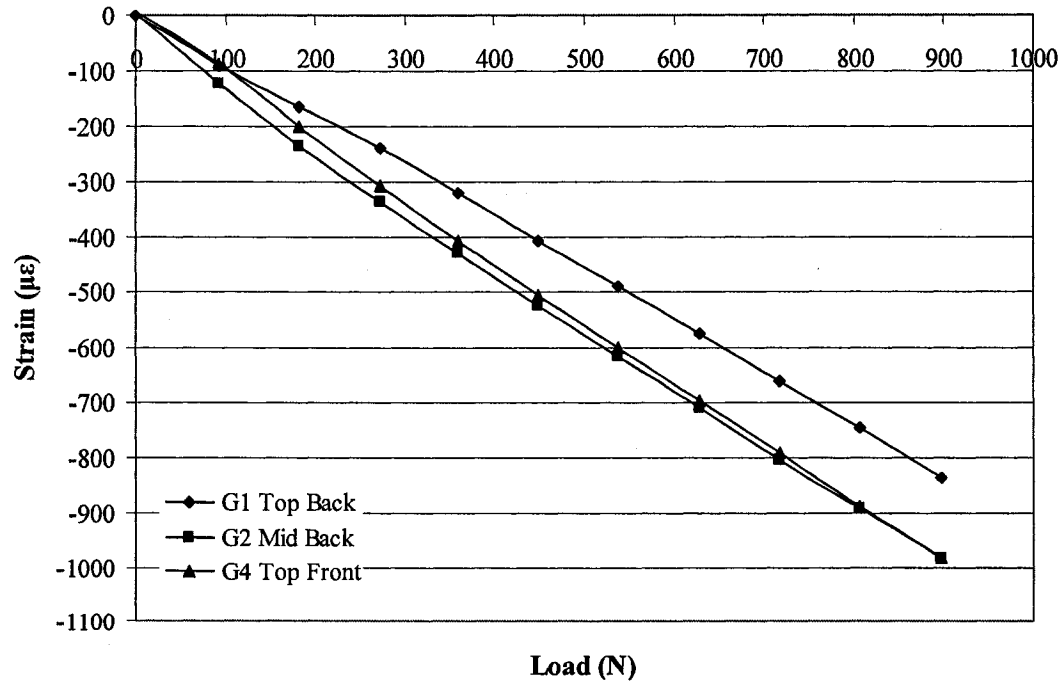
Figure G.6: Strain results from the fourth PVC specimen compression test in MABTA. G1, G2, and G4 are the individual strain readings at the specified location. Note lines are for visual purposes only.

229

Due to the wiring failure in the previous four tests, the PVC pipe was reinserted into MABTA and two more tests were completed. The maximum strain values for these tests are presented in Table G.3 and the complete strain results for the two tests are presented in Figure G.7 and Figure G.8.

Table G.3: Maximum strain values from retested PVC compression tests in MABTA

Test	Maximum Load (lb)	Maximum Load (N)	Strain (με)				
			G1 Top Back	G2 Mid Back	G3 Bottom Back	G4 Top Front	G5 Bottom Front
1	203.51	905.26	-772.94	-989.84	-1177.82	-1072.58	-648.94
2	200.99	894.04	-770.64	-976.20	-1140.72	-1035.60	-650.80
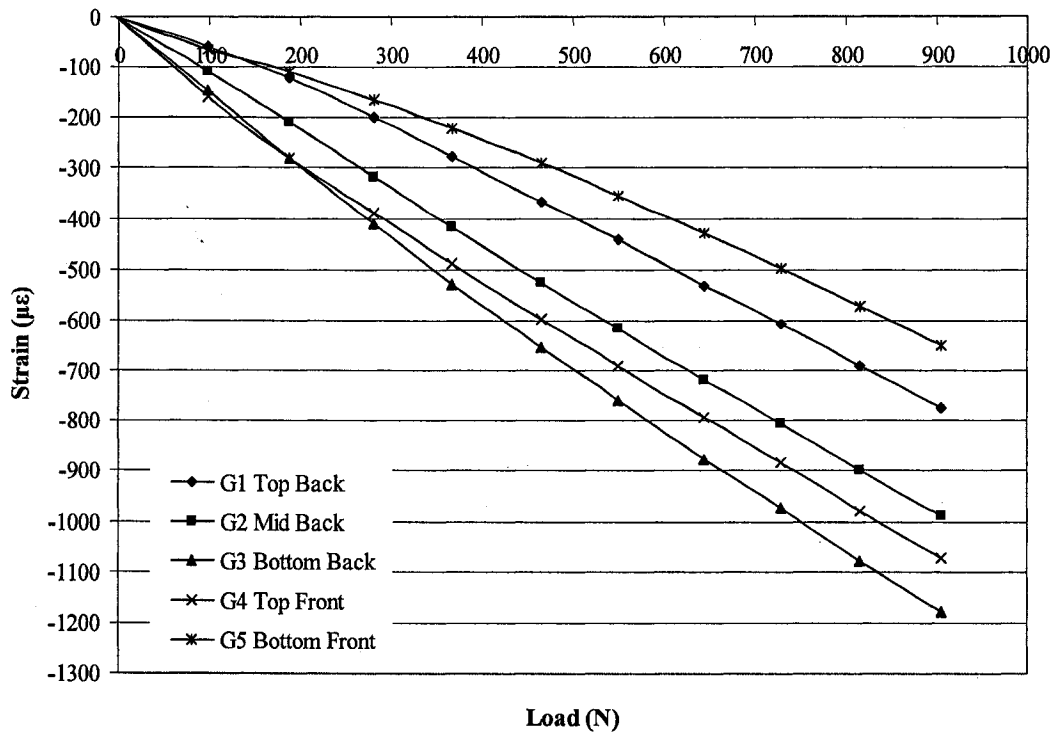
Figure G.7: Strain results from the first PVC specimen compression retest in MABTA. G1, G2, G3, G4, and G5 are the individual strain readings at the specified location. Note lines are for visual purposes only.

230
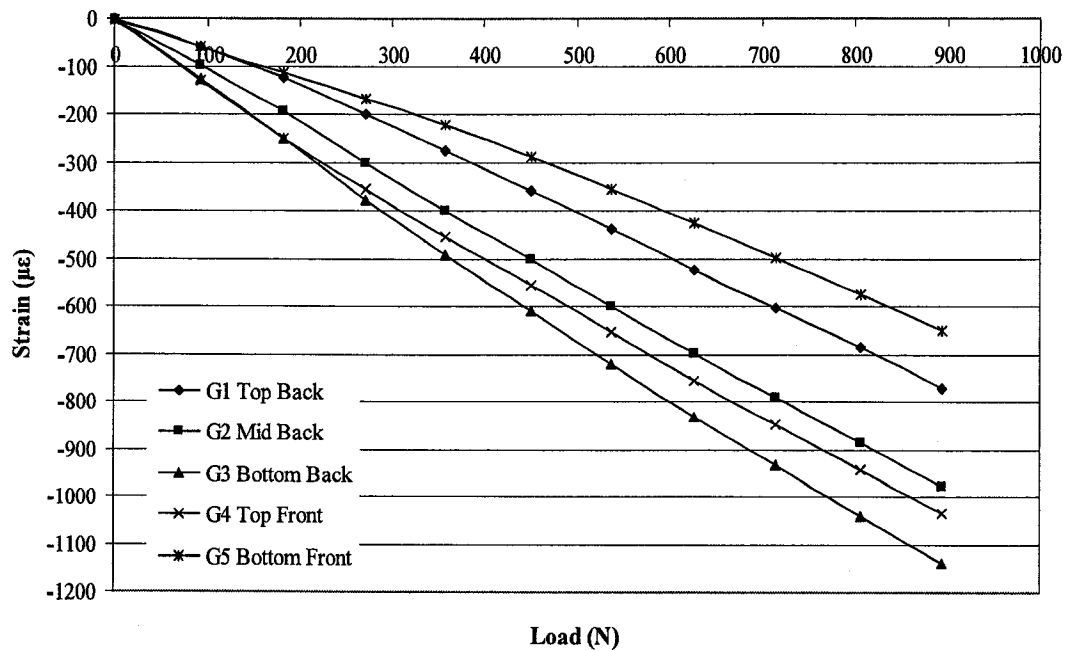
Figure G.8: Strain results from the second PVC specimen compression retest in MABTA. G1, G2, G3, G4, and G5 are the individual strain readings at the specified location. Note lines are for visual purposes only.

In theory, if a constant geometry specimen was subjected to pure axial compression along the specimen's central axis, all strain gauge values should be identical. However, reviewing the results in Table G.2 and Table G.3 as well as Figure G.3 through Figure G.8, the specimen appears to be subjected to bending as G1, the top back gauge, has measured a lower compressive strain than all the other gauges. Possible causes for these findings are specimen misalignment in the machine or a possibly warped specimen.

G.3.2 PVC Compression in MTS

In an attempt to determine the cause(s) of the bending seen in the previous PVC specimen tests, the specimen was placed into a 500N MTS Synergie 400 uniaxial testing machine (Model #2700094, MTS Systems Corporation, Eden Prairie, MN, USA) (Figure

231

G.9a). Loading ends of similar diameter to that of the specimen was chosen to produce the best alignment possible (Figure G.9b).
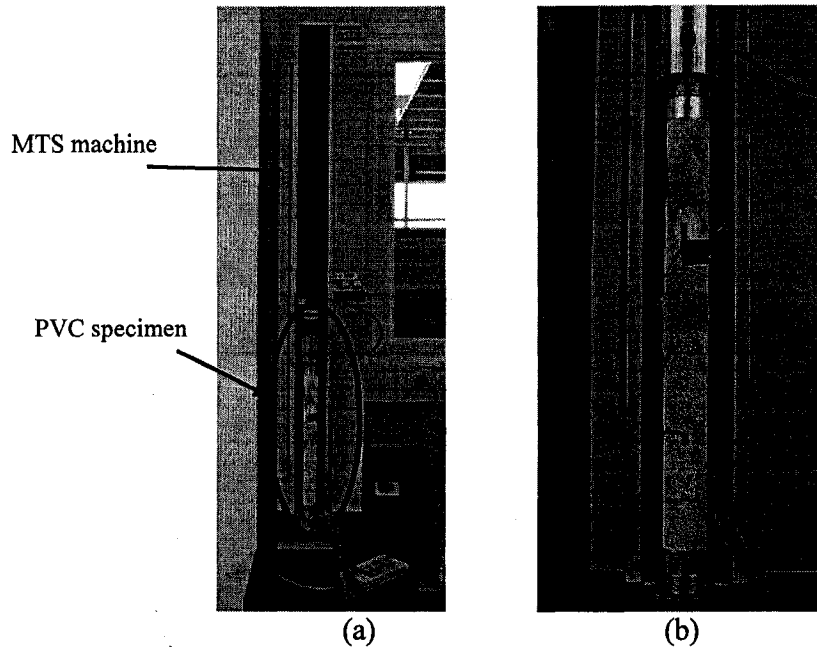
Figure G.9: a. MTS Synergie 400 uniaxial testing machine; b) PVC specimen situated in MTS machine

Due to the software and load constraints of the MTS Synergie 400, a slightly different loading protocol was used. Once the desired load has been reached, the MTS software automatically unloads the specimen hence requiring four separate tests each with a different final load value. Additionally, the MTS Synergie 400 has a loading capacity of 500 N, slightly half the original load placed on the specimen while in MABTA. To ensure that no damage was done to the MTS Synergie 400, a maximum load of 356 N (~80 lb) was applied to the specimen.

Considering the above-mentioned constraints, four tests were conducted on the PVC specimen with the first test loading the specimen up to approximately 89 N (~20 lb), second test loading to approximately 179 N (~40 lb), third test to approximately 269 N

232

(~60.5 lb) and the final test to approximately 356 N (~80 lb). The results of these tests are

summarized in Table G.4 and shown in Figure G.10.

Table G.4: PVC Strain results from MTS compression tests

Test	Load		Strain (με)				
	lb	N	G1 Top Back	G2 Mid Back	G3 Bottom Back	G4 Top Front	G5 Bottom Front
1	19.96	88.79	-112.68	-120.76	-117.98	-79.46	-68.06
2	40.17	178.66	-206.70	-222.44	-216.68	-159.98	-151.96
3	60.47	268.99	-312.30	-318.64	-302.44	-239.36	-246.28
4	80.14	356.49	-412.82	-413.08	-385.26	-313.90	-336.62
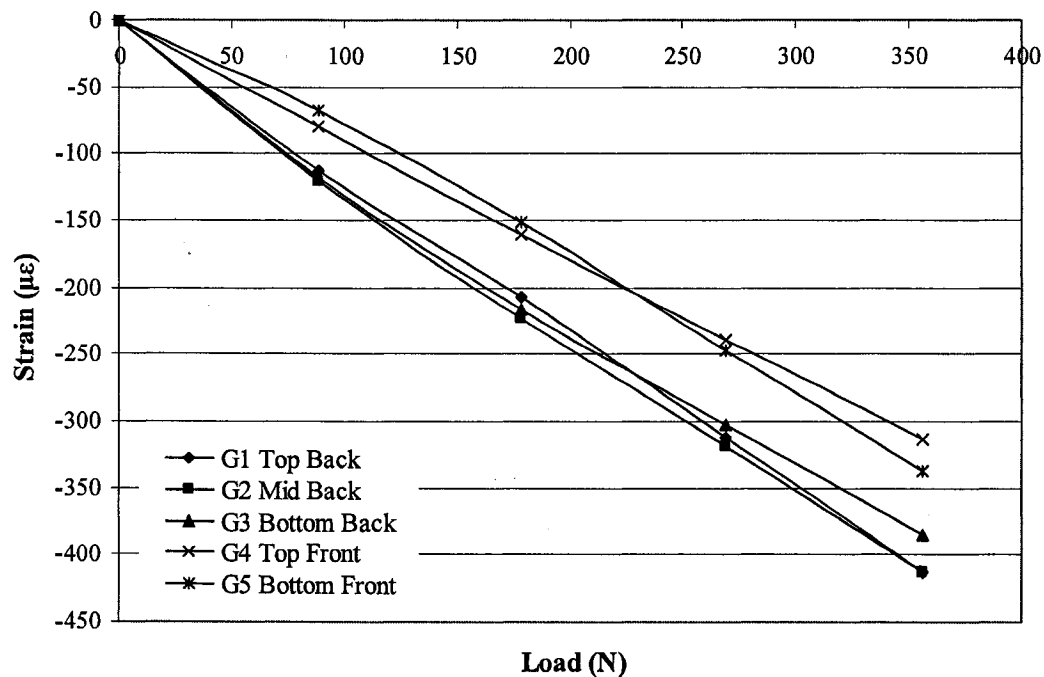
Figure G.10: PVC strain results for MTS compression test. Note lines are for visual purposes only.

If no bending occurred, all strain gauge values should be reading approximately

the same values. Unfortunately this did not occur as the three back gauges (G1, G2 and

G3) are reading much higher than the two front gauges (G4 and G5) with the top back

gauge (G1) reading approximately 100με higher than the top front gauge (G4) at the

maximum loading condition. This suggests that the specimen was subjected to bending which was not caused by MABTA.

G.4 Range of Error

While trying to adjust the alignment of the PVC specimen between the two loading ends, it was observed that the piece slightly pivoted on one end thus the bending results seen in both MTS and MABTA compression results could be caused from a slight angle at the end of the piece, meaning that the ends are not parallel. Even though both ends of the specimen were faced off in a manual lathe, slight rotation could have occurred due to the long length of the specimen, causing slight misalignment at the ends. Also the bending results could have been caused by slight misalignment in position in both MABTA and the MTS.

Calculations were done at a load of 269 N (~60 lb) to find out how much misalignment, δ, would cause 100$\mu\varepsilon$ difference between the front and back gauges. Figure G.11 is the free body diagram (FBD) of the PVC specimen in the MTS machine.

234
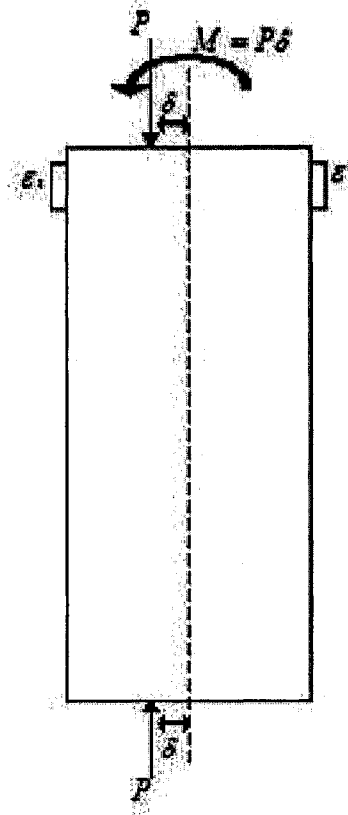
Figure G.11: FBD of PVC Specimen in MTS

To relate stress to strain in a purely axial stress state (i.e. no shear stress, internal pressure) Hooke's law is used

$$\sigma = E\varepsilon \tag{1}$$

Where, E is the elastic modulus, ε is the strain and the stress, σ, can be found using the above FBD as:

$$\sigma = -\frac{P}{A} \pm \frac{P\delta \cdot c}{I} \tag{2}$$

Where, c, the distance from the centroid to the outer wall position is:

$$c = \frac{dout}{2} \tag{3}$$

235

Substituting (2) into (1) and isolating strain we find:

$$\varepsilon = \left(-\frac{P}{A} \pm \frac{P\delta c}{I}\right) \cdot \frac{1}{E}$$ (4)

In the case of strain values at opposing outer walls, $c=\pm d_{out}/2$, we find:

$$\varepsilon_1 = \left(-\frac{P}{A} + \frac{P\delta c}{I}\right) \cdot \frac{1}{E}$$ (5)

$$\varepsilon_2 = \left(-\frac{P}{A} - \frac{P\delta c}{I}\right) \cdot \frac{1}{E}$$ (6)

The difference in strain is the subtraction of equations (5) and (6)

$$\Delta\varepsilon = \varepsilon_1 - \varepsilon_2$$ (7)

Using this diagram, equations (1) through (7) and the specimen's dimensions and material properties (Table G.1), a sample calculation was completed. The sample calculation was completed for a load (P) of 268.99 N (60.47 lb) and a misalignment (δ) of 1mm (3.94×10^{-6} in).

The strain values at opposing outer walls are:

$$\varepsilon_1(\delta) = \left(-\frac{60.47lb}{0.5485in} + \frac{60.47lb \cdot \delta \cdot (0.5 * 1.314in)}{9.44 \times 10^{-2} in^4}\right) \cdot \frac{1}{2.60 \times 10^2 \, psi}$$ (8)

$$\varepsilon_1(\delta) = (0.424 + 1.619\delta)in^{-1}$$ (9)

$$\varepsilon_2(\delta) = \left(-\frac{60.47lb}{0.5485in} - \frac{60.47lb \cdot \delta \cdot (0.5 * 1.314in)}{9.44 \times 10^{-2} in^4}\right) \cdot \frac{1}{2.60 \times 10^2 \, psi}$$ (10)

$$\varepsilon_2(\delta) = (0.424 - 1.619\delta)in^{-1}$$ (11)

Substituting strain values from (9) and (11) into (7), the strain difference becomes:

$$\Delta\varepsilon(\delta) = \varepsilon_1(\delta) - \varepsilon_2(\delta)$$
$$\Delta\varepsilon(\delta) = (0.424 + 1.619\delta)in^{-1} - (0.424 - 1.619\delta)in^{-1}$$ (12)

236

$$\Delta\varepsilon(\delta) = (3.236 \cdot \delta)in^{-1} \tag{13}$$

From the above calculation and Figure G.12, it was found that a 1 mm misalignment would cause a strain difference of 127µε.
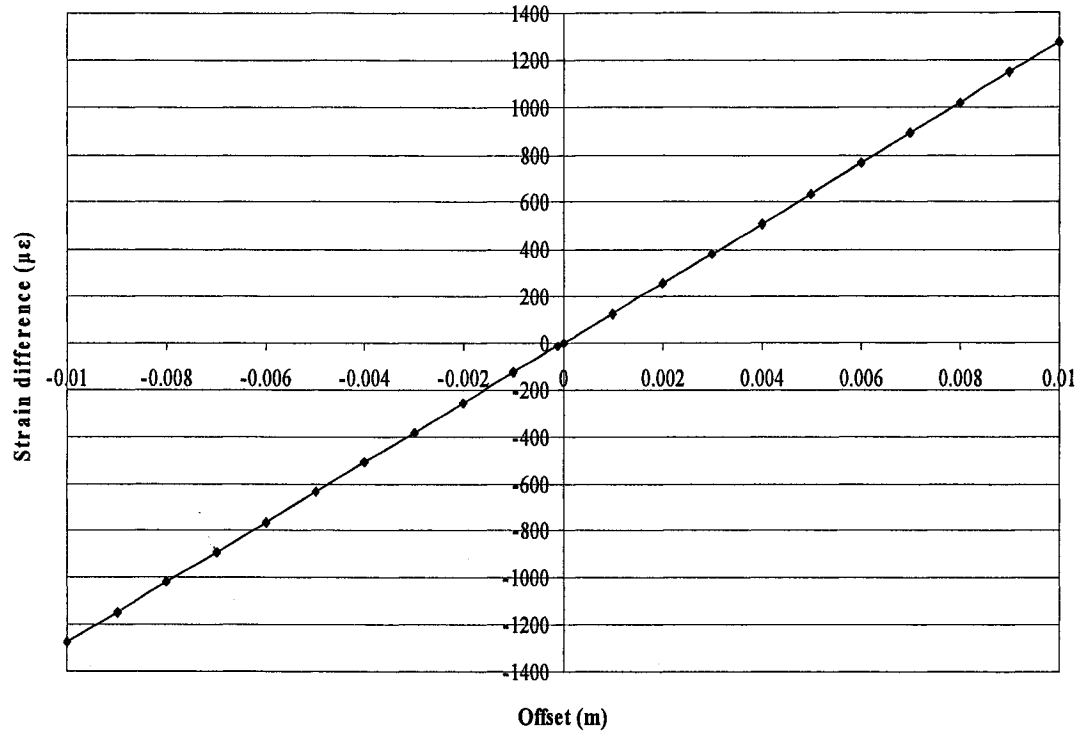
Figure G.12: Strain difference between front and back strain gauges if load was misaligned off the central axis of the PVC specimen. Note lines are for visual purposes only.

Calculations were done at each load increment to determine what angle, if ends were not perfectly flat, would cause the measured strain results. Figure G.13 is the FBD of the PVC specimen in the MTS machine.
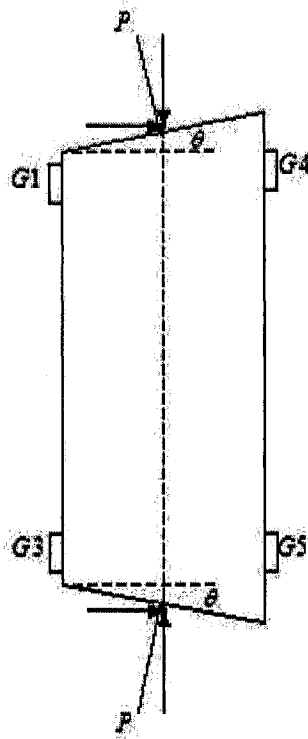
Figure G.13: FBD of PVC specimen in MTS if ends were uneven

Using Hooke's Law in equation (1) and the above FBD, the equation for strain is:

$$\varepsilon = \left(-\frac{P}{A} \pm \frac{P\delta c}{I} \right) \cdot \frac{1}{E} \tag{8}$$

In the case of strain values at opposing outer walls, we find:

$$\varepsilon_1 = \left(-\frac{P\cos\theta}{A} + \frac{P\sin\theta lc}{I} \right) \cdot \frac{1}{E} \tag{9}$$

$$\varepsilon_2 = \left(-\frac{P\cos\theta}{A} - \frac{P\sin\theta lc}{I} \right) \cdot \frac{1}{E} \tag{10}$$

The strain difference is the subtraction of equations (9) and (10):

$$\Delta\varepsilon = \varepsilon_1 - \varepsilon_2 = 2\left(\frac{P\sin\theta lc}{IE} \right) \tag{11}$$

238

Isolate and solve for the possible angle of inclination, θ at the ends of the specimen:

$$\theta = \sin^{-1}\left(\frac{\Delta\varepsilon EI}{Pldout}\right) \tag{12}$$

The experimental strain results for the PVC specimen in the MTS Synergie 400 indicated that the highest strain occurred in the middle of the specimen with lower strain occurring near the ends (Table G.4). From these results it was thought that both ends could have a small inclination. The angle required to produce the experimental strain results was calculated for both top and bottom ends. The FBD (Figure G.13), equations (8) through (12) and specimen dimensions and material properties (Table G.1) were all used in this calculation. In addition the material properties (Table G.1) for this specimen are not exactly known so the angle was calculated based on the maximum and minimum modulus of elasticity for extruded PVC pipe (Table G.5) (Online Information Materials Resource). A sample calculation of the possible inclination of the PVC pipe's ends for Test 9, using the minimum value for modulus of elasticity is presented below.

$P = 268.99N$
$P = 60.47lb$

The length of the PVC pipe is:

$$l = 12.7in \tag{13}$$

From the experimental results from Test 9:

$$\varepsilon_1 = -3.123x10^{-4} \tag{14}$$

$$\varepsilon_2 = -2.394x10^{-4} \tag{15}$$

Therefore,

$$\theta = \sin^{-1}\left(\frac{\left[-3.123x10^{-4} - \left(-2.394x10^{-4}\right)\right] \cdot 2.60x10^2\, psi \cdot 9.444x10^{-2}\, in^4}{60.47lb \cdot 12.7in \cdot 1.314in}\right) \tag{16}$$

239

$$\theta = -1.017x10^{-4}\,{}^{\circ}$$

Table G.5: Calculated angle of ends from measured maximum strain results

	Angle of offset (°)							
	Test 7		Test 8		Test 9		Test 10	
	Top	Bottom	Top	Bottom	Top	Bottom	Top	Bottom
E_{min}	$-1.40x10^{-4}$	$-2.11x10^{-4}$	$-9.81x10^{-5}$	$-1.36x10^{-4}$	$-1.02x10^{-4}$	$-7.83x10^{-5}$	$-1.04x10^{-4}$	$-5.12x10^{-5}$
E_{max}	-0.378	-0.568	-0.264	-0.366	-0.274	-0.211	-0.280	-0.138

From Table G.5 it can be seen that with using the maximum modulus of elasticity value, the angle required to produce the measured strain results has a maximum angle of 0.0002° for the top end and an angle of 0.6° for the bottom end.

G.5 Conclusions

From the above calculations, it was found that the experimental results are comparable to the theoretical results. If the specimen is only 1mm from centre then a strain difference greater than 100με can be measured for a PVC material. Also if the edges of the specimens are slightly uneven, then the recorded strain results are reasonable. This eliminates that MABTA was the source of the bending and therefore there is good agreement between experimental and theoretical strain values for the known geometry specimen.

These results indicate how imperative alignment is when comparing theoretical strain results to experimental strain results and as shown above slight misalignment can cause significant differences in results.

References

MatWeb: Material Property Data. Online Information Materials Resource. 8 May 2008 < http://www.matweb.com/search/DataSheet.aspx?MatID=78512>.

240

Appendix H: Composite Bone on Bone Experiments

Composite bones have been used extensively throughout the research community. Composite femurs have been used as substitutes for cadaveric specimens to investigate the performance of total knee and total hip prostheses and to validate finite element models (Waide et al., 2003; Completo et al., 2007a; Completo et al., 2007c; Papini et al., 2007; Szivek and Gealer, 1991; Heiner and Brown, 2001; Cristofolini et al., 1996) but only a few studies have been completed on the composite tibia (Completo et al., 2007b; Completo et al., 2008; Cristofolini and Viceconti, 2000; Gray, 2007). A third generation composite tibia (#3301) and composite femur (#3303) from Pacific Research Labs (Vashon Island, WA) were used for all composite bone experiments.

H.1 Experimental Set-up

The following instruments were used to measure the experimental strains along the cortex of composite bone (Figure H.1): a personal computer with data acquisition software (National Instruments LabVIEW 8.5) to record strain values, a data acquisition system (SCXI-1000 chassis with two SCXI-1314 and one SCXI-1317 strain gauge terminal blocks, National Instruments) to excite the system and sample values, a signal conditioner (AMTI MiniAmp MSA-6) to measure loads placed on the specimen, MABTA and a composite tibia (Figure H.2) and femur (Figure H.3) instrumented with strain gauges. Table H.1 and Table H.2 indicates the strain gauge positions with respect to the centre of the bottom face of the respective bone pots for the tibia and femur.

241

MSA-6 Signal
Conditioner

SCXI-1314
Front
Mounting
Terminal
Block

MABTA

Composite Bone   Personal computer
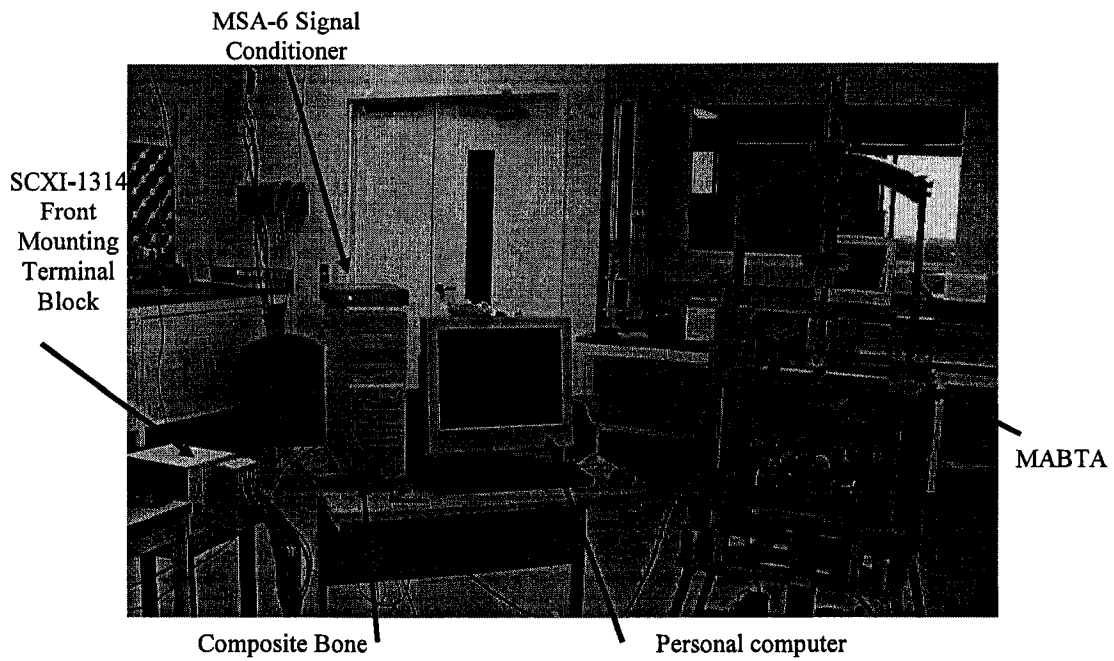
Figure H.1: Components required for finding the experimental strain along the cortex of composite bone

(a)   (b)   (c)   (d)
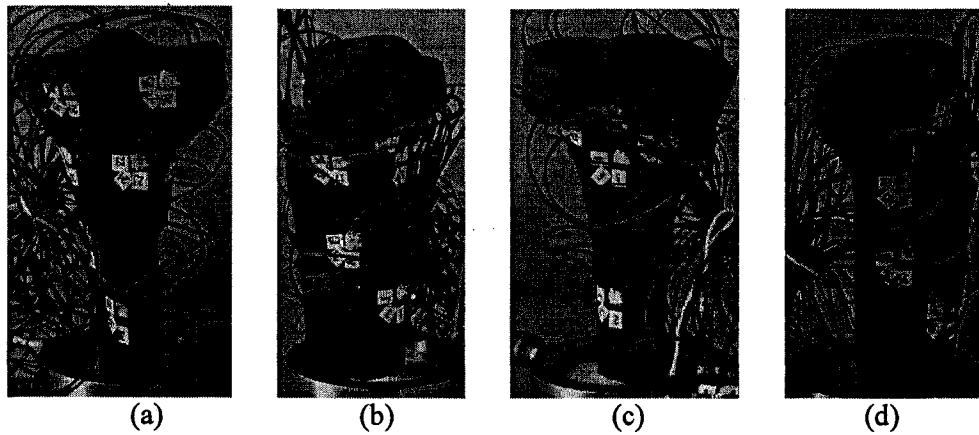
Figure H.2: The thirteen tibial strain rosette positions: a) Anterior: Rosettes 8-11 b) Lateral: Rosettes 6-7 c) Posterior: Rosettes 1-5 and d) Medial: Rosettes 12-13

242

Table H.1: Tibia strain gauge coordinates with respect to centre of the bottom face of bone pot (all dimensions are in mm)

Rosettes	Gauges	Distance of SG from Bone pot		
		X	Y	Z
1	SG1-3	-6.612	6.810	-75.057
2	SG4-6	-2.849	8.850	-127.176
3	SG7-9	14.955	15.798	-134.340
4	SG10-12	-3.753	14.358	-145.001
5	SG13-15	-19.522	7.000	-139.601
6	SG16-18	-21.288	-13.138	-129.221
7	SG19-21	-16.864	-7.934	-98.486
8	SG22-24	-7.254	-34.554	-130.762
9	SG25-27	-16.533	-27.159	-158.608
10	SG28-30	19.006	-24.616	-154.005
11	SG31-33	22.079	-8.047	-125.825
12	SG34-36	14.687	-7.651	-96.423
13	SG37-39	0.396	-25.347	-73.858

(a)   (b)   (c)   (d)

Figure H.3: The thirteen femoral strain rosette positions: a) Anterior: Rosettes 1-4 b) Medial: Rosettes 5-6 c) Posterior: Rosettes 7-11 and d) Lateral: Rosettes 12-13

243

Table H.2: Femur strain gauge positions with respect to centre of the bottom face of bone pot (all dimensions are in mm)

Rosettes	Gauges	X	Y	Z
1	SG1-3	-1.202	-24.097	-74.622
2	SG4-6	-0.547	-32.455	-122.579
3	SG7-9	12.509	-44.303	-143.597
4	SG10-12	-24.318	-32.132	-153.054
5	SG13-15	-19.831	-14.950	-102.224
6	SG16-18	-23.365	-14.728	-123.093
7	SG19-21	0.587	0.484	-78.934
8	SG22-24	2.081	-5.060	-126.829
9	SG25-27	-19.545	5.155	-147.140
10	SG28-30	24.730	-0.065	-139.873
11	SG31-33	4.973	-7.239	-164.800
12	SG34-36	21.535	-15.220	-101.474
13	SG37-39	26.126	-21.733	-124.200

H.2 Theoretical Validation

Experimental strains are recorded on the composite bone through thirteen Omega 45°, tri-axial rosettes (SGD-2/350-RY63). Theoretical strain calculations (Appendix I) were completed to examine if the obtained experimental results are as expected.

Throughout the experiment and the calculation of the theoretical strain values, many assumptions were considered and could be sources of difference, between theoretical and experimental von Mises (VM) strain values. Both experimental and theoretical calculations as well as the individual experiments can have associated errors; the theoretical and experimental assumptions or possible sources of difference are listed below.

- Material assumed isotropic.

- Only considered cortical bone material properties and not the combination of cortical and cancellous bone for bending calculations.

244

- Gauge is on a cubic element with the force acting parallel to the gauge position and perpendicular to the strain acting in the depth of the specimen.

- Loading occurred within the elastic range of composite bone.

- Measured loading contact positions, strain gauge positions and centre of gravity positions are accurate.

- Only considered theoretical strain values based on loads measured at the load cell centre.

- Coordinate system of load cell and coordinate system of reconstructed tibia used to find the strain gauge positions and relative distances may not be identical

H.3 Bone on Bone Loading

The third generation composite tibia and femur were placed into MABTA and used for bone on bone loading. Because of data acquisition limitations only strains on one bone could be only measured at a time. Also since the only recorded loads occur at the 6 DOF load cell at the base of the tibial bone pot, the specimen to be loaded and measured was placed in this position. For example in the composite tibia compression experiments, the specimens were placed in anatomical position with the tibia distal to the femur (Figure H.4). However, in the composite femur compression experiment, the femur was placed inferior to the tibia (Figure H.5).

245

Composite Femur
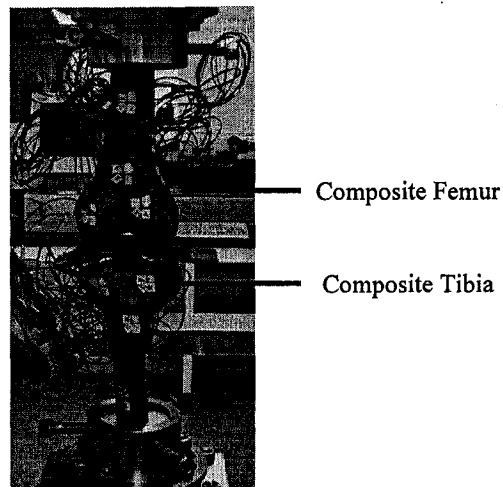
Composite Tibia

Figure H.4: Specimen position for composite tibia compression

Composite Tibia
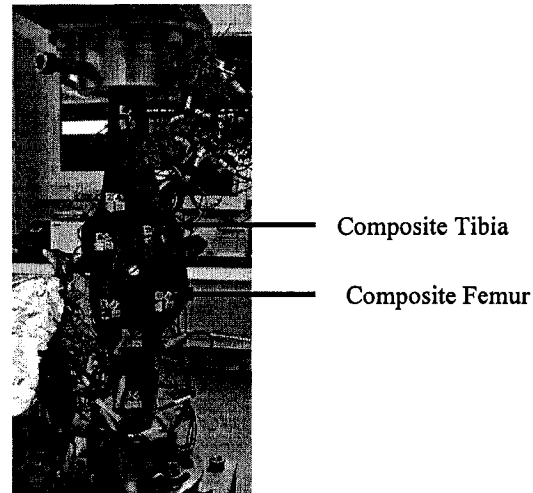
Composite Femur

Figure H.5: Specimen position for composite femur compression

Pieces of foam and rubber were placed in between the joint to act as artificial menisci, to distribute the load across the joint and to avoid point loading. The specimens were placed into MABTA and loaded to 1780 N (400 lb) compression using the procedures provided in Appendix F.

H.3.1 Composite Tibia Compression

The first composite bone on bone experiment measured the strains along the cortex of the composite tibia (Figure H.6).

246
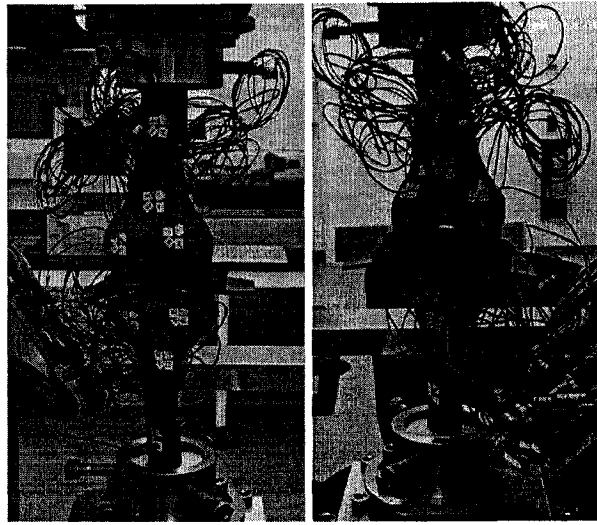
Figure H.6: Composite tibia and femur compression position

Experimental strains were recorded for 15 seconds at each 111 N (25 lb) increment until maximum load of 1780 N (400 lb). The test was repeated three times; at the end of each test the specimens were removed from MABTA and alignment of the tibial and femoral bone pot holders was recorded. It was measured that the alignment between the tibial and femoral bone pot holders had an overall maximum misalignment of 0.381 mm (30 divisions) after the completion of the first test. After the completion of the second and third test, the tibial and femoral bone pot holders were misaligned by 0.241mm (19 divisions) in the x-direction only for test 2 and 0.0762mm (6 divisions) in the x-direction and 0.1143 mm (9 divisions) in the y-direction for test 3. The experimental strain progression for test one, two and three are provided in Figure H.7 through Figure H.9.

247
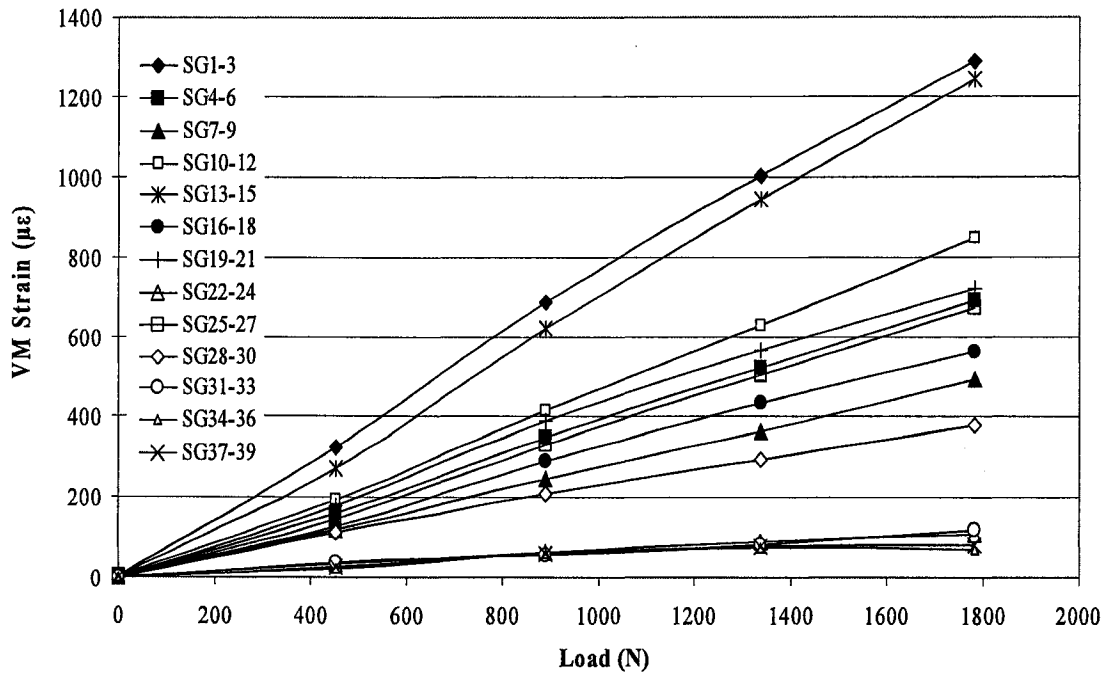
Figure H.7: Composite tibia experimental von Mises (VM) strain progression for test 1. Note lines are for visual purposes only.
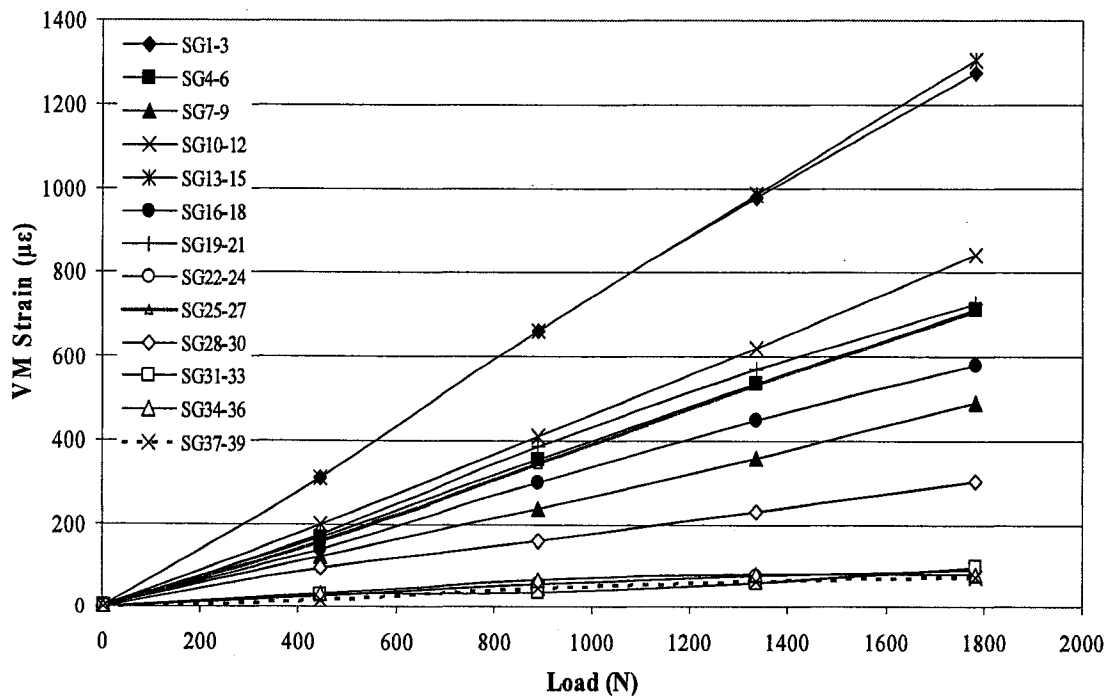
Figure H.8: Composite tibia experimental von Mises (VM) strain progression for test 2. Note lines are for visual purposes only.

248
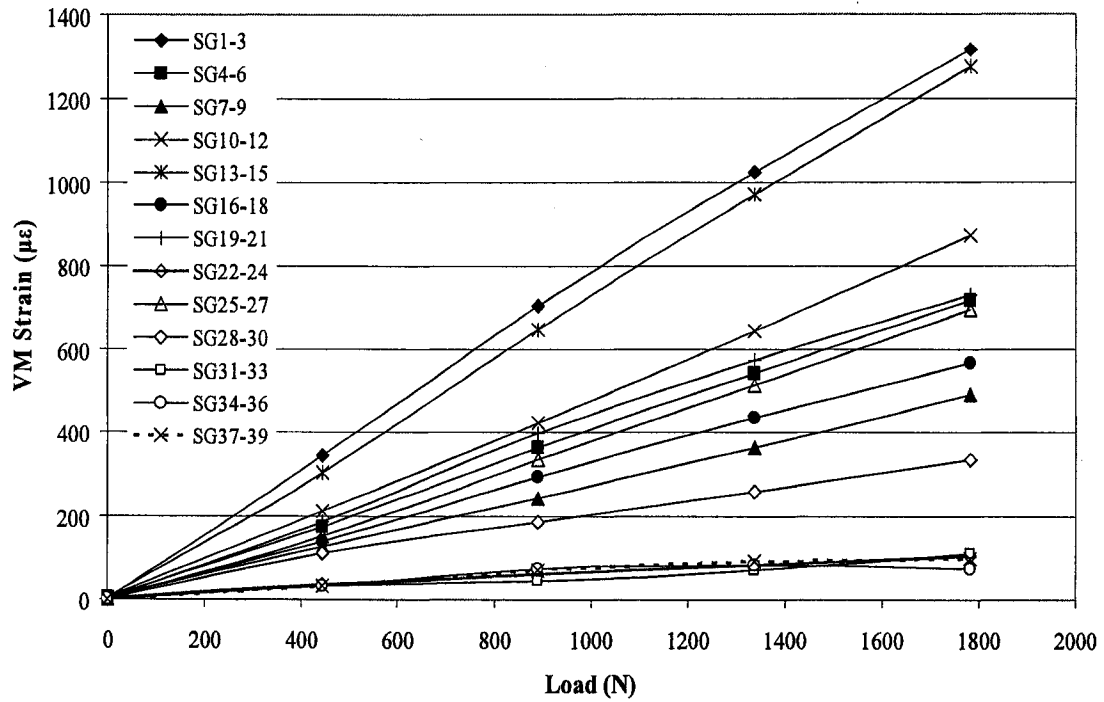
Figure H.9: Composite tibia experimental von Mises (VM) strain progression for test 3. Note lines are for visual purposes only.

Using the theoretical strain equations and the relative error equations found in Appendix I, the experimental and theoretical VM strains and their associated relative error were calculated for all three tests. Figure H.10 through Figure H.12 compare the theoretical and experimental values for all three tests, respectively. The error bars represent the calculated relative error for experimental and theoretical VM strains.

249
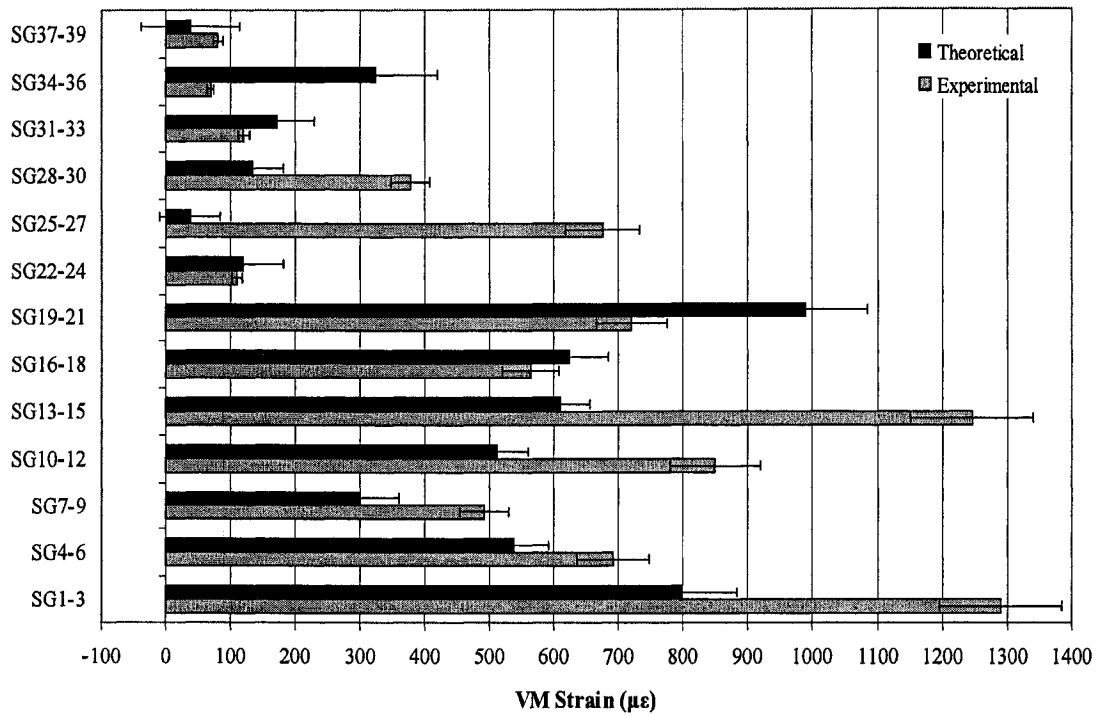
Figure H.10: Composite tibia first compression test experimental and theoretical von Mises (VM) strain with associated error at 1780 N
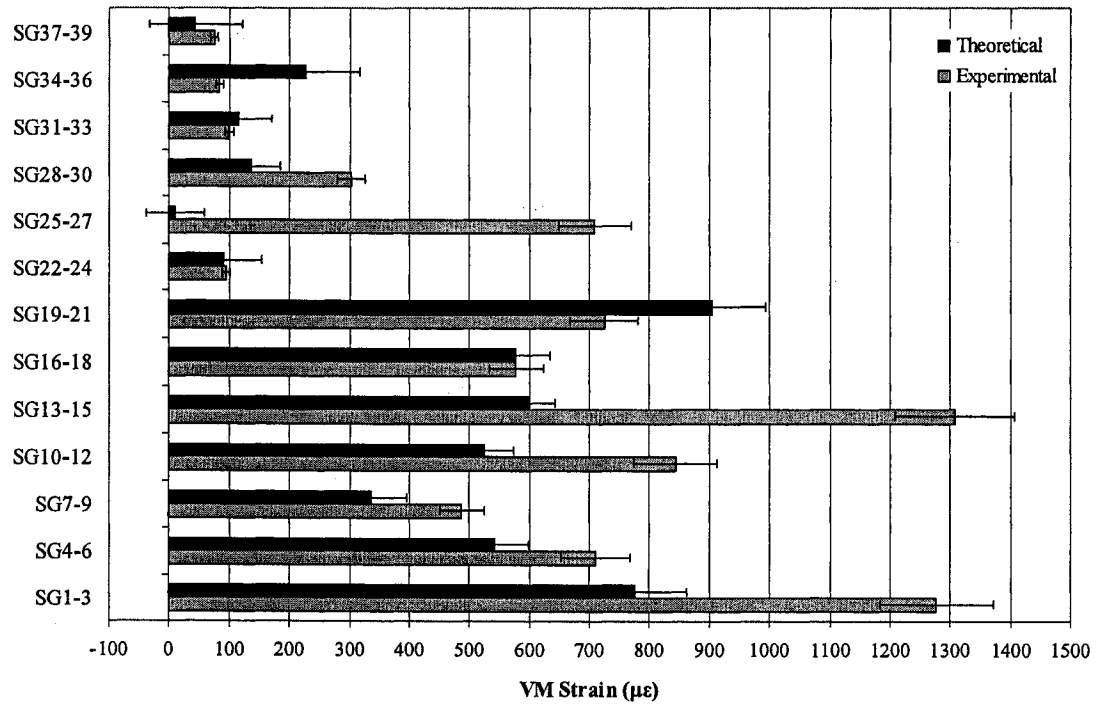
Figure H.11: Composite tibia second compression test experimental and theoretical von Mises (VM) strain with associated error at 1780 N

250
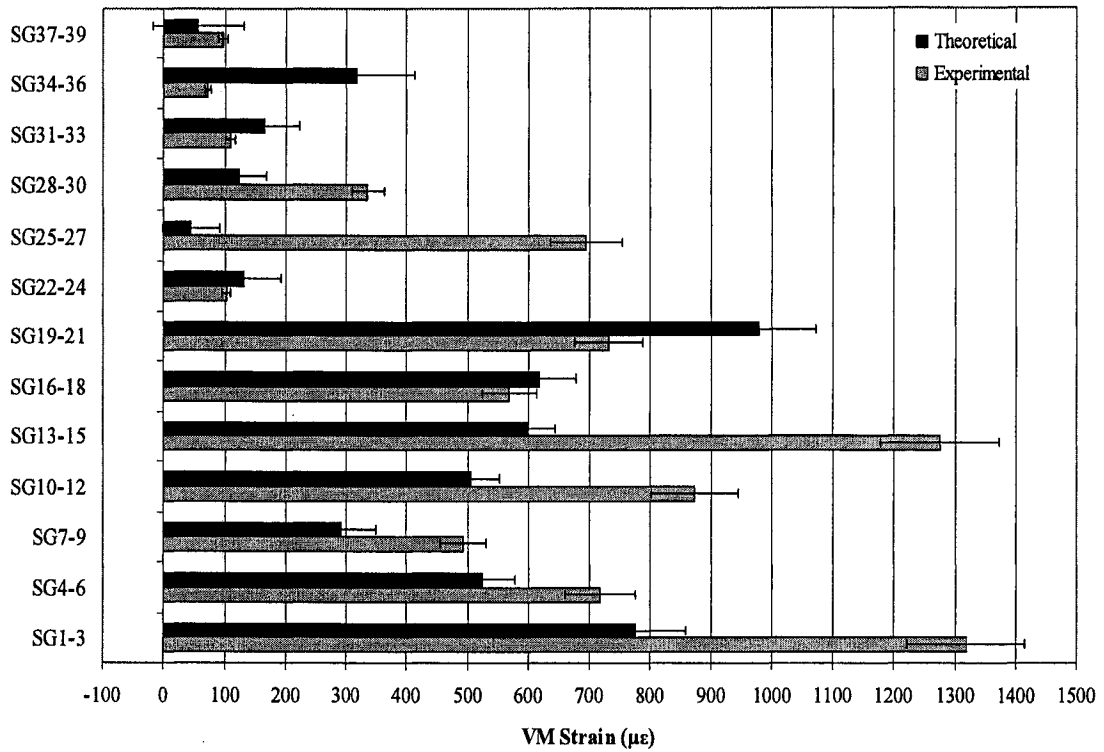
Figure H.12: Composite tibia third compression test experimental and theoretical von Mises (VM) strain with associated error at 1780 N

H.3.2 Composite Femur Compression

The second composite bone on bone experiment measured the strains along the cortex of the composite femur (Figure H.13).

Figure H.13: Composite femur and tibia compression femur.

251

Similar to the composite tibia compression, the composite femur was loaded to a maximum load of 1780 N (400 lb) with experimental strains recorded for 15 seconds at each 111 N (25 lb) increment. The test was repeated three times and at the end of each test the specimens were fully removed from MABTA and alignment of the tibial and femoral bone pot holders was recorded. The alignment between the tibial and femoral bone pot holders had a maximum misalignment of 0.2159 mm (17 divisions) in the x-direction after the completion of the first test. After the second and third test, the tibial and femoral bone pot holders were misaligned by 0.0762mm (6 divisions) in the x-direction for the second test and 0.0635 mm (5 divisions) in the x-direction for the third test. The experimental strain progressions for all three tests are provided in Figure H.14 through Figure H.16, respectively.
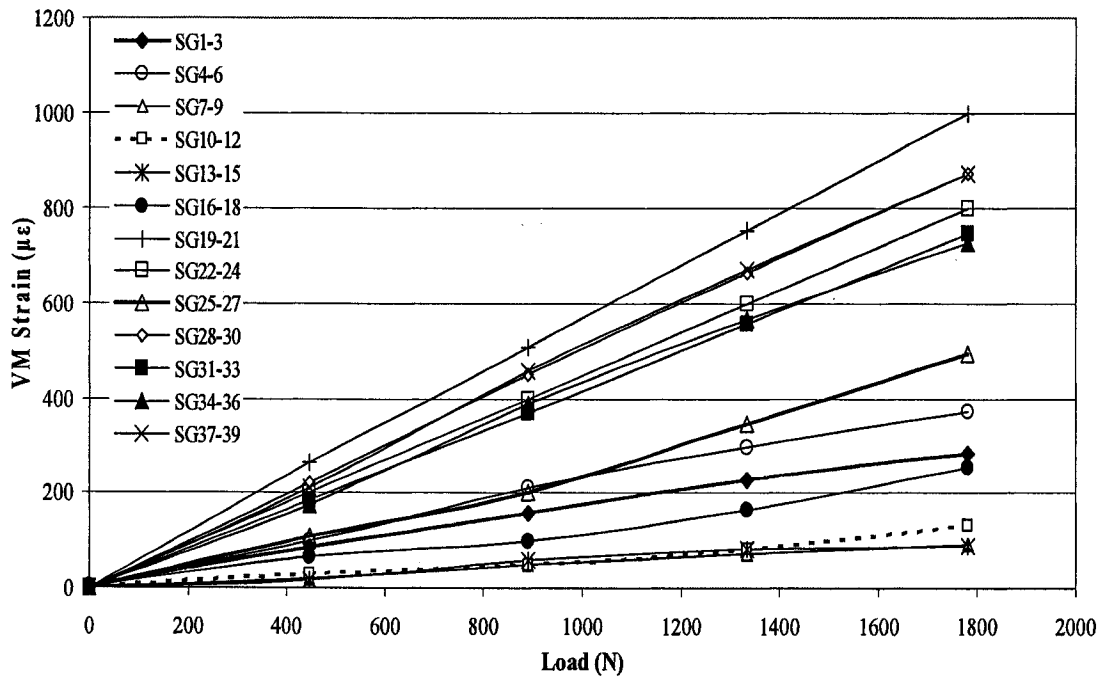
Figure H.14: Composite femur experimental von Mises (VM) strain progression for test 1. Note lines are for visual purposes only.

252
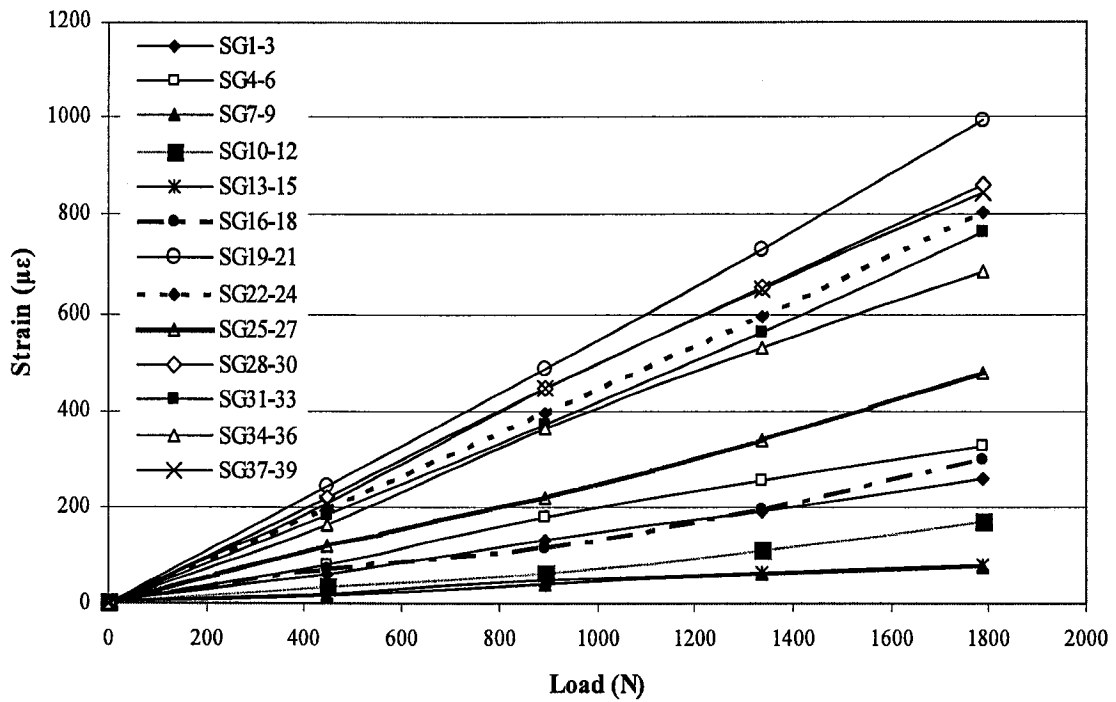
Figure H.15: Composite femur experimental von Mises (VM) strain progression for test 2. Note lines are for visual purposes only.
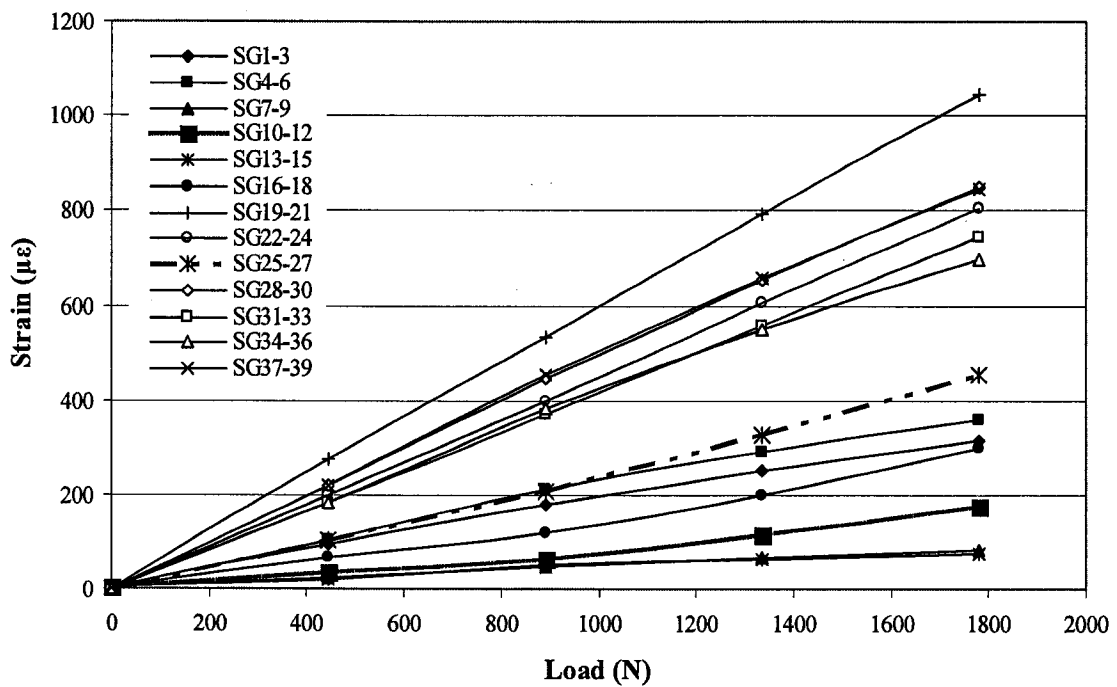
Figure H.16: Composite femur experimental von Mises (VM) strain progression for test 3. Note lines are for visual purposes only.

253

Using the theoretical strain equations and the relative error equations found in

Appendix I, the experimental and theoretical VM strains and their associated relative

error were calculated for all three tests. Figure H.17 through Figure H.19 compare the

theoretical and experimental values for all three tests, respectively. The error bars

represent the calculated theoretical and experimental error.
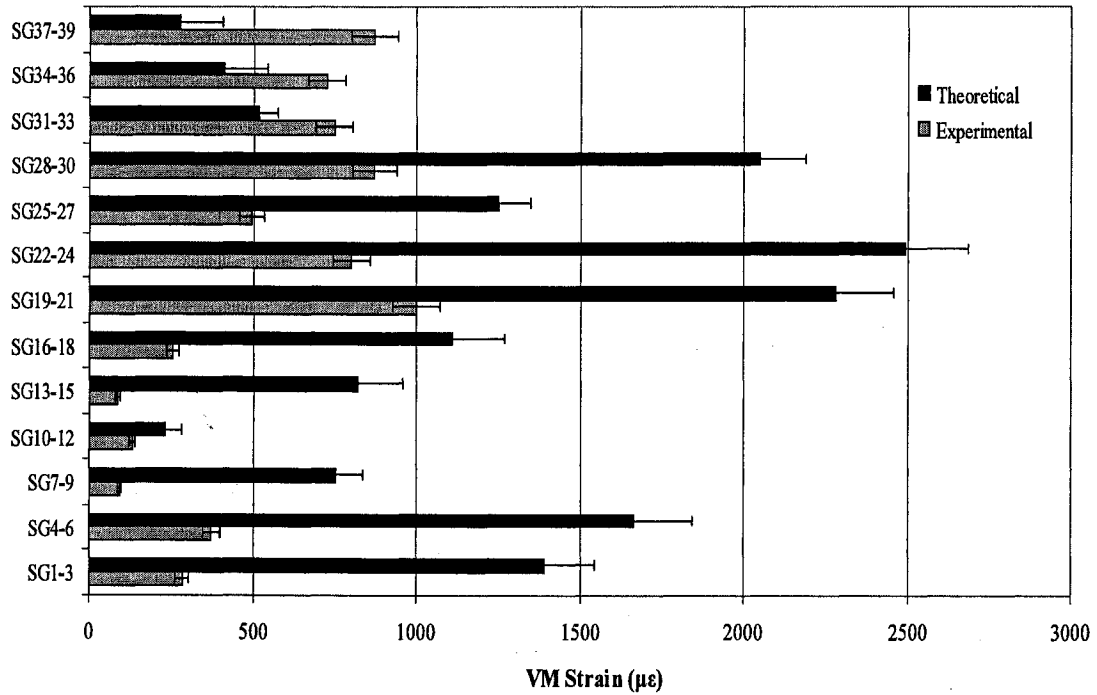
Figure H.17: Composite femur first compression test experimental and theoretical von Mises (VM) strain with associated error at 1780 N
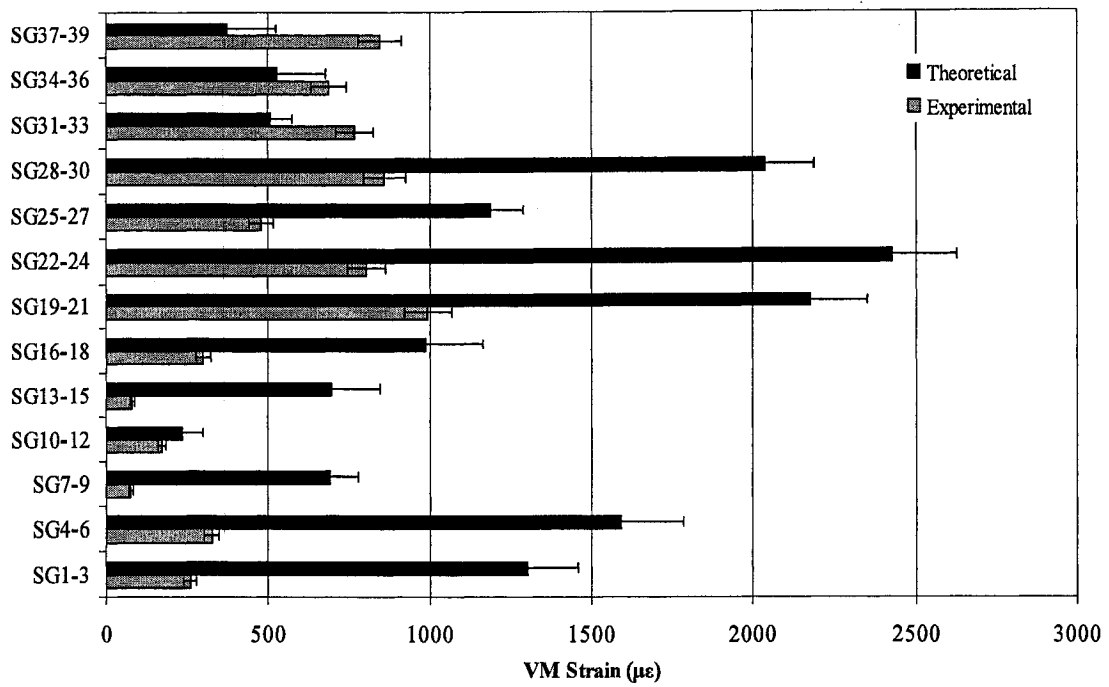
Figure H.18: Composite femur second compression test experimental and theoretical von Mises (VM) strain with associated error at 1780 N
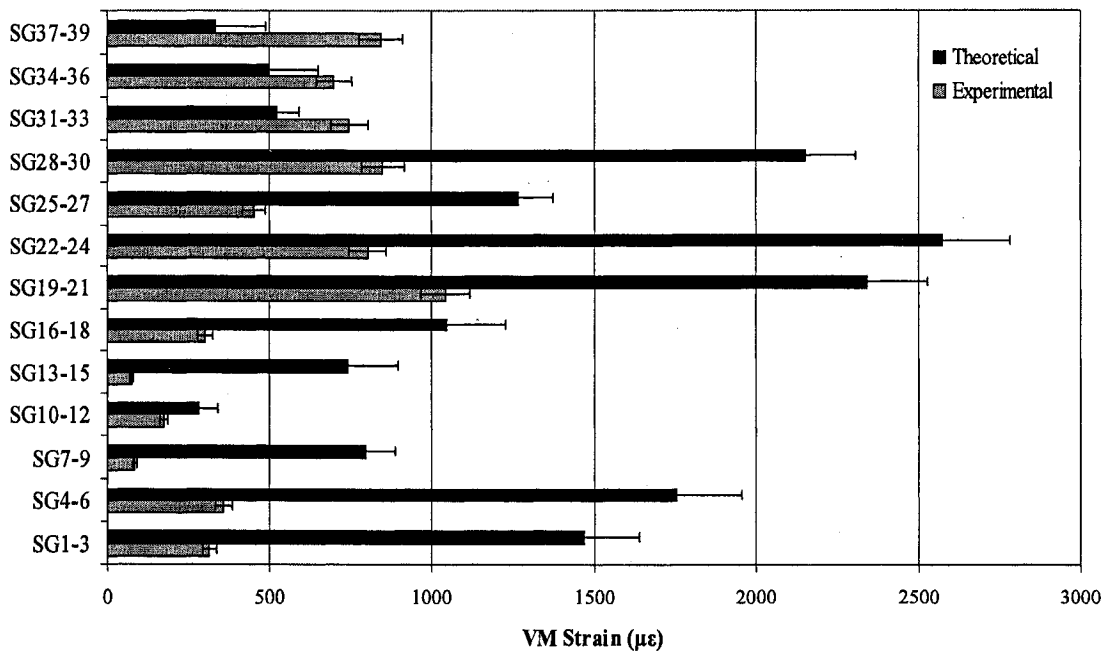
Figure H.19: Composite femur second compression test experimental and theoretical von Mises (VM) strain with associated error at 1780 N

255

References

Completo, A., Fonseca, F., Simões, J.A., 2007a. Experimental validation of intact and implanted distal femur finite element models. Journal of Biomechanics 40, 2467-2476.

Completo, A., Fonseca, F., Simões, J.A., 2007b. Finite Element and experimental cortex strains of the intact and implanted tibia. Journal of Biomechanical Engineering 129, 791-797.

Completo, A., Simões, J.A., Fonseca, F., 2007c. Experimental evaluation of strain shielding in distal femur in revision TKA. Experimental Mechanics, 1-8. (article in press)

Completo, A., Fonseca, F., Simões, J.A., 2008. Strain shielding in proximal tibia of stemmed knee prosthesis: experimental study. Journal of Biomechanics 41, 560-566.

Cristofolini, L., Viceconti, M., 2000. Mechanical validation of whole bone composite tibia models. Journal of Biomechanics 33, 278-288.

Cristofolini, L., Viceconti, M., Cappello, A., Toni, A., 1996. Mechanical validation of whole bone composite femur models. Journal of Biomechanics 29(4), 525-535.

Gray, H.A., Zavatsky, A.B., Taddei, F., Cristofolini, L., Gill, H.S., 2007. Experimental validation of a finite element model of a composite tibia. Journal of Engineering in Medicine 221 Part H, 315-324.

Heiner, A.D., Brown, T.D., 2001. Structural properties of a new design of composite replicate femurs and tibias. Journal of Biomechanics 34, 773-781.

Papini, M., Zdero, R., Schemitsch, E.H., Zalzal, P., 2007. The Biomechanics of Human Femurs in Axial and Torsional Loading: Comparison of Finite Element Analysis, Human Cadaveric Femurs, and Synthetic Femurs. Journal of Biomechanical Engineering 129, 12-19.

Szivek, J.A., Gealer, R.L., 1991. Comparison of the Deformation Response of Synthetic and Cadaveric Femora during Simulated One-Legged Stance. Journal of Applied Biomaterials 2, 277-280.

Waide, V., Cristofolini, L., Stolk, J., Verdonschot, N., Toni, A., 2003. Experimental investigation of bone remodelling using composite femurs. Clinical Biomechanics 18, 523-536.

Appendix I: Theoretical Strain Calculation

I.1 Theoretical Strain Equations

Theoretical analysis of composite and bovine bone used free body diagrams and equations (I.1) through (I.27), which cover beam theory, bending of asymmetric cross-sections and Mohr's circle, the theoretical and experimental von Mises (VM) strains at each rosette can be calculated. All listed equations are consistent between each theoretical analysis except for the bending moment equations; these change for each individual experiment and will be provided in the appropriate section.

I.1.1 Derivation of Axial Stress Equation

Due to the complicated geometry and material properties of bone, equations (I.1) to (I.13) were derived to determine the axial stress equation. Figure I.1 presents the cross section of a piece of bone with an applied force, F, moment, M and material properties. L_{cort}, A_{cort}, E_{cort} and I_{cort} represent length, area, modulus of elasticity and moment of inertia for cortical bone, respectively and L_{canc}, A_{canc}, E_{canc} and I_{canc} represent length, area, modulus of elasticity and moment of inertia for cancellous bone, respectively. The cross sectional area used in the following derivation was obtained from Au (Au, 2008), the elastic modulus for cortical bone was provided by Johnson (Johnson, 2007) and elastic modulus for cancellous bone was found from MatWeb (MatWeb).

257
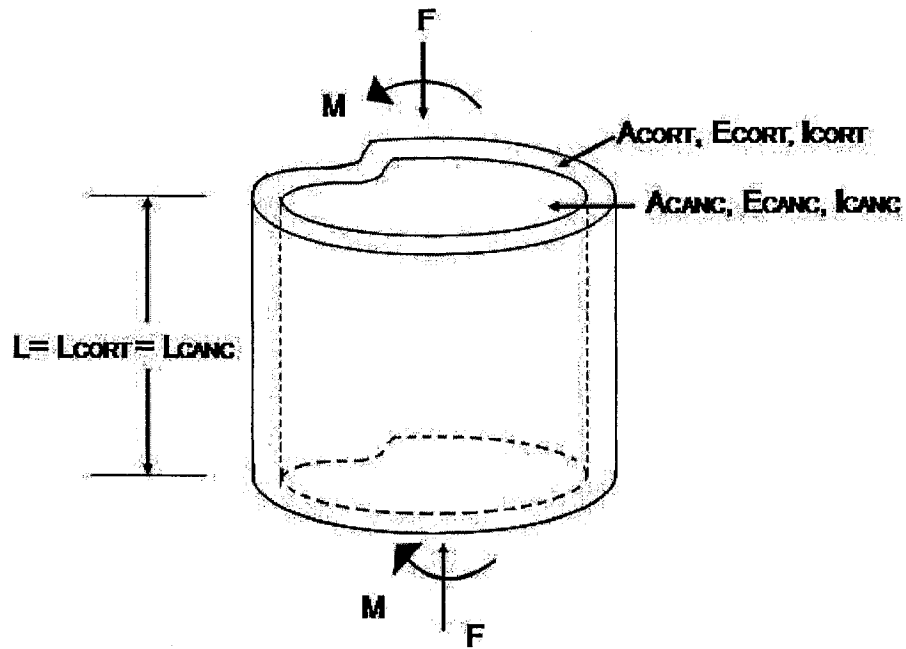
Figure I.1: Schematic of axially loaded bone cross section

From summation of forces:

$$F_{cort} + F_{canc} = F \tag{I.1}$$

The deflection of the cortical bone is:

$$\delta_{cort} = \frac{F_{cort} \cdot l_{cort}}{A_{cort} \cdot E_{cort}} \tag{I.2}$$

Similarly, the deflection of the cancellous bone is:

$$\delta_{canc} = \frac{F_{canc} \cdot l_{canc}}{A_{canc} \cdot E_{canc}} \tag{I.3}$$

Since both cortical and cancellous bone make up the specimen, the deflection, caused by axial forces only, of the cortical bone is equal to that of the cancellous:

$$\delta_{cort} = \delta_{canc} \tag{I.4}$$

Therefore,

$$\frac{F_{canc} \cdot l_{canc}}{A_{canc} \cdot E_{canc}} = \frac{F_{cort} \cdot l_{cort}}{A_{cort} \cdot E_{cort}} \tag{I.5}$$

258

Given that the cortical and cancellous bone are the same length

$$l_{cort} = l_{canc} \tag{I.6}$$

The force applied to the cancellous portion is:

$$F_{canc} = F_{cort} \frac{A_{canc} \cdot E_{canc}}{A_{cort} \cdot E_{cort}} \tag{I.7}$$

And the total force as a function of the force applied to the cortical bone is:

$$F = F_{cort} \left(1 + \frac{A_{canc} \cdot E_{canc}}{A_{cort} \cdot E_{cort}} \right) \tag{I.8}$$

The ratio between the two elastic modulus values for the composite tibia is:

$$\frac{E_{canc}}{E_{cort}} = \frac{0.104 GPa}{12.4 GPa \cdot} = 0.008387 \tag{I.9}$$

For rosette 1, strain gauges 1-3 on the composite tibia, the ratio of the two cross sectional areas is:

$$\frac{A_{canc}}{A_{cort}} = \frac{284 mm^2}{410 mm^2 \cdot} = 0.693 \tag{I.10}$$

Therefore,

$$F_{cort} = \frac{F}{\left(1 + \dfrac{A_{canc} \cdot E_{canc}}{A_{cort} \cdot E_{cort}} \right)} = \frac{F}{(1 + 0.0058)} \tag{I.11}$$

$$F_{cort} = 0.994 F \tag{I.12}$$

As a result the axial stress equation for the position of strain gauge 1-3 on the cortex is as follows:

$$\sigma_A = \frac{\dfrac{F}{\left(1 + \dfrac{A_{canc} \cdot E_{canc}}{A_{cort} \cdot E_{cort}} \right)}}{A_{cort}} \tag{I.13}$$

259

I.1.2 Derivation of Bending Stress Equation

Similar to the axial stress equation (I.13), the bending stress equation needs to be derived based on verified assumptions. Figure I.2 presents the cross section of a piece of bone labelled with the centre of gravity (CG) for the cortical cross section, the cancellous cross section and for the total cross section.
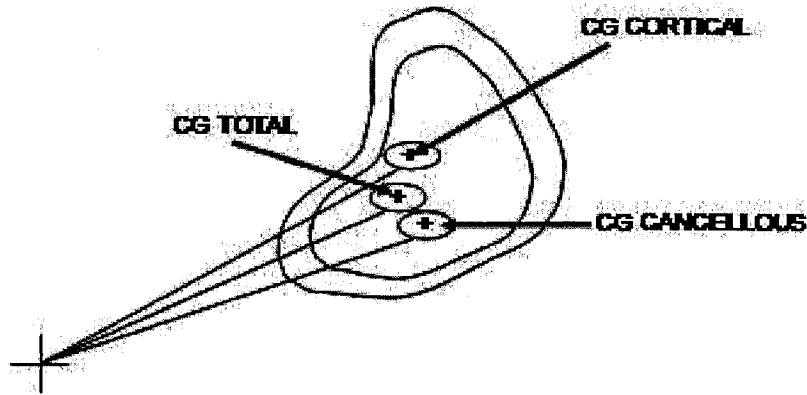
Figure I.2: Schematic of bending bone cross section

Comparing the flexural rigidities for the cortical ((I.14) and (I.15)) and cancellous ((I.16) and (I.17) bone, it was decided that the cancellous flexural rigidity is much smaller than the cortical and therefore can be ignored. Where *Ecort* has a modulus of elasticity of 12.4 GPa (Johnson, 2007), *Ecanc* has a modulus of elasticity of 0.104 GPa (MatWeb) and *Ixx* and *Iyy* for the cortical and cancellous bone were provided from Au (Au, 2008).

$$E_{cort}Ixx_{cort} = 12.4x10^9 * 5.53x10^4 = 685x10^{12}\,Nm^2 \tag{I.14}$$

$$E_{cort}Iyy_{cort} = 12.4x10^9 * 2.47x10^4 = 306x10^{12}\,Nm^2 \tag{I.15}$$

$$E_{canc}Ixx_{canc} = 0.104x10^9 * 1.22x10^4 = 1.2x10^{12}\,Nm^2 \tag{I.16}$$

$$E_{canc}Iyy_{canc} = 0.104x10^9 * 7.18x10^3 = 0.75x10^{12}\,Nm^2 \tag{I.17}$$

Therefore the bending stress equation using only cortical bone geometry is:

260

$$\sigma_B = \left(\frac{(MxIy + MyIxy)y - (MyIx + MxIxy)x}{IxIy - Ixy^2} \right) \tag{I.18}$$

The longitudinal stress, σ_L can be found by combining the equation for bending of asymmetric cross-sections with the stress equation for axial loading

$$\sigma_L = \sigma_A + \sigma_B \tag{I.19}$$

Thus,

$$\sigma_L = \frac{F \left/ \left(1 + \frac{A_{canc} \cdot E_{canc}}{A_{cort} \cdot E_{cort}} \right) \right.}{A_{cort}} + \left(\frac{(MxIy + MyIxy)y - (MyIx + MxIxy)x}{IxIy - Ixy^2} \right) \tag{I.20}$$

Where F is the total load placed on the composite tibia, A is the cross sectional area at the area of interest, Ix and Iy are the moment of inertias about the x and y axes, Ixy is the product of inertia, x and y are the distances from strain gauge to the centre of gravity and Mx and My are the moments about the x and y axes, respectively.

I.1.3 Composite Tibia and Femur Theoretical Equations

The shear stress is calculated from torsion of a thin walled asymmetric specimen. Mz is the torsion measured at the centre of the bone pot, A^* is the average cross sectional area between cortical and cancellous bone and t is the thickness of the wall at the position of the strain gauge:

$$\tau_{LT} = \frac{Mz}{2A^*t} \tag{I.21}$$

To calculate the theoretical VM stress, the only terms involved are the longitudinal stress, σ_L and the shear stress, τ_{LT}, thus:

$$\sigma' = \sqrt{\frac{2(\sigma_L)^2 + 6\tau_{LT}^2}{2}} \tag{I.22}$$

261

Using Hooke's Law for an isotropic material the theoretical VM strain is:

$$\varepsilon' = \frac{\sigma'}{E}$$

(I.23)

Where E is the modulus of elasticity for third generation composite bones and σ' is the VM stress acting on the composite tibia.

Similarly, the longitudinal strain, ε_L along the cortex of the composite tibia can be found:

$$\varepsilon_L = \frac{\sigma_L}{E}$$

(I.24)

Using Poisson's ratio, υ and the longitudinal strain, ε_L the strain in the transverse direction, ε_T and strain in the depth direction, ε_D can be found:

$$\varepsilon_T = \varepsilon_D = -\upsilon\varepsilon_L$$

(I.25)

The shear strain can be found with the following relationship:

$$\gamma_{LT} = \frac{\tau_{LT}}{G}$$

(I.26)

And the shear modulus, G can be computed using Poisson's ratio, υ and the modulus of elasticity, E:

$$G = \frac{E}{2(1+\upsilon)}$$

(I.27)

I.1.4 Bovine Tibia Theoretical Strain Equations

Bovine bone is considered transverse isotropic (Reilly and Burstein, 1974) and therefore the theoretical strain calculations vary from what was presented in Section I.1.3. All stress equations presented in the previous section are the same.

262

Using Hooke's Law for anisotropic materials, the longitudinal strain, ε_L, is:

$$\varepsilon_L = \frac{1}{E_L}\sigma_L - \frac{v_{LT}}{E_T}\sigma_T - \frac{v_{LD}}{E_D}\sigma_D \qquad \text{(I.28)}$$

Similarly, the transverse strain, ε_T, is:

$$\varepsilon_T = \frac{1}{E_T}\sigma_T - \frac{v_{TL}}{E_L}\sigma_L - \frac{v_{TD}}{E_D}\sigma_D \qquad \text{(I.29)}$$

The strain in the depth, ε_D, is:

$$\varepsilon_D = \frac{1}{E_D}\sigma_D - \frac{v_{DL}}{E_L}\sigma_L - \frac{v_{DT}}{E_T}\sigma_T \qquad \text{(I.30)}$$

Since longitudinal stress, σ_L, and torsion, τ_{LT}, are the only stresses acting on the bovine bone, the longitudinal strain, ε_L, becomes:

$$\varepsilon_L = \frac{1}{E_L}\sigma_L \qquad \text{(I.31)}$$

Since bone is transverse isotropic, the Poisson's ratio in the transverse direction equals the Poisson's ratio in the depth:

$$v_{LT} = v_{LD} \qquad \text{(I.32)}$$

And so,

$$\varepsilon_T = \varepsilon_D = -\frac{v_{TL}}{E_L}\sigma_L \qquad \text{(I.33)}$$

Using the shear stress equation (I.26) and the modulus of rigidity (I.27), the shear strain becomes:

$$\varepsilon_{LT} = \frac{\tau_{LT}}{2G_{LT}} \qquad \text{(I.34)}$$

The first and second theoretical principal strains are calculated from:

$$\varepsilon_{1,2} = \frac{\varepsilon_x + \varepsilon_y}{2} \pm \sqrt{\left(\frac{\varepsilon_x - \varepsilon_y}{2}\right)^2 + \left(\frac{\gamma_{xy}}{2}\right)^2} \qquad \text{(I.35)}$$

263

Where,

$\varepsilon_x = \varepsilon_L$

$\varepsilon_y = \varepsilon_T$

$\varepsilon_{LT} = \gamma_{xy}$

I.1.5 Bovine and Composite Bone Experimental Equations

VM stress can be computed to easily compare experimental values to theoretical values without having to account for the direction of the strain gauge. The generalized VM stress equation in terms of principal stresses, which will be used to calculate the experimental VM stress value, is:

$$\sigma' = \sqrt{\sigma_1^2 + \sigma_2^2 + \sigma_3^2 - \sigma_1\sigma_2 - \sigma_1\sigma_3 - \sigma_2\sigma_3} \tag{I.36}$$

Where the three principal stresses are calculated using generalized Hooke's Law:

$$\sigma_1 = \frac{E}{(1+\upsilon)(1-2\upsilon)}\left[(1-\upsilon)\varepsilon_1 + \upsilon(\varepsilon_2 + \varepsilon_3)\right] \tag{I.37}$$

$$\sigma_2 = \frac{E}{(1+\upsilon)(1-2\upsilon)}\left[(1-\upsilon)\varepsilon_2 + \upsilon(\varepsilon_1 + \varepsilon_3)\right] \tag{I.38}$$

$$\sigma_3 = \frac{E}{(1+\upsilon)(1-2\upsilon)}\left[(1-\upsilon)\varepsilon_3 + \upsilon(\varepsilon_1 + \varepsilon_2)\right] \tag{I.39}$$

The first and second principal strains are found using equation:

$$\varepsilon_{1,2} = \frac{1}{2}\left[\varepsilon_a + \varepsilon_c \pm \sqrt{(\varepsilon_a - \varepsilon_c)^2 + (2\varepsilon_b - \varepsilon_a - \varepsilon_c)^2}\right] \tag{I.40}$$

Where ε_a, ε_b and ε_c are the measured longitudinal strain, transverse strain and strain at 45°, respectively.

264

I.2 Theoretical Relative Error Equations

I.2.1 Background of Relative Error Equations and Propagation of Error

Each experimental measurement is associated with a measurement error. When an experimental measurement is taken, uncertainty in that measurement arises from imperfections in the equipment (Salem).

For example, if the cross sectional area of a rectangular specimen with sides a by b was measured using a standard ruler, both measurements are dependent on the accuracy of the ruler.

$$a = 20mm \pm 0.5mm \tag{I.41}$$

$$b = 40mm \pm 0.5mm \tag{I.42}$$

Therefore the area of the rectangle is:

$$A = a \cdot b \tag{I.43}$$

$$A = 800mm^2 \tag{I.44}$$

Since each measurement is associated with its own uncertainty, measurement error propagates throughout the calculation. For the above example, the error in equation (I.43) is dependent on the error in a (δa) and the error in b (δb).

The error in a is found by:

$$\delta a = \frac{\partial A}{\partial a} da \tag{I.45}$$

Similarly, the error in b is found by:

$$\delta b = \frac{\partial A}{\partial b} db \tag{I.46}$$

The error in equation (I.43) is, thus:

265

$$dA = \sqrt{(\delta a)^2 + (\delta b)^2}$$ (I.47)

Returning to the example the error is:

$$dA = \sqrt{\left(\frac{\partial A}{\partial a} da\right)^2 + \left(\frac{\partial A}{\partial b} db\right)^2}$$ (I.48)

$$dA = \sqrt{(b \cdot da)^2 + (a \cdot db)^2}$$ (I.49)

$$dA = \sqrt{(40mm \cdot 0.5mm)^2 + (20mm \cdot 0.5mm)^2}$$ (I.50)

$$dA = 22.4mm^2$$ (I.51)

Therefore,

$$A = 800 \pm 22mm^2$$ (I.52)

This method of determining the error propagation (Harrison, 2004) can be applied to any equation using the following general formula for the general case: $G=f(X, Y, Z)$, such that the error of G, dG, is:

$$dG = \sqrt{\left(\frac{f(X,Y,Z)}{\partial X} dX\right)^2 + \left(\frac{f(X,Y,Z)}{\partial Y} dY\right)^2 + \left(\frac{f(X,Y,Z)}{\partial Z} dZ\right)^2}$$ (I.53)

I.2.2 Theoretical Relative Strain Equations

Using Hooke's Law the longitudinal strain, ε_L along the cortex of the composite or bovine bone can be found:

$$\varepsilon_L = \frac{\sigma_L}{E} = \sigma_L E^{-1}$$ (I.54)

The error in the longitudinal strain, $d\varepsilon_L$ is:

$$d\varepsilon_L{}^2 = \left(\frac{\partial \varepsilon_L}{\partial \sigma_L} d\sigma_L\right)^2 + \left(\frac{\partial \varepsilon_L}{\partial E} dE\right)^2$$ (I.55)

266

Where,

$$\frac{\partial \varepsilon_L}{\partial \sigma_L} = \frac{1}{E}$$

(I.56)

$$\frac{\partial \varepsilon_L}{\partial E} = -\frac{\sigma_L}{E^2}$$

(I.57)

By substituting equations (I.56) and (I.57) into (I.55), we find:

$$d\varepsilon_L^{\ 2} = \left(\frac{d\sigma_L}{E}\right)^2 + \left(-\frac{\sigma_L \cdot dE}{E^2}\right)^2$$

(I.58)

Where E and dE are the modulus of elasticity and the error in the modulus of elasticity for the specimen, respectively and σ_L is the longitudinal stress acting on the tibia, which can be found by combining the equation for bending of asymmetric cross-sections combined with the stress equation due to axial load such that:

$$\sigma_L = \sigma_A + \sigma_B$$

(I.59)

The error in the longitudinal stress, $d\sigma_L$ is:

$$d\sigma_L^{\ 2} = \left(\frac{\partial \sigma_L}{\partial \sigma_A} d\sigma_A\right)^2 + \left(\frac{\partial \sigma_L}{\partial \sigma_B} d\sigma_B\right)^2$$

(I.60)

Before the error in the longitudinal stress can be found, the error in the axial and bending stress must be found. The axial stress equation is:

$$\sigma_A = \frac{F_{tot}}{\left(1 + \dfrac{A_{canc} \cdot E_{canc}}{A_{cort} \cdot E_{cort}}\right)} \bigg/ A_{cort}$$

(I.61)

The associated error in the axial stress equation is:

267

$$d\sigma_A{}^2 = \left(\frac{\partial \sigma_A}{\partial F_{tot}} dF_{tot}\right)^2 + \left(\frac{\partial \sigma_A}{\partial A_{canc}} dA_{canc}\right)^2 + \left(\frac{\partial \sigma_A}{\partial E_{canc}} dE_{canc}\right)^2 +$$

$$\left(\frac{\partial \sigma_A}{\partial A_{cort}} dA_{cort}\right)^2 + \left(\frac{\partial \sigma_A}{\partial E_{cort}} dE_{cort}\right)^2$$

(I.62)

Where,

$$\frac{\partial \sigma_A}{\partial F_{tot}} = \frac{E_{cort}}{E_{cort} \cdot A_{cort} + E_{canc} \cdot A_{canc}}$$

(I.63)

$$\frac{\partial \sigma_A}{\partial A_{canc}} = \frac{-F_{tot} \cdot E_{canc} \cdot E_{cort}}{\left(E_{canc} \cdot A_{canc} + E_{cort} \cdot A_{cort}\right)^2}$$

(I.64)

$$\frac{\partial \sigma_A}{\partial E_{canc}} = \frac{-F_{tot} \cdot E_{cort} \cdot A_{canc}}{\left(E_{canc} \cdot A_{canc} + E_{cort} \cdot A_{cort}\right)^2}$$

(I.65)

$$\frac{\partial \sigma_A}{\partial E_{cort}} = \frac{F_{tot} \cdot E_{canc} \cdot A_{canc}}{\left(E_{canc} \cdot A_{canc} + E_{cort} \cdot A_{cort}\right)^2}$$

(I.66)

$$\frac{\partial \sigma_A}{\partial A_{cort}} = \frac{-F_{tot} \cdot E_{cort}{}^2}{\left(E_{canc} \cdot A_{canc} + E_{cort} \cdot A_{cort}\right)^2}$$

(I.67)

Substituting equations (I.63) to (I.67) into (I.62), the error in the axial stress equation becomes:

$$d\sigma_A{}^2 = \left(\frac{E_{cort}}{E_{cort} \cdot A_{cort} + E_{canc} \cdot A_{canc}} dF_{tot}\right)^2 + \left(\frac{-F_{tot} \cdot E_{canc} \cdot E_{cort}}{\left(E_{canc} \cdot A_{canc} + E_{cort} \cdot A_{cort}\right)^2} dA_{canc}\right)^2$$

$$+ \left(\frac{-F_{tot} \cdot E_{cort} \cdot A_{canc}}{\left(E_{canc} \cdot A_{canc} + E_{cort} \cdot A_{cort}\right)^2} dE_{canc}\right)^2 + \left(\frac{-F_{tot} \cdot E_{cort}{}^2}{\left(E_{canc} \cdot A_{canc} + E_{cort} \cdot A_{cort}\right)^2} dA_{cort}\right)^2 \quad \text{(I.68)}$$

$$+ \left(\frac{F_{tot} \cdot E_{canc} \cdot A_{canc}}{\left(E_{canc} \cdot A_{canc} + E_{cort} \cdot A_{cort}\right)^2} dE_{cort}\right)^2$$

The bending stress equation is:

$$\sigma_B = \left(\frac{+(MxIy + MyIxy)y - (MyIx + MxIxy)x}{IxIy - Ixy^2}\right)$$

(I.69)

268

The error in the bending stress, $d\sigma_B$ is:

$$d\sigma_B{}^2 = \left(\frac{\partial \sigma_B}{\partial Mx}dMx\right)^2 + \left(\frac{\partial \sigma_B}{\partial Iy}dIy\right)^2 + \left(\frac{\partial \sigma_B}{\partial y}dy\right)^2 + \left(\frac{\partial \sigma_B}{\partial My}dMy\right)^2$$
$$+ \left(\frac{\partial \sigma_B}{\partial Ixy}dIxy\right)^2 + \left(\frac{\partial \sigma_B}{\partial Ix}dIx\right)^2 + \left(\frac{\partial \sigma_B}{\partial x}dx\right)^2$$

(I.70)

Where:

$$\frac{\partial \sigma_B}{\partial Mx} = \frac{Iy \cdot y - Ixy \cdot x}{IxIy - Ixy^2}$$

(I.71)

$$\frac{\partial \sigma_B}{\partial Iy} = \frac{\left[(IxMy + IxyMx)(Ix(x) - Ixy(y))\right]}{\left(IxIy - Ixy^2\right)^2}$$

(I.72)

$$\frac{\partial \sigma_B}{\partial y} = \frac{MxIy + MyIxy}{IxIy - Ixy^2}$$

(I.73)

$$\frac{\partial \sigma_B}{\partial My} = \frac{Ixy(y) - Ix(x)}{IxIy - Ixy^2}$$

(I.74)

$$\frac{\partial \sigma_B}{\partial Ixy} = \frac{-\left(Ixy^2\left[Mx(x) - My(y)\right] + 2Ixy\left[IxMy(x) - IyMx(y)\right] + IxIy\left[Mx(x) - My(y)\right]\right)}{\left(IxIy - Ixy^2\right)^2}$$

(I.75)

$$\frac{\partial \sigma_B}{\partial Ix} = \frac{(IxyMy + IyMx)(Ixy(x) - Iy(y))}{\left(IxIy - Ixy^2\right)^2}$$

(I.76)

$$\frac{\partial \sigma_B}{\partial x} = \frac{-(MyIx + MxIxy)}{IxIy - Ixy^2}$$

(I.77)

By substituting equations (I.71) through (I.77), the error in longitudinal stress becomes:

269

$$d\sigma_B{}^2 = \left(\left(\frac{Iy \cdot y - Ixy \cdot x}{IxIy - Ixy^2}\right)dMx\right)^2 + \left(\left(\frac{[(IxMy + IxyMx)(Ix(x) - Ixy(y))]}{(IxIy - Ixy^2)^2}\right)dIy\right)^2$$

$$+ \left(\left(\frac{MxIy + MyIxy}{IxIy - Ixy^2}\right)dy\right)^2 + \left(\left(\frac{Ixy(y) - Ix(x)}{IxIy - Ixy^2}\right)dMy\right)^2$$

$$+ \left(\left(\frac{-(Ixy^2[Mx(x) - My(y)] + 2Ixy[IxMy(x) - IyMx(y)] + IxIy[Mx(x) - My(y)])}{(IxIy - Ixy^2)^2}\right)dIxy\right)^2 \quad \textbf{(I.78)}$$

$$+ \left(\left(\frac{(IxyMy + IyMx)(Ixy(x) - Iy(y))}{(IxIy - Ixy^2)^2}\right)dIx\right)^2 + \left(\left(\frac{-(MyIx + MxIxy)}{IxIy - Ixy^2}\right)dx\right)^2$$

Where x, y, A, Ix, Iy and Ixy have been previously defined in Section I.1.2, dx and dy are the error in the distances from the strain gauge to centre of gravity, dA is the error in the cross sectional area at the area of interest, dIx and dIy are the errors in the moment of inertias about the x and y axes, respectively and $dIxy$ is the error in the product of inertia. The errors, dA, dIx, dIy and $dIxy$, all depend on the resolution of the CAD model (Au, 2008) and so a maximum error of 5% was used.

Mx and My are the moments about the x and y axes, respectively. dMx and dMy are the errors in the moments about the x and y axes, respectively. These formulas vary between each specimen and are presented at the end of this section.

Using Poisson's ratio, v and the longitudinal strain, ε_L, the transverse strain equation is as follows:

$$\varepsilon_T = -v\varepsilon_L \quad \textbf{(I.79)}$$

The error in the transverse strain, $d\varepsilon_T$ can be found using the error in the longitudinal strain direction, $d\varepsilon_L$ and the error in Poisson's ratio dv, producing:

$$d\varepsilon_T{}^2 = \left(\frac{\partial \varepsilon_T}{\partial v}dv\right)^2 + \left(\frac{\partial \varepsilon_T}{\partial \varepsilon_L}d\varepsilon_L\right)^2 \quad \textbf{(I.80)}$$

270

Where,

$$\frac{\partial \varepsilon_T}{\partial \upsilon} = -\varepsilon_L \tag{I.81}$$

$$\left(\frac{\partial \varepsilon_T}{\partial \varepsilon_L} d\varepsilon_L\right) = -\upsilon \tag{I.82}$$

Substituting equations (I.81) and (I.82) into (I.80), the error in the transverse strain, $d\varepsilon_T$ is:

$$d\varepsilon_T{}^2 = \left(-\varepsilon_L d\upsilon\right)^2 + \left(-\upsilon d\varepsilon_L\right)^2 \tag{I.83}$$

Similarly, the strain in the depth is:

$$\varepsilon_D = -\upsilon \varepsilon_L \tag{I.84}$$

Error in the depth strain direction, $d\varepsilon_D$ can be found using the error in the longitudinal strain direction, $d\varepsilon_L$ and the error in Poisson's ratio $d\upsilon$, producing:

$$d\varepsilon_D{}^2 = \left(\frac{\partial \varepsilon_D}{\partial \upsilon} d\upsilon\right)^2 + \left(\frac{\partial \varepsilon_D}{\partial \varepsilon_L} d\varepsilon_L\right)^2 \tag{I.85}$$

Where,

$$\frac{\partial \varepsilon_D}{\partial \upsilon} = -\varepsilon_L \tag{I.86}$$

$$\left(\frac{\partial \varepsilon_D}{\partial \varepsilon_L} d\varepsilon_L\right) = -\upsilon \tag{I.87}$$

Through substitution of equations (I.86) and (I.87) into (I.85), the error for the strain in the depth is:

$$d\varepsilon_D{}^2 = \left(-\varepsilon_L d\upsilon\right)^2 + \left(-\upsilon d\varepsilon_L\right)^2 \tag{I.88}$$

The theoretical von Mises (VM) stress equation consists of the longitudinal strain σ_L and the shear stress, τ_{LT}:

$$\sigma' = \sqrt{\frac{2(\sigma_L)^2 + 6\tau_{LT}{}^2}{2}} \tag{I.89}$$

271

The error in the theoretical VM stress, $d\sigma'$ is found from the longitudinal strain σ_L and the shear stress, τ_{LT} and their associated errors $d\sigma_L$ and $d\tau_{LT}$.

$$d\sigma'^2 = \left(\frac{\partial \sigma'}{\partial \sigma_L} d\sigma_L\right)^2 + \left(\frac{\partial \sigma'}{\partial \tau_{LT}} d\tau_{LT}\right)^2 \qquad (I.90)$$

Where,

$$\frac{\partial \sigma'}{\partial \sigma_L} = \frac{\sigma_L}{\sqrt{\sigma_L^2 + 3\tau_{LT}^2}} \qquad (I.91)$$

$$\frac{\partial \sigma'}{\partial \tau_{LT}} = \frac{3\tau_{LT}}{\sqrt{\sigma_L^2 + 3\tau_{LT}^2}} \qquad (I.92)$$

Substituting equations (I.91) and (I.92) into equation (I.90), the error in the theoretical VM stress, $d\sigma'$ becomes:

$$d\sigma'^2 = \left(\frac{\sigma_L \cdot d\sigma_L}{\sqrt{\sigma_L^2 + 3\tau_{LT}^2}}\right)^2 + \left(\frac{3\tau_{LT} \cdot d\tau_{LT}}{\sqrt{\sigma_L^2 + 3\tau_{LT}^2}}\right)^2 \qquad (I.93)$$

The shear stress, τ_{LT} equation is:

$$\tau_{LT} = \frac{Mz}{2A^*t} \qquad (I.94)$$

The error in the shear stress, τ_{LT}, is found in equation (I.95)

$$d\tau_{LT}^2 = \left(\frac{\partial \tau_{LT}}{\partial Mz} dMz\right)^2 + \left(\frac{\partial \tau_{LT}}{\partial A^*} dA^*\right)^2 + \left(\frac{\partial \tau_{LT}}{\partial t} dt\right)^2 \qquad (I.95)$$

Where,

$$\frac{\partial \tau_{LT}}{\partial Mz} = \frac{1}{2A^*t} \qquad (I.96)$$

$$\frac{\partial \tau_{LT}}{\partial A^*} = \frac{-Mz}{2(A^*)^2 t} \qquad (I.97)$$

$$\frac{\partial \tau_{LT}}{\partial t} = \frac{-Mz}{2(A^*)t^2} \qquad (I.98)$$

272

Substituting equations (I.96) through (I.98) into equation (I.95), the error in the shear stress, τ_{LT}, becomes:

$$d\tau_{LT}^2 = \left(\frac{dMz}{2A^*t}\right)^2 + \left(\frac{-Mz \cdot dA^*}{2(A^*)^2 t}\right)^2 + \left(\frac{-Mz \cdot dt}{2(A^*)t^2}\right)^2 \qquad \text{(I.99)}$$

Where Mz is the moment about the z-axis and dMz, its associated error, are both calculated at the centre of gravity at the area of interest. A^* and dA^*, were described previously and assumed to be 5%.

Similar to equation (I.54), Hooke's Law is used to find VM strain, ε':

$$\varepsilon' = \frac{\sigma'}{E} \qquad \text{(I.100)}$$

The error in VM strain, $d\varepsilon'$ is

$$d\varepsilon'^2 = \left(\frac{\partial \varepsilon'}{\partial \sigma'}d\sigma'\right)^2 + \left(\frac{\partial \varepsilon'}{\partial E}dE\right)^2 \qquad \text{(I.101)}$$

Where,

$$\frac{\partial \varepsilon'}{\partial \sigma'} = \frac{1}{E} \qquad \text{(I.102)}$$

$$\frac{\partial \varepsilon'}{\partial E} = -\frac{\sigma'}{E^2} \qquad \text{(I.103)}$$

By substituting equations (I.102) and (I.103) into equation (I.101), the error in VM strain, $d\varepsilon'$ becomes:

$$d\varepsilon'^2 = \left(\frac{1}{E}d\sigma'\right)^2 + \left(-\frac{\sigma'}{E^2}dE\right)^2 \qquad \text{(I.104)}$$

The moment equations vary between each specimen. The moment about the x axis for the Instron and custom-made loading jig compression test on the composite tibia is:

273

$$Mx = -Fmedial(y_{med}) - Flateral(y_{lat}) \tag{I.105}$$

The error in the x axis moment equation is:

$$dMx^2 = \left(\frac{\partial Mx}{\partial Fmed} dFmed\right)^2 + \left(\frac{\partial Mx}{\partial y_{med}} dy_{med}\right)^2 + \left(\frac{\partial Mx}{\partial Flat} dFlat\right)^2 + \left(\frac{\partial Mx}{\partial y_{lat}} dy_{lat}\right)^2 \tag{I.106}$$

Where,

$$\frac{\partial Mx}{\partial Fmed} = -y_{med} \tag{I.107}$$

$$\frac{\partial Mx}{\partial y_{med}} = -Fmed \tag{I.108}$$

$$\frac{\partial Mx}{\partial Flat} = -y_{lat} \tag{I.109}$$

$$\frac{\partial Mx}{\partial y_{lat}} = -Flat \tag{I.110}$$

Substituting (I.107) through (I.110) into equation (I.106), the error in Mx is:

$$dMx^2 = \left(-y_{med} \cdot dFmed\right)^2 + \left(-Fmed \cdot dy_{med}\right)^2 + \left(-y_{lat} \cdot dFlat\right)^2 + \left(-Flat \cdot dy_{lat}\right)^2 \tag{I.111}$$

Similarly, the moment about the y axis for the Instron and custom-made loading jig compression test on the composite tibia is:

$$My = Fmedial(x_{med}) - Flateral(x_{lat}) \tag{I.112}$$

The error in My becomes:

$$dMy^2 = \left(\frac{\partial My}{\partial Fmed} dFmed\right)^2 + \left(\frac{\partial My}{\partial x_{med}} dx_{med}\right)^2 + \left(\frac{\partial My}{\partial Flat} dFlat\right)^2 + \left(\frac{\partial My}{\partial x_{lat}} dx_{lat}\right)^2 \tag{I.113}$$

Where,

$$\frac{\partial My}{\partial Fmed} = x_{med} \tag{I.114}$$

$$\frac{\partial My}{\partial x_{med}} = Fmed \tag{I.115}$$

274

$$\frac{\partial My}{\partial Flat} = -x_{lat} \tag{I.116}$$

$$\frac{\partial My}{\partial x_{lat}} = -Flat \tag{I.117}$$

By substituting equations (I.114) through (I.117) into (I.113), the error in y moment equation, dMy becomes:

$$dMy^2 = \left(x_{med} \cdot dFmed\right)^2 + \left(Fmed \cdot dx_{med}\right)^2 + \left((-x_{lat}) \cdot dFlat\right)^2 + \left((-Flat) \cdot dx_{lat}\right)^2 \tag{I.118}$$

Where,

Fmed and Flat and dFmed and dFlat are the respective forces and relative errors of those forces applied to the medial and lateral tibial condyles, x_{med} and y_{med} and dx_{med} and dy_{med} are respectively the distances and their associated errors from Fmed to the centre of gravity of the bone at the area of interest, and x_{lat} and y_{lat} and dx_{lat} and dy_{lat} are respectively the distances and their associated errors from Flat to the centre of gravity of the bone at the area of interest.

When using the multi axis biomechanical testing apparatus, the installed six degree of freedom (DOF) load cell measures Fx, Fy, Fz, Mx, My, and Mz.

The moment equation about the centre of gravity of a particular slice for the x axis is as follows:

$$Mxcg = -Mxe + Fy(z) + Fz(y) \tag{I.119}$$

The error in the moment equation about the x axis, $dMxcg$, is:

$$dMxcg^2 = \left(\frac{\partial Mxcg}{\partial Mxe} dMxe\right)^2 + \left(\frac{\partial Mxcg}{\partial Fy} dFy\right)^2 + \left(\frac{\partial Mxcg}{\partial z} dz\right)^2$$
$$+ \left(\frac{\partial Mxcg}{\partial Fz} dFz\right)^2 + \left(\frac{\partial Mxcg}{\partial y} dy\right)^2 \tag{I.120}$$

Where,

275

$$\frac{\partial Mxcg}{\partial Mxe} = -1 \qquad\qquad\qquad (\text{I.121})$$

$$\frac{\partial Mxcg}{\partial Fy} = z \qquad\qquad\qquad (\text{I.122})$$

$$\frac{\partial Mxcg}{\partial z} = Fy \qquad\qquad\qquad (\text{I.123})$$

$$\frac{\partial Mxcg}{\partial Fz} = y \qquad\qquad\qquad (\text{I.124})$$

$$\frac{\partial Mxcg}{\partial y} = Fz \qquad\qquad\qquad (\text{I.125})$$

Substituting equations (I.121) through (I.125), the error in the x axis moment about the centre of gravity is:

$$dMxcg^2 = (dMxe)^2 + (z \cdot dFy)^2 + (Fy \cdot dz)^2 + (y \cdot dFz)^2 + (Fz \cdot dy)^2 \qquad (\text{I.126})$$

Where Mxe is the moment about the x-axis measured at the centre of the 6 DOF load cell, Fy and Fz are the forces measured by the 6 DOF load cell in the y and z directions, respectively and dFy and dFz are the errors associated with Fy and Fz, respectively, and y and z and dy and dz are the respective distances and the error in the distance from the bone pot centre to the centre of gravity of a particular slice.

Similarly, the moment about the centre of gravity around the y-axis is:

$$Mycg = -Mye - Fx(z) - Fz(x) \qquad\qquad\qquad (\text{I.127})$$

The error is:

$$dMycg^2 = \left(\frac{\partial Mycg}{\partial Mye} dMye\right)^2 + \left(\frac{\partial Mycg}{\partial Fx} dFx\right)^2 + \left(\frac{\partial Mycg}{\partial z} dz\right)^2$$
$$+ \left(\frac{\partial Mycg}{\partial Fz} dFz\right)^2 + \left(\frac{\partial Mycg}{\partial x} dx\right)^2 \qquad\qquad (\text{I.128})$$

Where,

$$\frac{\partial Mycg}{\partial Mye} = -1 \tag{I.129}$$

$$\frac{\partial Mycg}{\partial Fx} = -z \tag{I.130}$$

$$\frac{\partial Mycg}{\partial z} = -Fx \tag{I.131}$$

$$\frac{\partial Mycg}{\partial Fz} = -x \tag{I.132}$$

$$\frac{\partial Mycg}{\partial x} = -Fz \tag{I.133}$$

By substituting equations (I.129) through (I.133) into equation (I.128), the error in the moment about the centre of gravity of a particular slice around the y-axis, $dMycg$ becomes:

$$dMycg^2 = (dMye)^2 + (z \cdot dFx)^2 + (Fx \cdot dz)^2 + (x \cdot dFz)^2 + (Fz \cdot dx)^2 \tag{I.134}$$

Where, Mye is the moment about the y-axis measured at the centre of the 6 DOF load cell, Fx and Fz are the forces measured by the 6 DOF load cell in the x and z directions, respectively and dFx and dFz are the errors associated Fx and Fz, respectively, and x and z and dx and dz are the distances and the error in the distance from the bone pot centre to the centre of gravity of a particular slice.

Additionally the moment about the centre of gravity around the z-axis:

$$Mzcg = -Mze - Fx(y) + Fy(x) \tag{I.135}$$

The error in the moment about the centre of gravity of a particular slice around the z-axis, $dMzcg$ is:

$$dMzcg^2 = \left(\frac{\partial Mzcg}{\partial Mze} dMze\right)^2 + \left(\frac{\partial Mzcg}{\partial Fx} dFx\right)^2 + \left(\frac{\partial Mzcg}{\partial y} dy\right)^2$$
$$+ \left(\frac{\partial Mzcg}{\partial Fy} dFy\right)^2 + \left(\frac{\partial Mycg}{\partial x} dx\right)^2 \tag{I.136}$$

277

Where,

$$\frac{\partial Mzcg}{\partial Mze} = -1 \qquad (I.137)$$

$$\frac{\partial Mzcg}{\partial Fx} = y \qquad (I.138)$$

$$\frac{\partial Mzcg}{\partial y} = Fx \qquad (I.139)$$

$$\frac{\partial Mzcg}{\partial Fy} = x \qquad (I.140)$$

$$\frac{\partial Mzcg}{\partial x} = Fy \qquad (I.141)$$

Producing,

$$dMzcg^2 = (dMze)^2 + (y \cdot dFx)^2 + (Fx \cdot dy)^2 + (x \cdot dFy)^2 + (Fy \cdot dx)^2 \qquad (I.142)$$

1.2.2.1 Bovine Bone Theoretical Relative Error Equations

The first and second principal strains can be found using the following equation:

$$\varepsilon_{1,2} = \frac{\varepsilon_x + \varepsilon_y}{2} \pm \sqrt{\left(\frac{\varepsilon_x - \varepsilon_y}{2}\right)^2 + \left(\frac{\gamma_{xy}}{2}\right)^2} \qquad (I.143)$$

The error in the first principal strain is:

$$d\varepsilon_1^2 = \left(\frac{\partial \varepsilon_1}{\partial \varepsilon_x} d\varepsilon_x\right)^2 + \left(\frac{\partial \varepsilon_1}{\partial \varepsilon_y} d\varepsilon_y\right)^2 + \left(\frac{\partial \varepsilon_1}{\partial \gamma_{xy}} d\gamma_{xy}\right)^2 \qquad (I.144)$$

Where,

$$\frac{\partial \varepsilon_1}{\partial \varepsilon_x} = \frac{0.5(\varepsilon_x - \varepsilon_y)}{\sqrt{\varepsilon_x^2 - 2\varepsilon_x \varepsilon_y + 2\varepsilon_y^2 + 4\gamma_{xy}^2}} + \frac{1}{2} \qquad (I.145)$$

$$\frac{\partial \varepsilon_1}{\partial \varepsilon_y} = \frac{0.5(\varepsilon_y - \varepsilon_x)}{\sqrt{\varepsilon_y^2 - 2\varepsilon_y \varepsilon_x + \varepsilon_x^2 + 4\gamma_{xy}^2}} + \frac{1}{2} \qquad (I.146)$$

$$\frac{\partial \varepsilon_1}{\partial \gamma_{xy}} = \frac{-\gamma_{xy}}{\sqrt{\gamma_{xy}^2 - 0.25(\varepsilon_x + \varepsilon_y)^2}} \qquad (I.147)$$

278

Therefore the error in the first principal becomes:

$$d\varepsilon_1^{\;2} = \left(\left(\frac{0.5(\varepsilon_x - \varepsilon_y)}{\sqrt{\varepsilon_x^{\;2} - 2\varepsilon_x\varepsilon_y + 2\varepsilon_y^{\;2} + 4\gamma_{xy}^{\;2}}} + \frac{1}{2}\right)d\varepsilon_x\right)^2$$

$$+ \left(\left(\frac{0.5(\varepsilon_y - \varepsilon_x)}{\sqrt{\varepsilon_y^{\;2} - 2\varepsilon_y\varepsilon_x + \varepsilon_x^{\;2} + 4\gamma_{xy}^{\;2}}} + \frac{1}{2}\right)d\varepsilon_y\right)^2$$

$$+ \left(\frac{-\gamma_{xy}}{\sqrt{\gamma_{xy}^{\;2} - 0.25(\varepsilon_x + \varepsilon_y)^2}}d\gamma_{xy}\right)^2 \qquad\qquad \text{(I.148)}$$

Similarly, the error in the second principal strain is:

$$d\varepsilon_2^{\;2} = \left(\frac{\partial\varepsilon_2}{\partial\varepsilon_x}d\varepsilon_x\right)^2 + \left(\frac{\partial\varepsilon_2}{\partial\varepsilon_y}d\varepsilon_y\right)^2 + \left(\frac{\partial\varepsilon_2}{\partial\gamma_{xy}}d\gamma_{xy}\right)^2 \qquad \text{(I.149)}$$

Where,

$$\frac{\partial\varepsilon_2}{\partial\varepsilon_x} = \frac{1}{2} - \frac{0.5(\varepsilon_x - \varepsilon_y)}{\sqrt{\varepsilon_x^{\;2} - 2\varepsilon_x\varepsilon_y + 2\varepsilon_y^{\;2} + 4\gamma_{xy}^{\;2}}} \qquad\qquad \text{(I.150)}$$

$$\frac{\partial\varepsilon_2}{\partial\varepsilon_y} = \frac{1}{2} - \frac{0.5(\varepsilon_y - \varepsilon_x)}{\sqrt{\varepsilon_y^{\;2} - 2\varepsilon_y\varepsilon_x + \varepsilon_x^{\;2} + 4\gamma_{xy}^{\;2}}} \qquad\qquad \text{(I.151)}$$

$$\frac{\partial\varepsilon_2}{\partial\gamma_{xy}} = \frac{-\gamma_{xy}}{\sqrt{\gamma_{xy}^{\;2} - 0.25(\varepsilon_x + \varepsilon_y)^2}} \qquad\qquad \text{(I.152)}$$

Producing,

$$d\varepsilon_2^{\;2} = \left(\left(\frac{1}{2} - \frac{0.5(\varepsilon_x - \varepsilon_y)}{\sqrt{\varepsilon_x^{\;2} - 2\varepsilon_x\varepsilon_y + 2\varepsilon_y^{\;2} + 4\gamma_{xy}^{\;2}}}\right)d\varepsilon_x\right)^2$$

$$+ \left(\left(\frac{1}{2} - \frac{0.5(\varepsilon_y - \varepsilon_x)}{\sqrt{\varepsilon_y^{\;2} - 2\varepsilon_y\varepsilon_x + \varepsilon_x^{\;2} + 4\gamma_{xy}^{\;2}}}\right)d\varepsilon_y\right)^2$$

$$+ \left(\frac{-\gamma_{xy}}{\sqrt{\gamma_{xy}^{\;2} - 0.25(\varepsilon_x + \varepsilon_y)^2}}d\gamma_{xy}\right)^2 \qquad\qquad \text{(I.153)}$$

279

I.3 Experimental Relative Error Equations

The VM stress σ' for the experimental strain results takes the form:

$$\sigma' = \sqrt{\sigma_1^2 + \sigma_2^2 + \sigma_3^2 - \sigma_1\sigma_2 - \sigma_1\sigma_3 - \sigma_2\sigma_3}$$

(I.154)

Since we have a plane stress state $\sigma_3 = 0$, the VM stress equation becomes:

$$\sigma' = \sqrt{\sigma_1^2 + \sigma_2^2 - \sigma_1\sigma_2}$$

(I.155)

The experimental VM error, $d\sigma'$ is

$$d\sigma'^2 = \left(\frac{\partial\sigma'}{\partial\sigma_1}d\sigma_1\right)^2 + \left(\frac{\partial\sigma'}{\partial\sigma_2}d\sigma_2\right)^2$$

(I.156)

Where,

$$\frac{\partial\sigma'}{\partial\sigma_1} = \left[\frac{2\sigma_1 - \sigma_2}{2\sqrt{\sigma_1^2 + \sigma_2^2 - \sigma_1\sigma_2}}\right]$$

(I.157)

$$\frac{\partial\sigma'}{\partial\sigma_2} = \left[\frac{2\sigma_2 - \sigma_1}{2\sqrt{\sigma_1^2 + \sigma_2^2 - \sigma_1\sigma_2}}\right]$$

(I.158)

Substitute equations (I.157) and (I.158) into equation (I.156) to find the error in the experimental VM stress:

$$d\sigma'^2 = \left(\frac{2\sigma_1 - \sigma_2}{2\sqrt{\sigma_1^2 + \sigma_2^2 - \sigma_1\sigma_2}}d\sigma_1\right)^2 + \left(\frac{2\sigma_2 - \sigma_1}{2\sqrt{\sigma_1^2 + \sigma_2^2 - \sigma_1\sigma_2}}d\sigma_2\right)^2$$

(I.159)

For the rectangular rosette (90° strain rosettes - $\theta_a=0°$ $\theta_b=45°$ $\theta_c=90°$), the first and second principal strains can be found using the following equation:

$$\varepsilon_{1,2} = \frac{1}{2}\left[\varepsilon_a + \varepsilon_c \pm \sqrt{(\varepsilon_a - \varepsilon_c)^2 + (2\varepsilon_b - \varepsilon_a - \varepsilon_c)^2}\right]$$

(I.160)

280

The error in the first principal strain is:

$$d\varepsilon_1{}^2 = \left(\frac{\partial \varepsilon_1}{\partial \varepsilon_a} d\varepsilon_a\right)^2 + \left(\frac{\partial \varepsilon_1}{\partial \varepsilon_b} d\varepsilon_b\right)^2 + \left(\frac{\partial \varepsilon_1}{\partial \varepsilon_c} d\varepsilon_c\right)^2 \qquad \text{(I.161)}$$

Where,

$$\frac{\partial \varepsilon_1}{\partial \varepsilon_a} = \frac{\sqrt{2}(\varepsilon_a - \varepsilon_b)}{2\sqrt{\varepsilon_a{}^2 - 2\varepsilon_a\varepsilon_b + 2\varepsilon_b{}^2 - 2\varepsilon_b\varepsilon_c + \varepsilon_c{}^2}} + \frac{1}{2} \qquad \text{(I.162)}$$

$$\frac{\partial \varepsilon_1}{\partial \varepsilon_b} = \frac{\sqrt{2}(2\varepsilon_b - \varepsilon_a - \varepsilon_c)}{2\sqrt{2\varepsilon_b{}^2 - 2\varepsilon_b(\varepsilon_a + \varepsilon_c) + \varepsilon_c{}^2 + \varepsilon_a{}^2}} \qquad \text{(I.163)}$$

$$\frac{\partial \varepsilon_1}{\partial \varepsilon_c} = \frac{\sqrt{2}(\varepsilon_c - \varepsilon_b)}{2\sqrt{\varepsilon_c{}^2 - 2\varepsilon_c\varepsilon_b + \varepsilon_a{}^2 - 2\varepsilon_b\varepsilon_a + 2\varepsilon_b{}^2}} + \frac{1}{2} \qquad \text{(I.164)}$$

Thus, the error in the first principal strain is:

$$d\varepsilon_1{}^2 = \left(\left(\frac{\sqrt{2}(\varepsilon_a - \varepsilon_b)}{2\sqrt{\varepsilon_a{}^2 - 2\varepsilon_a\varepsilon_b + 2\varepsilon_b{}^2 - 2\varepsilon_b\varepsilon_c + \varepsilon_c{}^2}} + \frac{1}{2}\right) d\varepsilon_a\right)^2$$

$$+ \left(\frac{\sqrt{2}(2\varepsilon_b - \varepsilon_a - \varepsilon_c)}{2\sqrt{2\varepsilon_b{}^2 - 2\varepsilon_b(\varepsilon_a + \varepsilon_c) + \varepsilon_c{}^2 + \varepsilon_a{}^2}} d\varepsilon_b\right)^2 \qquad \text{(I.165)}$$

$$+ \left(\left(\frac{\sqrt{2}(\varepsilon_c - \varepsilon_b)}{2\sqrt{\varepsilon_c{}^2 - 2\varepsilon_c\varepsilon_b + \varepsilon_a{}^2 - 2\varepsilon_b\varepsilon_a + 2\varepsilon_b{}^2}} + \frac{1}{2}\right) d\varepsilon_c\right)^2$$

The error in the second principal strain is:

$$d\varepsilon_2{}^2 = \left(\frac{\partial \varepsilon_2}{\partial \varepsilon_a} d\varepsilon_a\right)^2 + \left(\frac{\partial \varepsilon_2}{\partial \varepsilon_b} d\varepsilon_b\right)^2 + \left(\frac{\partial \varepsilon_2}{\partial \varepsilon_c} d\varepsilon_c\right)^2 \qquad \text{(I.166)}$$

Where,

$$\frac{\partial \varepsilon_2}{\partial \varepsilon_a} = \frac{1}{2} - \frac{\sqrt{2}(\varepsilon_a - \varepsilon_b)}{2\sqrt{\varepsilon_a{}^2 - 2\varepsilon_a\varepsilon_b + 2\varepsilon_b{}^2 - 2\varepsilon_b\varepsilon_c + \varepsilon_c{}^2}} \qquad \text{(I.167)}$$

281

$$\frac{\partial \varepsilon_2}{\partial \varepsilon_b} = \frac{-\sqrt{2}(2\varepsilon_b - \varepsilon_a - \varepsilon_c)}{2\sqrt{2\varepsilon_b^2 - 2\varepsilon_b(\varepsilon_a + \varepsilon_c) + \varepsilon_c^2 + \varepsilon_a^2}}$$

(I. 168)

$$\frac{\partial \varepsilon_2}{\partial \varepsilon_c} = \frac{1}{2} - \frac{\sqrt{2}(\varepsilon_c - \varepsilon_b)}{2\sqrt{\varepsilon_c^2 - 2\varepsilon_c\varepsilon_b + \varepsilon_a^2 - 2\varepsilon_b\varepsilon_a + 2\varepsilon_b^2}}$$

(I.169)

Producing,

$$
\begin{aligned}
d\varepsilon_2^2 = {} & \left(\frac{1}{2} - \frac{\sqrt{2}(\varepsilon_a - \varepsilon_b)}{2\sqrt{\varepsilon_a^2 - 2\varepsilon_a\varepsilon_b + 2\varepsilon_b^2 - 2\varepsilon_b\varepsilon_c + \varepsilon_c^2}} d\varepsilon_a \right)^2 \\
& + \left(\frac{-\sqrt{2}(2\varepsilon_b - \varepsilon_a - \varepsilon_c)}{2\sqrt{2\varepsilon_b^2 - 2\varepsilon_b(\varepsilon_a + \varepsilon_c) + \varepsilon_c^2 + \varepsilon_a^2}} d\varepsilon_b \right)^2 \\
& + \left(\frac{1}{2} - \frac{\sqrt{2}(\varepsilon_c - \varepsilon_b)}{2\sqrt{\varepsilon_c^2 - 2\varepsilon_c\varepsilon_b + \varepsilon_a^2 - 2\varepsilon_b\varepsilon_a + 2\varepsilon_b^2}} d\varepsilon_c \right)^2
\end{aligned}
$$

(I.170)

Using generalized Hooke's law equations, the first principal stress, σ_1, can be computed:

$$\sigma_1 = \frac{E}{(1+\upsilon)(1-2\upsilon)} \left[(1-\upsilon)\varepsilon_1 + \upsilon(\varepsilon_2 + \varepsilon_3) \right]$$

(I.171)

The error in first principal stress, $d\sigma_1$ is:

$$d\sigma_1^2 = \left(\frac{\partial \sigma_1}{\partial E} dE \right)^2 + \left(\frac{\partial \sigma_1}{\partial \upsilon} d\upsilon \right)^2 + \left(\frac{\partial \sigma_1}{\partial \varepsilon_1} d\varepsilon_1 \right)^2 + \left(\frac{\partial \sigma_1}{\partial \varepsilon_2} d\varepsilon_2 \right)^2 + \left(\frac{\partial \sigma_1}{\partial \varepsilon_3} d\varepsilon_3 \right)^2$$

(I.172)

Where,

$$\frac{\partial \sigma_1}{\partial E} = \frac{\left[(1-\upsilon)\varepsilon_1 + \upsilon(\varepsilon_2 + \varepsilon_3) \right]}{(1+\upsilon)(1-2\upsilon)}$$

(I.173)

$$\frac{\partial \sigma_1}{\partial \upsilon} = \frac{(1-\upsilon-2\upsilon^2)\left[-\varepsilon_1 + (\varepsilon_2 + \varepsilon_3) \right] E - \left[E((1-\upsilon)\varepsilon_1 + \upsilon(\varepsilon_2 + \varepsilon_3))(-1-4\upsilon) \right]}{(1-\upsilon-2\upsilon^2)^2}$$

(I.174)

$$\frac{\partial \sigma_1}{\partial \varepsilon_1} = \frac{(1-\upsilon)E}{(1+\upsilon)(1-2\upsilon)}$$

(I.175)

282

$$\frac{\partial \sigma_1}{\partial \varepsilon_2} = \frac{\upsilon E}{(1+\upsilon)(1-2\upsilon)}$$ (I.176)

$$\frac{\partial \sigma_1}{\partial \varepsilon_3} = \frac{\upsilon E}{(1+\upsilon)(1-2\upsilon)}$$ (I.177)

By substituting equations (I.173) to (I.177) into (I.172), the first principal stress error is as follows:

$$d\sigma_1^{\ 2} = \left(\frac{[(1-\upsilon)\varepsilon_1 + \upsilon(\varepsilon_2 + \varepsilon_3)]}{(1+\upsilon)(1-2\upsilon)} dE \right)^2$$
$$+ \left(\frac{(1-\upsilon-2\upsilon^2)[-\varepsilon_1 + (\varepsilon_2 + \varepsilon_3)]E - [E((1-\upsilon)\varepsilon_1 + \upsilon(\varepsilon_2 + \varepsilon_3))(-1-4\upsilon)]}{(1-\upsilon-2\upsilon^2)^2} d\upsilon \right)^2$$ (I.178)
$$+ \left(\left(\frac{(1-\upsilon)E}{(1+\upsilon)(1-2\upsilon)} \right) d\varepsilon_1 \right)^2 + \left(\left(\frac{\upsilon E}{(1+\upsilon)(1-2\upsilon)} \right) d\varepsilon_2 \right)^2 + \left(\left(\frac{\upsilon E}{(1+\upsilon)(1-2\upsilon)} \right) d\varepsilon_3 \right)^2$$

Similarly, the second principal stress, σ_2 is:

$$\sigma_2 = \frac{E}{(1+\upsilon)(1-2\upsilon)} [(1-\upsilon)\varepsilon_2 + \upsilon(\varepsilon_1 + \varepsilon_3)]$$ (I.179)

The second principal stress error, $d\sigma_2$ is:

$$d\sigma_2^{\ 2} = \left(\frac{\partial \sigma_2}{\partial E} dE \right)^2 + \left(\frac{\partial \sigma_2}{\partial \upsilon} d\upsilon \right)^2 + \left(\frac{\partial \sigma_2}{\partial \varepsilon_1} d\varepsilon_1 \right)^2 + \left(\frac{\partial \sigma_2}{\partial \varepsilon_2} d\varepsilon_2 \right)^2 + \left(\frac{\partial \sigma_2}{\partial \varepsilon_3} d\varepsilon_3 \right)^2$$ (I.180)

Where,

$$\frac{\partial \sigma_2}{\partial E} = \frac{[(1-\upsilon)\varepsilon_2 + \upsilon(\varepsilon_1 + \varepsilon_3)]}{(1+\upsilon)(1-2\upsilon)}$$ (I.181)

$$\frac{\partial \sigma_2}{\partial \upsilon} = \frac{(1-\upsilon-2\upsilon^2)[-\varepsilon_2 + (\varepsilon_1 + \varepsilon_3)]E - [E((1-\upsilon)\varepsilon_2 + \upsilon(\varepsilon_1 + \varepsilon_3))(-1-4\upsilon)]}{(1-\upsilon-2\upsilon^2)^2}$$ (I.182)

$$\frac{\partial \sigma_2}{\partial \varepsilon_2} = \frac{(1-\upsilon)E}{(1+\upsilon)(1-2\upsilon)}$$ (I.183)

283

$$\frac{\partial \sigma_2}{\partial \varepsilon_1} = \frac{\upsilon E}{(1+\upsilon)(1-2\upsilon)} \tag{I.184}$$

$$\frac{\partial \sigma_2}{\partial \varepsilon_3} = \frac{\upsilon E}{(1+\upsilon)(1-2\upsilon)} \tag{I.185}$$

Through substitution of equations (I.181) to (I.185), the second principal stress error becomes:

$$d\sigma_2{}^2 = \left(\frac{[(1-\upsilon)\varepsilon_2 + \upsilon(\varepsilon_1 + \varepsilon_2)]}{(1+\upsilon)(1-2\upsilon)} dE\right)^2$$

$$+ \left(\frac{(1-\upsilon-2\upsilon^2)[-\varepsilon_2 + (\varepsilon_1 + \varepsilon_3)]E - [E((1-\upsilon)\varepsilon_2 + \upsilon(\varepsilon_1 + \varepsilon_3))(-1-4\upsilon)]}{(1-\upsilon-2\upsilon^2)^2} d\upsilon\right)^2 \tag{I.186}$$

$$+ \left(\frac{\upsilon E}{(1+\upsilon)(1-2\upsilon)} d\varepsilon_1\right)^2 + \left(\frac{(1-\upsilon)E}{(1+\upsilon)(1-2\upsilon)} d\varepsilon_2\right)^2 + \left(\frac{\upsilon E}{(1+\upsilon)(1-2\upsilon)} d\varepsilon_3\right)^2$$

Similarly, the third principal stress is:

$$\sigma_3 = \frac{E}{(1+\upsilon)(1-2\upsilon)}[(1-\upsilon)\varepsilon_3 + \upsilon(\varepsilon_1 + \varepsilon_2)] \tag{I.187}$$

For plane stress, $\sigma_3 = 0$.

$$0 = \frac{E}{(1+\upsilon)(1-2\upsilon)}[(1-\upsilon)\varepsilon_3 + \upsilon(\varepsilon_1 + \varepsilon_2)] \tag{I.188}$$

Using equation (I.188) and solving for ε_3:

$$\varepsilon_3 = -\frac{\upsilon(\varepsilon_1 + \varepsilon_2)}{(1-\upsilon)} \tag{I.189}$$

The error in ε_3 is:

$$d\varepsilon_3{}^2 = \left(\frac{\partial \varepsilon_3}{\partial \upsilon} d\upsilon\right)^2 + \left(\frac{\partial \varepsilon_3}{\partial \varepsilon_1} d\varepsilon_1\right)^2 + \left(\frac{\partial \varepsilon_3}{\partial \varepsilon_2} d\varepsilon_2\right)^2 \tag{I.190}$$

Where,

$$\frac{\partial \varepsilon_3}{\partial \upsilon} = \frac{-(\varepsilon_1 + \varepsilon_2)}{(1-\upsilon)^2} \tag{I.191}$$

284

$$\frac{\partial \varepsilon_3}{\partial \varepsilon_1} = \frac{\upsilon}{1-\upsilon} \tag{I.192}$$

$$\frac{\partial \varepsilon_3}{\partial \varepsilon_2} = \frac{\upsilon}{1-\upsilon} \tag{I.193}$$

Therefore the error in ε_3 becomes:

$$d\varepsilon_3{}^2 = \left(\frac{-(\varepsilon_1 + \varepsilon_2)}{(1-\upsilon)^2} d\upsilon\right)^2 + \left(\frac{\upsilon}{1-\upsilon} d\varepsilon_1\right)^2 + \left(\frac{\upsilon}{1-\upsilon} d\varepsilon_2\right)^2 \tag{I.194}$$

Shear stress, τ_{LT} can be found using shear strain, γ_{LT} and shear modulus, G:

$$\tau_{LT} = G\gamma_{LT} \tag{I.195}$$

The error in shear stress, $d\tau_{LT}$ is as follows:

$$d\tau_{LT}{}^2 = \left(\frac{\partial \tau_{LT}}{\partial G} dG\right)^2 + \left(\frac{\partial \tau_{LT}}{\partial \gamma_{LT}} d\gamma_{LT}\right)^2 \tag{I.196}$$

Where,

$$\frac{\partial \tau_{LT}}{\partial G} = \gamma_{LT} \tag{I.197}$$

$$\frac{\partial \tau_{LT}}{\partial \gamma_{LT}} = G \tag{I.198}$$

With equations (I.197) and (I.198), equation (I.196) becomes:

$$d\tau_{LT}{}^2 = \left(\gamma_{LT} \cdot dG\right)^2 + \left(G \cdot d\gamma_{LT}\right)^2 \tag{I.199}$$

The error in the experimental strain in the depth is similar to the theoretical error for strain in the depth, $d\varepsilon_D$:

$$\varepsilon_D = -\upsilon\varepsilon_L \tag{I.200}$$

The error is:

285

$$d\varepsilon_D{}^2 = \left(\frac{\partial\varepsilon_D}{\partial\upsilon}d\upsilon\right)^2 + \left(\frac{\partial\varepsilon_D}{\partial\varepsilon_L}d\varepsilon_L\right)^2 \tag{I.201}$$

Where,

$$\frac{\partial\varepsilon_D}{\partial\upsilon} = -\varepsilon_L \tag{I.202}$$

$$\left(\frac{\partial\varepsilon_D}{\partial\varepsilon_L}d\varepsilon_L\right) = -\upsilon \tag{I.203}$$

Substituting equations (I.202) and (I.203) into equation (I.201), the error in the experimental depth strain is:

$$d\varepsilon_D{}^2 = \left(-\varepsilon_L d\upsilon\right)^2 + \left(-\upsilon d\varepsilon_L\right) \tag{I.204}$$

The shear modulus, G can be computed using Poisson's ratio, υ and the modulus of elasticity, E:

$$G = \frac{E}{2(1+\upsilon)} \tag{I.205}$$

Similarly, the shear modulus error, dG is computed from the error in Poisson's ratio, $d\upsilon$ and the error in the modulus of elasticity, dE:

$$dG^2 = \left(\frac{\partial G}{\partial E}dE\right)^2 + \left(\frac{\partial G}{\partial\upsilon}d\upsilon\right)^2 \tag{I.206}$$

Where,

$$\frac{\partial G}{\partial E} = \frac{1}{2(1+\upsilon)} \tag{I.207}$$

$$\frac{\partial G}{\partial\upsilon} = \frac{-2E}{(2(1+\upsilon))^2} \tag{I.208}$$

Using equations (I.206), (I.207) and (I.208), the error in the shear modulus is:

$$dG^2 = \left(\frac{1}{2(1+\upsilon)}dE\right)^2 + \left(\frac{-2E}{(2(1+\upsilon))^2}d\upsilon\right)^2 \tag{I.209}$$

286

I.4 Sample Calculation

I.4.1 Theoretical Strain Sample Calculation

This theoretical strain calculation covers the analysis completed on the first third generation composite tibia compression test in MABTA for Rosette 1, strain gauges 1-3 at an axial load of 100 lbs.

Table I.1: Load values at centre of bone pot

Loads at Bone Pot Centre	lb, lb in	N, Nm
Fx	-7.486	-33.297
Fy	-3.916	-17.420
Fz	102.070	454.029
Mx	31.144	3.519
My	-47.280	-5.342
Mz	0.014	0.002

Table I.2: Distances from the bone pot to the centroid and the centroid to the strain gauge for the position of the first rosette.

	Distance from Bone Pot to Centroid (mm)	Distance from Centroid to Gauge (mm)
X	1.932	-4.680
Y	10.092	16.902
Z	75.057	-

Table I.3: Error values for loads, moments and material geometry and property values.

	Error
dFx	6%*Fx
dFy	4%*Fy
dFz	3%*Fz
dMx	14%*Mxe
dMy	12%*Mye
dMz	1%*Mze
dE	5%*E
dυ	5%*υ
dA	5%*A
dIx	5%*Ix
dIy	5%*Iy
dIxy	5%*Ixy

287
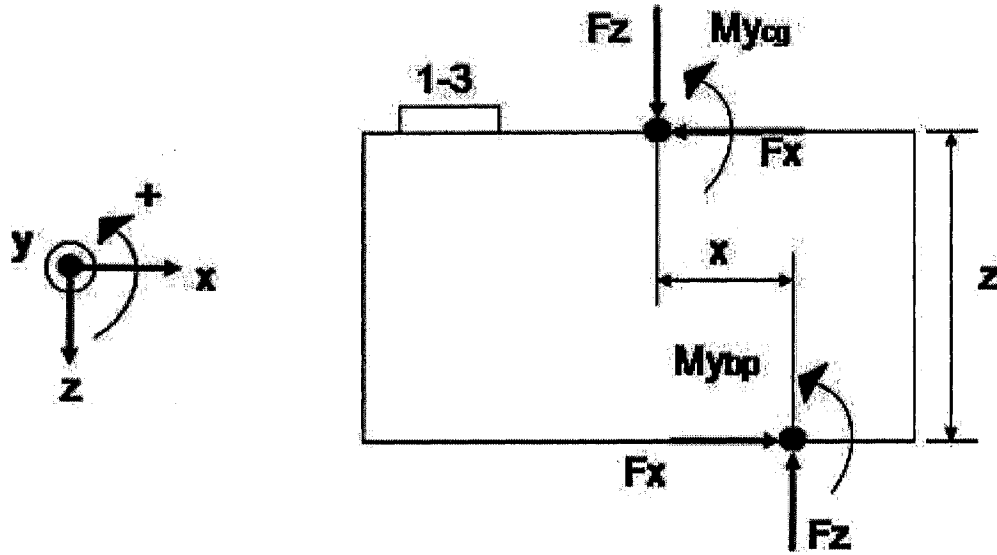
Figure I.3: Free body diagram of the posterior side of composite tibia at position of rosette #1

$$\sum Fx = 0$$
$$\sum Fy = 0$$
$$\sum Fz = 0$$
$$\sum M_{CG} = 0$$

(I.210)

Table I.4: Values for equations (I.211) and (I.212)

Fx	-33.297	N
Fz	454.029	N
My_{bp}	-5.342	Nm
x	1.932	mm
z	75.057	mm
dFx	6%*Fx	N
dFz	3%*Fz	N
dMy_{bp}	12%*My_{bp}	Nm
dx	0.4	mm
dz	0.4	mm

Using the free body diagram in Figure I.3 and the values presented in Table I.4, the moment in the y direction about the centre of gravity and its associated error are presented in equations (I.211) and (I.212), respectively.

288

$$My_{CG} = -My_{bp} - Fz(x) - Fx(z)$$

$$My_{CG} = 6.96 Nm \qquad \text{(I.211)}$$

$$dMycg^2 = \left(dMy_{bp}\right)^2 + \left(z \cdot dFx\right)^2 + \left(Fx \cdot dz\right)^2 + \left(x \cdot dFz\right)^2 + \left(Fz \cdot dx\right)^2$$

$$dMycg = 0.68 Nm \qquad \text{(I.212)}$$

Therefore,

$$My_{CG} = 7.03 \pm 0.68 Nm \qquad \text{(I.213)}$$
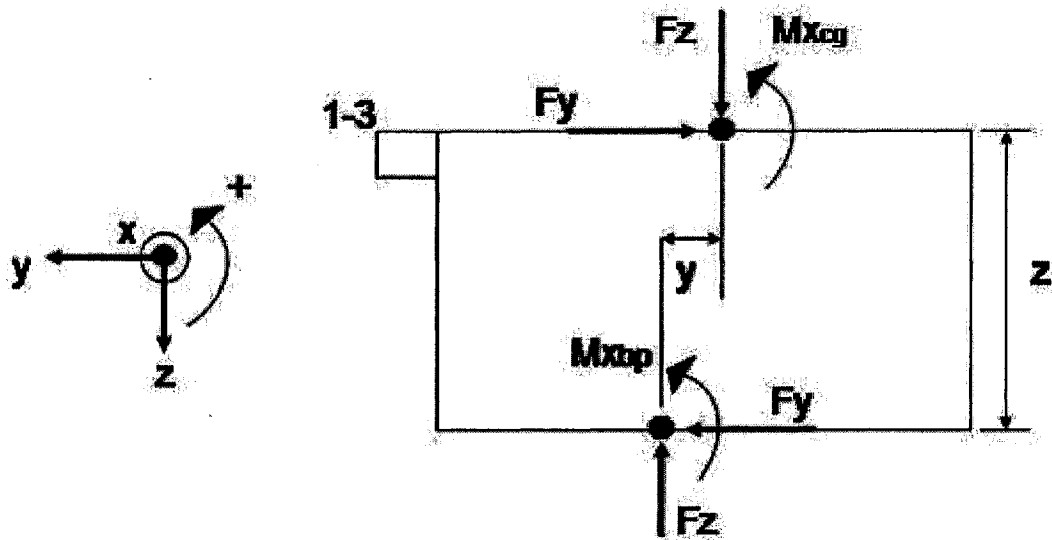
Figure I.4: Free body diagram of the medial side of the composite tibia at position of rosette #1

Table I.5: Values for equations (I.214) and (I.215)

Fy	-17.420	N
Fz	454.029	N
Mx_{bp}	3.519	Nm
y	10.092	mm
z	75.057	mm
dFy	4%*Fy	N
dFz	3%*Fz	N
dMx_{bp}	14%*Mx_{bp}	Nm
dy	0.4	mm
dz	0.4	mm

289

Similarly the free body diagram in Figure I.4 and the values presented in Table I.5 were used to calculate the moment in the x direction about the centre of gravity and its associated error.

$$Mx_{CG} = -Mx_{bp} + Fz(y) + Fy(z)$$
$$Mx_{CG} = -0.244 Nm$$

(I.214)

$$dMxcg^2 = \left(dMx_{bp}\right)^2 + \left(z \cdot dFy\right)^2 + \left(Fy \cdot dz\right)^2 + \left(y \cdot dFz\right)^2 + \left(Fz \cdot dy\right)^2$$
$$dMxcg = 0.5453 Nm$$

(I.215)

Thus,

$$Mx_{CG} = -0.244 \pm 0.545 Nm$$

(I.216)
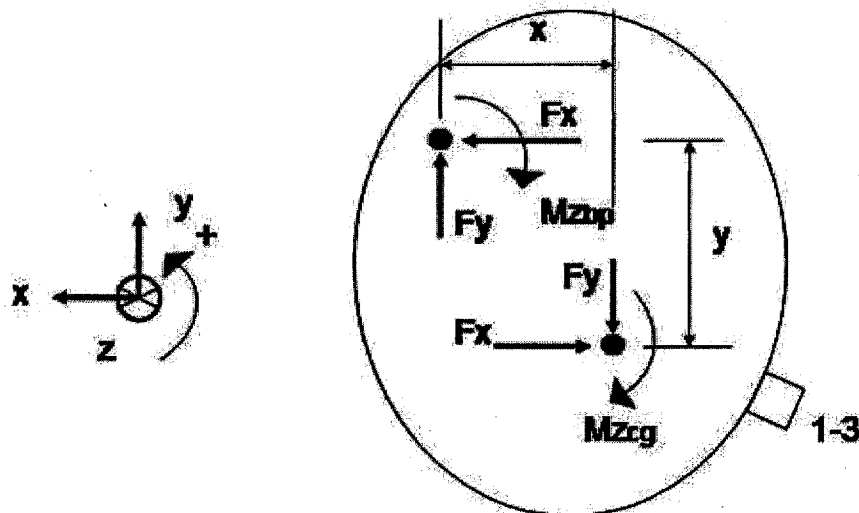
Figure I.5: Free body diagram from the top view of the composite tibia at position of rosette #1

Table I.6: Values for equations (I.217) and (I.218)

Fx	-33.297	N
Fy	-17.420	N
Mz$_{bp}$	0.0016	Nm
x	1.932	mm
y	10.092	mm
dFx	6%*Fx	N
dFy	4%*Fy	N
dMz$_{bp}$	1%*Mz$_{bp}$	Nm
dx	0.4	mm
dy	0.4	mm

290

Same as the previous two moment calculations, the free body diagram in Figure I.5 and the values presented in Table I.6 were used to calculate the moment in the z direction about the centre of gravity and its associated error.

$$Mz_{CG} = -Mz_{bp} + Fx(y) - Fy(x)$$
$$Mz_{CG} = -0.3040Nm$$

(I.217)

$$dMzcg^2 = (dMz_{bp})^2 + (y \cdot dFx)^2 + (Fx \cdot dy)^2 + (x \cdot dFy)^2 + (Fy \cdot dx)^2$$
$$dMzcg = 0.0252Nm$$

(I.218)

$$Mz_{CG} = -0.304 \pm 0.025Nm$$

(I.219)

Table I.7: Values to solve the axial stress and the error in the axial stress

Fz	454.029	N
Acancellous	283.546	m^2
Acortical	410.172	m^2
Ecancellous	1.04×10^8	Pa
Ecortical	1.24×10^{10}	Pa
dA	5%*A	m^2
dE	5%*E	N/m^2

The axial stress is found in equation (I.220) by using the values presented in Table I.7.

$$\sigma_A = \frac{\dfrac{F_{tot}}{\left(1 + \dfrac{A_{canc} \cdot E_{canc}}{A_{cort} \cdot E_{cort}}\right)}}{A_{cort}}$$

(I.220)

$$\sigma_A = -1100542 Pa$$

The error in the axial load is as follows:

$$d\sigma_A^2 = \left(\frac{\partial \sigma_A}{\partial F_{tot}} dF_{tot}\right)^2 + \left(\frac{\partial \sigma_A}{\partial A_{canc}} dA_{canc}\right)^2 + \left(\frac{\partial \sigma_A}{\partial E_{canc}} dE_{canc}\right)^2 +$$
$$\left(\frac{\partial \sigma_A}{\partial A_{cort}} dA_{cort}\right)^2 + \left(\frac{\partial \sigma_A}{\partial E_{cort}} dE_{cort}\right)^2$$

(I.221)

291

$$\left(\frac{\partial \sigma_A}{\partial F_{tot}} dF_{tot}\right)^2 = \left(\frac{E_{cort}}{E_{cort} \cdot A_{cort} + E_{canc} \cdot A_{canc}}\right)^2$$

(I.222)

$$\left(\frac{\partial \sigma_A}{\partial F_{tot}} dF_{tot}\right)^2 = 1.09x10^9 \, Pa^2$$

$$\left(\frac{\partial \sigma_A}{\partial A_{canc}} dA_{canc}\right)^2 = \left(\frac{-F_{tot} \cdot E_{canc} \cdot E_{cort}}{\left(E_{canc} \cdot A_{canc} + E_{cort} \cdot A_{cort}\right)^2}\right)^2$$

(I.223)

$$\left(\frac{\partial \sigma_A}{\partial A_{canc}} dA_{canc}\right)^2 = 1.715x10^6 \, Pa^2$$

$$\left(\frac{\partial \sigma_A}{\partial E_{canc}} dE_{canc}\right)^2 = \left(\frac{-F_{tot} \cdot E_{cort} \cdot A_{canc}}{\left(E_{canc} \cdot A_{canc} + E_{cort} \cdot A_{cort}\right)^2}\right)^2$$

(I.224)

$$\left(\frac{\partial \sigma_A}{\partial E_{canc}} dE_{canc}\right)^2 = 1.006x10^5 \, Pa^2$$

$$\left(\frac{\partial \sigma_A}{\partial E_{cort}} dE_{cort}\right)^2 = \left(\frac{F_{tot} \cdot E_{canc} \cdot A_{canc}}{\left(E_{canc} \cdot A_{canc} + E_{cort} \cdot A_{cort}\right)^2}\right)^2$$

(I.225)

$$\left(\frac{\partial \sigma_A}{\partial E_{cort}} dE_{cort}\right)^2 = 1.006x10^5 \, Pa^2$$

$$\left(\frac{\partial \sigma_A}{\partial A_{cort}} dA_{cort}\right)^2 = \left(\frac{-F_{tot} \cdot E_{cort}^2}{\left(E_{canc} \cdot A_{canc} + E_{cort} \cdot A_{cort}\right)^2}\right)^2$$

(I.226)

$$\left(\frac{\partial \sigma_A}{\partial A_{cort}} dA_{cort}\right)^2 = 2.439x10^{10} \, Pa^2$$

Therefore,

$$d\sigma_A^2 = \left(\frac{\partial \sigma_A}{\partial F_{tot}} dF_{tot}\right)^2 + \left(\frac{\partial \sigma_A}{\partial A_{canc}} dA_{canc}\right)^2 + \left(\frac{\partial \sigma_A}{\partial E_{canc}} dE_{canc}\right)^2 +$$

$$\left(\frac{\partial \sigma_A}{\partial A_{cort}} dA_{cort}\right)^2 + \left(\frac{\partial \sigma_A}{\partial E_{cort}} dE_{cort}\right)^2$$

(I.227)

$$d\sigma_A = 159615 Pa$$

And,

$$\sigma_A = -1.10x10^6 \pm 1.59x10^5 \, Pa$$

(I.228)

292

Table I.8: Values to solve the bending stress and bending stress error

Ix	$5.528\ 10^{-8}$	m^4
Ixy	-1.171×10^{-8}	m^4
Iy	2.466×10^{-8}	m^4
Mx_{bp}	3.519	Nm
My_{bp}	-5.342	Nm
x	-4.680	mm
y	16.902	mm
dIx	5%*Ix	m^4
dIxy	5%*Ixy	m^4
dIy	5%*Iy	m^4
dMx_{bp}	14%*Mx_{bp}	Nm
dMy_{bp}	12%*My_{bp}	Nm

The bending stress was found in equation (I.229) by using the values presented in Table I.8:

$$\sigma_B = \left(\frac{+(MxIy + MyIxy)y - (MyIx + MxIxy)x}{IxIy - Ixy^2} \right)$$

(I.229)

$$\sigma_B = -2687321 Pa$$

The error in the bending stress, $d\sigma_B$ is:

$$d\sigma_B^2 = \left(\frac{\partial \sigma_B}{\partial Mx} dMx \right)^2 + \left(\frac{\partial \sigma_B}{\partial Iy} dIy \right)^2 + \left(\frac{\partial \sigma_B}{\partial y} dy \right)^2 + \left(\frac{\partial \sigma_B}{\partial My} dMy \right)^2$$
$$+ \left(\frac{\partial \sigma_B}{\partial Ixy} dIxy \right)^2 + \left(\frac{\partial \sigma_B}{\partial Ix} dIx \right)^2 + \left(\frac{\partial \sigma_B}{\partial x} dx \right)^2$$

(I.230)

Where,

$$\left(\frac{\partial \sigma_B}{\partial Mx} dMx \right)^2 = \left(\frac{Iy \cdot y - Ixy \cdot x}{IxIy - Ixy^2} \right)^2$$

$$\left(\frac{\partial \sigma_B}{\partial Mx} dMx \right)^2 = 2.592 \times 10^{10}\ Pa^2$$

(I.231)

$$\left(\frac{\partial \sigma_B}{\partial Iy} dIy \right)^2 = \left(\frac{[(IxMy + IxyMx)(Ix(x) - Ixy(y))]}{(IxIy - Ixy^2)^2} \right)^2$$

$$\left(\frac{\partial \sigma_B}{\partial Iy} dIy \right)^2 = 0.952 Pa^2$$

(I.232)

293

$$\left(\frac{\partial \sigma_B}{\partial y} dy\right)^2 = \left(\frac{MxIy + MyIxy}{IxIy - Ixy^2}\right)^2$$

$$\left(\frac{\partial \sigma_B}{\partial y} dy\right)^2 = 8.160x10^8 Pa^2$$

<div align="right">(I.233)</div>

$$\left(\frac{\partial \sigma_B}{\partial My} dMy\right)^2 = \left(\frac{Ixy(y) - Ix(x)}{IxIy - Ixy^2}\right)^2$$

$$\left(\frac{\partial \sigma_B}{\partial My} dMy\right)^2 = 1.149x10^9 Pa^2$$

<div align="right">(I.234)</div>

$$\left(\frac{\partial \sigma_B}{\partial Ixy} dIxy\right)^2 = \left(\frac{-\left(Ixy^2[Mx(x) - My(y)] + 2Ixy[IxMy(x) - IyMx(y)] + IxIy[Mx(x) - My(y)]\right)}{\left(IxIy - Ixy^2\right)^2}\right)^2$$

$$\left(\frac{\partial \sigma_B}{\partial Ixy} dIxy\right)^2 = 0.0572 Pa^2$$

<div align="right">(I.235)</div>

$$\left(\frac{\partial \sigma_B}{\partial Ix} dIx\right)^2 = \left(\frac{(IxyMy + IyMx)(Ixy(x) - Iy(y))}{\left(IxIy - Ixy^2\right)^2}\right)^2$$

$$\left(\frac{\partial \sigma_B}{\partial Ix} dIx\right)^2 = 0.0699 Pa^2$$

<div align="right">(I.236)</div>

$$\left(\frac{\partial \sigma_B}{\partial x} dx\right)^2 = \left(\frac{-(MyIx + MxIxy)}{IxIy - Ixy^2}\right)^2$$

$$\left(\frac{\partial \sigma_B}{\partial x} dx\right)^2 = 1.600x10^{10} Pa^2$$

<div align="right">(I.237)</div>

Which produces:

$$d\sigma_B^2 = \left(\frac{\partial \sigma_B}{\partial Mx} dMx\right)^2 + \left(\frac{\partial \sigma_B}{\partial Iy} dIy\right)^2 + \left(\frac{\partial \sigma_B}{\partial y} dy\right)^2$$

$$+ \left(\frac{\partial \sigma_B}{\partial My} dMy\right)^2 + \left(\frac{\partial \sigma_B}{\partial Ixy} dIxy\right)^2 + \left(\frac{\partial \sigma_B}{\partial Ix} dIx\right)^2 + \left(\frac{\partial \sigma_B}{\partial x} dx\right)^2$$

<div align="right">(I.238)</div>

$$d\sigma_B = 209510 Pa$$

$$\sigma_B = -2.69x10^6 \pm 2.10x10^6 Pa$$

<div align="right">(I.239)</div>

294

Now that the axial and bending stresses are calculated:

$$\sigma_A = -1.10x10^6 \pm 1.59x10^5\,Pa$$
$$\sigma_B = -2.69x10^6 \pm 2.10x10^6\,Pa$$

(I.240)

The longitudinal stress becomes:

$$\sigma_L = \sigma_A + \sigma_B$$
$$\sigma_L = -3.788x10^6$$

(I.241)

The error in the longitudinal stress is as follows:

$$d\sigma_L = \sqrt{\left(\frac{\partial \sigma_L}{\partial \sigma_A} d\sigma_A\right)^2 + \left(\frac{\partial \sigma_L}{\partial \sigma_B} d\sigma_B\right)^2}$$
$$d\sigma_L = 2.63x10^6\,Pa$$

(I.242)

Therefore,

$$\sigma_L = -3.788x10^6 \pm 2.63x10^6\,Pa$$

(I.243)

The shear stress was calculated by substituting the values found in Table I.9 into equation (I.244).

Table I.9: Values to calculate shear stress

A*	488.632	mm^2
Mzbp	0.002	Nm
t	3.093	mm
dA*	5%(A*)	m^2
dMz	1%*Mze	Nm
dt	0.4	mm

$$\tau_{LT} = \frac{Mz}{2A^*t}$$
$$\tau_{LT} = -100587\,Pa$$

(I.244)

295

$$dt_{LT}^{2} = \left(\frac{dMz}{2A^{*}t}\right)^{2} + \left(\frac{-Mz \cdot dA^{*}}{2(A^{*})^{2}t}\right)^{2} + \left(\frac{-Mz \cdot dt}{2(A^{*})t^{2}}\right)^{2}$$ (I.245)

$$d\tau_{LT} = 19593 Pa$$

Thus,

$$\tau_{LT} = -1.01x10^{6} \pm 1.96x10^{5} Pa$$ (I.246)

Using values (I.243) and   (I.243) the von Mises stress is:

$$\sigma' = \sqrt{\frac{2(\sigma_{L})^{2} + 6\tau_{LT}^{2}}{2}}$$ (I.247)

$$\sigma' = 3.79x10^{6} Pa$$

Using:

$$\sigma_{L} = -3.788x10^{6} \pm 2.63x10^{6} Pa$$

$$\tau_{LT} = -1.01x10^{6} \pm 1.96x10^{5} Pa$$ (I.248)

The error in the VM stress is:

$$d\sigma'^{2} = \left(\frac{\sigma_{L} \cdot d\sigma_{L}}{\sqrt{\sigma_{L}^{2} + 3\tau_{LT}^{2}}}\right)^{2} + \left(\frac{3\tau_{LT} \cdot d\tau_{LT}}{\sqrt{\sigma_{L}^{2} + 3\tau_{LT}^{2}}}\right)^{2}$$ (I.249)

$$d\sigma' = 2.63x10^{5} Pa$$

$$\sigma' = 3.79x10^{6} \pm 2.63x10^{5} Pa$$ (I.250)

Using the values found in Table I.10, the VM strain and the longitudinal strain becomes:

Table I.10: Values for equations

Ecortical	1.240x10^{10}	Pa
σ_L	-3.788x10^6	Pa
σ'	3.792x10^6	Pa
dEcortical	5%*E	Pa
dσ_L	2.634x10^5	Pa
dσ'	2.631x10^5	Pa

$$\varepsilon' = \frac{\sigma'}{E}$$

$$\varepsilon' = 3.058x10^{-4}$$ (I.251)

$$\varepsilon' = 305.8\mu$$

$$d\varepsilon'^2 = \left(\frac{1}{E}d\sigma'\right)^2 + \left(-\frac{\sigma'}{E^2}dE\right)^2$$

$$d\varepsilon' = 2.62 \times 10^{-5} \qquad \qquad \text{(I.252)}$$

$$d\varepsilon' = 26.2\mu$$

$$\varepsilon' = 305.8\mu \pm 26.2\mu \qquad \qquad \text{(I.253)}$$

Similarly, the longitudinal strain is:

$$\varepsilon_L = \frac{\sigma_L}{E}$$

$$\varepsilon_L = -3.055 \times 10^{-4} \qquad \qquad \text{(I.254)}$$

$$\varepsilon_L = -305.5\mu$$

The error in the longitudinal strain is:

$$d\varepsilon_L^{\ 2} = \left(\frac{d\sigma_L}{E}\right)^2 + \left(-\frac{\sigma_L \cdot dE}{E^2}\right)^2$$

$$d\varepsilon_L = 2.62 \times 10^{-5} \qquad \qquad \text{(I.255)}$$

$$d\varepsilon_L = 26.2\mu$$

$$\varepsilon_L = -305.5\mu \pm 26.2\mu \qquad \qquad \text{(I.256)}$$

Using the longitudinal strain in equation (I.256), a Poisson's ratio of 0.26 and the error in Poisson's ratio of 5%* 0.26, the transverse strain and the strain in the depth can be calculated:

$$\varepsilon_D = \varepsilon_T = -\upsilon\varepsilon_L$$

$$\varepsilon_D = \varepsilon_T = 79.4\mu \qquad \qquad \text{(I.257)}$$

$$d\varepsilon_D^{\ 2} = d\varepsilon_T^{\ 2} = \left(-\varepsilon_L d\upsilon\right)^2 + \left(-\upsilon d\varepsilon_L\right)^2$$

$$d\varepsilon_D = d\varepsilon_T = 7.9 \times 10^{-6} \qquad \qquad \text{(I.258)}$$

$$d\varepsilon_D = d\varepsilon_T = 7.9\mu$$

Thus,

$$\varepsilon_D = \varepsilon_T = 79.4\mu \pm 7.9\mu \qquad \qquad \text{(I.259)}$$

297

I.4.2 Experimental Strain Sample Calculation

The experimental strain sample calculation covers the computation of the VM strain using experimental strain values from rosette #1, strain gauges 1-3. The first and second principal strains were calculated in equations (I.260) and (I.261), respectively using the experimental strain values presented in Table I.11.

Table I.11: Experimental strain values and their error

ε_a	96.576μ
ε_b	-175.900μ
ε_c	-299.133μ
$d\varepsilon_a$	$3\%*\varepsilon_a$
$d\varepsilon_b$	$3\%*\varepsilon_b$
$d\varepsilon_c$	$3\%*\varepsilon_c$

$$\varepsilon_1 = \frac{1}{2}\left[\varepsilon_a + \varepsilon_c + \sqrt{(\varepsilon_a - \varepsilon_c)^2 + (2\varepsilon_b - \varepsilon_a - \varepsilon_c)^2}\right]$$

$$\varepsilon_1 = 110.2\mu$$

(I.260)

$$\varepsilon_2 = \frac{1}{2}\left[\varepsilon_a + \varepsilon_c - \sqrt{(\varepsilon_a - \varepsilon_c)^2 + (2\varepsilon_b - \varepsilon_a - \varepsilon_c)^2}\right]$$

$$\varepsilon_2 = -312.7\mu$$

(I.261)

The error in the first principal strain is:

$$d\varepsilon_1^2 = \left(\frac{\partial \varepsilon_1}{\partial \varepsilon_a}d\varepsilon_a\right)^2 + \left(\frac{\partial \varepsilon_1}{\partial \varepsilon_b}d\varepsilon_b\right)^2 + \left(\frac{\partial \varepsilon_1}{\partial \varepsilon_c}d\varepsilon_c\right)^2$$

(I.262)

Where,

$$\left(\frac{\partial \varepsilon_1}{\partial \varepsilon_a}d\varepsilon_a\right)^2 = \left(\frac{\sqrt{2}(\varepsilon_a - \varepsilon_b)}{2\sqrt{\varepsilon_a^2 - 2\varepsilon_a\varepsilon_b + 2\varepsilon_b^2 - 2\varepsilon_b\varepsilon_c + \varepsilon_c^2}} + \frac{1}{2}\right)^2$$

$$\left(\frac{\partial \varepsilon_1}{\partial \varepsilon_a}d\varepsilon_a\right)^2 = 1.09x10^{-11}$$

(I.263)

298

$$\left(\frac{\partial \varepsilon_1}{\partial \varepsilon_b} d\varepsilon_b\right)^2 = \left(\frac{\sqrt{2}(2\varepsilon_b - \varepsilon_a - \varepsilon_c)}{2\sqrt{2\varepsilon_b^2 - 2\varepsilon_b(\varepsilon_a + \varepsilon_c) + \varepsilon_c^2 + \varepsilon_a^2}}\right)^2$$ (I.264)

$$\left(\frac{\partial \varepsilon_1}{\partial \varepsilon_b} d\varepsilon_b\right)^2 = 3.47x10^{-12}$$

And lastly,

$$\left(\frac{\partial \varepsilon_1}{\partial \varepsilon_c} d\varepsilon_c\right)^2 = \left(\frac{\sqrt{2}(\varepsilon_c - \varepsilon_b)}{2\sqrt{\varepsilon_c^2 - 2\varepsilon_c\varepsilon_b + \varepsilon_a^2 - 2\varepsilon_b\varepsilon_a + 2\varepsilon_b^2}} + \frac{1}{2}\right)^2$$ (I.265)

$$\left(\frac{\partial \varepsilon_1}{\partial \varepsilon_c} d\varepsilon_c\right)^2 = 1.38x10^{-12}$$

Thus, the error in the first principal stress is:

$$d\varepsilon_1^2 = \left(\left(\frac{\sqrt{2}(\varepsilon_a - \varepsilon_b)}{2\sqrt{\varepsilon_a^2 - 2\varepsilon_a\varepsilon_b + 2\varepsilon_b^2 - 2\varepsilon_b\varepsilon_c + \varepsilon_c^2}} + \frac{1}{2}\right)d\varepsilon_a\right)^2$$

$$+ \left(\frac{\sqrt{2}(2\varepsilon_b - \varepsilon_a - \varepsilon_c)}{2\sqrt{2\varepsilon_b^2 - 2\varepsilon_b(\varepsilon_a + \varepsilon_c) + \varepsilon_c^2 + \varepsilon_a^2}} d\varepsilon_b\right)^2$$

$$+ \left(\left(\frac{\sqrt{2}(\varepsilon_c - \varepsilon_b)}{2\sqrt{\varepsilon_c^2 - 2\varepsilon_c\varepsilon_b + \varepsilon_a^2 - 2\varepsilon_b\varepsilon_a + 2\varepsilon_b^2}} + \frac{1}{2}\right)d\varepsilon_c\right)^2$$ (I.266)

$$d\varepsilon_1 = 3.98x10^{-6}$$
$$d\varepsilon_1 = 3.98\mu$$

299

Similarly, the error in the second principal strain is:

$$d\varepsilon_2^2 = \left(\frac{1}{2} - \frac{\sqrt{2}(\varepsilon_a - \varepsilon_b)}{2\sqrt{\varepsilon_a^2 - 2\varepsilon_a\varepsilon_b + 2\varepsilon_b^2 - 2\varepsilon_b\varepsilon_c + \varepsilon_c^2}} d\varepsilon_a \right)^2$$

$$+ \left(\frac{-\sqrt{2}(2\varepsilon_b - \varepsilon_a - \varepsilon_c)}{2\sqrt{2\varepsilon_b^2 - 2\varepsilon_b(\varepsilon_a + \varepsilon_c) + \varepsilon_c^2 + \varepsilon_a^2}} d\varepsilon_b \right)^2$$

$$+ \left(\frac{1}{2} - \frac{\sqrt{2}(\varepsilon_c - \varepsilon_b)}{2\sqrt{\varepsilon_c^2 - 2\varepsilon_c\varepsilon_b + \varepsilon_a^2 - 2\varepsilon_b\varepsilon_a + 2\varepsilon_b^2}} d\varepsilon_c \right)^2 \tag{I.267}$$

$$d\varepsilon_2 = 4.52x10^{-6}$$

$$d\varepsilon_2 = 4.52\mu$$

As a result, the first and second principal strains are:

$$\varepsilon_1 = 110.2\mu \pm 3.98\mu$$

$$\varepsilon_2 = -312.7\mu \pm 4.52\mu \tag{I.268}$$

With the plane stress assumption, the third principal stress is zero therefore the third

principal strain can be calculated.

For plane stress, $\sigma_3 = 0$.

$$0 = \frac{E}{(1+\upsilon)(1-2\upsilon)} \left[(1-\upsilon)\varepsilon_3 + \upsilon(\varepsilon_1 + \varepsilon_2) \right] \tag{I.269}$$

Using equation (I.269), the first and second principal strain values in (I.268) and

Poisson's ratio of 0.26, the third principal strain, ε_3 is:

$$\varepsilon_3 = -\frac{\upsilon(\varepsilon_1 + \varepsilon_2)}{(1-\upsilon)} \tag{I.270}$$

$$\varepsilon_3 = 71.2\mu$$

The error in ε_3 is:

$$d\varepsilon_3^2 = \left(\frac{\partial \varepsilon_3}{\partial \upsilon} d\upsilon \right)^2 + \left(\frac{\partial \varepsilon_3}{\partial \varepsilon_1} d\varepsilon_1 \right)^2 + \left(\frac{\partial \varepsilon_3}{\partial \varepsilon_2} d\varepsilon_2 \right)^2 \tag{I.271}$$

300

Where,

$$\left(\frac{\partial \varepsilon_3}{\partial \upsilon} d\upsilon\right)^2 = \left(\frac{-(\varepsilon_1 + \varepsilon_2)}{(1-\upsilon)^2}\right)^2$$

(I.272)

$$\left(\frac{\partial \varepsilon_3}{\partial \upsilon} d\upsilon\right)^2 = 23.1$$

$$\left(\frac{\partial \varepsilon_3}{\partial \varepsilon_1} d\varepsilon_1\right)^2 = \left(\frac{\upsilon}{1-\upsilon}\right)^2$$

(I.273)

$$\left(\frac{\partial \varepsilon_3}{\partial \varepsilon_1} d\varepsilon_1\right)^2 = 1.955x10^{-12}$$

$$\left(\frac{\partial \varepsilon_3}{\partial \varepsilon_2} d\varepsilon_2\right)^2 = \left(\frac{\upsilon}{1-\upsilon}\right)^2$$

(I.274)

$$\left(\frac{\partial \varepsilon_3}{\partial \varepsilon_2} d\varepsilon_2\right)^2 = 2.53x10^{-12}$$

Therefore the error in ε_3 becomes:

$$d\varepsilon_3{}^2 = \left(\frac{-(\varepsilon_1 + \varepsilon_2)}{(1-\upsilon)^2} d\upsilon\right)^2 + \left(\frac{\upsilon}{1-\upsilon} d\varepsilon_1\right)^2 + \left(\frac{\upsilon}{1-\upsilon} d\varepsilon_2\right)^2$$

(I.275)

$$d\varepsilon_3 = 4.8\mu$$

$$\varepsilon_3 = 71.2\mu \pm 4.8\mu$$

(I.276)

Table I.12: Values need to calculate the first and second principal stresses

Ecortical	$1.240x10^{10}$	Pa
dEcortical	5%*E	Pa
υ	0.26	-
$d\upsilon$	5%*υ	-
ε_1	110.18μ	-
ε_2	-312.74μ	-
ε_3	71.17μ	-
$d\varepsilon_1$	3.98μ	-
$d\varepsilon_2$	4.52μ	-
$d\varepsilon_3$	4.81μ	-

301

Using Table I.12, the first principal stress, σ_1, can be computed:

$$\sigma_1 = \frac{E}{(1+\upsilon)(1-2\upsilon)}\left[(1-\upsilon)\varepsilon_1 + \upsilon(\varepsilon_2 + \varepsilon_3)\right]$$

(I.277)

$$\sigma_1 = 3.84x10^5 Pa$$

The error in first principal stress, $d\sigma_1$ is:

$$d\sigma_1^2 = \left(\frac{\partial\sigma_1}{\partial E}dE\right)^2 + \left(\frac{\partial\sigma_1}{\partial\upsilon}d\upsilon\right)^2 + \left(\frac{\partial\sigma_1}{\partial\varepsilon_1}d\varepsilon_1\right)^2 + \left(\frac{\partial\sigma_1}{\partial\varepsilon_2}d\varepsilon_2\right)^2 + \left(\frac{\partial\sigma_1}{\partial\varepsilon_3}d\varepsilon_3\right)^2$$

(I. 278)

Where,

$$\left(\frac{\partial\sigma_1}{\partial E}dE\right)^2 = \left(\frac{\left[(1-\upsilon)\varepsilon_1 + \upsilon(\varepsilon_2 + \varepsilon_3)\right]}{(1+\upsilon)(1-2\upsilon)}\right)^2$$

$$\left(\frac{\partial\sigma_1}{\partial E}dE\right)^2 = 3.68x10^8 Pa^2$$

(I.279)

$$\left(\frac{\partial\sigma_1}{\partial\upsilon}d\upsilon\right)^2 = \left(\begin{array}{c}\frac{(1-\upsilon-2\upsilon^2)\left[-\varepsilon_1 + (\varepsilon_2 + \varepsilon_3)\right]E}{(1-\upsilon-2\upsilon^2)^2} \\ -\frac{\left[E((1-\upsilon)\varepsilon_1 + \upsilon(\varepsilon_2 + \varepsilon_3))(-1-4\upsilon)\right]}{(1-\upsilon-2\upsilon^2)^2}\end{array}\right)^2$$

$$\left(\frac{\partial\sigma_1}{\partial\upsilon}d\upsilon\right)^2 = 5.92x10^9 Pa^2$$

(I.280)

$$\left(\frac{\partial\sigma_1}{\partial\varepsilon_1}d\varepsilon_1\right)^2 = \left(\frac{(1-\upsilon)E}{(1+\upsilon)(1-2\upsilon)}\right)^2$$

$$\left(\frac{\partial\sigma_1}{\partial\varepsilon_1}d\varepsilon_1\right)^2 = 3.64x10^9 Pa^2$$

(I.281)

$$\left(\frac{\partial\sigma_1}{\partial\varepsilon_2}d\varepsilon_2\right)^2 = \left(\frac{\upsilon E}{(1+\upsilon)(1-2\upsilon)}\right)^2$$

$$\left(\frac{\partial\sigma_1}{\partial\varepsilon_2}d\varepsilon_2\right)^2 = 5.82x10^8 Pa^2$$

(I.282)

302

$$\left(\frac{\partial \sigma_1}{\partial \varepsilon_3} d\varepsilon_3\right)^2 = \left(\frac{\upsilon E}{(1+\upsilon)(1-2\upsilon)}\right)^2$$

(I.283)

$$\left(\frac{\partial \sigma_1}{\partial \varepsilon_3} d\varepsilon_3\right)^2 = 6.57x10^8 \, Pa^2$$

The first principal stress error is as follows:

$$d\sigma_1{}^2 = \left(\frac{[(1-\upsilon)\varepsilon_1 + \upsilon(\varepsilon_2 + \varepsilon_3)]}{(1+\upsilon)(1-2\upsilon)} dE\right)^2$$

$$+ \left(\frac{(1-\upsilon-2\upsilon^2)[-\varepsilon_1 + (\varepsilon_2 + \varepsilon_3)]E - [E((1-\upsilon)\varepsilon_1 + \upsilon(\varepsilon_2 + \varepsilon_3))(-1-4\upsilon)]}{(1-\upsilon-2\upsilon^2)^2} d\upsilon\right)^2$$

(I.284)

$$+ \left(\left(\frac{(1-\upsilon)E}{(1+\upsilon)(1-2\upsilon)}\right)d\varepsilon_1\right)^2 + \left(\left(\frac{\upsilon E}{(1+\upsilon)(1-2\upsilon)}\right)d\varepsilon_2\right)^2 + \left(\left(\frac{\upsilon E}{(1+\upsilon)(1-2\upsilon)}\right)d\varepsilon_3\right)^2$$

$$d\sigma_1 = 1.06x10^5 \, Pa$$

Thus,

$$\sigma_1 = 3.84x10^5 \pm 1.06x10^5 \, Pa$$

(I.285)

Similarly, the second principal stress, σ_2 is:

$$\sigma_2 = -3.78x10^6 \pm 2.07x10^5 \, Pa$$

(I.286)

Now that the first and second principal stresses are determined, the experimental VM stress can be found.

$$\sigma' = \sqrt{\sigma_1^2 + \sigma_2^2 - \sigma_1 \sigma_2}$$

(I.287)

$$\sigma' = 3.98x10^6 \, Pa$$

And the experimental VM error, $d\sigma'$ is:

$$d\sigma'^2 = \left(\frac{\partial \sigma'}{\partial \sigma_1} d\sigma_1\right)^2 + \left(\frac{\partial \sigma'}{\partial \sigma_2} d\sigma_2\right)^2$$

(I.288)

Where,

303

$$\left(\frac{\partial \sigma'}{\partial \sigma_1} d\sigma_1\right)^2 = \left[\frac{2\sigma_1 - \sigma_2}{2\sqrt{\sigma_1^2 + \sigma_2^2 - \sigma_1\sigma_2}}\right]^2$$

(I.289)

$$\left(\frac{\partial \sigma'}{\partial \sigma_1} d\sigma_1\right)^2 = 3.64x10^9 \, Pa^2$$

$$\left(\frac{\partial \sigma'}{\partial \sigma_2} d\sigma_2\right)^2 = \left[\frac{2\sigma_2 - \sigma_1}{2\sqrt{\sigma_1^2 + \sigma_2^2 - \sigma_1\sigma_2}}\right]^2$$

(I.290)

$$\left(\frac{\partial \sigma'}{\partial \sigma_2} d\sigma_2\right)^2 = 4.24x10^{10} \, Pa^2$$

Producing,

$$d\sigma'^2 = \left(\frac{2\sigma_1 - \sigma_2}{2\sqrt{\sigma_1^2 + \sigma_2^2 - \sigma_1\sigma_2}} d\sigma_1\right)^2 + \left(\frac{2\sigma_2 - \sigma_1}{2\sqrt{\sigma_1^2 + \sigma_2^2 - \sigma_1\sigma_2}} d\sigma_2\right)^2$$

(I.291)

$$d\sigma' = 2.14x10^5 \, Pa$$

$$\sigma' = 3.98x10^5 \pm 2.14x10^5 \, Pa$$

(I.292)

Using the same equation as the theoretical VM strain (I.251), the experimental VM strain is:

$$\varepsilon' = 321.3\mu \pm 23.6\mu$$

(I.293)

304

References

Au A.G., 2008. A comprehensive approach to constructing human bone models: from CT to FE. PhD thesis. University of Alberta.

Harrison, D.M., 2004. Error Analysis in Experimental Physical Science. Propagation of Errors of Precision. 13, Aug. 2008.
<http://www.upscale.toronto.edu/GeneralInterest/Harrison/ErrorAnalysis/Propagation.html>.

Johnson, A. 21 Nov. 2007. Email Communication.

MatWeb: Material Property Data. Online Information Materials Resource. 8 May 2008 < http://www.matweb.com/search/DataSheet.aspx?MatGUID=01f9890437db401d90e120d5d97c4272>.

Reilly, D.T., Burstein, A.H., 1974. The mechanical properties of cortical bone: a review. Journal of Bone and Joint Surgery 56-A (5), 1001-1002.

Salem, M.P. Notes on experimental uncertainty and error analysis. 12 Aug. 2008.
<http://www.theory.caltech.edu/people/politzer/error.pdf>.

Appendix J: Bovine Bone Experiments

The following appendix provides the experimental and theoretical strain comparisons on a bovine tibia (Figure J.1) for the second and third tests as indicated in Chapter 4. Figure J.2 and Figure J.3 present the experimental longitudinal strain values for tests two and three, respectively. Figure J.4 and Figure J.5 compare the theoretical and experimental fi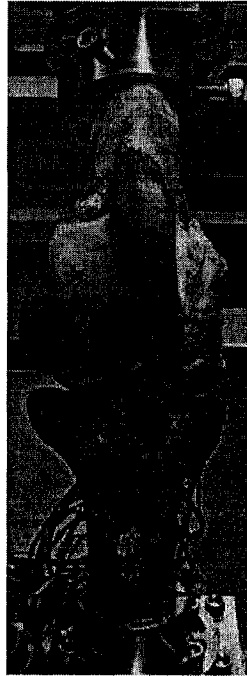rst principal strains for tests two and three, respectively. Lastly, Figure J.6 and Figure J.7 compare the theoretical and experimental second principal strains for tests two and three, respectively.

Figure J.1: Bovine tibia and femur positioned in MABTA

306
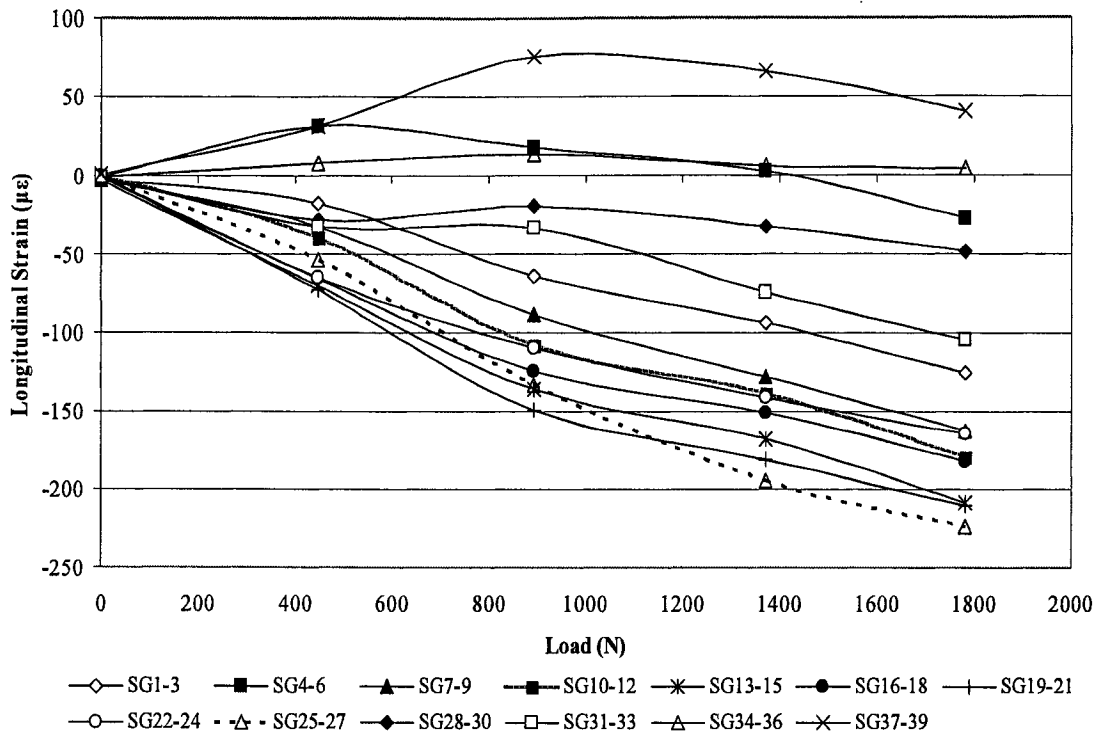
Figure J.2: Experimental longitudinal strains along bovine tibia for test two at 1780 N. Note lines are for visual purposes only.
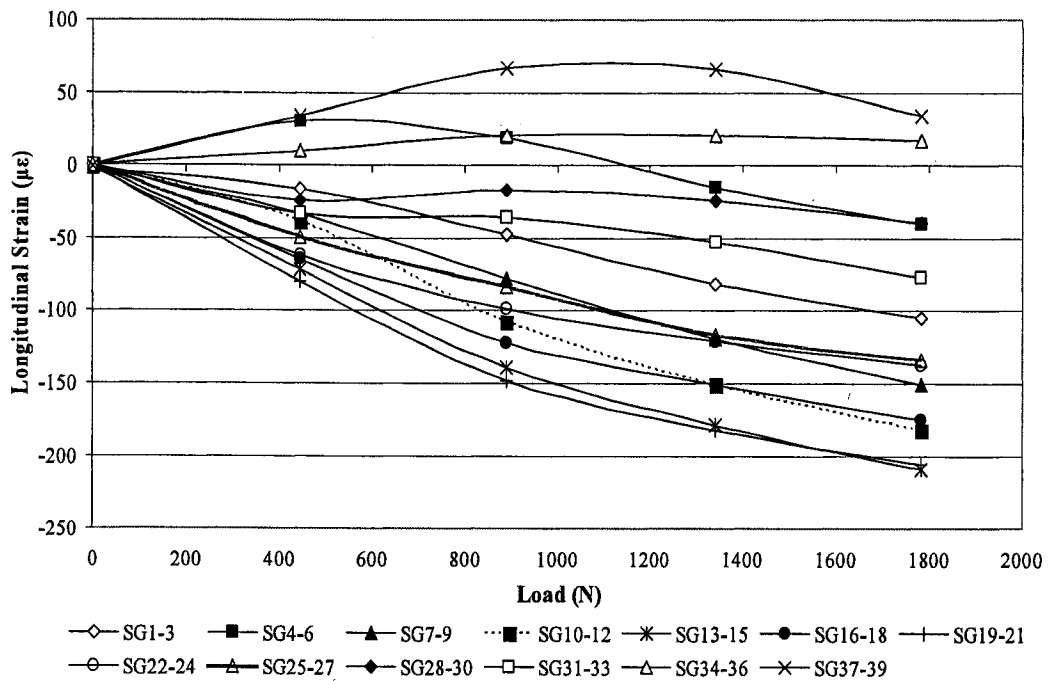

Figure J.3: Experimental longitudinal strains along bovine tibia for test three at 1780 N. Note lines are for visual purposes only.
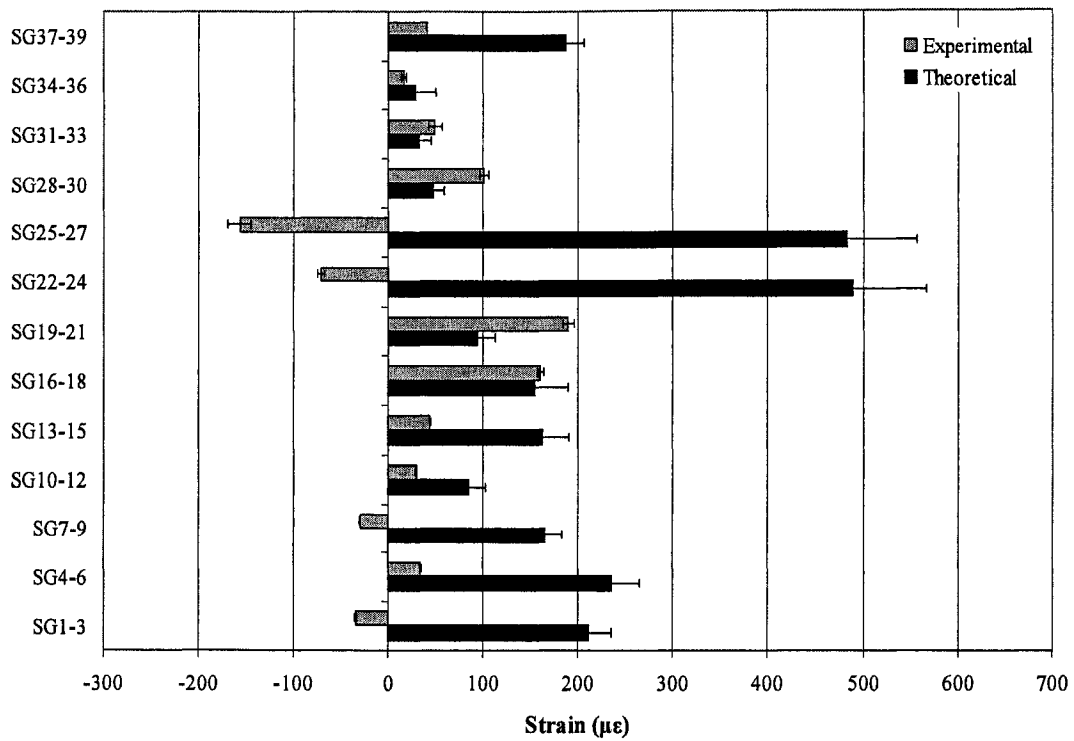
307

Figure J.4: Comparison of first principal strains for test 2 at maximum load. Error bars represent the calculated theoretical and experimental error.
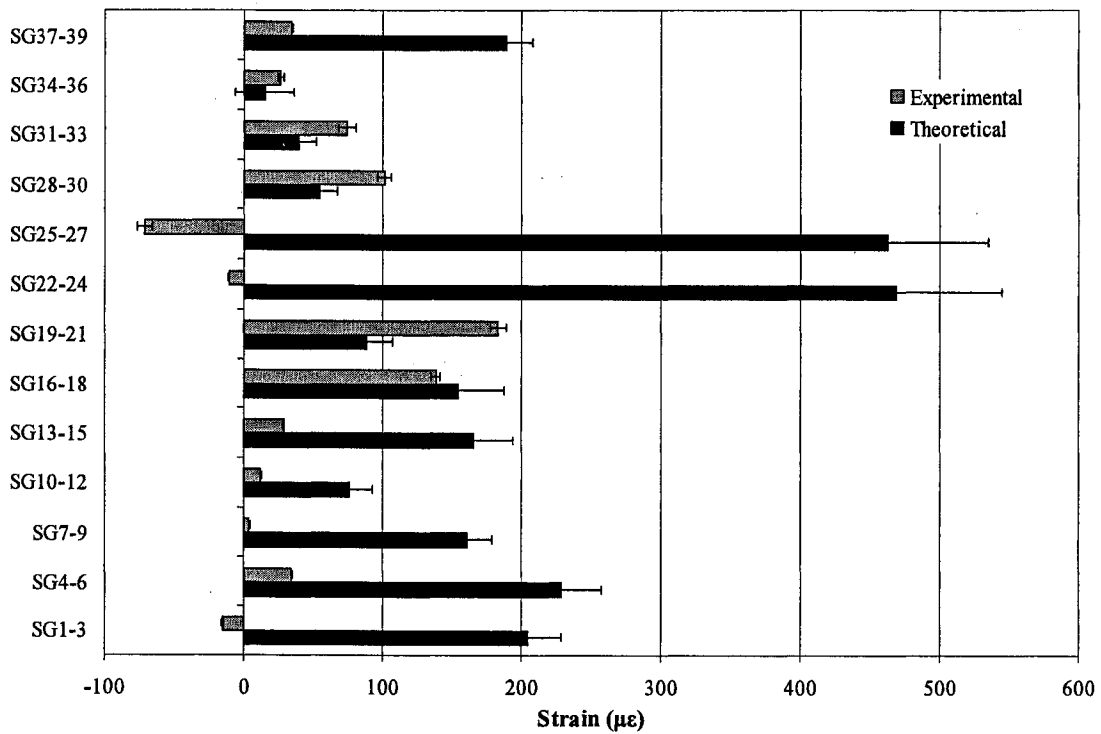

Figure J.5: Comparison of first principal strains for test 3 at maximum load. Error bars represent the calculated theoretical and experimental error.
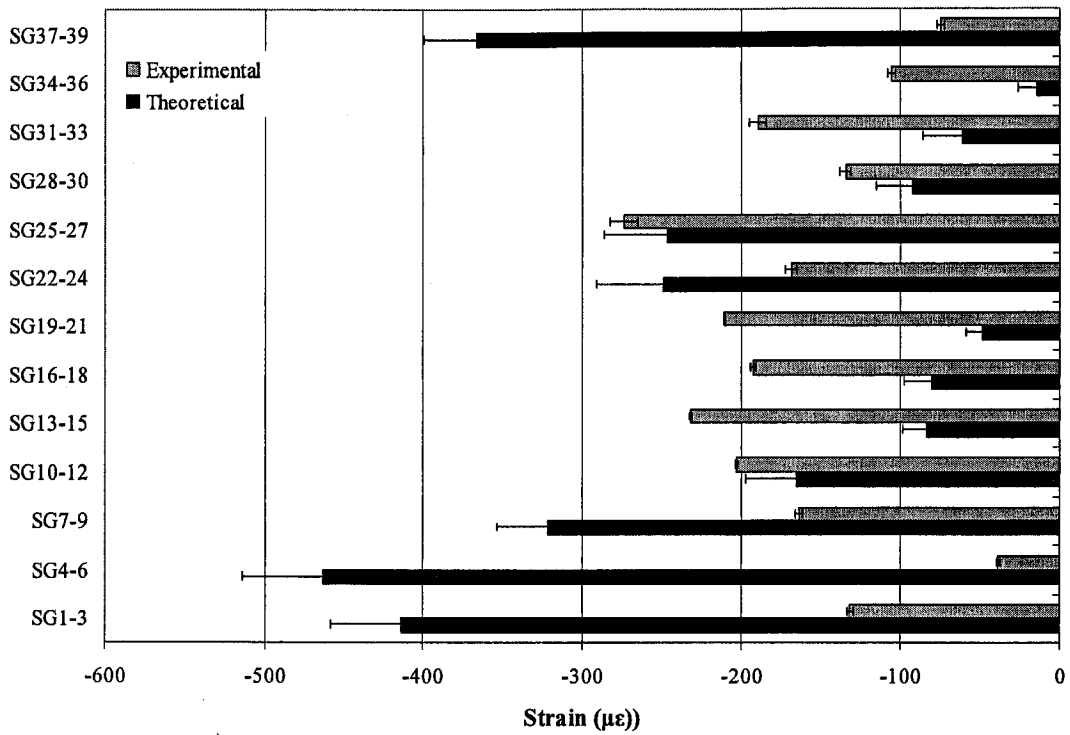
308

Figure J.6: Comparison of second principal strains for test 2 at maximum load. Error bars represent the calculated theoretical and experimental error.
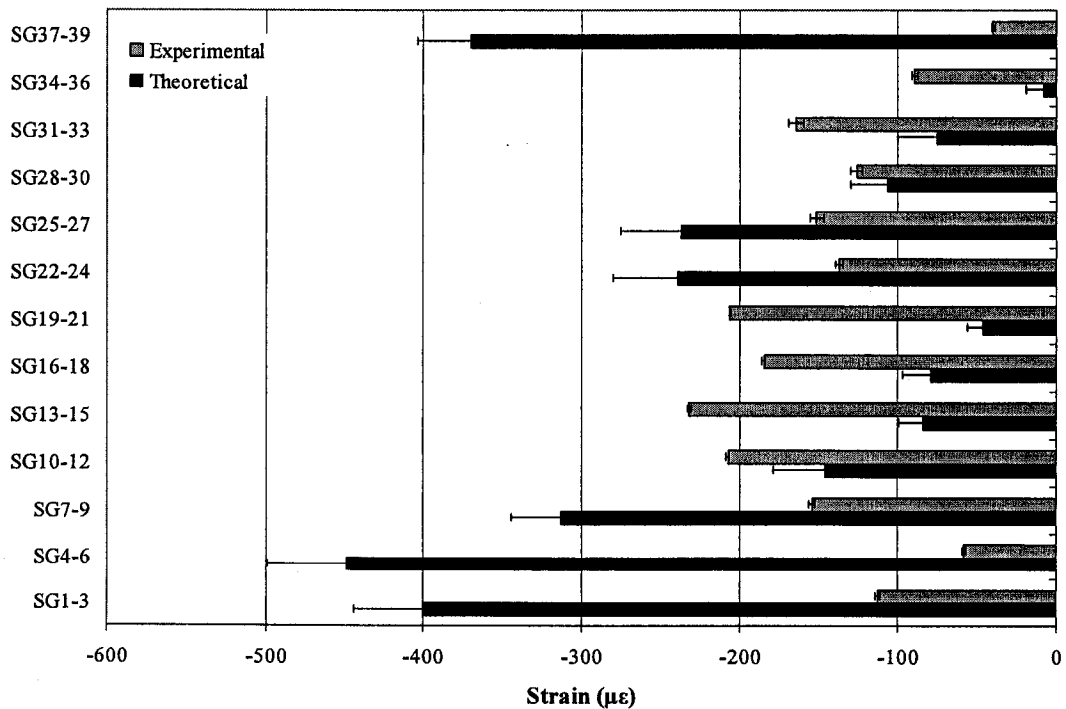

Figure J.7: Comparison of second principal strains for test 3 at maximum load. Error bars represent the calculated theoretical and experimental error.

309